University of Strathclyde

Department of Mechanical & Aerospace Engineering

A Numerical & Experimental Investigation into Size Effects within Loaded Additively Manufactured Cellular Solids

Martin A. Dunn

Submission for the Degree of Doctor of Philosophy,

2018

This thesis is the result of the author's original research. It has been composed by the author and has not been previously submitted for examination which has led to the award of a degree.

Signed: _____ Date: _____

Acknowledgements

Firstly, I would like express my sincere gratitude to my academic supervisor Dr Marcus Wheel for the continued support and guidance that he has given me throughout my postgraduate studies. I would also like to thank the EPSRC for their funding which has made conducting this PhD research possible.

Thank you to all the technicians and support staff within the department of Mechanical & Aerospace Engineering and the wider university who have assisted me throughout my studies. I must also thank Dr Philip Riches and the Biomedical Engineering department for allowing me access to their mechanical testing equipment. I would like to thank my friends and fellow PhD colleagues who have contributed with advice, insightful discussions and technical assistance while generally making my time at the University of Strathclyde a very enjoyable experience.

Finally, I wish to thank my parents, family and girlfriend for all the encouragement, patience and assistance that they have shown during the completion of this thesis and my life in general.

Without your support this would not be possible.

Thank You.

Abstract

The behaviour of heterogeneous materials when loaded cannot be adequately described by classical elasticity as it doesn't account for the presence of internal length-scales. Higher order theories such as micropolar elasticity may be more appropriate, though the additional elastic constants required to fully describe such materials are hard to identify experimentally. In micropolar theory a size effect is predicted in bending and torsion which is revealed as an increase in relative stiffness with decreasing size at scales approaching the cellular microstructure. Thus, at the microstructural level, size and scale becomes an important consideration. Hence, materials which appear homogeneous at a large scale may be heterogeneous at smaller scales when overall size approaches that of the cellular structure. Addressing this issue requires a clear understanding of how scale influences the material's mechanical properties.

Here, the mechanical response of periodic, cellular lattices has been explored within the context of micropolar theory by conducting discrete numerical simulations and experimental tests. It will be shown that the size effects displayed in bending and torsion are strongly dependent on the cellular volume fraction and sample section second moment of area associated with the distribution of the matrix material within the cells comprising the section. Crucially however, these effects may be masked by surface texture and localised loading conditions.

Despite the inherent difficulties associated with experimental testing, the size effects which are predicted by micropolar theory are identified experimentally in an additively manufactured cellular material. The observed size effects showed reasonable agreement to numerical simulations performed in ANSYS. Demonstrating that the behaviour of structured cellular materials with deterministic properties, fabricated by additive manufacturing, can be described by more generalised deformation theories is important as it enables the design and development of new and novel materials to be explored and exploited in lightweight structural applications.

Contents

Acknowledgements **ii**

Abstract **iii**

List of Symbols **viii**

List of Figures **xi**

List of Tables **xviii**

1 Introduction & Background **1**

1.1 Introduction to Cellular Materials 2
1.2 Cellular Structures 2
1.3 Theoretical Investigations in Micropolar Elasticity 4
1.4 Experimental Investigations within the Bounds of Micropolar Elasticity . . . 6
1.5 Edge Effects within a Micropolar Continuum 10
1.6 Analytical & Numerical Modelling of Materials which Exhibit Size Effects . 11
1.7 Additive Manufacturing and 3D Printing Processes 13
1.8 Summary of Previous Work 14
1.9 Research Aims & Overview 15

2 Elasticity Theories **16**

2.1 Linear Cauchy Elasticity 17
2.1.1 Isotropic Solids 17
2.1.2 Anisotropic & Orthotropic Solids 18
2.2 Linear Micropolar Elasticity 20
2.2.1 Constitutive Equations 21
2.2.2 Bending of a Micropolar Beam 22
2.2.3 Torsion of a Micropolar Beam 25
2.3 Summary and Conclusion 27

3 2-Dimensional Lattice Structures **29**

3.1 Sample Loading Modes 30
3.1.1 Numerical (FEA) Simulations of Lattice Structures 30

3.2 Flexural Loading . . . 33
3.2.1 Pure Bending . . . 33
3.2.2 3-Point Flexural Tests . . . 34
3.2.3 Results . . . 36
3.2.4 4-Point Flexural Loading . . . 39
3.2.5 Results . . . 39
3.3 Cell Wall Thickness and Surface Topology Effects . . . 41
3.3.1 Results & Discussion . . . 41
3.4 Summary and Conclusion . . . 44
3.5 Extruded Microstuctured Beam . . . 46
3.5.1 Characteristic Length of Extruded Microstructure Beams . . . 54
3.5.2 Summary and Conclusion . . . 56

4 Numerical & Analytical Identification of Mechanical Properties of a 3D Orthogonal Lattice 58

4.1 Mechanical Properties of a 3D Orthogonal Lattice . . . 59
4.1.1 ANSYS Meshing . . . 59
4.2 Uniaxial Loading . . . 61
4.2.1 Poisson's Ratio . . . 61
4.2.2 Young's Modulus . . . 64
4.3 Shear Loading . . . 67
4.3.1 Shear Modulus . . . 67
4.4 Flexure of Beams Comprising of a Lattice Microstructure . . . 73
4.4.1 Results . . . 75
4.5 Twisting of a Bar with Lattice Microstructure . . . 80
4.5.1 Results and Discussion . . . 82
4.5.2 Characteristic Length . . . 86
4.6 Anticlastic Effects . . . 91
4.6.1 Results & Discussion . . . 92
4.7 Summary & Conclusions . . . 97

5 Numerical Investigation of an Orthogonal Lattice with Internal Braced Members 98

5.1 Introduction . . . 99
5.2 Numerical Simulation Boundary Conditions . . . 100
5.3 Numerical FE Simulation Setup . . . 101
5.4 Results of FE Simulations . . . 102
5.4.1 Uniaxial and Pure Shear Loading . . . 102
5.4.2 Numerical Simulations in Flexure . . . 106
5.4.3 Torsional Characteristics . . . 107
5.4.4 Mixed Cruciform Unit Cell in Torsion . . . 111
5.5 Beam Element Model . . . 113
5.5.1 Beam Element Results . . . 114
5.6 Summary & Conclusion . . . 116

6 Effective Mechanical Properties of a 3D Printed Material 118

6.1 Introduction . . . 119
6.2 Additive Manufacturing Printing Process . . . 121
6.3 Polymer Material Characteristics . . . 124
6.4 Tensile Testing of a 3D Printed Photopolymer . . . 125
6.4.1 Experimental Setup . . . 125
6.4.2 Tensile Test Results . . . 129
6.5 3-Point Bending of Vero Black Samples . . . 136
6.5.1 Experimental Setup . . . 136
6.5.2 3-Point Flexural Test Results . . . 138
6.5.3 Discussion . . . 140
6.6 Conclusion . . . 142

7 Flexural Properties of a Polymer Heterogeneous Beam Sample 143

7.1 Introduction . . . 144
7.1.1 Model Heterogeneous Material . . . 145
7.2 3-Point Flexural Loading of a Cellular Lattice Beam Sample . . . 147
7.2.1 Experimental Setup . . . 147
7.2.2 Experimental Results . . . 150
7.2.3 Computational FE Simulations . . . 155
7.2.4 Results of Computational FE Analysis . . . 155
7.2.5 Discussion of 3-Point Bending Experimental Results . . . 157
7.3 4-Point Flexural Loading of a Cellular Lattice Beam Sample . . . 160
7.3.1 Experimental Setup . . . 160
7.3.2 Preliminary Experiments . . . 163
7.3.3 Experimental Results . . . 166
7.3.4 Discussion of 4-Point Experimental Results . . . 172
7.4 Summary of Flexural Testing Experiments . . . 173

8 Experimental Analysis of a 3D Cellular Lattice in Torsion 175

8.1 Introduction . . . 176
8.2 Experimental Procedure . . . 177
8.3 Results of the Torsion Tests . . . 180
8.4 Discussion . . . 185
8.5 Conclusion . . . 187

9 Summary, Future Work & Conclusions 189

9.1 Summary Discussion of Present Work . . . 190
9.2 Future Work and Further Recommendations . . . 192
9.3 Concluding Remarks . . . 193

Appendix A Verification of Loading Modes in ANSYS 195

A.1 Torsional Loading 195
A.2 Results of Numerical Simulations 199
A.3 Summary 200

Appendix B Validation of Experimental Torsional Loading Setup 205

B.1 Numerical FE Model of Experimental Apparatus 205
B.2 Results of Numerical Simulations 208

Appendix C Experimental Tests 214

C.1 Development of a 3 and 4-Point Bending Support 214
C.2 Specimen Grips for Torsion Tests 220
C.3 MATLAB Data Analysis 224

Appendix D Results of Numerical Simulations 227

D.1 Braced Cubic Lattice - Mechanical Properties 227

Bibliography 228

Image Bibliography 232

List of Symbols

Roman letters

AR	Sample aspect ratio.
A_f	Area fraction.
A	Area.
C	Constant.
E^*	Micropolar Young's modulus.
E_s	Young's modulus.
G^*	Micropolar shear modulus.
G_s	Shear modulus.
I^*	Discrete second moment of area.
I_p	Torsion constant.
I_s	Second moment of area.
J'	Micropolar flexural rigidity ; Micropolar torsional rigidity.
J	Flexural rigidity ; Torsional rigidity.
K^*	Micropolar bulk modulus.
K	Beam stiffness ; Bulk modulus.
L	Beam length.
M	Bending moment.
N	Coupling number.
P	Applied force.
Q	Shear Force.
R	Radius of curvature.
SX	Cell spacing in x-direction.

SY	Cell spacing in y-direction.
SZ	Cell spacing in z-direction.
T	Torque.
U	Translational displacement.
V_f	Volume fraction.
a_r	Zener ratio.
a	Cell size.
b	Beam breadth.
d	Beam depth.
l_b	Characteristic length in bending.
l_c	Magnitude of the characteristic length.
l_t	Characteristic length in torsion.
m_{ij}	Couple stress tensor.
r	Radius.
t	Cell wall thickness.
u_i	Displacement vector.
w	Displacement.
y	Distance from the neutral axis.

Greek letters

Δ	Change in length.
Ω	Rigidity ratio.
α	Micropolar elastic constant.
β	Micropolar elastic constant.
χ	Micropolar torsion tensor.
ϵ'	Transverse strain.
ϵ_{ij}	Strain tensor.
ϵ	Axial strain.
η	Ratio of cell wall thickness to depth.
γ	Micropolar couple modulus ; Shear strain (linear elastic Cauchy solids).
κ	Micropolar elastic constant ; Timoshenko shear coefficient.
λ	Micropolar Lamé's constant.

μ	Micropolar shear modulus ; Shear modulus (linear elastic Cauchy solids).
ν^*	Micropolar Poisson's ratio.
ν	Poisson's ratio.
ϕ_i	Rotation vector.
ϕ	Diameter.
ψ	Polar ratio.
σ	Direct stress.
τ	Shear stress.
θ	Angle of rotation.

Mathematical letters

C_{ijkl}	Stiffness matrix.
S_{ijkl}	Compliance matrix.
δ_{ij}	Kronecker delta.
e_{ijk}	Permutation tensor.

List of Figures

Chapter 1

1.1 Examples of naturally occurring cellular materials. (a) cork oak, (b) beehive honeycomb and (c) natural sponge. 3
1.2 Examples of man-made foamed materials. (a) closed cell metallic foam, (b) open celled polyurethane and (c) digitally printed foamed lattice structure. . . 3

Chapter 2

2.1 General stress components in an element of material 17
2.2 Stress, τ_{ij} and couple stress, m_{ij} components required to fully describe a micropolar material. 20
2.3 Stresses and couple stresses acting in a micropolar beam under bending. . . . 22
2.4 (a) 3-Point bending setup, (b) 4-Point bending setup. 24
2.5 Stresses and couple stresses acting in a micropolar beam subjected to a torsional load. 26

Chapter 3

3.1 Two possible unit cell configurations that can be used to define a matrix of orthogonally connected bars in a lattice configuration. (a) 'Closed' cell configuration, (b) 'Open' cell case. 32
3.2 Variation in flexural stiffness of samples with specimen size. Smaller samples are relatively stiffer than larger ones. 34
3.3 3-point bend tests modelled using half symmetry boundary conditions. 35
3.4 Variation in observed stiffness with beam aspect ratio. Sample size increases with decreasing $1/\text{depth}^2$. The stiffness of the beams is normalised by the Young's modulus of the cellular material. 36
3.5 Variation in stiffness of samples at different aspect ratios derived analytically from a modified Timoshenko formula. Data is compared to the simulated results in ANSYS. All tests are based on a unit cell with dimensions; SX=SY=1 mm , t=0.1 mm. The stiffness of the beams are normalised by the Young's modulus of the cellular material. 38
3.6 Variation in stiffness of beams with change in sample depth. The inner section of the beams have an aspect ratio of 6 and 12. The overall aspect ratio of the beams are 10 and 20 respectively. 40

3.7 Variation in normalised rigidity with variation in cell wall thickness. Solid lines represent beams with a solid outer surface. Dashed lines represent beams whereby the voids are intersected by the specimen surface. 43
3.8 Variation in the magnitude of the size effect of beams with an in-line square lattice microstructure with respect to void area fraction. Samples with a continuous outer surface are represented by the solid line while the dashed line represents the case where the voids are exposed at the surface of the beams. . 44
3.9 2D cross section of unit cell 46
3.10 Extruded beam from a 2D cross section of a unit cell. 47
3.11 Variation in beam rigidity with normalised cell wall thickness for various cell area fractions. 49
3.12 Extruded microstructure beam and 2D cross section of a typical sample. . . . 50
3.13 Variation in normalised rigidity with cell wall thickness for various cell area fractions. The rigidity is seen to decrease with increasing sample size. 52
3.14 Variation in normalised rigidity with cell wall thickness for various cell area fractions. The rigidity is seen to decrease with increasing sample size. 53

Chapter 4

4.1 (a) Beam with cubic lattice microstructure, (b) Unit cell of the material. . . . 59
4.2 A meshed unit cell. 60
4.3 Unit cell of lattice material subjected to an axial load. 62
4.4 Variation in observed Poisson's ratio with relative cell density. The analytical estimation presented in equation 4.8 generally overestimates the contraction within the material. 63
4.5 Magnitude in the difference between the Poisson's ratio derived from FEA and the closed form approximation. 64
4.6 Comparison between the variation in the analytical approximation of the Young's modulus and FE prediction. 66
4.7 3x3 cellular lattice subjected to a symmetric shear stress. 67
4.8 Unit cell connectivity. 69
4.9 A unit cell of material. Displacement boundary conditions are applied at the external surfaces which are denoted in relation to the major perpendicular axes. 70
4.10 FE results for the variation in shear modulus with varying cell wall thickness, expressed in terms of the cell volume fraction. 71
4.11 Variation in the analytical approximation of the shear modulus against simulated values with varying normalised cell wall thickness, η. A linear relationship can be observed when η is less than 40%. 72
4.12 Simulated shear modulus normalised against $E_s/2(1+\nu^*)$. A linear variation can be observed when plotted against the volume fraction cubed. 72
4.13 Variation in the numerical estimation of the shear modulus normalised against the finite element solution. Equation 4.29 is valid at volume fractions below 50% and equation 4.30 applies above 50%. 73
4.14 Unit cells representative of the bulk lattice material. (a) 'Cubic' unit cell, (b) '3D Cruciform' unit cell. 74

4.15 Variation in the size effect when the flexural rigidity divided by the sample cross sectional area is plotted against sample depth squared. The Flexural modulus can be obtained from the slope of the linear portion of the graph. Size effects are interpreted from the intercept with the vertical axis. Samples generated by the cruciform lattice have a discontinuous exterior surface. . . . 75
4.16 Variation in the size effect when flexural rigidity is plotted against the inverse of the sample depth. Samples generated by the cruciform lattice have a discontinuous exterior surface. . . . 76
4.17 Variation in the uniaxial and flexural material modulus with change in volume fraction. . . . 77
4.18 Variation in the magnitude of the size effect in bending, ${l_c}^2$ with void volume fraction. Here, the horizontal axis increases with decreasing sample density. . 78
4.19 Variation in characteristic length in bending with void volume fraction. Here, the horizontal axis increases with decreasing sample density. . . . 78
4.20 Variation in the rigidity ratio with sample size for various cell void volume fractions. . . . 79
4.21 Translational forces applied to the end face of the bar by the pilot node. . . . 81
4.22 Variation torsional rigidity with size for a typical square bar consisting of a lattice microstructure. . . . 83
4.23 Variation in simulated shear modulus with material volume fraction. . . . 84
4.24 Variation in analytical approximation of the shear modulus against simulated values with varying normalised cell wall thickness, η. A linear relationship can be observed when η is less than 40 %. . . . 85
4.25 Variation in analytical approximation from the simulated values with volume fraction. Equation 4.37 is valid below 50% volume fraction while equation 4.36 is applicable to samples which are greater than 50%. The calculated values are accurate to 5% in this range. . . . 85
4.26 Variation in torsional rigidity with varying cell wall thickness with increasing sample depth (Cubic unit cell.). . . . 87
4.27 Variation in torsional rigidity with varying cell wall thickness with increasing sample depth. (3D Cruciform unit cell.) . . . 87
4.28 Variation in the magnitude of the characteristic length with varying void volume fraction for a lattice beam comprised of orthogonal bars. Negative values indicate that a softening effect is seen with diminishing sample size. The increase in size effect observed with diminishing cell volume fraction is only valid when $t > 0$. . . . 88
4.29 Variation in the characteristic length in torsion with varying void volume fraction. The increase in size effect observed with diminishing cell volume fraction is only valid when $t > 0$. . . . 89
4.30 Variation in the ratio of characteristic length in torsion to the characteristic length in bending with volume fraction. . . . 90
4.31 Beams subjected to a constant moment load. Wide beams display a distinct out of plane bending effect. . . . 91
4.32 Variation in micropolar modulus, γ, when out of plane bending effects are suppressed (Plane strain). . . . 95

4.33 Variation in micropolar modulus, γ, when beam is free to bend in the out of plane direction. 96

Chapter 5

5.1 Braced cube with diagonal cross members. 99
5.2 Variation in Young's modulus with material volume fraction. Here, the interior beams are of fixed diameter while the exterior beam diameter is varied. . 102
5.3 Variation in Young's modulus with material volume fraction. Here, the exterior beams are of fixed diameter while the interior beam diameter is varied. . 103
5.4 Variation in shear modulus with material volume fraction. Here, the exterior beams are of fixed diameter while the interior beam diameter is varied. 104
5.5 Variation in shear modulus with material volume fraction. Here, the interior beams are of fixed diameter while the exterior beam diameter is varied. 104
5.6 Variation in Poisson's ratio with material volume fraction. Here, the interior beams are of fixed diameter while the exterior beam diameter is varied. 105
5.7 Variation in bulk modulus with material volume fraction. Here, the interior beams are of fixed diameter while the exterior beam diameter is varied. 105
5.8 Influence of sample aspect ratio on the normalised beam rigidity for a sample where $\phi_E = \phi_I = 0.5$ mm $SX = 5$ mm. Samples converge with increasing aspect ratio and number of cells through the depth. Beams of equivalent depth are normalised against the sample with an aspect ratio of 10. 107
5.9 Variation in the magnitude of the characteristic length with fixed exterior beam diameter. 108
5.10 Variation in the magnitude of the characteristic length with fixed interior beam diameter. 108
5.11 Variation in the magnitude of the characteristic length for torsion with void volume fraction when exterior beam diameters are fixed. 110
5.12 Variation in the magnitude of the characteristic length for torsion with void volume fraction when interior beam diameters are fixed. 110
5.13 Alternate unit cell configuration of the braced cubic lattice. 111
5.14 Variation in the size effect with volume fraction in torsion observed when the unit cell is intersected by the sample surface. (Denoted by broken lines.) The diameter of the exterior beams are fixed. Solid lines denote 'closed' cell samples. 112
5.15 Variation in the size effect with volume fraction in torsion observed when the unit cell is intersected by the sample surface. (Denoted by broken lines.) The diameter of the interior beams are fixed. Solid lines denote 'closed' cell samples. 113
5.16 Comparison between the flexural modulus derived by beam elements and solid elements at varying volume fraction. The beam element model is represented by solid lines. Solid elements are denoted by broken lines. 115
5.17 Comparison between the shear modulus derived by beam elements and solid elements at varying volume fraction. The beam element model is represented by the solid lines. Solid elements are denoted by broken lines. 115

5.18 Variation in the characteristic length in bending with void volume fraction. Beam elements models are represented by the solid lines while solid elements are denoted by broken line. 116
5.19 Variation in characteristic length for torsion with void volume fraction. Beam element model are represented by solid lines while solid elements are denoted by broken lines. 117

Chapter 6

6.1 Print head injection process. A fine layer of the liquid polymer is sprayed onto the top surface before being cured with UV light. 122
6.2 Possible orientation of the samples within the printer. Samples have been aligned to either the x, y or z axis. 123
6.3 Orientation of the layers within a printed sample with respect to the placement within the printer. Alternating blue and white cylinders denote incrementation in the y-axis. Each sample can be orientated in two different ways after production. 123
6.4 Tensile test specimen (All units are in mm.). 126
6.5 Tensile test experimental setup. 126
6.6 A selection of the tensile test specimens printed at different orientations within the printer. The outer white markings denote the positioning of the grips on the sample. 127
6.7 Comparison of the typical response of the material subjected to different rates of loading for samples printed in the x orientation. 129
6.8 Variation in load with displacement for a typical set of tensile test specimens. 131
6.9 Variation in load with time for a typical set of tensile test specimens. 131
6.10 Variation in observed tangent modulus with time for samples that are aligned to the x-axis during manufacturing. 133
6.11 Variation in observed tangent modulus with time for samples that are aligned to the y-axis during manufacturing. 134
6.12 Variation in observed tangent modulus with time for samples that are aligned to the z-axis during manufacturing. 135
6.13 Possible dumbbell sample orientations within the testing apparatus. 137
6.14 3-point bending setup of small specimen samples. 137
6.15 Typical load response for a sample of VeroBlackPlus in 3-point bending. . . . 139
6.16 Typical variation in displacement with time of a VeroBlackPlus sample in 3-point bending. 139
6.17 Variation in flexural modulus with sample print direction. 140
6.18 Samples aligned to the Z-axis during printing have visible distortion of the layers on the specimen surface. 141

Chapter 7

7.1 Beam with cubic lattice microstructure and example unit cell. 145
7.2 A typical set of samples used to perform 3 & 4-point bend tests. 146

7.3 Deflection of a typical beam sample in 3-point flexural loading within the experimental apparatus. 148
7.4 Variation in load with deflection for a typical sample tested in 3-point bending. 149
7.5 Variation in normalised flexural stiffness with sample size at an aspect ratio of 16 when loaded at 0.08 mms^{-1}. 152
7.6 Variation in normalised flexural stiffness with sample size at an aspect ratio of 16 when loaded at 0.08 mms^{-1}. 152
7.7 Variation in normalised flexural stiffness with sample size at an aspect ratio of 16 when loaded at 0.08 mms^{-1}. 153
7.8 Variation in normalised flexural stiffness with sample size at an aspect ratio of 16 when loaded at 0.08 mms^{-1}. 153
7.9 Variation in the flexural modulus of the lattice samples with print direction and sample orientation at an aspect ratio of 16. 154
7.10 Variation in the flexural modulus of the lattice samples with print direction and sample orientation at an aspect ratio of 10. 154
7.11 Variation in sample stiffness with aspect ratio for beams subjected to 3-point bending as predicted from finite element analysis. 156
7.12 Four-point bending experimental test setup. 161
7.13 A slender beam subjected to four-point flexural loading. 162
7.14 Comparison between normalised stiffness of FEA models with experimental samples. A poor correlation between sample size and stiffness is observed when equation 7.5 is used to derive the mechanical properties. 164
7.15 Variation in flexural stiffness with sample size at an aspect ratio of 16-8. . . . 167
7.16 Variation in flexural stiffness with sample size at an aspect ratio of 16-8. . . . 168
7.17 Variation in flexural stiffness with sample size at an aspect ratio of 16-12. . . 169
7.18 Variation in flexural stiffness with sample size at an aspect ratio of 16-12. . . 170
7.19 Variation in normalised flexural stiffness of all experimental data as compared with FE simulations in ANSYS. Data is normalised to account for the variation in sample breadth and test aspect ratio. 172

Chapter 8

8.1 Top down view of a grip used to constrain the samples with an even number of rows. The cross-section of a 4×4 specimen has been superimposed to indicate the typical specimen placement. 178
8.2 A typical set of samples used to investigate the torsional properties of the material. 179
8.3 A specimen loaded in torsion. The load cell and rotational actuator not shown in this picture are connected to the upper pneumatic air grip. 181
8.4 Variation in torque with applied angle of rotation for a beam printed in the x orientation with 6 rows of cells through the breadth and depth. The sample stiffness can be interpreted from the linear region in the loading and unloading slope. 182

8.5 Variation in the torsional rigidity of the material at varying size scales when printed in the x orientation. Here, pins are inserted 10 mm into each sample under test. 182
8.6 Variation in discrete sample stiffness with size. Pins are inserted to a depth of 1 mm. 184
8.7 Variation in discrete sample stiffness with size. Pins are inserted to a depth of 10 mm. 184

Appendix A

A.1 Boundary conditions for rotational loading with unrestrained warping. 197
A.2 Circular, Square and I-shaped cross-sectional samples used to validate loading method. 198
A.3 Comparison of the variation in torsional rigidity with aspect ratio for an I-section beam subjected to free and restrained axial displacement on the end faces. 200
A.4 Cylindrical bar 202
A.5 Bar with square cross-section 203
A.6 I-beam 204

Appendix B

B.1 Simulated setup for experimental torsion tests. 207
B.2 Variation in apparent shear modulus for individual samples with a pin insert depth of 10 mm. The stiffness is seen to converge with increasing sample size. 208
B.3 Variation in apparent shear modulus for individual samples with a pin insert depth of 1 mm. The stiffness is seen to converge with increasing sample size. 209
B.4 Typical variation in axial displacement (mm) within the cross-section for a slender bar of various sizes loaded in torsion. 212

Appendix C

C.1 Support beam manufactured for use in the 3-point and 4-point flexural experiments. 215
C.2 Variation in load with applied deflection for a slender beam sample. The normalised stiffness, K/b, was calculated to be $0.4458Nmm^{-2}$. Noisy data is filtered in MATLAB during processing. 225
C.3 Variation in load with applied deflection for a slender beam sample. The normalised stiffness, K/b, was calculated to be $0.4534Nmm^{-2}$. 226

List of Tables

Chapter 3

3.1 Mechanical properties for a planar square lattice of varying void fraction derived from samples with a continuous surface subject to a constant moment loading. 42
3.2 Mechanical properties for a planar square lattice of varying void fraction derived from samples with a discontinuous surface subject to a constant moment loading. The magnitude of the characteristic length, l_b in this case is a representative value as ${l_b}^2$ is negative. 42

Chapter 4

4.1 Variation in the maximum and minimum values of the flexural properties derived from numerical tests. 93

Chapter 6

6.1 Tensile test specimen geometry. 125

Chapter 7

7.1 Variation in observed micropolar material properties derived from experimental 3-point bend tests of samples loaded at 0.08 mms^{-1}. 151
7.2 Variation in observed micropolar material properties derived from experimental 3-point bend tests of samples loaded at 0.05 mms^{-1}. 151
7.3 Variation in apparent micropolar material properties derived from 3-point bend test simulations. 156
7.4 Comparison of the variation in flexural modulus and characteristic length obtained by experiment and numerical simulation for samples tested in 3-point bending at an aspect ratio of 16. 158
7.5 Summary of the results of the 4-point flexural tests. 166
7.6 Micropolar properties from 4-point bending simulations in ANSYS. 171

Chapter 8

8.1 Observed shear modulus and characteristic length in torsion for experiments conducted with a pin depth of 1 mm. 185

8.2 Observed shear modulus and characteristic length in torsion for experiments conducted with a pin depth of 10 mm. 186

Appendix A

A.1 Comparison of the beam stiffness for various cross-sections. 199

Appendix B

B.1 Comparison of the mechanical properties obtained for the sample under ideal conditions and from a simulation of the experimental setup. Separate measurements were recorded using the reaction forces of the machine and also those on the sample itself. 211

Appendix D

D.1 Calculated mechanical properties at varying interior beam diameters. 227

Chapter 1

Introduction & Background

Materials which are either naturally occurring or man-made can exhibit a wide array of mechanical properties which are dependent on the composition of the solid constituents from which they are comprised. In heterogeneous materials, the presence of microstructural features at the macroscopic level can give rise to size dependent effects which are not captured through general homogeneous theories of deformation. The presence of scale in materials requires that higher order theories be developed which account for the variations in the material behaviour with size.

In this chapter, a general overview is given of existing higher order theories and experimental verification procedures which are in use along with a summary of how they have been utilised to mechanically characterise existing materials with significant microstructural features.

1.1 Introduction to Cellular Materials

The emergence of digital manufacturing processes in recent years, has given engineers the opportunity to create new and novel materials which has not been possible with traditional manufacturing techniques. Cellular solids such as honeycombs and structural foams are examples of materials which are of particular interest due to the relatively high strength to mass ratios that can be achieved in comparison to more traditional solids such as metals (Gibson & Ashby, 1999). While foamed materials offer many advantages, there has been a reluctance to exploit them in structurally critical applications due to the uncertainty that is brought upon by the random nature of the microstructure composition. Honeycombs on the other hand, while more deterministic, are inherently anisotropic which may limit the scope of their use. Regular foamed materials such as lattice structures can exhibit an increase in strength when compared to stochastically distributed foams of similar density (Deshpande et al., 2001). The design and implementation of more deterministic and potentially isotropic foamed materials is of great interest as it could go a long way to enhancing the range of materials which are currently on offer to engineers.

At present, a wide array of additive manufacturing processes are available which utilise a variety of different materials (Gibson et al., 2015). The consequence of this is that generated components may be unique to both the matrix material used and the underlying manufacturing technology (Mueller et al., 2015). In order to fully exploit the potential of structured foamed materials, there is a need for a robust and thorough investigation into the mechanical behaviour of both the cellular structure and underlying solid matrix. A review of the current standard testing procedures may also be required as they are not inherently designed to be applied to materials which have a discernible microstructure.

1.2 Cellular Structures

Cellular solids are defined as materials whose internal structure consists of interconnected cells. A cell in this case can be described as an enclosed space. Each cell may be classified as either open or closed. Closed cells are defined as those which are isolated from the neighbouring cell. Open cells on the other hand are porous in nature which allows for transport between neighbouring cells. Foamed materials are generally thought of as cellular solids that are constructed with the aid of gas bubbles. Honeycombs are a particular subset of cellular structures whereby the cells within the material are orientated in one plane.

Naturally occurring materials such as wood, honeycomb, sponge and bone are examples of cellular solids commonly found in nature (see figure 1.1). Man-made cellular structures are also widely available, ranging from simple honeycombed or layered materials commonly used

(a) (b) (c)

Figure 1.1: Examples of naturally occurring cellular materials. (a) cork oak[1], (b) beehive honeycomb[2]and (c) natural sponge[3].

in lightweight structural design, to complex polymeric and metal foamed cellular materials (see figure 1.2). A structured foamed material such as that seen in figure 1.2 (c) illustrates the detail which can be achieved by utilising additive manufacturing technologies.

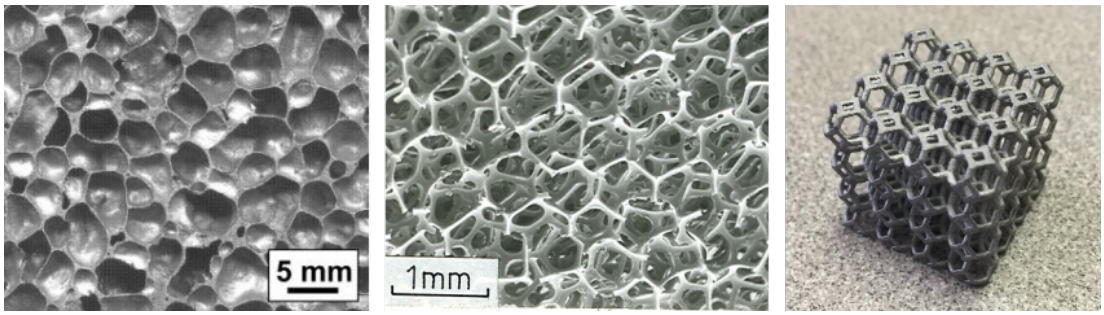

(a) (b) (c)

Figure 1.2: Examples of man-made foamed materials. (a) closed cell metallic foam[4], (b) open celled polyurethane[5]and (c) digitally printed foamed lattice structure[6].

Functionally designed cellular materials such as lattices fall into the category of hierarchical structures. Such materials are categorised as having more than one length scale within their composition. A consequence of this is that the observed mechanical properties may be dependent on the size of the sample relative to the internal microstructure from which it is comprised. In order to fully understand the mechanical behaviour of such materials, both size and scale must be considered. The mechanical properties of heterogeneous materials generally converge with increasing sample size. In the intermediate region where the specimen size is of similar order to the internal cells, the mechanical behaviour may be influenced by the local response of the material microstructure. Below the cellular level, the mechanical properties will revert

[1] (Montserrat López-Mesas et al, 2011) [2] Anonymous / CC1.0 [3] Original image by Johan / CC3.0 [4] Original image by Curran2 / CC BY-SA 3.0 [5] Gibson LJ & Ashby MF [6] Dahlon P Lyles & 3rd Dimension Industrial 3D Printing. *(See **Image Bibliography** for full source information.)*

to that of the underlying solid matrix material. In the case of additively manufactured materials, these properties may also be influenced by factors such as variations in the manufacturing process, the thickness of the internal layers and the direction in which the layers are printed. The solid matrix material may be unique to the individual manufacturing process or indeed hierarchical in itself. To fully understand how the mechanical properties vary with differing scales, care must be taken to make sure that the manufacturing processes are consistent and repeatable. In particular, it is beneficial if the underlying matrix material initially conforms to that of a linear elastic solid over the required range of size scales to minimise the number of variables which influence the behaviour of the material.

Many traditional materials such as metals can be treated as a homogeneous continuum solid and conform to the theory of linear elasticity. Size scale is not considered in Cauchy elasticity as the microstructure which defines the solid is several orders of magnitude smaller than the general macrostructure. Localised effects within the material composition become statistically insignificant at this size scale. Heterogeneous materials such as foams and various types of bone on the other hand cannot be treated as a simple continuum due to the significant porosity which exists at the mesoscale. Here, the presence of voids or inclusions may introduce localised stress fields which are not accounted for in Cauchy elasticity. The mesoscale in this case is defined as the intermediate region between the microstructure of the solid matrix and the macroscopic structural size. In the characterisation of such materials, the question of size and scale becomes an important consideration in the determination of a constitutive model which can capture the parameters that define the mechanical behaviour of the material. In literature, the term size effect is commonly used to describe the change in behaviour of heterogeneous materials at differing size scales (Lakes, 1983; Tekoglu & Onck, 2008; Dai & Zhang, 2008). The size dependent nature of such materials has led to the development of more involved elasticity theories which are capable of capturing the higher order effects not seen in classically elastic materials.

1.3 Theoretical Investigations in Micropolar Elasticity

The theory of classical linear elasticity is widely used in the field of solid mechanics to accurately describe the behaviour of many common materials. It is limited however to solids composed of a microstructure which is significantly smaller than the macroscopic structural size. In materials such as foams, ceramics, polymers, composites and some naturally occurring minerals like bone (see figures 1.1 & 1.2) the microstructure can play a significant role in the observed material properties and must be accurately described in order to fully capture the mechanical behaviour. Early attempts to address this issue can be traced back to the works of Voigt (1887) who introduced the idea of a couple stress which incorporated localised rotations

along with the displacements, as seen in Cauchy solids, to analyse the elastic properties of crystals.

This idea was further developed by E. & F. Cosserat (Cosserat & Cosserat, 1909) into the theory of non-symmetric elasticity. Here, they considered micro-rotations within the system as a separate entity to the conventional displacement field. The work of the Cosserat brothers was largely ignored for the next 50 years. However, Eringen & Suhubi (1964); Eringen (1966, 1967) later built upon this work to produce a generalised Cosserat theory, the Micropolar elasticity theory. This theory enables materials with a significant microstructure to be analysed by accounting for localised contributions to the displacement field not observed in classical elasticity. Other authors who have made considerable contributions to the field around this time include Nowacki (1974, 1986), Mindlin & Tiersten (1962); Mindlin (1964, 1965) and Cowin (1970).

Micropolar theory can be shown to be a simplification of the higher order micromorphic and microstretch theories (Tekoglu & Onck, 2008). More recently Hassanpour & Heppler (2014) demonstrated that classical elasticity is a special case of couple-stress theory and couple-stress theory is a simplification of micropolar elasticity for a linear elastic material. In this review, a detailed outline of the simplification process that is required to transfer from the 6 elastic constants seen in micropolar elasticity to the 4 constants that are required to fully describe a couple-stress material and subsequently the 2 elastic constants in Cauchy elasticity is given. Couple stress theory is a special case of the micropolar theory which occurs when the micropolar couple modulus, κ, and the micropolar twist coefficient, α, tends to infinity. In this case, the rotation vector, ϕ_i, is not independent of the displacement vector, u_i, as in the case of micropolar theory, and can be fully described by the displacement vector itself.

While a large amount of information can be found in the literature regarding the theoretical aspects of micropolar elasticity, there is a comparatively small volume of experimental research dedicated to describing the behaviour of physical materials within a micropolar continuum context. In the following section, a detailed review of the experimental aspects of micropolar theory will be undertaken.

The theories which have been discussed above are classed as higher order theories as they incorporate additional degrees of freedom within the constitutive equations. Higher grade theories, of which Couple stress theory is the simplest derivation, are another branch of continuum models which incorporate additional gradients of strain within the displacement vectors to describe deformations within the material. Strain gradient theory and Multipolar theory are examples of more involved higher grade theories which have been developed to explain size dependent material behaviour. However, such models are not considered within the scope of this investigation.

1.4 Experimental Investigations within the Bounds of Micropolar Elasticity

Experimental investigations attempting to validate micropolar elasticity and couple-stress theory have been published in literature since the latter part of the 20th century (e.g. Gauthier & Jahsman (1975)). However, in this time, limited progress has taken place. Several authors have made note of this with Eringen (1999) himself describing the amount of experimental work being put forward in comparison to the theoretical research output as "*meagre*". Indeed more recently this has been highlighted by Hassanpour & Heppler (2014, p.1) in reference to materials that consist of a defined internal structure where it was said;

> "...experimental verification of the micropolar theory for these materials is not fully accomplished yet and one is faced with a situation when theory precedes experiment."

One reason for this is that the experimental validation of the theory has proved less than straightforward. While experimental errors can be reduced with refined techniques, the sensitivity to loading mode and stochastic nature of many micropolar materials gives rise to large variations in experimental results which may be hard to resolve. The use of numerical simulations is one way in which such materials may be characterised in virtual form. While experimental uncertainties may be reduced through the application of idealised boundary conditions, the computational resources required to fully describe the material microstructure may be prohibitive (Goda & Ganghoffer, 2015).

Some of the first experimental investigations undertaken with respect to micropolar and couple stress theory investigated if couple stress effects could be observed in solid metals. Ellis & Smith (1967) performed cylindrical bending experiments on flat plates of varying thickness in an attempt to capture the characteristic length in bending for the test material. It was concluded that no discernible couple-stress related size effect could be detected in the steel and aluminium plates that were tested and that if indeed couple-stresses were present, they would have to be of an order similar to the grain size. Another observation made, which was first highlighted by Mindlin & Tiersten (1962) was that a small scatter in the sample thickness of specimens can have a noticeable effect on the calculated rigidity of plates with the increasing thickness which could potentially be interpreted as couple stress effects. In order to distinguish between a classically elastic material and a couple stress material, thin specimens should also be tested.

Once it was established that size effects were largely related to the size of the microstructure with respect to the macroscopic sample size, the experimental focus started to shift towards materials which have a distinguishable microstructure that is significantly larger than the grain

size of the matrix material. One of the first studies that attempted to capture micropolar constitutive properties was undertaken by Gauthier & Jahsman (1975). In this paper, Gauthier et al. proposed a simple method of testing supposedly micropolar materials with the aim of obtaining the flexural and torsional characteristic length by relating the rigidity of the material to sample diameter. The theoretical predictions presented were followed by a set of inconclusive experiments that were aimed at capturing the predicted micropolar behaviour in torsion. Here, a composite material that consisted of aluminium shot evenly dispersed through a body of epoxy was tested. This material was chosen on the basis that the characteristic length of a material should be of similar order to the microstructure as has been previously noted by Mindlin and Schijve (Schijve, 1966). The results showed that in most tests, sample stiffness decreased with specimen size which does not conform to the theoretical predictions for a micropolar material. One possible reason for the results was that the aluminium which is dispersed through the sample is much stiffer than the matrix material. Micropolar elasticity theory may not readily handle materials with more rigid inclusions, which accounts for the lack of a distinguishable size effect in the results of the torsion tests.

Similar results were also observed by Lakes (1986). Here, two different types of cylindrical foam rods were tested in torsion and bending in an attempt to derive the micropolar constitutive properties through the method of size effects. Syntactic foam which consisted of hollow glass microbubbles embedded in an epoxy matrix did not show any size effect when loaded in torsion, while polyurethane foam was observed to show a measurable size dependency. It was concluded by Lakes (1986, p.62) that

> "...these microballoons may behave more like inclusions than pores in governing the micromechanics..."

The syntactic foam behaved almost like a classically elastic material due to the fact that the glass bubbles are much stiffer than the epoxy matrix. The polyurethane however did produce a measurable sample-size dependant stiffening effect when compared to a classical material. More recently, Bigoni & Drugan (2007) showed by analytical means that a Cosserat solid cannot readily model a material which has more rigid inclusions.

The experimental method proposed by Gauthier was used to extract the micropolar constants by relating changes in sample size to the variation in stiffness which is observed in flexure and torsion. This approach is commonly referred to as the method of size effects. Experimental tests in flexure and torsion can be used to extract the micropolar elastic material constants when the variation in rigidity with specimen size is plotted graphically. In the case of samples with a square cross-section, a plot of rigidity divided by the cross-sectional area against the depth squared can be used to reveal the size effect. While the flexural and shear modulus of the material can be deduced from the slope of the rigidity plot as in the classical

cases, the characteristic length for torsion and bending are interpreted from the intercept of the linear portion with the vertical, rigidity, axis. Additional micropolar constants, which will be discussed in a following chapter, such as the Coupling number, N and Polar ratio, ψ are inferred by fitting experimental data to theoretical predictions as the sample size diminishes. Beveridge and Frame (Beveridge, 2010; Frame, 2013) took a slightly different approach to interpreting the size effects by plotting the variation in stiffness against the inverse of the sample depth squared. Here, the size effect can be interpreted from the gradient while the flexural modulus is found from the intercept with the vertical, stiffness, axis. Plotting the data in this way allows for a more detailed depiction of how small samples influence the observed size effects. However, this alternative approach requires the testing of samples that are of different size but geometrically similar.

The fact that the stiffness is dependent on the inverse of sample depth squared means that this method may be problematic. Small deviations in the recorded data can lead to large variations in the apparent mechanical response if care is not taken to minimise external factors which do not contribute to the constitutive properties of the material. This was highlighted by Beveridge (2010) who showed that the length to depth aspect ratio of test samples can have a significant effect on the relative stiffness of a cellular solid. Again this highlights the need for accurate experimental techniques to be performed which minimise localised variations in measured sample stiffness.

The use of this method was further explored and developed by Lakes et al who have spent a considerable amount of time experimentally testing materials which exhibit micropolar characteristics. Torsion experiments carried out by Yang & Lakes (1981) on compact bone showed that it behaved in accordance with couple stress theory rather than classical elasticity. Tests were performed by taking a cylindrical sample of bone and twisting it to determine the rigidity. Each sample was then machined to a smaller diameter and retested. The process was repeated several times. Samples of PMMA (Acrylic) were shown to conform to Cauchy elasticity under similar test conditions. From the experiments that were carried out, the characteristic length of the bone was calculated and found to be of a similar order to the radius of an osteon, which makes up the majority of the voids in the bone. This study was complemented by an analysis on compact bone in bending by the same authors (Yang & Lakes, 1982). Again multiple sets of cylindrical samples of varying size were tested and a discernible characteristic length was obtained for the material in bending. The characteristic length for bending reported was greater than the torsional characteristic length observed in the previous paper, though still of the same order as the radius of the osteons which make up the bulk of the matrix material.

Leading on from his experiments on bone, Lakes started to investigate other materials such as foam to further demonstrate experimental methods for capturing micropolar effects (Lakes, 1983). Attempts were also made to identify the coupling number of the material by matching

the experimental results with theoretical predictions. Due to the compliant nature of the foam, an experimental setup was devised to minimise the effects of friction induced on the samples by local loads. Here, a magnet was attached to the free end of the specimen, and a torque induced using the electric current from a Helmholtz coil. The resulting rotation was determined by the change in angle of a laser beam which is shone at the specimen. Results from this experiment show that polyurethane foam can be described by a Cosserat continuum, while syntactic foam does not show any appreciable size dependant effects. Reticulated open-cell foams were also shown to exhibit size effects in bending and torsion (Rueger & Lakes, 2016).

Heterogeneous materials comprised of a structured array of internal voids have been shown to display size effects which are consistent with micropolar theory. Beveridge et al. (2013) and Waseem et al. (2013) investigated both the flexure of beams and stretching of ring shaped samples, determining both the flexural modulus and characteristic length for bending of the material in each case. The coupling number was estimated from the results of complementary finite element (FE) numerical simulations of the material tests. Sample aspect ratio was significant in the experimental investigations with slender samples producing more consistent results.

More recently, Lakes & Drugan (2015) noted that in the pure bending of bars with a square cross-section comprised from a micropolar material non classical effects were observed on the lateral surfaces of the beams. As well as the tilt that is seen in the linear elastic case of pure bending due to anticlastic effects, the side walls were observed to bulge in a sinusoidal fashion. Lakes found that this effect could be accurately described through micropolar theory by applying an approximate Cosserat solution. An approximate solution is required for this problem as it was reported that an exact closed-form solution is only possible when $\beta/\gamma = -\nu$. It was also concluded from this investigation, that due to the presence of these non-classical effects in bending, the Poisson's ratio of the material should be calculated from tension and compression tests rather than from bending for materials with a significant characteristic length.

In torsion the effects of warping need to be considered in samples which do not have a circular cross-section. Park & Lakes (1987) proposed a solution to the problem of a linear isotropic Cosserat solid bar of square cross-section being loaded in torsion. While an exact analytical solution was determined, the number of variables which need to be identified in order to fully define the constitutive properties does not favour it in resolving experimental tests. It is possible however that this analysis may be simplified by disregarding those variables which have the least experimental influence. Another notable forecast made in this paper demonstrated that micropolar materials will display a non-zero shear stress at the exterior edges of the bar when twisted which is not predicted in classical elasticity.

1.5 Edge Effects within a Micropolar Continuum

The general trend in materials which display micropolar behaviour is for the relative stiffness to increase with decreasing sample size (e.g. Gauthier & Jahsman (1976); Reddy & Venkatasubramanian (1979); Yang & Lakes (1981)). Micropolar theory does not forecast size effects which do not follow this general trend. This can be readily observed in specimens where the material microstructure intersects the exterior surfaces of the material test sample.

It has been highlighted in the literature that a problem exists in characterising materials within the micropolar continuum context when edge effects exist. Brezny & Green (1990) demonstrated that surface damage on cellular materials can significantly reduce the mechanical stiffness when the specimen is of similar size to the heterogeneities within the material. In this paper the authors also present a model to predict the edge effects in samples with a square cross-section. Anderson & Lakes (1994) applied the method of Brezny & Green (1990) to the micropolar model correcting for the effects of surface damage on samples of a closed cell foam. It was also observed that the Cosserat effects which were seen in this material were largely dependent on minimising the surface damage through careful sample preparation.

Surface damage has been stated as a significant contributing factor to deviations in size effects away from those predicted by micropolar elasticity (Anderson & Lakes, 1994). However, such effects may be attributed to the heterogeneities themselves which would indicate that careful sample preparation has its limits. An investigation by Frame (2013), demonstrated that samples of a structured heterogeneous material display size effects in bending which are inconsistent with micropolar theory when the internal cellular structure is exposed at the exterior surface of the samples. It was also concluded through a statistical analysis that samples of cortical bone could not be prepared without having some portion of voids exposed at the surfaces. Recently Wheel and Frame, (Wheel et al., 2014) undertook a simple closed form analysis to confirm this. It was shown that a laminate with alternating layers of stiff and compliant material could exhibit size effects consistent with Cosserat elasticity when the stiff layers were on the outer surfaces. Samples generated with compliant outer surfaces exhibited a size softening consistent with surface damage. It was also clearly shown that these effects were attributed to the second moment of area of the samples and therefore dependent on the local distribution of the heterogeneities at this size scale. As the maximum stress in bending occurs at the upper and lower surfaces of a beam during flexure, it is easy to see that surface damage or localised variations in the second moment of area may play a significant role in determining the nature of any size effect observed.

1.6 Analytical & Numerical Modelling of Materials which Exhibit Size Effects

Periodic cellular lattices and honeycombs are commonly studied in the literature as they are well suited to lightweight structural applications. Both analytical and numerical techniques have been developed to further understand the mechanical response of such materials. Gibson & Ashby (Gibson et al., 1982; Gibson & Ashby, 1982) studied both 2D and 3D low density cellular structures, determining the effective Young's modulus, shear modulus and Poisson's ratio by representing the internal members within the unit cell of material as a series of interconnecting beam elements for both hexagonal and cubic lattices. Wang & McDowell (2004) investigated a range of different lattice configurations in addition to the hexagonal lattice which had previously been studied by Gibson & Ashby. No higher order effects were considered by either author in this case.

In materials which have a complex microstructure, homogenisation techniques are commonly used to determine the constitutive properties within the context of micropolar elasticity. In this method, a continuum representation of the physical material is constructed by determining the average properties over a unit cell or representative volume element (RVE) of the material under consideration. Drugan & Willis (1996, p.498) defined the RVE as:

> "the smallest material volume element of the composite for which the usual spatially constant 'overall modulus' macroscopic constitutive representation is a sufficiently accurate model to represent mean constitutive response."

In the case of a repetitive cellular structure, the RVE is generally defined in terms of a unit cell which captures the periodic microstructural features and may be propagated to create the overall material sample. The size and composition of the RVE may not necessarily be unique for a given material, but the chosen bounds may influence the observed global properties.

Cellular solids consisting of structured lattices are one of the most common materials to be studied. Pradel & Sab (1998) developed a Cosserat continuum model for a 2D hexagonal lattice by considering the translations and rotations of the internal beams and connecting nodes. Kumar & McDowell (2004) extended this by implementing a finite element code to model the deformation of the homogenised continuum. In this analysis higher order effects were considered and the resulting code was compared to discrete models. Kumar & McDowell (2009) applied this approach to optimise honeycombs for structural and thermal design parameters. More recently Dos Reis & Ganghoffer (2011, 2012) determined the micropolar constitutive parameters of both square and hexagonal lattices with the resulting homogenised moduli showing good agreement with those found by previous authors. Analytical solutions were produced to determine the individual components of the stiffness matrices for each ma-

terial, but the results are generally only applicable to unit cells comprised of slender beam elements.

Homogenisation methods have also been utilised for the analysis of 3-dimensional periodic lattices. Yoo & Jasiuk (2006) investigated an idealised representation of trabecular bone enclosed in a compliant matrix. In this investigation, a unit cell of the open cell material was investigated to determine the apparent Couple-stress moduli from the change in strain energy under load. Both displacement and traction boundary conditions were considered in the analysis, with the latter giving much more compliant results. While traction boundary conditions were used to define a lower bounds of the Couple-stress moduli in this analysis, it may not be truly representative of the material as the deformation is largely dependent on a localised distribution of forces rather than the global response. No predictions for the characteristic length of the material were reported in this investigation, but it was highlighted that one could be obtained from the relevant couple-stress tensors. As only one unit cell was considered in this analysis, no assessment of the higher order parameters which may be size dependent were made. Further tests are required to determine how the parameters converge with increasing sample size.

Goda has applied a similar method to the modelling of various materials including cellular lattices, porous solids and textiles (Goda et al., 2014; Goda & Ganghoffer, 2015; Rahali et al., 2016; Goda & Ganghoffer, 2016). Displacement boundary conditions were applied to several RVE of differing sizes in order to determine the variation in strain energy with mode of loading and resolve the components of the stiffness matrix within the bounds of Couple-stress theory. The stiffness tensor which relates to the uniaxial and shear properties of the material was found to be independent of the sample cell size while the Couple-stress tensor varied with unit cell size which is consistent with a micropolar material. It was reported that the characteristic length calculated was of similar order to the RVE being simulated, demonstrating the importance of size scales in the materials. In these investigations, the authors were restricted in their attempts to obtain converged solutions to the second stiffness tensor as the size of the RVE domain was limited by the computational resources which were available. This highlights the importance of considering scale when modelling such materials, as a continuum model based on single RVE's may not be able to capture the correct response with varying size. Ultimately, physical testing of samples may be required to fully characterise materials which are too complex to simulate at larger size-scales.

While the majority of experimental investigations into materials which display micropolar characteristics have focussed on those with a stochastic distribution of microstructure, there is a distinct lack of physical testing on materials which have a structured or periodic microstructure. Complex 3D lattices in particular are particularly hard to reproduce through traditional manufacturing means, but the advent of additive processes such as 3D printing may offer a

solution which can be exploited.

1.7 Additive Manufacturing and 3D Printing Processes

Additive manufacturing is the general term used to describe the construction of components by an incremental layering process. In comparison to traditional technologies which rely on subtracting matter from a block of raw material, additive manufacturing has the advantage of being able to produce complex and detailed parts without the need for further machining. 3D printing is a form of manufacturing which utilises additive techniques to build up an object by layers, depositing material onto the surface of the part as it is being constructed. Various different types of additive manufacturing exist, such as stereolithography, fused deposition modelling, PolyJet and laser sintering, each with their own merits (Underdahl, 2015). As this technology has advanced, rapid prototyping has given engineers the opportunity to manufacture and test novel composite materials which are not possible with traditional manufacturing techniques. In order to fully exploit them however, a clear understanding of the characteristic properties of the printed solid comprising the material matrix is required.

Blanco et al. (2014) showed that the flexural modulus of parts composed of the RGD240 photopolymer, produced in an Objet30 PolyJet printer were time dependent. Sample orientation within the printer was also shown to have a significant effect on the flexural modulus of the specimens, with parts produced at an angle to the print surface displaying a decreasing modulus as the angle of inclination increases. Mueller et al. (2015) conducted an extensive review into the tensile properties of samples which were produced by additive manufacturing in a 3D printer. It was reported that a variety of different factors influenced the mechanical strength of samples including the number of layers and intersections within the printed part with respect to load direction. The amount of exposure to ultra-violet light and sample orientation within the printer were also shown to be significant. It was also highlighted that machine specific factors such as blocked nozzles and the warm-up time may negatively impact on the properties of the samples produced. The mean tensile modulus recorded by specimens which were orientated in the 'Z' axis of the printer (perpendicular to the print surface) was 10% smaller than those aligned to the 'X' or 'Y' axis, indicating that the material may be slightly anisotropic.

Several authors have demonstrated the capabilities of 3D printing technologies to reproduce cellular solids by producing prototype samples of the material (Luxner et al., 2005; Ha et al., 2016). Evaluation of the materials however, was limited to numerical simulations rather than physical tests. Some experiments have been carried out on cellular solids produced through additive manufacturing processes. Afshar et al. (2016) conducted compression tests on a novel material comprising of a periodic structure of varying cell volume fraction. More recently Abueidda et al. (2017) also produced a variety of cellular materials by 3D printing, conducting

tensile and compression tests to compare the properties of a variety of cellular configurations. Li & Wang (2017) investigated the bending response of 3D printed honeycombs within a sandwich core construction to investigate how the cellular topology influenced the bending and failure characteristics of the beams under test. In each of the investigations, experimental data was used to refine the constitutive parameters used in the finite element simulations of the material. However, none of the above investigations considered the consequences of scale or the presence size effects within the materials. There therefore exists a need to perform more detailed experimental investigations in order to better understand any size effects which may influence the mechanical response of such materials. It is an aim of this work to explore this further.

1.8 Summary of Previous Work

It is clear to see that modelling and understanding size effects is an active area of research. However, the characterisation of novel materials has been primarily limited to numerical simulations. Physical experimental tests have mainly focussed on materials with a stochastic microstructural distribution. In particular, very few experiments exists which analyse materials with a periodic cellular structure in bending and none were found which consider torsion. It is the aim of this thesis to explore the use of structured materials manufactured through additive means by comparing numerical simulations with physical tests to determine their suitability for exploitation in lightweight structural applications.

1.9 Research Aims & Overview

With recent advancements in additive manufacturing technology, it is now possible to create complex geometric structures tailored to a specific application. One such application is the manufacture of novel lightweight materials with a periodic tailored microstructure. Such materials may offer more deterministic and consistent properties in comparison to more traditional materials such as stochastic foams. It is an aim of this research to characterise and investigate the utilisation of such novel materials in structural applications through numerical simulation and experimental testing.

The initial aim of this thesis was to model structured heterogeneous materials using the finite element (FE) method to determine the characteristic constitutive parameters required to describe a micropolar material. Chapter 3 looks at how the mode of loading influences the observed stiffness of samples, with samples being subjected to three-point, four-point and constant moment loading. It was shown that a Euler-Bernoulli based micropolar beam theory may not provide a sufficient description of the deformation of slender specimens in three-point and four-point flexural loading when the sample volume fraction is very low. A Timoshenko based approach was shown to be beneficial in this case.

The nature of the size effect was explored in 2D representations of the orthogonal lattice at varying volume fractions. Surface effects were also considered within the analysis of the samples which were found to have a strong effect on the observed size effect.

Also in this chapter, the origin of the size effect within a heterogeneous material has been explored. It was shown using an analytical model that the size effect is closely related to the second moment of area and the distribution of mass within the cells which make up the heterogeneous material.

Chapters 4 & 5 further develop the numerical methods which were introduced in the previous chapter to investigate 3-dimensional representations of heterogeneous solids within a micropolar continua. The material constants were interpreted from the numerical data by utilising the formulation introduced in chapter 2.

In chapter 6, a thorough experimental investigation was undertaken to verify the suitability of a 3D printed solid as the matrix material for the structured heterogeneous material introduced in chapter 4. Finally, in chapters 7 & 8 the numerical method is validated through a series of experimental investigations on a manufactured material with a cubic lattice microstructure.

Chapter 2

Elasticity Theories

In this chapter, a brief summary of linear elasticity has been introduced, explaining the need for higher order or higher grade theories to capture the size dependent nature of materials which consist of significant microstructural features. The constitutive equations for micropolar elasticity are then defined. Further to this, some generalised formula for the bending and twisting of a micropolar beam will be introduced to show how the higher order parameters used to define the material can be captured experimentally.

2.1 Linear Cauchy Elasticity

Classical linear elasticity theory is the standard method used to describe the deformation of continuous solid materials. It is a simplification of the more general non-linear theory of elasticity and is based on the assumption that there is a linear relationship between the stress and strain components under small strain conditions as defined by Hooke's law (Figure 2.1). The

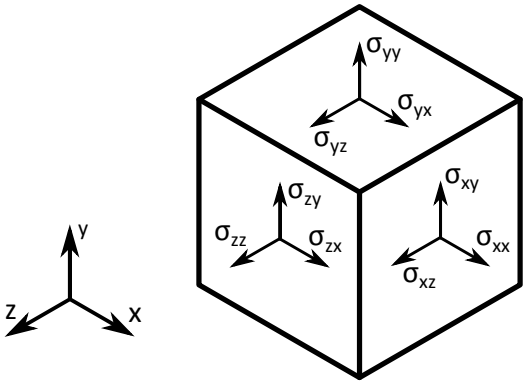

Figure 2.1: General stress components in an element of material

constitutive equations for a 3-dimensional linear elastic Cauchy solid can be given as

$$\tau_{ij} = \lambda \epsilon_{kk} \delta_{ij} + 2\mu \epsilon_{ij} \tag{2.1}$$

where τ_{ij} is the stress component, ϵ_{ij} is the strain, ϵ_{kk} is the dilatation which is a measure of the local volumetric strain, δ_{ij} is the Kronecker delta, defined as 1 if $i = j$ and 0 if $i \neq j$. Two material dependent parameters are defined in Cauchy elasticity, λ and μ which are Lamé's first and second parameters respectively. In linear elasticity, μ is analogous to the shear modulus, G_s for an isotropic solid.

Lamé's first parameter, λ, and second parameter, μ, are defined in terms of the material Young's modulus, E_s and Poisson's ratio, ν as

$$\lambda = \frac{E_s \nu}{(1+\nu)(1-2\nu)} \qquad \mu = \frac{E_s}{2(1+\nu)} \tag{2.2}$$

2.1.1 Isotropic Solids

A linear elastic isotropic homogeneous solid is one whose mechanical properties are independent with respect to direction. Such materials can be defined from 2 independent variables. In practical engineering terms, there are 3 interdependent material parameters, (Young's modulus, E_s, Shear modulus, G_s & Poisson's ratio, ν) only two of which need to be resolved in order to determine the third. Linear elasticity does not have any length scale dependency. It is assumed

that the material is independent of size as the internal microstructure is sufficiently small to be considered as a uniform continuum over the entire range of size scales.

The constitutive relation given in equation 2.1 can be better expressed in matrix form to show the stress-strain relationship in terms of the material constants (Equation 2.4).

$$\sigma_{ij} = C_{ijkl}\epsilon_{kl} \tag{2.3}$$

Where C_{ijkl} is the general stiffness matrix.

$$\begin{bmatrix} \sigma_{11} \\ \sigma_{22} \\ \sigma_{33} \\ \sigma_{23} \\ \sigma_{13} \\ \sigma_{12} \end{bmatrix} = \begin{bmatrix} \lambda+2\mu & \lambda & \lambda & 0 & 0 & 0 \\ \lambda & \lambda+2\mu & \lambda & 0 & 0 & 0 \\ \lambda & \lambda & \lambda+2\mu & 0 & 0 & 0 \\ 0 & 0 & 0 & \mu & 0 & 0 \\ 0 & 0 & 0 & 0 & \mu & 0 \\ 0 & 0 & 0 & 0 & 0 & \mu \end{bmatrix} \begin{bmatrix} \epsilon_{11} \\ \epsilon_{22} \\ \epsilon_{33} \\ \epsilon_{23} \\ \epsilon_{13} \\ \epsilon_{12} \end{bmatrix} \tag{2.4}$$

By substituting in for Lamé's constants and inverting the matrix, the compliance matrix, S_{ijkl} can be written in terms of the engineering constants, E_s, G_s and ν as

$$\epsilon_{ij} = S_{ijkl}\sigma_{kl} \tag{2.5}$$

$$\begin{bmatrix} \epsilon_{11} \\ \epsilon_{22} \\ \epsilon_{33} \\ \epsilon_{23} \\ \epsilon_{13} \\ \epsilon_{12} \end{bmatrix} = \begin{bmatrix} \frac{1}{E_s} & -\frac{\nu}{E_s} & -\frac{\nu}{E_s} & 0 & 0 & 0 \\ -\frac{\nu}{E_s} & \frac{1}{E_s} & -\frac{\nu}{E_s} & 0 & 0 & 0 \\ -\frac{\nu}{E_s} & -\frac{\nu}{E_s} & \frac{1}{E_s} & 0 & 0 & 0 \\ 0 & 0 & 0 & \frac{1}{G_s} & 0 & 0 \\ 0 & 0 & 0 & 0 & \frac{1}{G_s} & 0 \\ 0 & 0 & 0 & 0 & 0 & \frac{1}{G_s} \end{bmatrix} \begin{bmatrix} \sigma_{11} \\ \sigma_{22} \\ \sigma_{33} \\ \sigma_{23} \\ \sigma_{31} \\ \sigma_{12} \end{bmatrix} \tag{2.6}$$

The shear modulus is related to the Young's modulus and Poisson's ratio by

$$G_s = E_s/2(1+\nu) \tag{2.7}$$

for an isotropic solid.

2.1.2 Anisotropic & Orthotropic Solids

Materials which posses a directional dependence or are heterogeneous in composition are by their very nature anisotropic to some degree. The most general anisotropic material will have 36 components which need to be resolved in order to fully define the material, however many

materials possess some degree of symmetry that allow for simplification of the number of required variables.

Cubic materials are a subset of orthotropic materials which are invariant with respect to 90 degrees rotation with respect to the principle axis. Due to the symmetrical nature, there is an additional constant which needs to be resolved in order to fully define the material. The general compliance matrix for an orthotropic material can be expressed as

$$S_{ijkl} = \begin{bmatrix} \frac{1}{E_1} & -\frac{\nu_{21}}{E_2} & -\frac{\nu_{31}}{E_3} & 0 & 0 & 0 \\ -\frac{\nu_{12}}{E_1} & \frac{1}{E_2} & -\frac{\nu_{32}}{E_3} & 0 & 0 & 0 \\ -\frac{\nu_{13}}{E_1} & -\frac{\nu_{23}}{E_2} & \frac{1}{E_3} & 0 & 0 & 0 \\ 0 & 0 & 0 & \frac{1}{G_{23}} & 0 & 0 \\ 0 & 0 & 0 & 0 & \frac{1}{G_{31}} & 0 \\ 0 & 0 & 0 & 0 & 0 & \frac{1}{G_{12}} \end{bmatrix} \tag{2.8}$$

In the case where cubic symmetry exists, the stiffness matrix can be simplified to 3 independent elements.

$$C_{ijkl} = \begin{bmatrix} C_{11} & C_{12} & C_{12} & 0 & 0 & 0 \\ C_{12} & C_{11} & C_{12} & 0 & 0 & 0 \\ C_{12} & C_{12} & C_{11} & 0 & 0 & 0 \\ 0 & 0 & 0 & C_{44} & 0 & 0 \\ 0 & 0 & 0 & 0 & C_{44} & 0 \\ 0 & 0 & 0 & 0 & 0 & C_{44} \end{bmatrix} \tag{2.9}$$

Here, the mechanical behaviour is similar to that of an isotropic material, except that the shear modulus does not necessarily relate to the Young's modulus and Poisson's ratio as in the isotropic case thereby leading to a degree of anisotropy. The Zener ratio (anisotropy ratio) is a dimensionless number that is used to quantify the level of anisotropy within a cubic crystal, but is also applicable to orthotropic solids and can be given as:

$$a_r = \frac{2C_{44}}{C_{11} - C_{12}} \tag{2.10}$$

It is a measure of how the resistance to shear within the material compares to that of its isotropic equivalent. Materials with a Zener ratio of 1 are classified as isotropic.

While linear elasticity can be readily used to model many structural materials, it is dependent on the macroscopic behaviour being independent of the underlying microstructure. Materials comprised of a significant microstructure, such as bone, foams and laminates, or that include large stress gradients do not necessarily conform to this model and require the deve-

lopment of more complex theories which take into account localities within the stress field.

In the next section, the linear theory of micropolar elasticity will be introduced which is one such higher order theory that attempts to account for the effects seen in materials which do not conform to classical elasticity theory.

2.2 Linear Micropolar Elasticity

Micropolar elasticity theory is a higher order model that augments classical or Cauchy elasticity theory. Introduced by Cosserat & Cosserat (1909) and further developed by Eringen (1966), micropolar elasticity describes the behaviour of heterogeneous solids by introducing an independent rotational degree of freedom in addition to the translational displacements in classical elasticity. This additional rotational parameter is accompanied by a couple-stress, m_{ij}, acting within the material to balance the internal actions resulting from an externally applied load (Figure 2.2). It is predicted that micropolar elasticity theory will converge on the classical solution as the microstructure of the material reduces to an order much less than that of the general macrostructure. In linear micropolar theory, six independent elastic constants

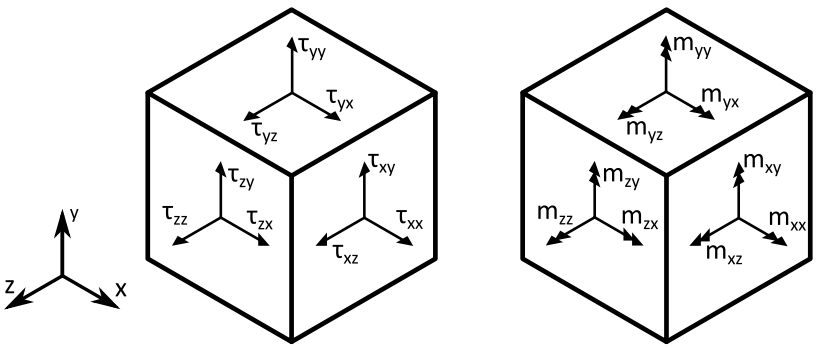

Figure 2.2: Stress, τ_{ij} and couple stress, m_{ij} components required to fully describe a micropolar material.

are required to fully describe a general isotropic elastic body. This is in contrast to the two which are required to define a linear elastic material. Couple-stress theory is a special case of the micropolar theory whereby the microrotations within the body are not independent and can be fully described in terms of the displacement vectors. The number of parameters reduces to four in this instance.

Micropolar theory has received more attention over other higher order theories such as micromorphic elasticity due to fact that there are significantly fewer constants that need to be identified to fully characterise an isotropic solid. This theory is used as the basis of the

undertaken research to model size effects in materials with an idealised microstructure.

2.2.1 Constitutive Equations

The constitutive equations for a 3-dimensional micropolar elastic solid have been derived by Eringen (1966).

$$\tau_{ij} = \lambda\epsilon_{kk}\delta_{ij} + (2\mu + \kappa)\,\epsilon_{ij} + \kappa e_{ijk}\,(\theta_k - \phi_k) \tag{2.11}$$

$$m_{ij} = \alpha\phi_{k,k}\delta_{ij} + \beta\phi_{i,j} + \gamma\phi_{j,i} \tag{2.12}$$

Where τ_{ij} is the asymmetric force stress tensor, m_{ij} is the couple stress tensor (moment per unit area), θ is the macrorotation, ϕ is the microrotation, ϵ_{ij} is the small strain tensor, ϵ_{kk} is the dilatation, e_{ijk} is the permutation symbol and δ_{ij} is the Kronecker delta.

To fully categorise a micropolar material 6 elastic constants are required; λ, μ, α, β, γ and κ. The terms λ, μ and κ are expressed in terms of a $force/length^2$ while the micropolar constants α, β, γ are defined in terms of a force ($couple/length$). In classically elastic materials, the higher order terms α, β, γ and κ will disappear. Due to positive definiteness of internal energy, these material moduli are restricted as follows:

$$\begin{aligned} 3\lambda + 2\mu + \kappa \geq 0, \quad 2\mu + \kappa \geq 0, \quad \kappa \geq 0 \\ 3\alpha + \beta + \gamma \geq 0, \quad -\gamma \leq \beta \leq \gamma, \quad \gamma \geq 0 \end{aligned} \tag{2.13}$$

The elastic constants above can be better defined in terms of the general engineering constants:

Young's Modulus, $$E_s = \frac{(2\mu + \kappa)(3\lambda + 2\mu + \kappa)}{(2\lambda + 2\mu + \kappa)} \tag{2.14}$$

Shear Modulus, $$G_s = \frac{(2\mu + \kappa)}{2} \tag{2.15}$$

Poisson's Ratio, $$\nu = \frac{\lambda}{(2\lambda + 2\mu + \kappa)} \tag{2.16}$$

Characteristic Length for Torsion, $$l_t = \left[\frac{(\beta + \gamma)}{(2\mu + \kappa)}\right]^{1/2} \tag{2.17}$$

Characteristic Length for Bending, $$l_b = \left[\frac{\gamma}{2\,(2\mu + \kappa)}\right]^{1/2} \tag{2.18}$$

Coupling Number, $$N = \left[\frac{\kappa}{2\left(\mu + \kappa\right)}\right]^{1/2} \tag{2.19}$$

Polar Ratio, $$\psi = \frac{(\beta + \gamma)}{(\alpha + \beta + \gamma)} \tag{2.20}$$

2.2.2 Bending of a Micropolar Beam

The bending of a slender sample of a micropolar material that can be represented by an extruded 2-dimensional section as seen in figure 2.3 has been previously derived by Huang et al. (2000), Beveridge (2010), Lakes & Drugan (2015) among others.

The deformation of a beam subjected to a pure bending moment can be derived from the constitutive equations for a Euler-Bernoulli beam.

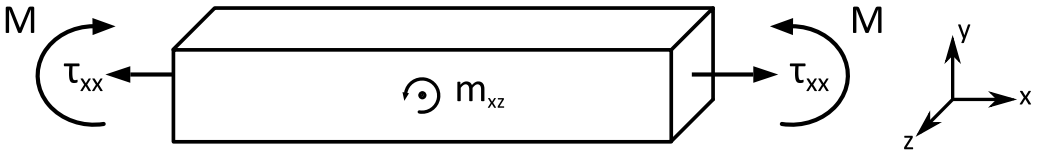

Figure 2.3: Stresses and couple stresses acting in a micropolar beam under bending.

The radius of curvature, R of a slender beam subjected to a small angle of rotation, θ by a constant bending moment, M is as follows;

$$\frac{1}{R} = \frac{d\theta}{dx} = \frac{d\phi}{dx} = -\frac{d^2w}{dx^2} \tag{2.21}$$

where x denotes the axial coordinate of the beam, and w the transverse displacement.

Considering only the in-plane couple stress, m_{xz} and direct stress, τ_{xx}

$$m_{xz} = \gamma\frac{d\phi}{dx} \tag{2.22}$$

$$\tau_{xx} = \frac{E^* y}{R} \tag{2.23}$$

where E^* is the micropolar flexural modulus in this case. Assuming that the applied moment, M, is equal to the internal resisting moment within the beam,

$$M = \int_z \int_y \left(\tau_{xx} y + m_{xz}\right) dydz \tag{2.24}$$

where

$$m_{xz} = \frac{\gamma}{R} \tag{2.25}$$

and

$$\tau_{xx} = \frac{E^* y}{R} \tag{2.26}$$

$$M = \frac{1}{R} \int_{-b/2}^{b/2} \int_{-h/2}^{h/2} \left(E^* y^2 + \gamma \right) dydz \tag{2.27}$$

$$= \frac{1}{R} \left(E^* I_s + \gamma A \right) \tag{2.28}$$

Substituting in for equation 2.21, the moment curvature relationship is

$$\frac{d^2 w}{dx^2} = \frac{-M}{E^* I_s + \gamma A} \tag{2.29}$$

Under small rotational displacements, the curvature is related to the angle of rotation along the length of the beam by

$$\frac{d^2 w}{dx^2} = \frac{\theta}{L} \tag{2.30}$$

The flexural rigidity, J' of the beam is therefore:

$$J' = \frac{ML}{\theta} = E^* I_s + \gamma A \tag{2.31}$$

where the cross-sectional area, A, and second moment of area, I_s, of a rectangular section can be given as

$$A = bd \tag{2.32}$$

$$I_s = \frac{bd^3}{12} \tag{2.33}$$

with b and d being the breadth and depth of the samples respectively. By substituting in equations 2.32 and 2.33 into 2.31, the total rigidity of the beam can be given as

$$\frac{ML}{\theta} = E^* I_s \left(1 + \frac{12\gamma}{E^* d^2} \right) \tag{2.34}$$

The characteristic length in bending, l_b for a micropolar material can be expressed in terms of

the micropolar flexural modulus as

$$l_b = \sqrt{\frac{\gamma}{2E^*}} \tag{2.35}$$

Therefore

$$\frac{ML}{\theta} = E^* I_s \left(1 + 24\left[\frac{l_b}{d}\right]^2\right) \tag{2.36}$$

It is worth noting that previous experimental work carried out by Beveridge (2010) and subsequently Frame (2013) used the parameter, l_c to denote the magnitude of the size effect for a beam with a rectangular section. It is related to the characteristic length in bending, l_b, defined here by $l_c = \sqrt{24} l_b$.

As stated in the previous chapter, this equation only holds true when $\beta/\gamma = -\upsilon$. When the characteristic length, l_b is much smaller than sample depth, the higher order terms in 2.36 vanish, and the resulting equation reverts to the classical elasticity solution.

Similar derivations can be made for slender beams subjected to other flexural loading modes by changing the boundary conditions. The equivalent solution for the stiffness, K of a micropolar beam under 3-point bending and 4-point bending are given respectively as

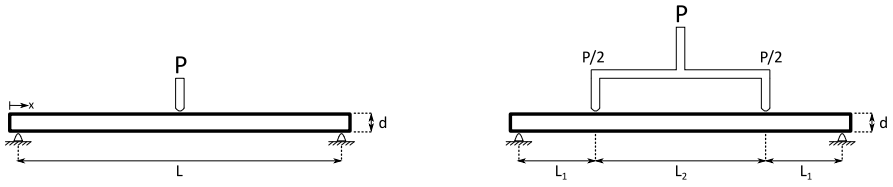

(a) (b)

Figure 2.4: (a) 3-Point bending setup, (b) 4-Point bending setup.

$$K = \frac{P}{w_{max}} = 4E^* b \left(\frac{d}{L}\right)^3 \left(1 + 24\left[\frac{l_b}{d}\right]^2\right) \quad \text{3-Point bending} \tag{2.37}$$

$$K_{L_2} = \frac{P}{w_2 - w_1} = \frac{4bd^3 E^*}{3L_1 L_2^2} \left(1 + 24\left[\frac{l_b}{d}\right]^2\right) \quad \text{4-Point bending} \tag{2.38}$$

L_1 defines the length of the sample between the outer support and the nearest loading point while L_2 is the length between the loading arms as can be seen in figure 2.4. K_{L_2} is the stiffness of the beam across the central section of the sample.

2.2.3 Torsion of a Micropolar Beam

Size effects are predicted to be seen in micropolar materials loaded in torsion. Generally speaking, experimental tests that have been conducted on supposedly micropolar materials used cylindrical samples to obtain the characteristic torsional behaviour.

The approximate solution for the rigidity ratio, Ω of a cylindrical beam of large radius loaded in torsion is expressed in terms of the ratio of the sample rigidity, J' to its equivalent linear elastic solid, J as

$$\Omega = \frac{J'}{J} = 1 + 6\left(\frac{l_t}{r}\right)^2 \tag{2.39}$$

where l_t is the characteristic length for torsion and r is the radius of the sample (Rueger & Lakes, 2016).

This equation holds true when the coupling number, N, is equal to 1. The exact solution for materials with a coupling number which is not unity is more complicated and is given by Gauthier & Jahsman (1975) as

$$\Omega = \left(1 + 6\left(\frac{l_t}{r}\right)^2\right)\left[\frac{(1 - 4\psi\chi/3)}{1 - \psi\chi}\right] \tag{2.40}$$

Here, ψ denotes the polar ratio and $\chi = I_1(pr)/[prI_0(pr)]$ and $p^2 = 2\kappa/(\alpha+\beta+\gamma)$. I_0 and I_1 are Bessel functions of the first kind.

One of the problems with using cylindrical samples for materials with a regular periodic microstructure is that the unit cell which defines the material is geometrically incompatible. Constructing cylindrical samples out of such materials cannot be done without significantly truncating the cells at the outer surface of the sample. As surface damage has been shown to have a detrimental effect of the stiffness of samples at size scales approaching that of the unit cell (Wheel et al., 2014), this geometry may not be appropriate for testing such materials.

Rectangular sections often simplify the production of material samples for testing purposes. The standard analytical solution for the rigidity, J, of a linear elastic beam with square cross section can be given as

$$J = \frac{TL}{\theta} = G_s I_p \tag{2.41}$$

where I_p is the warping constant (Roark et al., 2002).

$$I_p = \frac{2.25d^4}{16} \tag{2.42}$$

For a bar with a square section (Figure 2.5), determining the magnitude of the size effect

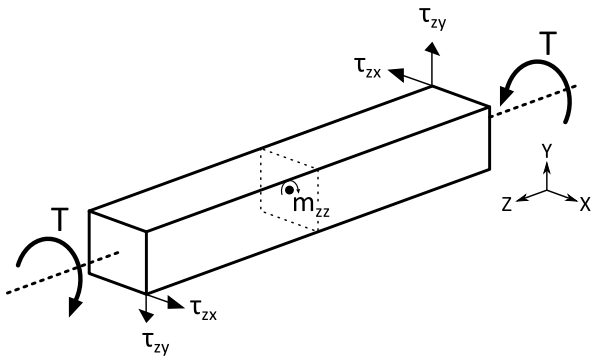

Figure 2.5: Stresses and couple stresses acting in a micropolar beam subjected to a torsional load.

requires a much more involved analysis to obtain an exact solution for the rigidity. As in the case of bending, the applied twisting moment (Torque) to the beam must be equal to the shear stresses and couple stresses acting within the sample and is obtained from

$$T = \int_A (x\tau_{zy} - y\tau_{zx} + m_{zz})dA \tag{2.43}$$

An approximation to the solution for the rigidity of a micropolar square bar was derived by Park & Lakes (1987) to be

$$\begin{aligned} J' = G^* \Bigg\{ & \frac{(1+C)d^4}{(1+2C)3} - \frac{64}{(1+2C)} \sum_{n=0}^{\infty} \frac{1}{dk_n^5} \tanh\left(k_n \frac{d}{2}\right) + 2{l_t}^2 d^2 \\ & + \frac{C}{1+2C} \Bigg[\sum_{n=0}^{\infty} \frac{4(-1)^n dA_n}{p_n} \cosh\left(p_n \frac{d}{2}\right) \\ & - \sum_{n=0}^{\infty} 8(-1)^n A_n \left(\frac{1}{k_n^2} + \frac{1}{p_n^2}\right) \sinh\left(p_n \frac{d}{2}\right) \\ & + \left(\frac{1}{\psi} - 1\right) {l_t}^2 \sum_{n=0}^{\infty} (F_n p_n - D_n k_n) \frac{16(-1)^n}{k_n p_n} \sinh\left(p_n \frac{d}{2}\right) \Bigg] \Bigg\} \end{aligned} \tag{2.44}$$

where k_n , p_n , A_n , D_n and F_n are additional parameters which are defined in Park & Lakes (1987). l_t defines the characteristic length for torsion and is a measure of the size effect displayed in the material relative to an equivalent elastic solid material.

The value of the coefficient 'C' is chosen to minimise the couple stresses that are applied to the lateral surfaces of the beam. It has been suggested by Park & Lakes (1987) that $C = 25Nl_t/d$ is sufficient to minimise the error in the parameters over a wide range. As 'C' is

dependent on the depth of the sample, its influence will diminish with increasing size.

The first two terms within the brackets are equal to the warping constant of a classically elastic square prism when C tends to zero and can be simplified to

$$I_p = \frac{2.25d^4}{16} \tag{2.45}$$

The next term is only dependent on the characteristic length in torsion and the breadth of the sample. As C tends to zero, the influence of the other terms within the square brackets will also diminish. As the warping constant and the characteristic length term are dependent on d^4 and d^2 respectively, it can be assumed that these terms will dominate the response if a large enough range of sample sizes is tested.

For the purposes of this investigation, a simplification of the beam rigidity was made to approximate the characteristic length of the structures. Thus,

$$J' = G^* \left[I_p + 2{l_t}^2 d^2 \right] \tag{2.46}$$

substituting in equation 2.45

$$= G^* \left[\frac{2.25d^4}{16} + 2{l_t}^2 d^2 \right] \tag{2.47}$$

By plotting J'/d^2 against d^2 it is possible to identify the shear modulus from the gradient of the linear portion of the slope which will appear when a large enough set of samples are tested. The characteristic length, l_t is estimated from the intercept of this plot when it is extrapolated to intersect the horizontal, d^2, axis.

The measure of the characteristic length from this is therefore only an approximated value which is used to quantify the size dependencies that the material exhibits in samples of similar size scale to the underlying microstructure. To determine the other constitutive parameters, N and ψ would require more involved methods to match the experimental data to the full analytical solution presented in equation 2.44.

2.3 Summary and Conclusion

In this chapter, the constitutive equations for a micropolar material have been summarised. The derivation for the flexural and torsional stiffness of a slender bar have also been presented which will form the basis of the experimental investigations that will follow in chapters 7 & 8. The general formulation for the deformation of a micropolar beam has been defined for various flexural loading modes. An approximation has been taken to derive a practical experimental solution to observe the size effects that are predicted when a bar is subjected to

a twisting moment. The additional parameters that have been shown in the derivation here will be calculated through a series of computational and experimental tests which have been designed to identify the key parameters.

Chapter 3

2-Dimensional Lattice Structures

In this chapter, the mechanical properties of a 2-dimensional planar material comprised of a square lattice is investigated within a micropolar continuum. Size effects were observed in bending and found to be strongly dependent on the density of the sample and generally decrease with increasing volume fraction. It will also be shown that the relative position of the cell microstructure with respect to the sample surface can significantly alter the displayed size effect which may have significant implications for testing real materials with a stochastic distribution of voids.

It has also been observed that Euler-Bernoulli beam theory may not offer an appropriate solution to low density heterogeneous materials subjected to 3-Point bending. A modified Timoshenko theory has shown to be capable of capturing the localised effects which are introduced with a material that has a weak resistance to shearing due to square symmetry.

Further to this an analytical model has been constructed for a square lattice extruded longitudinally. It was observed that in bending, the magnitude of the size effect is highly dependent on the spacial distribution of the material within the unit cell.

3.1 Sample Loading Modes

It has been shown by both Beveridge (2010) & Frame (2013) that the nature in which heterogeneous samples are loaded can affect the observed material properties of the sample. It was observed in 3-point bending experiments that as the aspect ratio of a sample was decreased, the rate at which stiffness increased with reducing size was diminished. This diminishing was mainly attributed to the increase in shear deformation effects which are induced in a shorter beam subjected to 3-point loading. To fully describe a low aspect ratio heterogeneous beam within the micropolar continuum a more complex theory such as a modified Timoshenko beam formulation is required.

In the Euler-Bernoulli beam theory, it is assumed that cross-sections of a beam sample will remain both plane and normal to the axis when loaded in flexure. Timoshenko theory accounts for both bending and shear deformation, which cannot be neglected in shorter samples. Timoshenko beam theory will converge to classical beam theory when the length to depth aspect ratio of the sample is sufficiently large that these effects can be neglected.

The above theories have been formulated for linear elastic homogeneous materials of constant cross section. Heterogeneous materials by their very nature do not necessarily have a uniform cross section meaning that any correlation between the apparent sample behaviour and classical theories should be treated with caution.

3.1.1 Numerical (FEA) Simulations of Lattice Structures

As was previously discussed in chapter 1, cellular structures are of great interest to engineers due the potential strength to weight benefits that can be obtained. The mechanical behaviour of regular lattice honeycombed structures in particular has been a keen focus of researchers as the geometrically regular nature lends itself well to mathematical modelling.

While such structures can be modelled analytically when the connecting members are slender (e.g. Masters & Evans (1997); Wang & McDowell (2004)), it has long been recognised that under experimentation care must be taken to minimise any localised loading effects which can be introduced at high porosity levels. Work carried out by Brezny & Green (1990) showed that in bend tests of a honeycombed lattice material, the experimental elastic modulus was heavily dependent on the ratio of the macroscopic sample size to the underlying cell size. It was concluded that as sample size diminishes, edge effects brought about by truncated cells on the outer surface of the samples adversely affect the observed stiffness. Other such effects which become significant at such low densities include localised shearing and buckling of individual cell walls within the samples. Sample aspect ratio has also been shown to be a contributing factor in determining the correct flexural parameters of heterogeneous materials (Beveridge, 2010; Frame, 2013).

To capture the size scale dependent material properties that are predicted with higher order theories such as micropolar elasticity, localised effects need to be accounted for or ideally eliminated in order to obtain an accurate measure of the mechanical behaviour. For this reason, a set of virtual experiments were undertaken using the finite element analysis (FEA) software ANSYS to investigate how the mode of loading affects the observed mechanical properties. The material investigated was a 2D planar square lattice structure (Figure 3.1.). This configuration was chosen as the mechanical properties have been previously investigated in literature (Kumar & McDowell, 2004; Wang & McDowell, 2004; Dos Reis & Ganghoffer, 2012).

A parametric investigation was undertaken to observe how the samples responded at differing size scales and aspect ratios. The mechanical response of the samples at differing aspect ratios was found by utilising the method of size effects as introduced by Gauthier & Jahsman (1975) and Yang & Lakes (1981). Here, samples of differing size, but constant aspect ratio are tested in flexure. Under ideal conditions, a linear response is predicted to be observed when the normalised rigidity, Ω is plotted against the reciprocal of the sample depth squared, $\frac{1}{d^2}$ (See section 2.2.2.).

Three different modes of flexure were considered within this analysis to ascertain how the material is likely to respond when subjected to mechanical tests and which mode is most suitable to capture the additional parameters that are required to fully define the matrix material.

Models were constructed in ANSYS using the higher order BEAM189 elements. This element is a 3-dimensional, quadratic three-node beam representation with six degrees of freedom (3 translational and 3 rotational) at each node. It is based on Timoshenko beam theory and includes shear deformation effects.

The material consists of an array of interconnecting square unit cells which are evenly spaced horizontally and vertically from the neighbouring cell. Two possible symmetrical unit cells can be chosen for this material which are capable of describing it at any size scale. These are shown in figure 3.1.

In the first case which is defined as the 'closed' unit cell, (Figure 3.1 a), the material is distributed around the perimeter of the cell by beams of thickness t. The length of each beam is defined by the horizontal and vertical cell wall spacing. In the region of adjoining cells, the cell wall thickness can be expressed as $2t$. In the second unit cell, which is defined as the 'open' cell case (Figure 3.1 b), the beams are centred around a central node and have a thickness of $2t$. The main difference between the two unit cells, is that in the 'open' cell case, the surface of the sample intersects the cellular structure at the centre of the cell thus exposing the internal void. In the closed cell case, all voids are totally enclosed within the bounds of the sample. While both cell configurations are representative of the bulk material and appear identical at a sufficiently large size scale, samples of an order approaching that of the unit cell are clearly very distinct as the cell topology at the surface of the sample cannot be ignored.

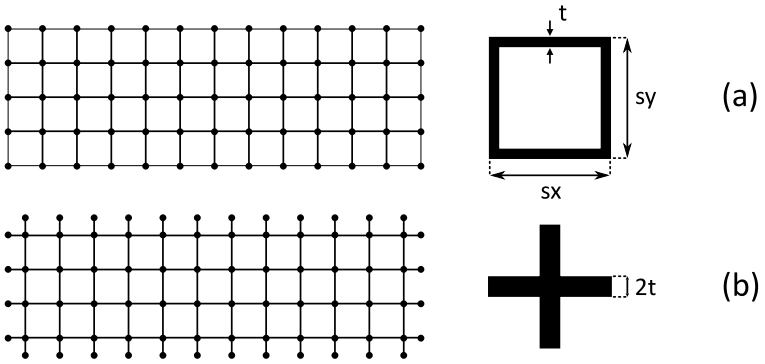

Figure 3.1: Two possible unit cell configurations that can be used to define a matrix of orthogonally connected bars in a lattice configuration. (a) 'Closed' cell configuration, (b) 'Open' cell case.

As micropolar theory does not account for surface topology, the initial investigation will be based around the closed cell configuration. Each beam consists of an array of orthogonal bars that were spaced 1 mm apart. Internal beams within the sample were assigned a thickness of 0.2 mm while those adjacent to the exterior surfaces had a thickness of 0.1 mm. A Young's modulus of 70 GPa and a Poisson's ratio of 0.3 was used to define the matrix material.

The model was constructed from an array of keypoints which were connected by individual lines. As the beam elements are represented by one dimensional lines, the outer lines which correlated to the surfaces of the model were offset by half of their thickness in order to maintain a consistent distribution of mass throughout the sample. This is important as small changes in the second moment of area can have a significant effect on the stiffness of individual samples as the size approaches that of the unit cell. In total, each cell wall was discretised using 10 elements which was deemed sufficient to capture the deflection of the beams under load.

The modulus of the bulk material, E^* in this case is directly related to the global stress that acts on a sample that is subjected to a fixed axial strain. In the case of a thin walled square lattice this can be approximated from the ratio of the total beam thickness to the overall size of the unit cell (Wang & McDowell, 2004) and is given as:

$$E^* = E_s \eta \tag{3.1}$$

where

$$\eta = \frac{2t}{SY} \tag{3.2}$$

Here, E_s is the Young's modulus of the solid material and η is the ratio of the total cell wall

thickness, $2t$ to the unit cell spacing, SY in the direction perpendicular to the axial spacing. The micropolar modulus for this material is therefore approximately 14 GPa. The Poisson's ratio, ν^* can be approximated as 0 as there is no contraction within the lattice. This approximation is only valid for low density square beams with slender internal members.

3.2 Flexural Loading

Mechanical testing is commonly used to determine the physical properties of materials and to assess their behaviour under different loading conditions. Recent investigations by Frame (2013) and Beveridge (2010) have shown that it is possible to capture the size-dependent mechanical properties of materials with significant heterogeneities from flexural tests. The samples in question however were sufficiently dense that localised deformations due to the mode of loading could be neglected assuming that care was taken when loading the samples. Experimental results can drastically vary from theoretical predictions when localised loading effects that are induced on the specimen become significant and are not fully accounted for in the global deformation field. Such variations can be easily accounted for in linear elastic homogeneous materials as there are only a few variables which need to be considered. When modelling heterogeneous materials that display size-scale dependencies, localised structural effects need to be considered and minimised in order to capture the true nature of the overall mechanical behaviour.

Initial investigations are therefore based on simulating the apparent stiffness of idealised heterogeneous materials in common experimental loading configurations. A two-dimensional square lattice was chosen as the model material since a general solution is available for the case of a thin walled lattice which can be used as a basis for comparison. Three loading modes were chosen, namely 3-point bending, 4-point bending and pure bending with constant moment load. Various beam aspect ratios and unit cell densities were also considered in order to assess the material response under different parametric conditions.

3.2.1 Pure Bending

As a basis of comparison, initial tests were conducted by applying a constant moment load to the end face of each beam sample. Samples with between 1 and 5 cells through the depth were tested at an aspect ratio of 10 in order to obtain the micropolar constitutive properties. In equation 2.36 it was shown how the rigidity of a micropolar material is expected to vary with sample size. By dividing both sides of equation 2.36 by the second moment of area of the homogenised section, the influence of the size effect can be deduced with respect to the

modulus of the material under investigation from:

$$\frac{12ML}{\theta bd^3} = E^* \left(1 + 24\left[\frac{l_b}{d}\right]^2\right) \tag{3.3}$$

It was found that the flexural modulus, E^* for this material, determined from the intercept, was 14000 MPa which was in line with the analytical prediction for the Young's modulus. The modulus of micropolar bending, γ and characteristic length, l_b were found to be 20160 N and 0.25 mm respectively from the gradient of the linear portion of the experimental plot (Figure 3.2.).

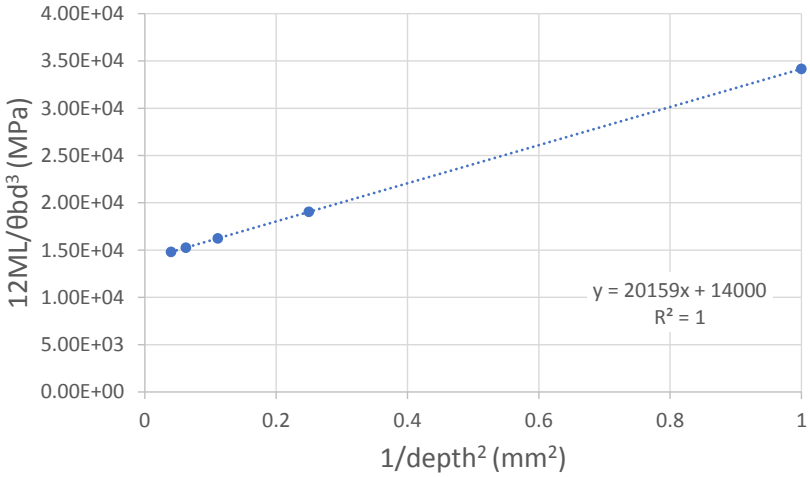

Figure 3.2: Variation in flexural stiffness of samples with specimen size. Smaller samples are relatively stiffer than larger ones.

3.2.2 3-Point Flexural Tests

A three-point bend test is one of the most common loading modes used to determine the flexural modulus of a material due to the ease of specimen preparation and testing. However, it has been shown that heterogeneous samples are sensitive to geometric parameters such as the aspect ratio (Beveridge, 2010; Frame, 2013). A thorough investigation is therefore required to determine how applicable this mode of loading is for capturing the size dependent effects that are seen in micropolar elasticity.

The maximum deflection, $w(x)$ of a micropolar beam subjected to 3-point bending can be derived from the standard Euler-Bernoulli relationship shown in equation 2.36 and can be

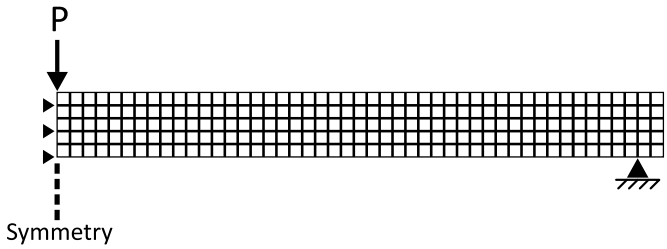

Figure 3.3: 3-point bend tests modelled using half symmetry boundary conditions.

given as:

$$w(x)_{max} = \frac{PL^3}{48(E^* I_s + \gamma A)} \tag{3.4}$$

where P is the applied load, L is the length of the section, E^* is the micropolar modulus, I_s is the second moment of area of the section, γ is the micropolar bending modulus and A is the cross-sectional area of the beam.

The rigidity ratio, Ω can be expressed as the ratio of the rigidity of the discrete sample to the homogenised value and is defined as:

$$\Omega = \left(\frac{P}{w(x)_{max}}\right)\frac{(AR)^3}{4E^* b} = \left(1 + \frac{12\gamma}{E^* d^2}\right) \tag{3.5}$$

where AR is the length to depth aspect ratio, b the breath and d is the sample depth.

Simulations were carried out in ANSYS to calculate the relative stiffness of beams with a square unit cell that were subjected to a 3-point flexural load.

Tests were conducted with half symmetry boundary conditions applied in order to reduce the size of the models being generated. To minimise the effect of the boundary conditions on the results of the experiments, each beam was generated slightly larger that required so that the supports did not rest on the end face of the beam. Care was also taken to place the applied load and the reaction supports on nodes which corresponded to a joint at a vertical column (Figure 3.3.). In total, 4 different aspect ratios were also analysed in order to observe the effect that this had on the apparent stiffness of the material and the observed size effects.

3.2.3 Results

The results of the experiment showed that in the case of the thin walled lattice tested here, the normalised stiffness of the beam was highly sensitive to the aspect ratio of the sample under investigation (Figure 3.4.). Low aspect ratio samples tended to largely underestimate the stiffness of the material. Samples with only one void through the depth also displayed the greatest reduction in stiffness compared to a similar beam that was subjected to a constant moment load. Further to this, some of the samples were apparently slightly less stiff at smaller size scales which contradicts micropolar theory.

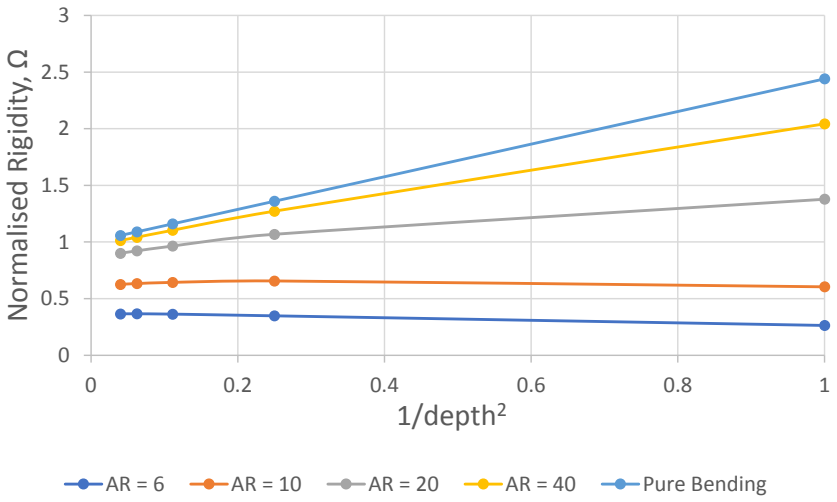

Figure 3.4: Variation in observed stiffness with beam aspect ratio. Sample size increases with decreasing $1/\text{depth}^2$. The stiffness of the beams is normalised by the Young's modulus of the cellular material.

Euler-Bernoulli theory does not take into account local shear deformations which occur within beams subjected to flexure at low aspect ratios. Timoshenko beam theory on the other hand does not assume that sections of a material remain plane under bending forces by taking into account the shear stresses within the beam. In Timoshenko theory, a homogeneous beam subjected to 3-point bending will have a maximum deflection that is dependent on both the rotational bending effects and shear deformations by

$$w(x)_{max} = \frac{PL}{4\kappa AG_s} + \frac{PL^3}{48E_sI_s} \tag{3.6}$$

where w is the displacement of the beam, P is the applied load, L is the length of the sample, A is the cross sectional area, κ in this case is the Timoshenko shear coefficient, I_s is the second moment of area. G_s and E_s are the shear modulus and Young's modulus of the solid material

respectively.

In the case of a square lattice structure, the shear modulus, G^* does not relate to the Young's modulus and Poisson's ratio in the usual way due to the orthotropic nature of the material (Wang & McDowell, 2004; Dos Reis & Ganghoffer, 2011). For a slender lattice it can be given as

$$G^* = \frac{E_s \eta^3}{2} \tag{3.7}$$

When the Timoshenko theory is adapted to include the homogenised shear modulus of the lattice, it can be observed that the first term in equation 3.6 has a significant contribution to the overall deflection of the beam and cannot be ignored unless the sample is very slender.

This increase in deflection is due to the decreased resistance to shearing of the lattice structure in comparison to an equivalent homogeneous material and accounts for the degradation in sample performance with increasing void volume fraction. In order to be able to fully capture the size dependant nature of the material in bending, another method of loading is required which does not include a significant shearing component.

While incorporating the shear modulus of the lattice into the Timoshenko beam model offers a closer approximation to the response of the samples under 3-point bending, it does not take into consideration the size dependent nature of the material. The general formulation for a linear elastic homogeneous Timoshenko beam is set out in many engineering text books (Javanbakht & Öchsner, 2018) and is dependent on both the shear forces and bending moments acting on it. The bending moment, M and the shear force, Q are related to the displacement, w and rotation, θ by

$$M = -(E^* I_s + \gamma A)\frac{d\theta}{dx} \tag{3.8}$$

$$Q = \kappa A G^* \left(\frac{dw}{dx} - \theta\right) \tag{3.9}$$

where equation 3.8 is expressed in terms of a micropolar beam as in equation 2.28. The homogenised micropolar shear modulus, G^* is also incorporated in equation 3.9. The total displacement at a given point along the length of the beam can thus obtained by integrating equation 3.8 and substituting it into equation 3.9 while applying the correct boundary conditions for three-point flexural loading.

$$w(x) = \frac{Px}{2\kappa A G^*} + \frac{Px}{4(E^* I_s + \gamma A)}\left(\frac{L^2}{4} - \frac{x^2}{3}\right) \qquad \text{for } (0 \leq x \leq L/2) \tag{3.10}$$

$$w(x)_{max} = P\left(\frac{L}{4\kappa A G^*} + \frac{L^3}{48(E^* I_s + \gamma A)}\right) \tag{3.11}$$

Equation 3.10 defines the deflection of a Timoshenko beam that has been modified to include the micropolar bending constants. For a linear elastic isotropic material of rectangular section κ is given as $5/6$. Equation 3.11 provides a closer representation to the observed bending solution for beams which consist of a low density planar lattice. The stiffness of the beams are overestimated however. To resolve this, an approximation for the Timoshenko shear coefficient is required to be made in order for the analytical model to fit the experiment. A two stage approach was taken in order to correct the shearing coefficient in equation 3.11 to match the experimental results. Samples with only one unit cell through the depth displayed the biggest deviation in shear coefficient from the classical value. This effect is seen to diminish with increasing sample size. The first step taken was to identify the magnitude of the difference at the smallest size scale. This value was found to be insensitive to sample aspect ratio. As the variation in shear coefficient reduces to the homogenised value with increasing sample size a second parameter was added to take this into account. Each parameter was then minimised for the smallest sample in the set, then the largest respectively in order to find a converged solution.

It was found that using the approximation $\kappa = 5/6\left(1 - \frac{0.507}{d^{1.25}}\right)$ provided an adequate correction factor to the standard value of a rectangular beam section and is accurate to within 2% over the range that was considered. This can be clearly seen in figure 3.5.

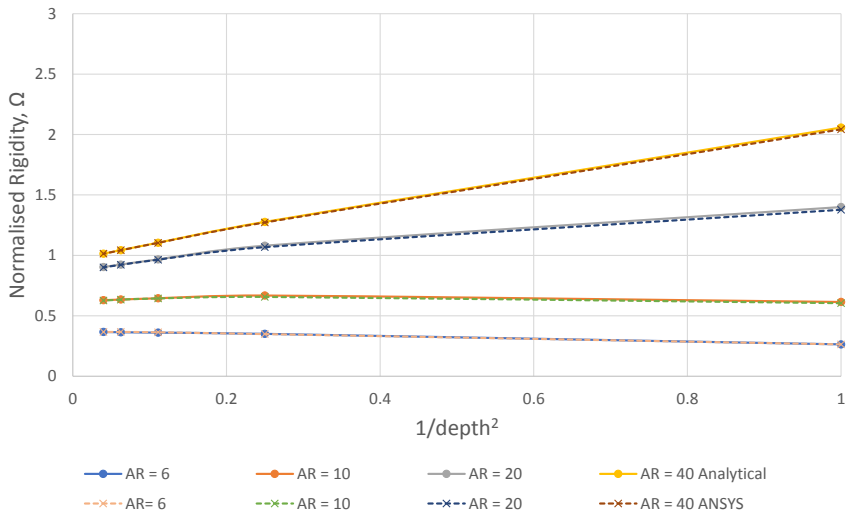

Figure 3.5: Variation in stiffness of samples at different aspect ratios derived analytically from a modified Timoshenko formula. Data is compared to the simulated results in ANSYS. All tests are based on a unit cell with dimensions; SX=SY=1 mm , t=0.1 mm. The stiffness of the beams are normalised by the Young's modulus of the cellular material.

This correction factor, while indicative of the overall change in shear correction factor should be treated with caution as it based on a fixed cell density and cell size. Additional experimentation would need to be carried out in order to identify if there is any dependence on

the unit cell size and also the lattice density.

A correction factor is required as equation 3.11 does not account for the loss of stiffness that is seen as the sample size diminishes. By taking into account the localised variations, the characteristic length of the material can still be derived under 3-Point loading. It may not be practical however to simulate the material to be tested, therefore a more consistent method of loading should be sought for more general low density materials.

3.2.4 4-Point Flexural Loading

The second loading mode that was chosen to conduct mechanical tests was four-point bending. In this configuration, a beam which is rested horizontally on two equally spaced supports is loaded by two actuator arms that are equally spaced around the centre of the beam. The stiffness of a beam within the linear elastic micropolar continuum has been derived in terms of the deflection of the central section in equation 2.38 and has been recapped below.

$$K = \frac{4bd^3E^*}{3L_1L_2^2}\left(1 + 24\left[\frac{l_b}{d}\right]^2\right) \tag{3.12}$$

Recalling, L_1 and L_2 denote the length of the beam in the outer section and centre section of the beam respectively. All other values have there usual meaning.

A beam loaded in 4-point bending is expected to have zero shear forces across the actuator arms assuming that the applied load is evenly distributed and equal at each actuator. A shear component still exists however in the outer section of the beam. In order to determine the flexural modulus, the applied force and the relative displacement between the maximum deflection and the displacement of the actuator arms needs to be obtained.

As in the previous case, samples were tested at various aspect ratios for differing sample sizes in order to obtain the apparent variation with size. The results were compared to a set of samples subjected to a constant moment load.

3.2.5 Results

The results of the 4-point flexural tests showed an improvement in the normalised sample stiffness in comparison to the 3-point bending experiments. Some variation can be observed with respect to the aspect ratio of the samples under test, with more slender specimens displaying less reduction in stiffness as compared to the ideal case (Figure 3.6.). Samples with two or less cells through the depth show the greatest reduction in stiffness. This loss in stiffness can be attributed to the localised effects which appear when applying a point load to the samples. Shear forces which are present in the outer section of the beam are more dominant when there are less cells through the depth as the square configuration is weak under shearing. To improve the de-

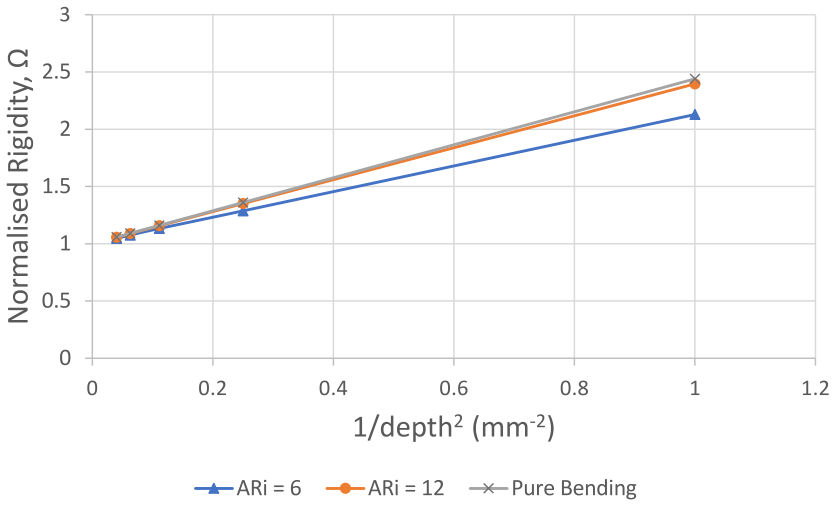

Figure 3.6: Variation in stiffness of beams with change in sample depth. The inner section of the beams have an aspect ratio of 6 and 12. The overall aspect ratio of the beams are 10 and 20 respectively.

flection of the outer section and reduce the influence it has on the central section of the beam, then it is beneficial to increase the aspect of the outer section. A balance however must be made between the ratio of the outer section to the centre section. This parameter is also highly dependent on the density of the unit cell which makes up the material under investigation.

It was observed that the calculated flexural modulus was fairly insensitive to the change in aspect ratio. The beam which had an inner aspect ratio of 6 was less than 1% stiffer than the model which was loaded under idealised conditions. The characteristic length calculated for this beam however was only 88% of the true value. This result could be improved however by evaluating a larger sample set and discounting the smallest samples which are most influenced by the boundary conditions of the test setup.

Generally however 4-point bending offers significant improvement over 3-point flexural tests when trying to capture the size dependant nature of low density planar lattice structures. If a suitable aspect ratio is selected to test the material in question, then a Euler-Bernoulli approximation has been shown to provide a sufficiently accurate solution to the problem. A Timoshenko based approach may be required to deal with more complicated solutions.

3.3 Cell Wall Thickness and Surface Topology Effects

While idealised predictions have been made for various 2-dimensional lattice structures with very slender internal beam members, there appears to be a lack of data available which captures how the lattice behaves when the cell wall thickness (cell density) is varied. Such data would be useful as it could help to determine the range over which the higher order model is applicable and also allow for optimising of the structure for a given application. Another aspect of the investigation is that many of the formulations are based on infinite lattice structures rather than discrete models. The use of discrete models is a more useful approach as it allows for a more realistic representation of the local characteristics of the material rather than a global field representation.

Surface effects have been shown to negatively impact the size dependent stiffening properties of a micropolar material (Brezny & Green, 1990; Frame, 2013). While samples with a random distribution of voids which are relatively large in comparison to the heterogeneities which define the microstructure can be prepared in such a way which minimises the influence of surface defects, at size scales approaching the typical voids size within the material, surface effects can become significant and must be accounted for. In order to quantify how the magnitude of the size effect changes with finite specimen size, tests were conducted using the method of size effects described in the previous section under constant moment loading conditions to minimise any unwanted localised loading effects that might influence the response.

Virtual samples were tested at varying void volume fractions in both the 'open' and 'closed' unit cell configurations as defined in figure 3.1. Models were generated with the 2D higher order quadratic Plane183 continuum elements as beam elements are not sufficient to accurately capture the deformation when the connecting internal members are not slender.

Samples with between 1 and 10 voids through the depth were tested at each void area fraction and the calculated stiffness was plotted against sample size in order to obtain the magnitude of the size effect. The characteristic length in bending, l_b and the flexural modulus, E^* were inferred from the intercept and gradient of the linear portion of the slope.

3.3.1 Results & Discussion

Two distinct size effects were observed when the material was tested in flexure. Samples with a continuous surface that comprised of the 'closed' unit cell displayed a size stiffening effect, while those constructed from the 'open' unit cell displayed a size softening effect. The magnitude of the size effect, ${l_c}^2$ is largely dependent on the void area fraction of the cell and has been summarised in tables 3.1 & 3.2. It is related to the characteristic length in bending by ${l_c}^2 = 24{l_b}^2$. The void area fraction, A_f in this case is defined as the ratio of the void area

within the unit cell and the overall cell area and increases with decreasing cell wall thickness.

$$\text{Void } A_f = \frac{(SY - 2t)^2}{SY^2} \tag{3.13}$$

Continuous Surfaces

t	Void A_f	E^*	${l_c}^2$	${l_b}^2$	l_b
mm		GPa	mm^2	mm^2	mm
0.5	0	70	0	0	0
0.4	0.04	62.44	0.121	0.005	0.071
0.3	0.16	45.86	0.462	0.019	0.139
0.2	0.36	29.50	0.912	0.038	0.195
0.1	0.64	14.34	1.424	0.059	0.244
0.01	0.96	1.4	2	0.083	0.289

Table 3.1: Mechanical properties for a planar square lattice of varying void fraction derived from samples with a continuous surface subject to a constant moment loading.

Voids Intersected by Surfaces

t	Void A_f	E^*	${l_c}^2$	${l_b}^2$	Magnitude of l_b
mm		GPa	mm^2	mm^2	mm
0.5	0	70	0	0	0
0.4	0.04	62.3	(-)0.20	(-)0.008	0.091
0.3	0.16	46.02	(-)0.561	(-)0.023	0.153
0.2	0.36	29.79	(-)0.819	(-)0.034	0.185
0.1	0.64	14.44	(-)0.958	(-)0.04	0.2
0.01	0.96	1.4	(-)1	(-)0.042	0.204

Table 3.2: Mechanical properties for a planar square lattice of varying void fraction derived from samples with a discontinuous surface subject to a constant moment loading. The magnitude of the characteristic length, l_b in this case is a representative value as ${l_b}^2$ is negative.

The flexural modulus of the material is strongly dependent on the density of the unit cell, but is independent of the variation in surface topology of the sample. This is in line with theoretical predictions which suggest that the modulus is size independent.

Figure 3.7 captures the variation in rigidity with increasing sample size. Values have been normalised against an equivalent homogeneous beam. The largest increase in rigidity can be observed in the 'closed' cell samples when there is only one unit cell through the depth of the sample. It should be noted that from the resulting plots in figure 3.7 no indication of material stiffness can be derived for a sample smaller than one unit cell ($1/\text{depth}^2 = 1$) as this would imply an infinite increase in stiffness which would be unphysical.

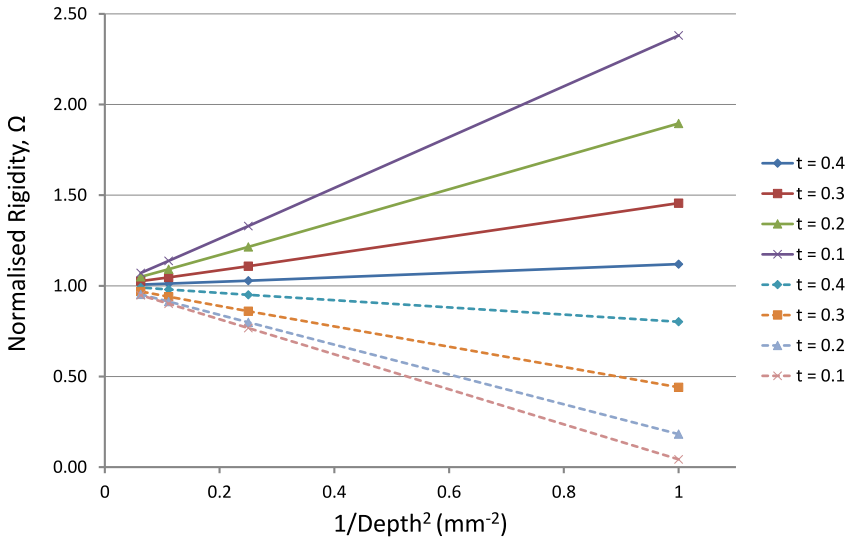

Figure 3.7: Variation in normalised rigidity with variation in cell wall thickness. Solid lines represent beams with a solid outer surface. Dashed lines represent beams whereby the voids are intersected by the specimen surface.

The magnitude of the size effect is seen to increase with decreasing cell wall thickness. From figure 3.8 it can be observed that the positive size effect appears to continuously increase with decreasing cell wall thickness (Void fraction). In reality however this effect is limited by the relative decrease in stiffness associated with decreasing cell density. It is also quite clear to see in figure 3.8 that the magnitude of the size softening when there are surface defects is different to that when the surfaces are solid.

As the two unit cells considered represent the upper and lower bounds of the square lattice under flexure, discrepancies in the specimens due to surface preparation may have a significant influence on the magnitude of the size effect which can be observed experimentally.

The theoretical value of the characteristic length in bending has been given as $SY/\sqrt{24}$ mm for a 2D thin walled square lattice (Dos Reis & Ganghoffer, 2011). It was found however that the characteristic length in this investigation converged on $SY/\sqrt{12}$ mm in the case where a continuous sample surface was defined. Others have reported differences in the characteristic length for bending depending on the theory used to derive it (e.g. Tekoğlu (2007)). Here, the material characteristic length presented differed from the characteristic length defined by Mindlin for couple stress theory by a factor of $\sqrt{2}$. For samples with a discontinuous surface, determination of the material characteristic length is not straightforward due to the negative square root that appears when micropolar theory is applied. Nevertheless, it is interesting to note that the characteristic length derived from the absolute value of the magnitude of the size softening effect is $SY/\sqrt{24}$ mm. Therefore, the characteristic length that is found here is just

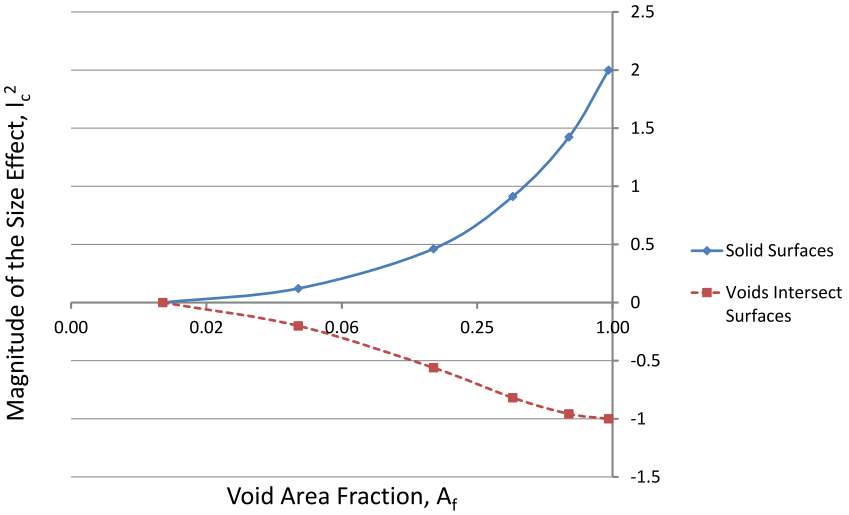

Figure 3.8: Variation in the magnitude of the size effect of beams with an in-line square lattice microstructure with respect to void area fraction. Samples with a continuous outer surface are represented by the solid line while the dashed line represents the case where the voids are exposed at the surface of the beams.

indicative of the magnitude of the size effect rather than being definitive.

Normalising the stiffness of the beams against the micropolar modulus of the material, the results were plotted against the inverse of sample depth squared. It can be seen from figure 3.7 that this alternative unit cell configuration displays a size dependent softening effect whereby the larger samples are stiffer that the smaller ones. This is contrary to the size stiffening effect that can be seen in the closed cell configuration. The magnitude of this stiffening effect is used as the basis of determining the characteristic length of the lattice material. It was found that for the closed cell case that the maximum characteristic length is $1/\sqrt{12}$ mm while the samples which intersect the unit cells at the surface have a characteristic length of $1/\sqrt{24}$ mm.

3.4 Summary and Conclusion

In this chapter, it has been shown that size dependencies can be observed in a 2-dimensional lattice that was loaded in flexure which can be described by micropolar elasticity. Size softening effects can be observed when the internal cellular structure of the lattice is intersected by the macroscopic sample upper and lower surfaces. While this effect is not accounted for by micropolar elasticity, it can be observed that the general variation with sample size is linear under ideal conditions albeit with a negative gradient. The magnitude of the size effect does not match that of the closed cell samples, but may be related in some manner.

It was observed that the size effect increases with decreasing volume fraction. The maximum obtainable increase in stiffness is predicted to be found when the mass of material diminishes. As this is unphysical, the maximum practical increase in material stiffness is obtained from the least dense sample which can be manufactured and tested accurately. A similar effect is seen in the case of the sample size reduction although the magnitude is clearly distinct.

It was also highlighted that the method of loading plays a significant role in the observed response. Low density samples which were subjected to 3-point bending may not respond in the manner which is predicted with size softening effects being observed. This response can be attributed to localised shearing effects which dominate the bending response. Timoshenko beam theory modified to include the higher order components of micropolar elasticity was shown to provide a more accurate representation of the deformation which occurs when the material is loaded in this manner.

4-point bending was shown to be a more consistent mode of loading and may perform better in physical tests. Pure bending is the most reliable method of testing the structures in flexure and should ideally be used to derive the higher order parameters computationally.

The maximum characteristic length as defined for a square lattice was found to be $SY/\sqrt{12}$ mm. This is in contrast to the theoretical value of $SY/\sqrt{24}$ mm that has been predicted by Dos Reis & Ganghoffer (2012). Interestingly however, the magnitude of the size effect obtained with surface defects matches this prediction, but the negative value that appears here presents difficulties resolving a physical interpretation.

Beam elements have also shown to be an appropriate method of modelling lattice structures assuming that the internal members within the sample are slender. For denser samples, continuum elements are better placed to model the interaction within the material.

3.5 Extruded Microstuctured Beam

It has been well documented that size effects can be observed in materials with significant microstructure when the sample size approaches that of the major heterogeneities within the material (Huang et al., 2000; Beveridge et al., 2013; Wheel et al., 2014). For a closed cell lattice structure the maximum size effect is generally observed in bending with a beam that has one void through the depth of the sample. The magnitude of this size effect is largely dependant on the distribution of the material within the unit cell and the relative volume fraction. In order to quantify how this effect varies with these parameters, an analytical investigation has been undertaken to determine this.

For this investigation, a square unit cell of material is considered (Figure 3.9). The microstructure of the unit cell consists of a square lattice configuration, with two internal size variables, t_1 & t_2, that is then extruded in the longitudinal axis. It should be noted that the voids in this case are orientated axially through the length of the samples rather than aligned to the transverse plane as seen in the previous section (Figure 3.10).

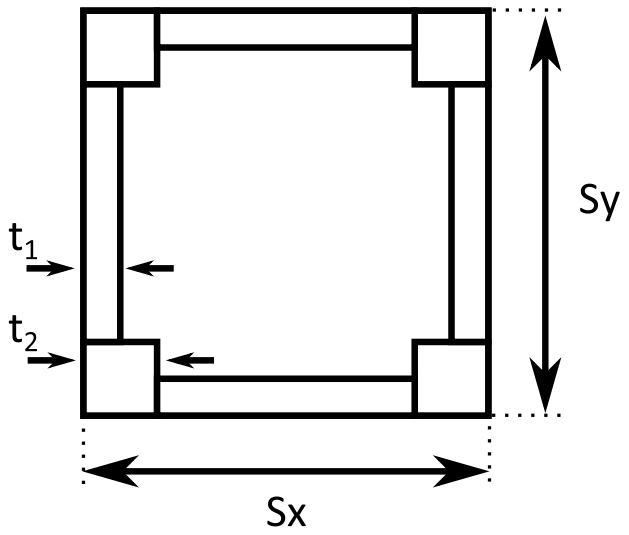

Figure 3.9: 2D cross section of unit cell

In the analysis, a density is set for each unit cell, and the size of both t_1 and t_2 are varied with respect to each other in order to keep the density constant. The resulting size effect is then derived from the variation in second moment of area with respect to a homogeneous continuum with an equivalent flexural modulus.

Classical elasticity Bernoulli beam theory relates the applied bending moments and re-

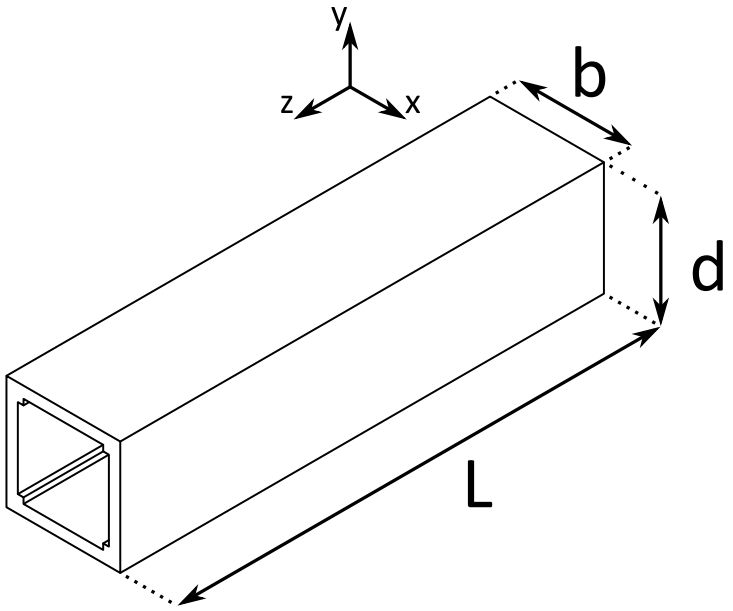

Figure 3.10: Extruded beam from a 2D cross section of a unit cell.

sulting deflection of a beam in flexure by the following relation:

$$\frac{M}{I_s} = \frac{\sigma}{y} = \frac{E_s}{R} \tag{3.14}$$

where M is the applied bending moment, I_s is the second moment of area, σ denotes the stress, y is the distance from the neutral axis, E_s is the modulus of the solid material and R is the radius of curvature of the beam.

The flexural rigidity is defined as the resistance to bending and can be given as

$$MR = E_s I_s \tag{3.15}$$

The rigidity of a micropolar beam was shown in equation 2.31 to be

$$\frac{ML}{\theta} = E^* I_s + \gamma A \tag{3.16}$$

To determine the magnitude of the size effect for a given cell configuration, two values of the flexural rigidity are calculated. The first value is obtained from calculating the second moment of area of the cross section of the beam using the particular geometric features along with the modulus of the solid matrix material. This value is then compared with the rigidity of a solid beam section which has a Young's modulus that is equal to the bulk value for the overall

beam.

$$E_s I^* = n E^* I_s \tag{3.17}$$

where n designates the magnitude of the difference between the discrete rigidity, $E_s I^*$ and the homogenised rigidity, $E^* I_s$.

The second moment of area of the discrete cross section for a single cell can be calculated by dividing it into several areas and using the parallel axis theorem to calculate the total moment of area around the centre of the beam.

For a beam comprised of one square cell, the total value for the second moment of area can be expressed as:

$$\begin{aligned} {I^*}_{xx} = {I^*}_{yy} = \sum_{i=1}^{n} \left(I_i + A_i d_i^2\right) = \\ 4\left(\frac{t_2^4}{12} + t_2^2\left(\frac{SY - t_2}{2}\right)^2\right) + \\ 2\left(\frac{t_1\left(SY - 2t_2\right)^3}{12} + \frac{\left(SX - 2t_2\right)t_1^3}{12} + \left(SX - 2t_2\right)t_1\left(\frac{SY - t_1}{2}\right)\right) \end{aligned} \tag{3.18}$$

where $A_i$is the area of the part under consideration and d_i is the distance from the axis to the centroid of the part.

The homogenised modulus of the material can be obtained from the variation in direct stress due to the change in cross sectional area for a given longitudinal strain on the material and can be shown to be dependent on the ratio of the solid material in the cross section, A_2 to the overall cross sectional area, A_1.

$$\begin{aligned} E_s = \frac{P_2 L}{A_2 w} \Rightarrow P_2 = \frac{E_s w A_2}{L} \\ \Rightarrow E^* = \frac{P_2 L}{A_1 w} = E_s\left(\frac{A_2}{A_1}\right) \end{aligned} \tag{3.19}$$

This equation is valid assuming that the cross-sectional area under consideration is constant throughout the length of the sample material.

The ratio of $\frac{A_2}{A_1}$ for an extruded material is equivalent to the volume fraction of the solid material within the unit cell. For a given volume fraction, the parameters t_1 and t_2 fall within

the bounds:

$$t_1 = \frac{\frac{A_f S X^2}{4} - t_2^2}{(SX - 2t_2)} \tag{3.20}$$

$$0 \leq t_1 \leq t_2 \tag{3.21}$$

The cell volume fraction defines the thickness of the cell wall when $t_1 = t_2$. The maximum value of t_2 is set when t_1 tends to zero. This value is unphysical however as it would relate to a material that has no internal connectivity between discrete nodes within the microstructure.

In order to quantify the magnitude of the size effect for a given configuration the rigidity ratio is plotted against the variation in wall thickness t_1. The normalised rigidity of the beam is defined as the ratio of the rigidity of beam that is under consideration to the rigidity of an equivalent homogenised beam that has the same axial modulus. It was observed from figure 3.11 that as the volume fraction of the material decreases, the rigidity ratio for the sample tends to increase. A lower limit of 1 is observed when the volume fraction tends to that of a homogeneous continuum. The upper bounds of the variation in rigidity is observed to depend on the normalised cell wall thickness. In the case where t_1 is equal to t_2 the maximum increase in rigidity is observed to be twice as large as the converged value. By comparison, as t_1 is reduced towards 0 then the increase in rigidity increases to 3 times the converged value. The

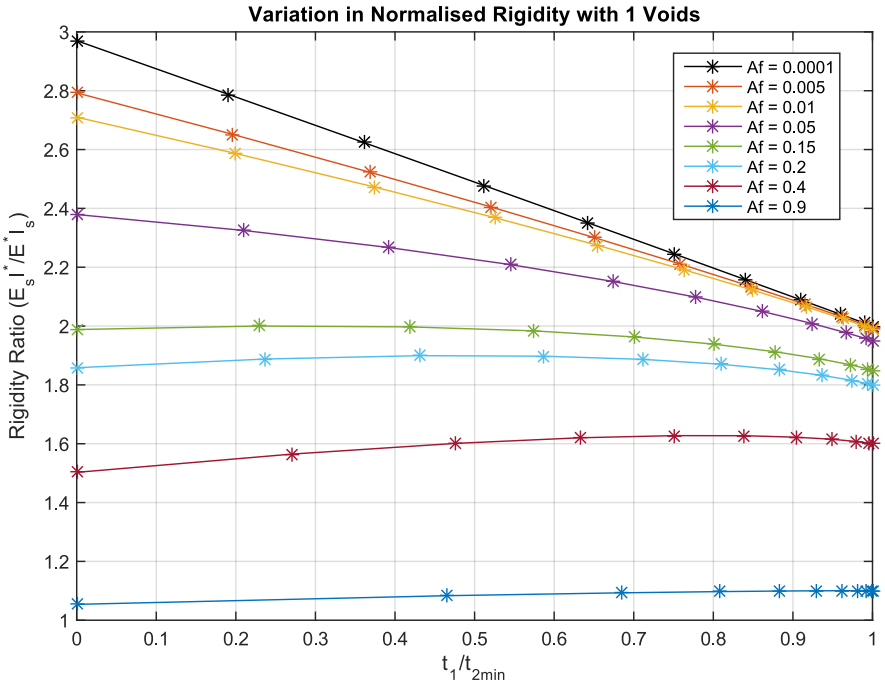

Figure 3.11: Variation in beam rigidity with normalised cell wall thickness for various cell area fractions.

above analysis only considers one unit cell through the length of the beam. It is expected that as the number of cells through the depth is increased, then the rigidity will eventually converge to the homogenised system. To verify this, and further gauge how the flexural rigidity changes with sample size, a code was generated in MATLAB to calculate the variation in rigidity over a range of sample sizes and unit cell configurations. Each sample was varied from 1 to 10 cells through the depth of the structure. The breadth of each sample was set equal to the depth in all analyses.

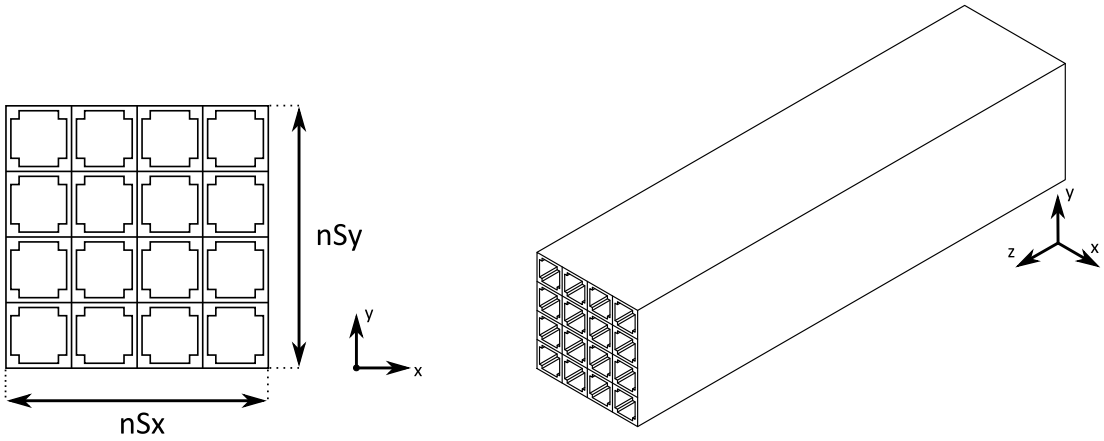

Figure 3.12: Extruded microstructure beam and 2D cross section of a typical sample.

For a multi cell beam (Figure 3.12), the second moment of area of the cross-section can be expressed in terms of the summation of the second moment of area of a each individual cell with respect to the centroid of the overall sample.

$$
\begin{aligned}
I^*{}_{xx} = I^*{}_{yy} = \sum_{i=1}^{n}\sum_{j=1}^{n}\left(I_{(i,j)} + A_{(i,j)}d^2_{(i,j)}\right) = \\
\sum_{i=1}^{n}\sum_{j=1}^{n}\Bigg[\frac{SX\cdot SY^3}{12} + \left(SX\cdot SY\left(\frac{D}{2} - (i-0.5)SY\right)\right) \\
- \frac{(SX-2t_2)(SY-2t_1)^3}{12} \\
- (SX-2t_2)(SY-2t_1)\left(\frac{D}{2} - (i-0.5)\,SY\right) \\
- 2\frac{(t_2-t_1)(s_y-2t_2)^3}{12}
\end{aligned}
$$

$$- 2(t_2 - t_1)(SY - 2t_2)\left(\frac{D}{2} - (i - 0.5)SY\right)\Bigg] \tag{3.22}$$

I^*_{xx} and I^*_{yy} will be identical for a square cross section of material, thus a similar formulation to equation 3.22 can be found for I^*_{yy}.

The variation in rigidity for beams with between 1 and 4 cells through the depth have been plotted in figures 3.13 and 3.14. It can be seen that the as the number of cells through the depth increases, the relative stiffness decreases towards that of a homogeneous beam.

The optimum value of stiffness will be different depending on the application for which the material is being used. It can be observed that for a single cell of the material under consideration that both the cell density and mass distribution play a significant role in the variation in rigidity that is recorded. As the flexural modulus in the longitudinal direction of the material is observed to be the same for a given density, it can be seen that the change in rigidity is directly related to the mass distribution and the second moment of area.

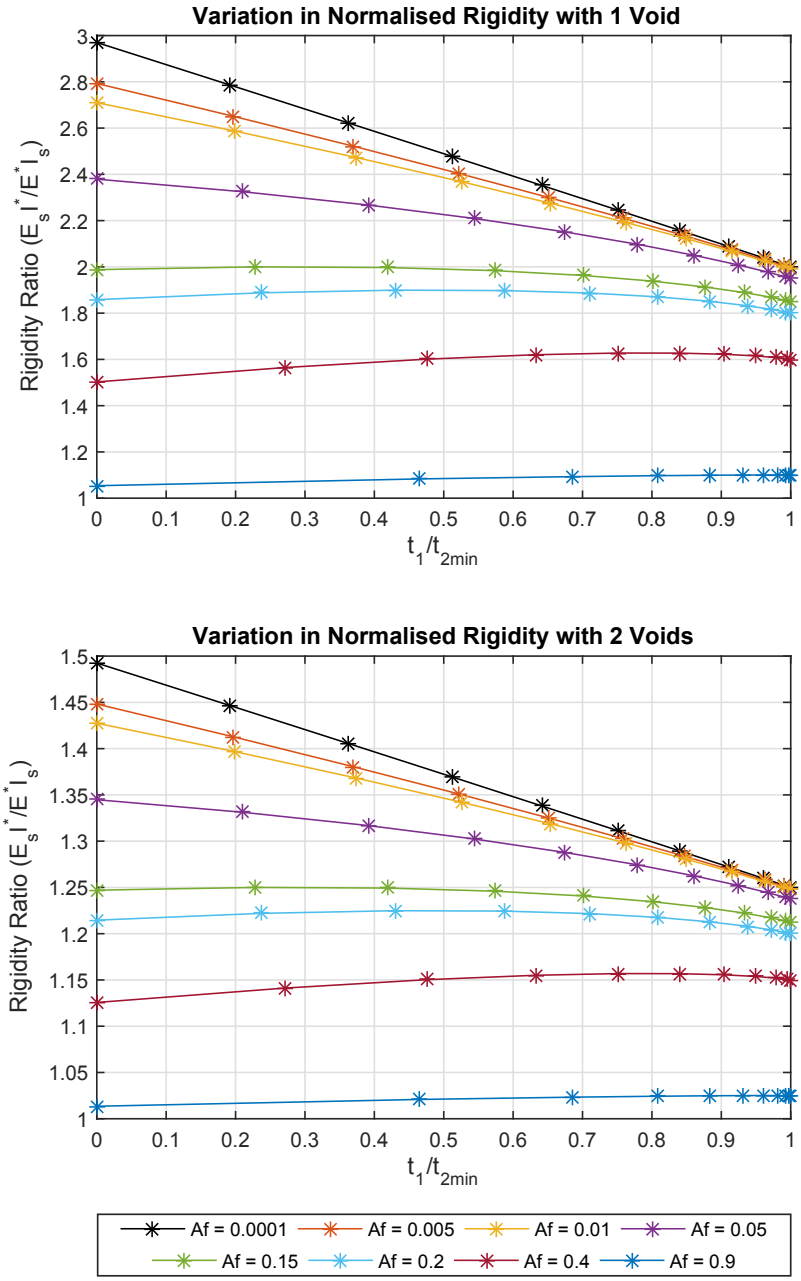

Figure 3.13: Variation in normalised rigidity with cell wall thickness for various cell area fractions. The rigidity is seen to decrease with increasing sample size.

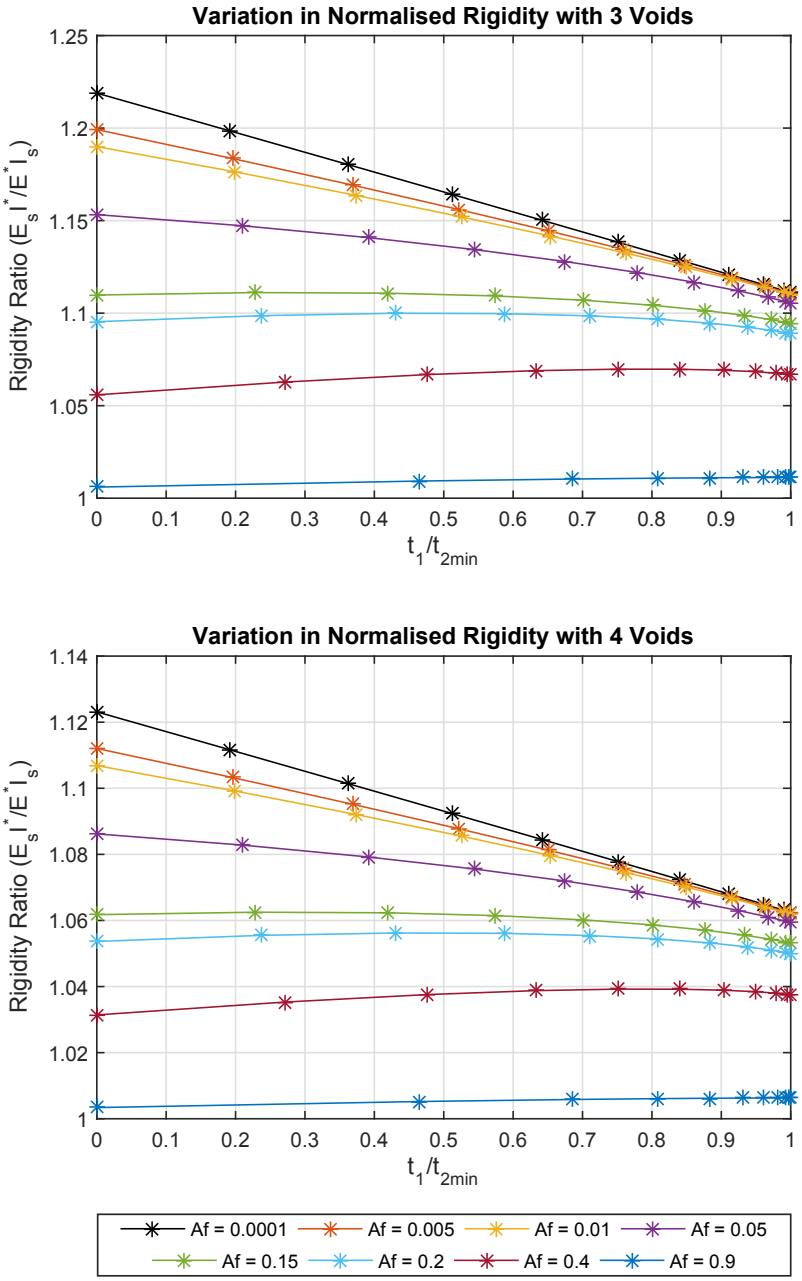

Figure 3.14: Variation in normalised rigidity with cell wall thickness for various cell area fractions. The rigidity is seen to decrease with increasing sample size.

3.5.1 Characteristic Length of Extruded Microstructure Beams

The characteristic length in bending of a micropolar material can be defined in terms of the longitudinal modulus as

$$l_b = \sqrt{\frac{\gamma}{2E^*}} \tag{3.23}$$

(Anderson & Lakes, 1994).

Recalling that in equation 3.5 the characteristic length can be defined in terms of the change in rigidity by rearranging in terms of the coupling modulus, γ and substituting into equation 3.23. The rigidity ratio, Ω can be shown to relate to the characteristic length in bending by,

$$\Omega = \frac{J'}{J} = 1 + \frac{24{l_b}^2}{d^2} \tag{3.24}$$

From figure 3.13 it can be seen that the maximum size effect is observed when the beam section is comprised of just one unit cell. The rigidity ratio is observed to vary between 2 (when $t_1 = t_2$) and 3 (as $t_1 \Rightarrow 0$) when the area fraction of the sample tends towards 0. When t_1 & t_2 are equal, the characteristic length of a single cell is found to be $\sqrt{\frac{SY^2}{24}}$ mm which is identical to the characteristic length reported by Dos Reis & Ganghoffer (2011). The upper bound displays an increase in rigidity that is 50% larger than when $t_2 \gg t_1$ and corresponds to a maximum characteristic length of $\sqrt{\frac{SY^2}{12}}$ mm. In general, it is predicted that moving the mass of the cell towards the outer corners of the unit cells has the effect of increasing the measured rigidity of the material. This effect is limited by the density of the sample as increasing it forces a greater proportion of the mass towards the centre of the cell thus limiting the observed size effect. It has also been seen that for a volume fraction of over 15% a maximum rigidity ratio is found to peak at an ever-increasing value of $\frac{t_1}{t_{2min}}$.

The maximum rigidity value can also be determined analytically by investigating the flexural rigidity for one unit cell. For the cellular material seen in figure 3.10 when $t_1 = t_2$;

$$\begin{aligned} E^* &= E_s \frac{A^*}{A_s} \\ &= E_s \left(\frac{d^2 - (d-2t)^2}{d^2} \right) \\ &= E_s \left(1 - \left(1 - \frac{2t}{d} \right)^2 \right) \end{aligned} \tag{3.25}$$

$$\Rightarrow \frac{E^*}{E_s} = \left(1 - \left(1 - \frac{2t}{d} \right)^2 \right) \tag{3.26}$$

$$I_s = \frac{d^4}{12} \tag{3.27}$$

$$I^* = \frac{d^4}{12} - \frac{(d-2t)^4}{12} = I_s - \frac{(d-2t)^4}{12} \tag{3.28}$$

$$\Rightarrow \frac{I^*}{I_s} = 1 - \left(1 - \frac{2t}{d}\right)^4 \tag{3.29}$$

$$\text{let} \quad \frac{2t}{d} = x$$

$$\Rightarrow \frac{E_s}{E^*} = \frac{1}{x(2-x)};$$

$$\frac{I^*}{I_s} = 1 - (1-x)^4 = x(4 + x(2 - x(4-x))) \tag{3.30}$$

$$\Rightarrow \quad \frac{E_s I^*}{E^* I_s} = \frac{4 + x(2-x)(4-x)}{2-x}$$

$$\Rightarrow \text{if} \quad \frac{2t}{d} \to 0 \quad \text{then} \quad \frac{E_s I^*}{E^* I_s} = 2 \tag{3.31}$$

Thus for a cell with uniform internal wall thickness ($t_1 = t_2$), the maximum increase in rigidity that can be observed when compared to a solid beam with the same overall modulus, is two.

Similarly it can be shown that when $t_2 \gg t_1$ the maximum increase in rigidity is a factor of three.

$$E^* = E_s \left(\frac{A_2}{A_1}\right)$$

$$= E_s \left(\frac{4\left(t_2^2 + t_1(d-2t_2)\right)}{d^2}\right) \tag{3.32}$$

$$I_s = \frac{d^4}{12} \tag{3.33}$$

$$I^* = 2\left(\frac{t_1\left(d-2t_2\right)^3}{12} + \frac{(d-2t_2)t_1^3}{12} + (d-2t_2)t_1\left(\frac{d-t_1}{2}\right)^2\right.$$

$$\left. +2\left(\frac{t_2^4}{12} + t_2^2\left(\frac{d-t_2}{2}\right)^2\right)\right) \tag{3.34}$$

$$\text{let} \quad (d-2t_2) = x$$

$$\frac{E^*}{E_s} = \frac{4(t_2^2 + t_1 x)}{d^2} \tag{3.35}$$

$$\frac{I^*}{I_s} = \frac{2x^3 t_1 + 2t_1^3 x + 6t_1 \left(d - t_1\right)^2 x + 4t_2^4 + 12t_2^2 (d - t_2)^2}{d^4} \tag{3.36}$$

if $t_1 \to 0$ then

$$\frac{E^*}{E_s} = 4\left(\frac{t_2}{d}\right)^2 \tag{3.37}$$

$$\frac{I^*}{I_s} = \frac{4t_2^4 + 12t_2^2(d - 2t_2)^2}{d^4}$$

$$= 16\left(\frac{t_2}{d}\right)^4 - 24\left(\frac{t_2}{d}\right)^3 + 12\left(\frac{t_2}{d}\right)^2 \tag{3.38}$$

$$\Rightarrow \frac{E_s I^*}{E^* I_s} = 4\left(\frac{t_2}{d}\right)^2 - 6\left(\frac{t_2}{d}\right) + 3 \Rightarrow \quad \text{as} \quad t_2 \to 0 \quad \text{then} \quad \frac{E_s I^*}{E^* I_s} = 3 \tag{3.39}$$

Increasing the number of cells through the depth of the sample has the effect of decreasing the observed size effect (Figure 3.14). Interestingly from this simplified analysis, it can be seen that the magnitude of the size effect with respect to the cell density for a given number of rows appears to scale with the number of rows (Figure 3.13). As this model is somewhat simplified, it is expected that including effects such as the Poisson's ratio and the associated anticlastic deformations will alter this behaviour slightly, but the general trend should be similar.

3.5.2 Summary and Conclusion

It has been demonstrated in this section that size effects consistent with micropolar elasticity can be observed in analytical models of a beam with voids extruded parallel to the longitudinal axis in flexure. It was shown that the observed size effect was strongly dependent on both the cell density and the second moment of area of the cross section.

The upper limit of the size effect was observed when the sample rigidity was normalised against the homogenised global value for a given material volume fraction and was realised with diminishing sample size. Two distinct size effects were found depending on the distribution of mass within the unit cell. As the rigidity is strongly dependent on the second moment of area of a given sample, moving mass away from the centre of the cell has the general effect of increasing the size effect. The maximum increase in localised rigidity was observed when the thickness of the parameter $t_2 \gg t_1$, due to the cubic dependence on the depth within the second moment of area of the section. A lower limit for the size effect which is obtainable in this model for a given volume fraction arises when $t_1 = t_2$.

Micropolar effects can be partially explained through an analysis of the second moment of area within the cross section of the specimens under investigation. While this simplified analysis may be limited by other structural effects, it indicates that in order to maximise the increase in stiffness of a lattice structure under flexure, the mass should be distributed as far away from the centre of the cell as possible in order maximise the increase in second moment of area for a given modulus.

Chapter 4

Numerical & Analytical Identification of Mechanical Properties of a 3D Orthogonal Lattice

In the previous chapter, size effects in bending were investigated for 2-dimensional square lattices of varying volume fraction. The mode of loading and sample surface topology were also shown to be important factors in the characterisation of the material.

The following chapter contains an investigation into the mechanical properties of a 3-dimensional orthogonal lattice structure comprised of a regular array of unit cells. Here, geometrically similar samples are numerically simulated at varying size scales to determine if any relationship with size exists in the material. The influence of the solid volume fraction within the unit cell is also considered and quantified in relation to the overall mechanical properties.

Numerical predictions for the variation in Young's modulus, shear modulus and Poisson's ratio have also been made in an attempt to capture their dependency on the volume fraction within the material. These predictions are compared to the available solutions which exist for a thin walled lattice structure.

The characteristic length for each material has also been calculated numerically in flexure and torsion to quantify the size effects within the micropolar continuum. In addition to this, the influence of sample breadth has been investigated to determine whether anticlastic effects influence the measured micropolar material parameters.

4.1 Mechanical Properties of a 3D Orthogonal Lattice

In the previous chapter, 2-dimensional materials were investigated within the context of a micropolar continuum to define the flexural behaviour of a square lattice.

In this chapter, the mechanical properties of a 3-dimensional orthogonal lattice have been investigated within the micropolar continuum framework. The variation in cell density and surface topology have been considered to quantify the magnitude of any size effects and provide a comparison between closed form analytical solutions and idealised FE simulations. The lattice is defined in terms of a unit cell which is the smallest representation of the microstructural features that make up the bulk material structure. The unit cell consists of 12 rectangular bars of length, a, and breadth / depth, t, which intersect at the corners of the cell as seen in figure 4.1 (b).

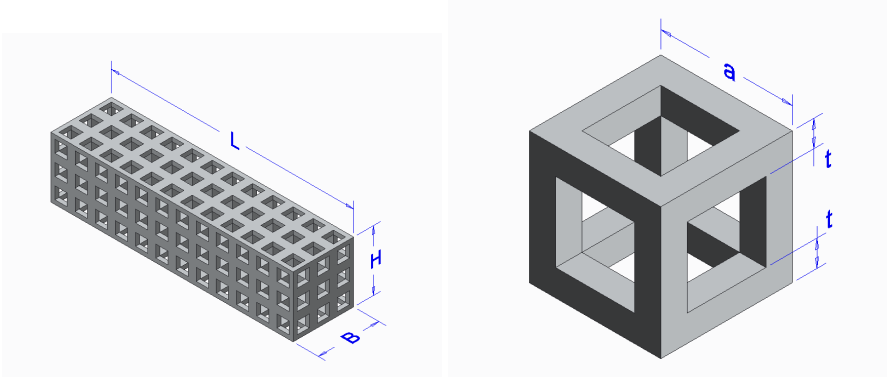

(a) (b)

Figure 4.1: (a) Beam with cubic lattice microstructure, (b) Unit cell of the material.

While analytical approximations exist for the mechanical behaviour of a 2 dimensional lattice, (Gibson & Ashby, 1999; Wang & McDowell, 2004; Dos Reis & Ganghoffer, 2012) they are usually based on the assumption that the beams within the lattice are sufficiently slender that any local deformation at the joints within the lattice are insignificant since bending of the beams is the primary mode of deformation. In practise however, this assumption will only hold for a small range of lattices.

The following sections will attempt to derive more exact approximations for the mechanical properties of a lattice with varying cell wall thickness by conducting simulations of the material in ANSYS and comparing the results to numerical predictions.

4.1.1 ANSYS Meshing

One of the difficulties with modelling 3-dimensional materials at the microstructural level is that the number of nodes and elements which are required to accurately resolve the stress

and displacement fields during deformation can become very large and subsequently computationally intensive due to the fact that each individual feature needs to be represented at a sufficiently high resolution. This becomes very apparent when modelling such materials at different size scales as the sample volume is proportional to the depth cubed for a bar with a square cross-section and constant aspect ratio. On top of this, as the density of the material decreases, the number of elements needed within the unit cell also has to increase to maintain a reasonable element aspect ratio. A trade-off was therefore required in order to obtain reasonable accuracy within the computational limits of the computing hardware that was available.

Models were constructed in ANSYS by sequentially propagating a unit cell of the material in each of the 3 major axes due to the repetitive nature of the lattice. As the solid internal volumes within the unit cell consisted of a series of interconnecting cuboidal beams, a structured mesh was used as it offered an efficient way to segment them.

Each cubic joint in the cell consisted of 4 element divisions per axis, with 64 elements in total. The connecting members had a varying number of elements that was determined from the ratio of the cell wall thickness, t to the overall unit cell size, a by the function

$$n_{elem} = n_{div}^3 \left(\frac{a - 2t}{t} \right) \tag{4.1}$$

where n_{div} is the number of elements through the thickness of the internal beams. The element size was chosen by setting n_{div} to 4 as this offered a reasonably converged solution, without being overly computationally expensive. An example of a meshed unit cell can be seen in figure 4.2.

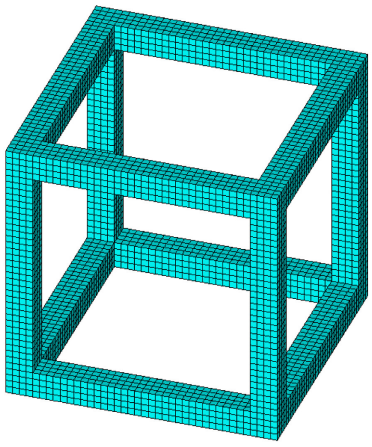

Figure 4.2: A meshed unit cell.

Both the SOLID185 and SOLID186 continuum elements available in ANSYS are well suited to generating 3-dimensional mapped structural meshes. SOLID185 is an eight node

element, while SOLID186 is a higher order 20 node quadratic element with an additional node on the mid point of each edge. Both elements have three translational degrees of freedom per node. SOLID185 continuum elements were used in the construction of the models in this analysis as it was found that the additional resources required to compute the solution using the higher order SOLID186 elements limited the size of the models which could be generated without adding any great improvement in accuracy to the overall results.

4.2 Uniaxial Loading

The lattice structure which has been defined in figure 4.1 is to be investigated to ascertain how the mechanical properties vary with cell density. The results will be compared to theoretical approximations where appropriate and some suggestions will be made on how this could be improved.

No size effect is predicted in tension for micropolar materials, meaning that the modulus and Poisson's ratio should be independent of sample size. To determine the effective Young's modulus and Poisson's ratio of the lattice, a unit cell similar to figure 4.1 (b) was generated in ANSYS and subjected to a fixed displacement, w_x. The boundary conditions were as follows:

$$\begin{aligned} &\text{On face } X = 0 && u_x = 0 \\ &\text{On face } X = a && u_x = w_x \\ &\text{On plane } Y = a/2 && u_y = 0 \\ &\text{On plane } Z = a/2 && u_z = 0 \end{aligned} \tag{4.2}$$

The X, Y & Z faces denote the exterior surface perpendicular to the corresponding axes as seen in figure 4.3. After each simulation, the reaction forces were determined and the effective properties were calculated from the homogenised stress across the unit cell section.

4.2.1 Poisson's Ratio

In continuum mechanics, the Poisson's ratio, ν_s is used to describe the relationship between the direct strain, ϵ_1 and transverse strain, ϵ_2 in a material subjected to direct stress. For a linear elastic solid homogeneous material the relationship between the Young's modulus, E_s, Poisson's ratio, ν and Shear modulus, G_s is:

$$E_s = 2G_s(1 + \nu) \tag{4.3}$$

For a heterogeneous cellular material, this relationship does not necessarily hold true and is dependent on the topology of the particular features which define the underlying microstructure. In the case of a thin walled cubic lattice structure, the Poisson's ratio can be estimated by analysing the individual beams which make up a unit cell within the structure. The derivation for a planar 2D lattice is given by Wang & McDowell (2004) and can be expanded to estimate the 3D lattice of figure 4.1.

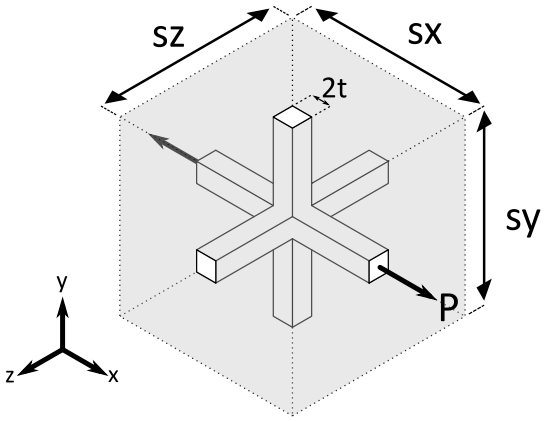

Figure 4.3: Unit cell of lattice material subjected to an axial load.

In a slender cubic lattice subjected to a direct stress, (Figure 4.3) the axial deformation will be directly related to the stress that is acting on the beams in the axial direction. The beams which are perpendicular to the axial load will have zero axial stress and the effective Poisson's ratio will therefore be dependant on the deformation of the axial beams. The axial stress σ_1 can be given as:

$$\sigma_1 = \frac{P}{A} = \frac{P}{(2t)^2} \tag{4.4}$$

where P is the applied load and A is the cross sectional area over which the applied load acts. $2t$ denotes the total cell wall thickness within the unit cell.

The axial strain, ϵ_1 is therefore:

$$\epsilon_1 = \frac{\sigma_1}{E_s} = \frac{P}{E_s(2t)^2} \tag{4.5}$$

The transverse strain, ϵ_2' acting in the column will therefore be:

$$\epsilon'_2 = \epsilon_1 \nu \tag{4.6}$$

The total transverse strain acting over the unit cell is just the ratio of the change in width of the

cell, Δa to the original length in this direction.

$$\epsilon_2 = \frac{\Delta a}{a} = \frac{2t\epsilon_2'}{a} = -\frac{\nu P}{E_s 2ta} \tag{4.7}$$

The effective Poisson's ratio in a slender 3D cubic lattice is therefore:

$$\nu_{12}^* = -\frac{\epsilon_2}{\epsilon_1} = \nu\left(\frac{2t}{a}\right) \tag{4.8}$$

As the lattice structure has orthogonal symmetry, the effective Poisson's ratio will be the same in each of the three major axes. It appears from this analysis that there is no significant difference between the in plane Poisson's ratio of a 2D square lattice and a 3D cubic lattice of similar cell size and wall thickness. However, plotting the Poisson's ratio found experimentally for a lattice of varying density it is observed that there is a measurable difference between the analytical solution of equation 4.8 and the FE simulations as can be seen in figure 4.4.

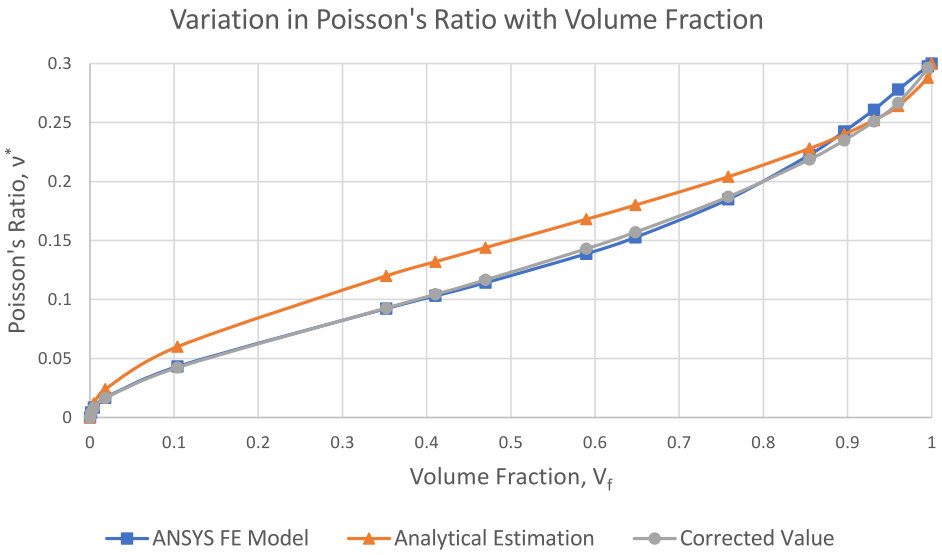

Figure 4.4: Variation in observed Poisson's ratio with relative cell density. The analytical estimation presented in equation 4.8 generally overestimates the contraction within the material.

In general, it is observed that the numerical prediction overestimates the magnitude of the contraction when the volume fraction is below 85%. Above this, the difference in effective Poisson's ratio is smaller, but does converge on the classical solution as the volume fraction tends to 1. The change in calculated Poisson's ratio varies by as much as 50% across the full range of densities as can be seen in figure 4.5. Crucially though the biggest deviation occurs when the lattice has a very low volume fraction. Here the Poisson's ratio is very small and

is effectively zero anyway. Small variations become more important as the volume fraction increases due to the fact that the transverse contraction is not negligible.

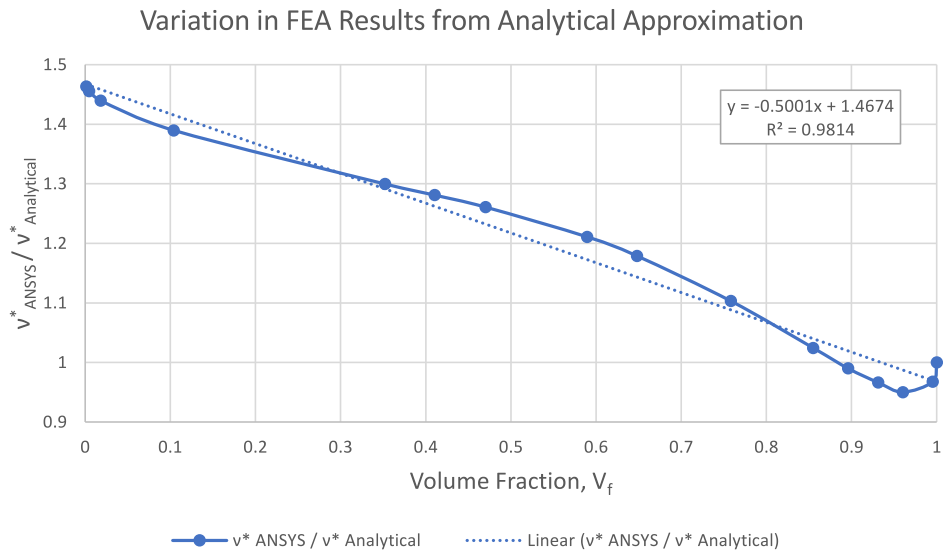

Figure 4.5: Magnitude in the difference between the Poisson's ratio derived from FEA and the closed form approximation.

One problem that has been noted with the experimental results is that the transverse displacement is not consistent, it varies across the surface of the unit cell. Some estimation therefore needs to be used when discerning what the effective Poisson's ratio is for a given cellular material. For general purposes however, the numerical estimation is a sufficient representation of the behaviour of the material.

$$\nu^* = \nu \frac{2t}{a} \left(1.467 - \frac{V_f}{2}\right) \tag{4.9}$$

To improve the numerical estimation in comparison to the experimental Poisson's ratio, a linear approximation of the change in observed Poisson's ratio with variation in volume fraction was made (Figure 4.5). It has been estimated as $(1.467 - 0.5V_f)$, where V_f is the cell volume fraction, and can be clearly seen to provide a good correction for volume fractions below 85% (Figure 4.4). Although the linear fit that is used here is only an approximation, the resulting values are within 4% of the simulated Poisson's ratio when equation 4.9 is applied.

4.2.2 Young's Modulus

The Young's modulus in a linear elastic material relates the strain at a given point to the applied stress. In a heterogeneous material however, the localised stress variation may be significant

and not representative of the global response. For a 2-dimensional low density lattice with slender internal connecting members, theoretical predictions exist for the effective Young's modulus (Wang & McDowell, 2004). In this case it can be assumed that the response of the material is dominated by stretching in the axial members. As the density of the lattice increases however, such approximations may not be appropriate since the deformation in the transverse beams cannot be ignored.

For a 3-dimensional orthogonal lattice, an approximation of the homogenised Young's modulus can be derived analytically in terms of the effective stress within the lattice when it is subjected to an axial strain by recognising that the deformation is dominated by the stretching of the axial members within the cell. For a fixed constant strain, ϵ_1 that has a reaction force, P this relationship can be given as;

$$\sigma_1 = \frac{P}{A} = \frac{P}{4t^2} \tag{4.10}$$

$$\epsilon_1 = \frac{w_a}{a} \tag{4.11}$$

$$E_s = \frac{\sigma_1}{\epsilon_1} = \frac{Pa}{4t^2 w_a} \tag{4.12}$$

$$\sigma_2 = \frac{P}{A} = \frac{P}{a^2} \tag{4.13}$$

$$E^* = \frac{\sigma_2}{\epsilon_1} = \frac{P}{w_a a} \tag{4.14}$$

If strain is constant then;

$$\frac{E_s 4t^2}{P} = \frac{E^* a^2}{P} \tag{4.15}$$

$$\Rightarrow E^* = E_s \left(\frac{2t}{a}\right)^2 \tag{4.16}$$

This approximation works well for a very slender lattice as the Poisson's ratio will tend to zero since there is no contraction within the lattice. It was observed however that the above approximation does not hold when $\left(\frac{2t}{a}\right) > 0.2$ which correlates to a cell volume fraction of 10%. The modulus is better expressed by taking into account the Poisson's ratio, ν^* of the material and can be given as:

$$E^* = E_s(1 + \nu^*)\eta^2 \tag{4.17}$$

where

$$\eta = \frac{2t}{a} \tag{4.18}$$

The Poisson's ratio, ν^*, expressed here is the micropolar Poisson's ratio and is clearly distinct from the classical value which is related to the solid material of the lattice.

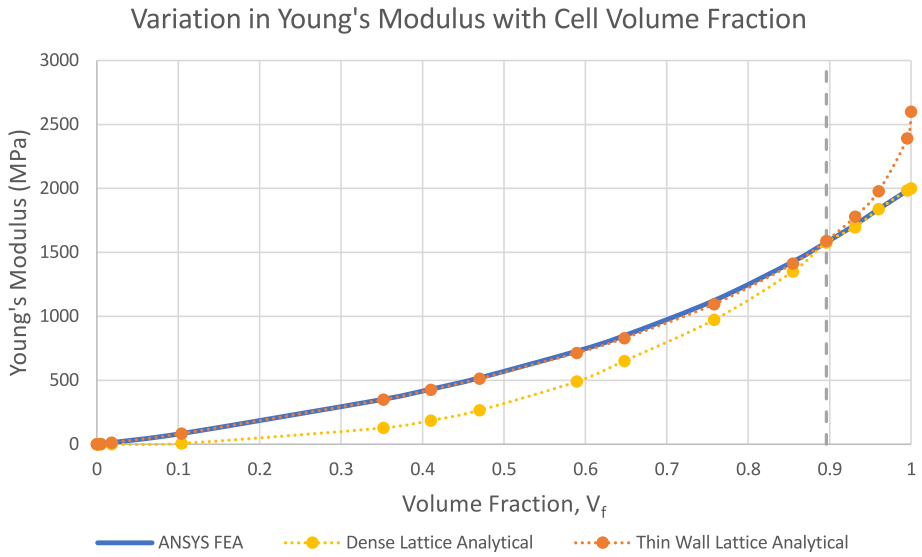

Figure 4.6: Comparison between the variation in the analytical approximation of the Young's modulus and FE prediction.

From figure 4.6 it can be seen that equation 4.17 is valid when the total cell volume fraction is less than approximately 90% solid. Denser samples can no longer be treated in terms of a series of connected beams and will converge on the homogeneous linear approximation model thus this equation will overestimate the material modulus within this range. A better approximation of the modulus can be found in this region by relating the micropolar shear modulus, G^* and Poisson's ratio, ν^* to the bulk materials Poisson's ratio, ν_s by;

$$E^* = \left(3 - \frac{\nu^*}{\nu_s}\right) G^*(1 + \nu^*) \tag{4.19}$$

This equation was derived empirically by observing the variation in the calculated modulus to the general Lamé relationship of a linear elastic material. As the sample density approaches unity, the micropolar Poisson's ratio converges to that of the bulk material and equation 4.19 reduces to the usual relationship for a linear elastic material. While equation 4.19 is accurate to within 2% of the calculated modulus, it is reliant on obtaining the global shear modulus and Poisson's ratio. Uniaxial tensile or flexural tests would be more appropriate in this range to determine the material modulus.

4.3 Shear Loading

4.3.1 Shear Modulus

It is predicted in micropolar theory that the shear modulus of a heterogeneous material is constant and independent of sample size. The size effects which are observed are characterised by a characteristic length that accounts for the microrotations within the sample. Under a simple or pure shearing load, the deformation is only a function of the translational deformation and as such no microrotations are predicted to appear in the model. While numerical estimations exist for a thin walled lattice subjected to a constant shear stress, it is only applicable to a limited range of cell densities. In order to be able to fully categorise and quantify this effect in a lattice material, a clear understanding of how the shear modulus varies with cell density is required.

The shear modulus for a cellular lattice structure of cubic composition does not relate to the modulus of elasticity in the conventional sense due to the orthotropic nature of the unit cell. For a thin walled lattice it can be approximated by analysing the deformation of the individual beams which make up the unit cell when subjected to a shear stress. The mechanical properties of 2D lattice structures subjected to shear loads have been studied by Gibson & Ashby (1999) and Gu et al. (2001) among others. It has been reported that for a planar square lattice consisting of orthogonal bars, that the shear modulus is approximately related to the modulus of the solid material by the relation:

$$G^* = \frac{E_s}{2}\left(\frac{2t}{a}\right)^3 \tag{4.20}$$

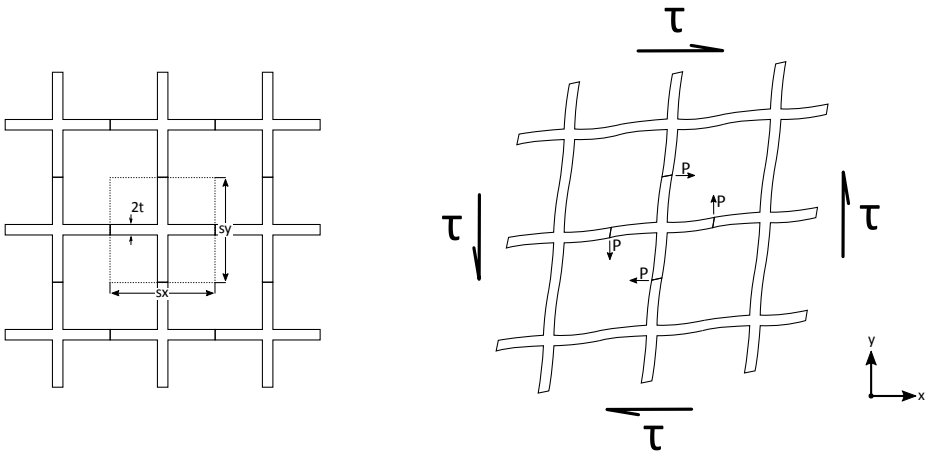

Figure 4.7: 3x3 cellular lattice subjected to a symmetric shear stress.

where $2t$ denotes the total thickness of the beams through the depth of the cell and 'a' is

the cell depth. The derivation for this formula can be found by calculating the total deflection and rotation that results on a unit cell of material subjected to a constant shear stress.

In the case of a 3-dimensional lattice of the kind seen in figure 4.1 the shear stress, τ acting on a unit cell is related to the applied force, P and the total cross-sectional area, A of the unit cell and is given as:

$$\tau = \frac{P}{A} \tag{4.21}$$

Under small deflections and rotations, the shear strain, γ can be found by considering the deformation of each connecting member within the unit cell of material. The unit cell in this case can be described in terms of nodes and interconnecting beams as shown in figure 4.8. When a symmetric shear stress is applied to the X-Y plane of the unit cell (Figure 4.7), beams 'o-b', 'o-c', 'o-e' and 'o-f' will deflect by bending and may be treated as a cantilever beam.

The total shear strain, γ acting on a 3D unit cell of length, L is therefore:

$$\gamma = \frac{4w}{L} \tag{4.22}$$

where

$$w = \frac{P(L/2)^3}{3E_s I_s} \tag{4.23}$$

$$\Rightarrow \quad \gamma = \frac{PL^2}{6E_s I_s} = \frac{2PL^2}{E_s\,(2t)^4} \tag{4.24}$$

$$G^* = \frac{\tau}{\gamma} = \left(\frac{P}{L^2}\right)\left(\frac{E_s\,(2t)^4}{2PL^2}\right) \tag{4.25}$$

$$G^* = \frac{E_s \eta^4}{2} \tag{4.26}$$

where η is the ratio of the total thickness of the internal beams to the cell spacing ($2t/L$).

It can be seen for a low density thin walled lattice that the shear modulus can be approximated from the tensile modulus of the solid material within the lattice and the ratio of the cell size to the thickness of the internal members. In practise however, equation 4.26 is just an estimation which does not take into consideration the interaction of the solid material at the joints of the structure.

As the samples being considered here, do not have particularly slender ligaments with regards to the cell size, the derivations shown above can only be used as an approximation at best when modelling the mechanical properties of the material. As the aspect ratio of the ligaments is seen to decrease, the deflection of the beams cannot be approximated by that of a Euler Bernoulli beam in bending. Shear stresses within the ligaments will become a contributing factor

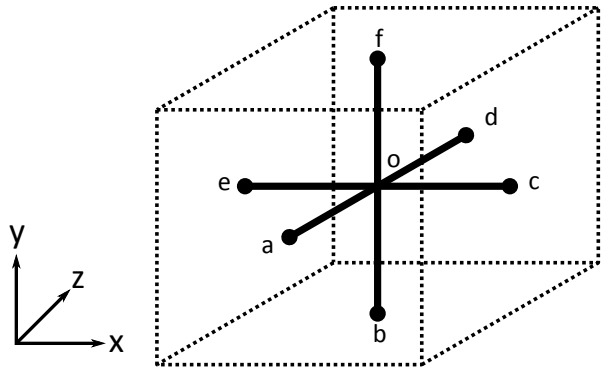

Figure 4.8: Unit cell connectivity.

to its deformation, and a Timoshenko based solution may be more appropriate. It is also expected that with increasing sample density, the ability of the joints to rotate under loading will diminish until a classical solution is reached.

To ascertain the limitations of this approximation, further finite element simulations were carried out on unit cells with a varying volume fraction by altering the thickness of the internal beams. The unit cell of material was subjected to a constant shear strain under displacement boundary conditions, with the shear stress calculated from the reaction solution. The boundary conditions applied to the cubic unit cell were as follows:

$$\begin{aligned} &\text{X1 Face: } u_y = 0 && \text{X2 Face: } u_y = w_y \\ &\text{Y1 Face: } u_x = 0 && \text{Y2 Face: } u_x = w_x \\ &\text{Z1 Face: } u_z = 0 && \text{Z2 Face: } u_z = 0 \end{aligned} \tag{4.27}$$

where X1, X2, Y1, Y2 and Z1, Z2 denote the exterior faces on the unit cell perpendicular to the three major axes (Figure 4.9).

In the case of the 3D cruciform lattice, an extra node needs to be restrained in the X and Y plane at the centre of the cell in order to prevent rigid body motion in the analysis. The boundary conditions also need to be modified so that the displacement at the opposing faces are equal and opposite to each other. The total displacement across each face is kept the same in order to maintain a constant shear strain on each cell. The shear modulus of the material can then be calculated in the usual manner by relating the applied shear strain to the resulting shear stress. The engineering shear strain is defined as the relative change in angle between the

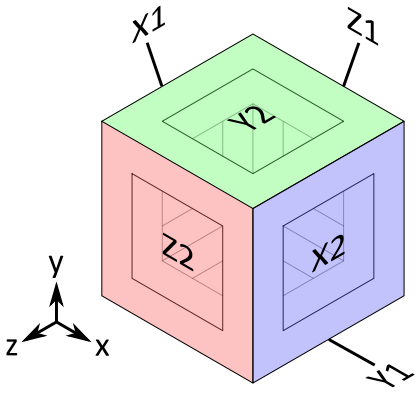

Figure 4.9: A unit cell of material. Displacement boundary conditions are applied at the external surfaces which are denoted in relation to the major perpendicular axes.

perpendicular vertices on the XY plane of the unit cell. For small deflections, the change in angle is approximately the same as the deflection of the vertex with respect to its length. The total shear strain can be approximated as:

$$\gamma = \frac{du_y}{dx} + \frac{du_x}{dy} \tag{4.28}$$

The total area that the shear stress is acting on is defined as the total cross-sectional area of the unit cell. The results of the FE simulations are displayed in figure 4.10. It can be seen that there is a non-linear dependence on the shear modulus with respect to the volume fraction, V_f of solid material.

From the analysis it was found that equation 4.26 does not accurately represent the observed shear modulus when the cell wall thickness is greater than 2% of the cell width. A much closer approximation was found empirically by incorporating the global Poisson's ratio, ν^*, of the lattice unit cell into equation 4.26 and normalising it against the experimentally derived shear modulus (Figure 4.11). It was observed that a linear variation exists when the normalised value is plotted against the normalised cell wall thickness, η in the range of $0 - 0.4$. The resulting shear modulus in this range can be approximated as

$$G^* = \frac{E_s \eta^4}{2(1+\nu^*)}(2.15\eta + 1) \tag{4.29}$$

By using this correction factor, the shear modulus can be accurately calculated to within 5% of the simulated value when the material volume fraction is below 50%.

An empirical relationship has also been observed in denser samples. It was found by com-

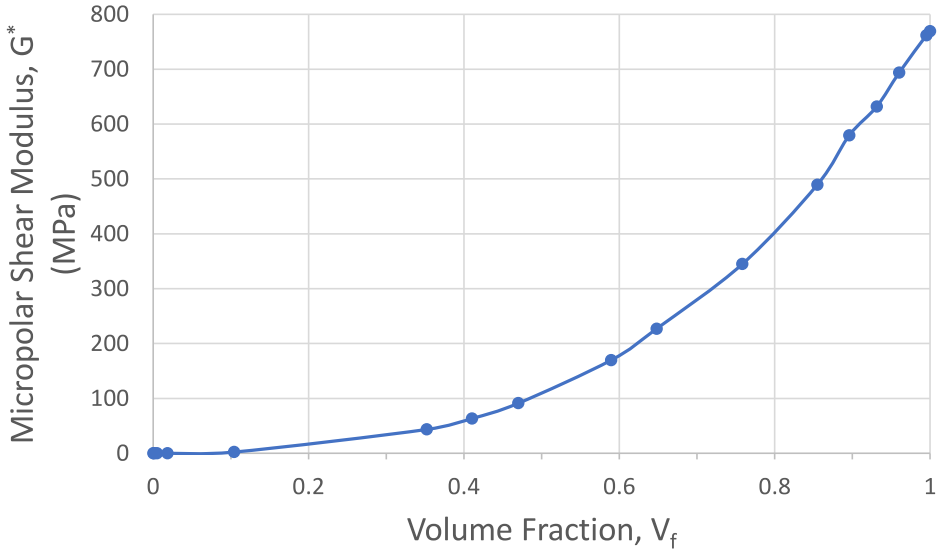

Figure 4.10: FE results for the variation in shear modulus with varying cell wall thickness, expressed in terms of the cell volume fraction.

paring the calculated shear modulus with the usual relationship for the shear modulus of a linear elastic solid, [G_s=E_s/2(1+ν)]. By modifying the Poisson's ratio in this equation to be that of the global value of a given sample rather than the solid material within the lattice, it was observed that a linear correlation exists with the volume fraction cubed, ${V_f}^3$ (Figure 4.12.). The shear modulus within this region can therefore be expressed as:

$$G^* = \frac{E_s}{2(1+\nu^*)} {V_f}^3 \tag{4.30}$$

When the volume fraction within the lattice is above 50%, it can be observed that the predicted shear modulus is within 5% of the approximate analytical value. The variation in normalised shear modulus has been plotted in figure 4.13.

While the approximations formulated here are reasonably accurate, FE simulations in the intermediate region may give more accurate results.

In all the analyses that have been undertaken, it has been assumed that only small deflections are applied to the system and the effects of buckling and other means of failure have not been considered.

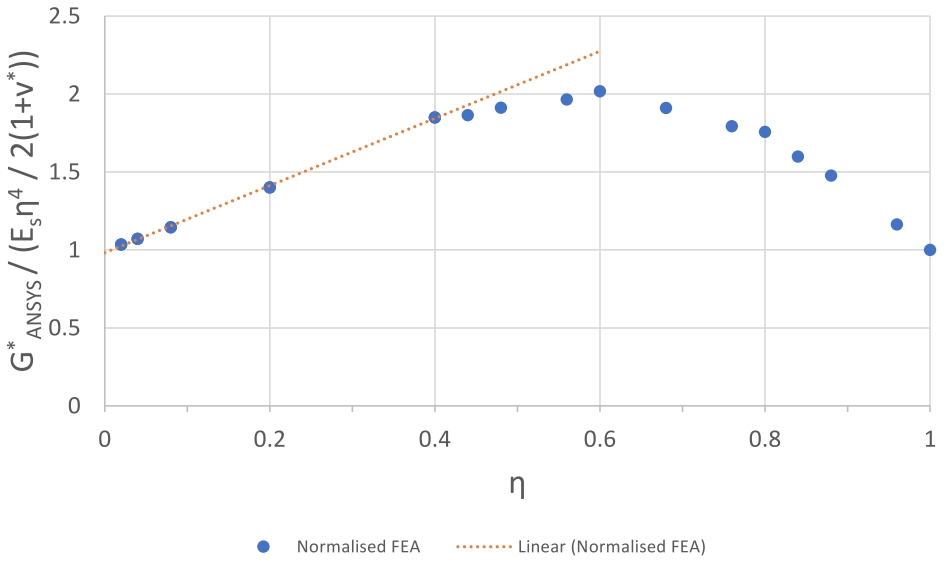

Figure 4.11: Variation in the analytical approximation of the shear modulus against simulated values with varying normalised cell wall thickness, η. A linear relationship can be observed when η is less than 40%.

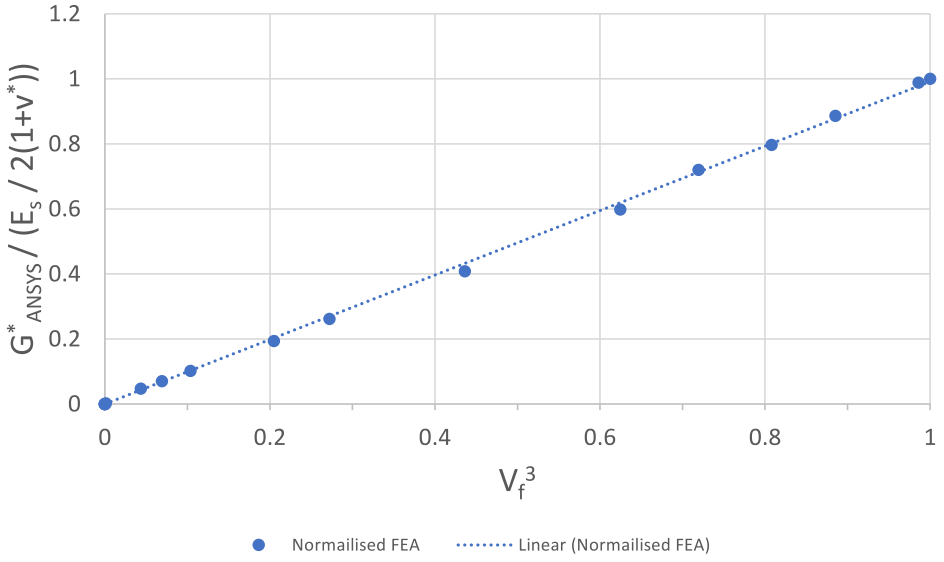

Figure 4.12: Simulated shear modulus normalised against $E_s/2(1+\nu^*)$. A linear variation can be observed when plotted against the volume fraction cubed.

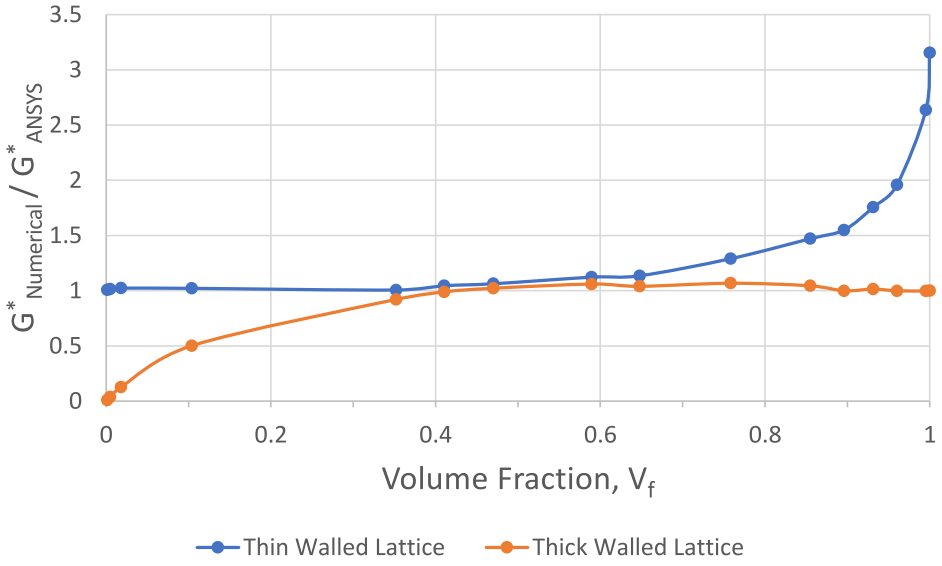

Figure 4.13: Variation in the numerical estimation of the shear modulus normalised against the finite element solution. Equation 4.29 is valid at volume fractions below 50% and equation 4.30 applies above 50%.

4.4 Flexure of Beams Comprising of a Lattice Microstructure

The two main methods for obtaining the modulus of a structural material involve conducting either uniaxial or flexural tests. In heterogeneous materials that exhibit size dependencies the former test can be used to determine the modulus from a single sample of material. It is not expected that any size effects will be observed in tension or compression of such materials assuming that the material which makes up the solid constituent can be considered isotropic. In flexure however, multiple tests at differing size scales need to be performed in order to determine the flexural modulus and the resulting characteristic length, l_b which is used to quantify how the stiffness of the material behaves as the sample size approaches the order of the dominant microstructural features.

In chapter 2 it was shown that in micropolar elasticity, the flexural modulus, E^* and characteristic length, l_b can be derived in terms of the bending of a slender beam subjected to a constant moment, M as

$$\frac{ML}{\theta} = E^* I_s \left[1 + 24\left(\frac{l_b}{d}\right)^2\right] \tag{4.31}$$

where L is the sample length, θ is the angle of rotation across the length, I_s is the second moment of area of the section and d is the sample depth. It can be seen that as the depth of the

sample increases, the influence of the characteristic length diminishes.

The aim of this section is to verify that the flexural modulus found through numerical simulation closely matches the uniaxial tests for finite sized samples. Further to this, the characteristic length in bending will be investigated over a range of cell volume fractions to observe how it varies with cell density and compares to the numerical predictions formulated.

As before, the models were constructed in ANSYS with SOLID185 continuum elements in the manner described in section 4.1.1. A structured mesh was developed that consisted of an array of cubic elements within each model. The size of the elements within the mesh was determined by the thickness of the members within the unit cell. As a consequence, the number of elements within the model increases dramatically with decreasing cell wall thickness as the number of elements is directly related to the inverse of the parameter η and the cube of the number of elements defined through the thickness of the internal beams.

To minimise the computational resources required to analyse the material, the beams were modelled using half symmetry to reduce the span of the beam. A low aspect ratio of 4 was also applied which significantly reduced the total size of the models. Generally speaking low aspect ratios should be avoided when testing beams in flexure, however it was found that when the beams were subjected to a pure bending moment that the aspect ratio did not influence the results of the predicted stiffness. This is due to the fact a constant curvature exists across the beam subjected to a constant moment loading which is independent of the length.

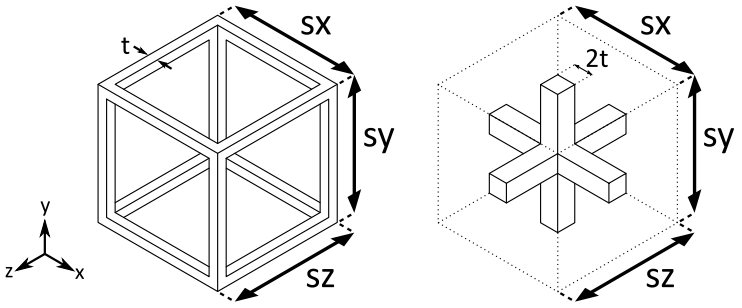

(a) (b)

Figure 4.14: Unit cells representative of the bulk lattice material. (a) 'Cubic' unit cell, (b) '3D Cruciform' unit cell.

Two different unit cells were considered in the analysis. The first as seen in figure 4.14 (a) had the mass of material distributed around the edges of the unit cell. The second unit cell considered the case whereby the solid material extends from the centre of the unit cell (Figure

4.14 (b)). When assembled into an array, the cellular materials are identical, with the exception that the outer surface of the samples are offset by half a unit cell.

To apply the constant moment load, constraint equations were attached to one end of the beam which were controlled by a pilot node at the centre of the cross-section. As the continuum elements only have translational degrees of freedom, the constraint equations are used to calculate the individual displacement components on each node that will produce an equivalent moment loading on the sample. The analyses were performed under displacement control conditions using a static solver.

4.4.1 Results

Each sample was deflected to a fixed angle of rotation, θ and the resultant reaction moments, M were recorded. For a given set of samples, the converged flexural modulus is found from the gradient of the linear portion of a plot where the flexural rigidity, J' divided by the cross sectional area, A, of the samples is plotted against the depth squared according to:

$$\frac{12J'}{A} = \frac{12ML}{\theta bd} = E^* \left(d^2 + 24{l_b}^2\right) \tag{4.32}$$

where b is the sample breadth, d is the depth and l_b is the characteristic length in bending. An example of a typical plot can be seen in figure 4.15. It was observed that in the case whereby the

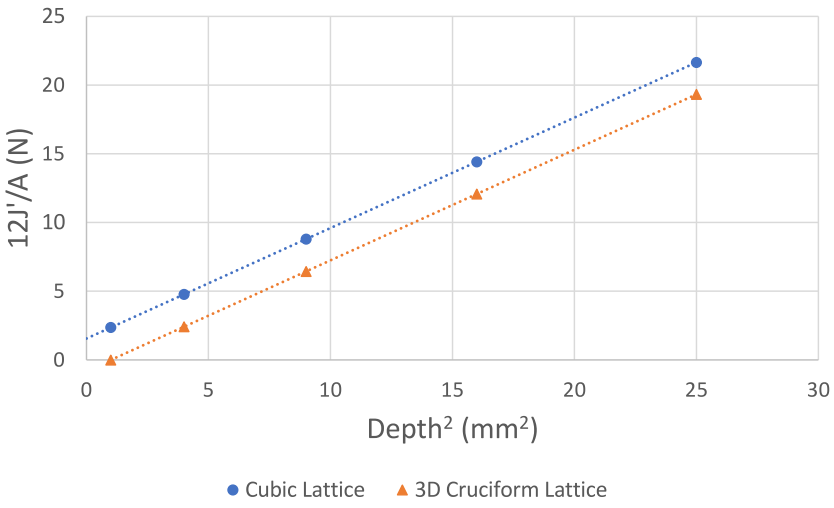

Figure 4.15: Variation in the size effect when the flexural rigidity divided by the sample cross sectional area is plotted against sample depth squared. The Flexural modulus can be obtained from the slope of the linear portion of the graph. Size effects are interpreted from the intercept with the vertical axis. Samples generated by the cruciform lattice have a discontinuous exterior surface.

unit cell has continuous surfaces that a positive size effect occurs wherein the smaller samples are stiffer than the larger ones when the specimen depths are of a similar order of size to the unit cell. If the unit cell is intersected in the centre by the surface of the sample, then a distinctly negative size effect occurs.

The modulus of micropolar bending, γ and the characteristic length, l_b can also be obtained from the intercept of this plot with the vertical axis. In the case whereby the samples contain surface defects, the parameter γ is negative due to the size softening that can be observed.

An alternative method of displaying the data is to divide the flexural rigidity by the second moment of area of the section and plot it against the inverse of the sample depth squared (Figure 4.16). Here, the converged modulus corresponds to the intercept with the vertical axis of the plot. The characteristic length is a function of the linear portion of the slope in this case.

$$\frac{J'}{I_s} = E^* \left(1 + 24 \left(\frac{l_b}{d}\right)^2\right) \tag{4.33}$$

While both plots can be used to determine the same parameters, the main difference is that by plotting the data against $1/\text{depth}^2$ small discrepancies in the size effect at diminishing sample size can be observed more readily.

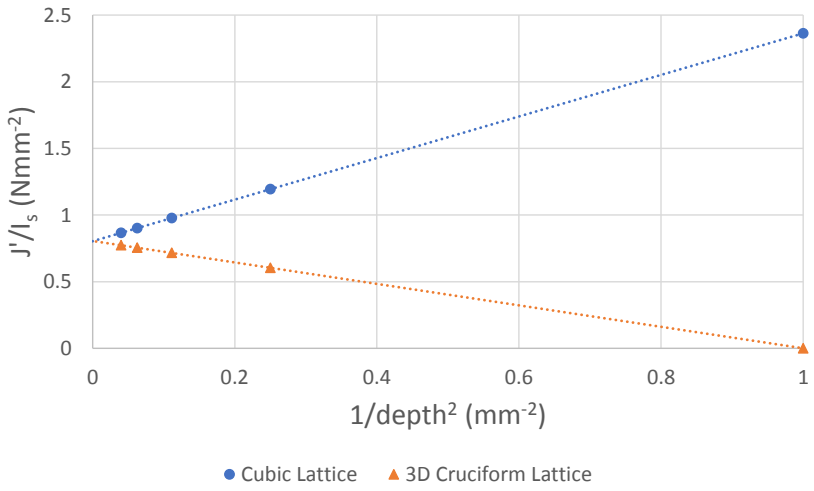

Figure 4.16: Variation in the size effect when flexural rigidity is plotted against the inverse of the sample depth. Samples generated by the cruciform lattice have a discontinuous exterior surface.

The converged modulus for each set of samples was calculated and compared to that which was found under uniaxial loading. It can be seen in figure 4.17 that the variation in flexural modulus with cell volume fraction is nearly identical to the uniaxial tests. As expected, there

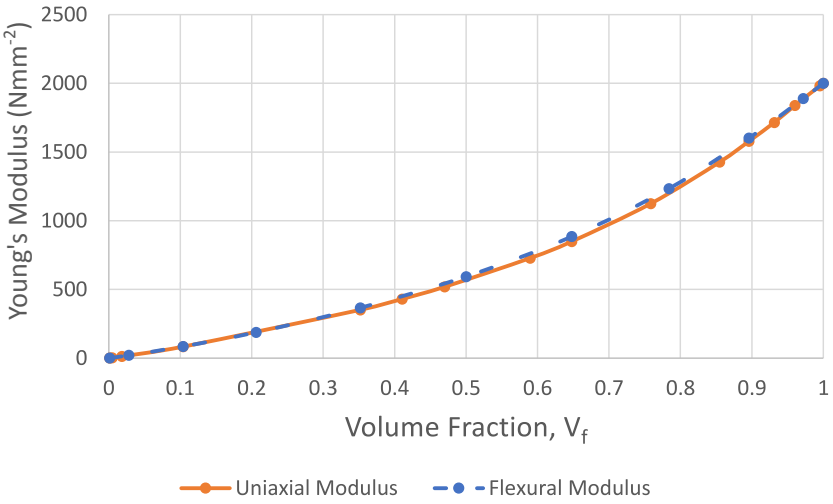

Figure 4.17: Variation in the uniaxial and flexural material modulus with change in volume fraction.

is no difference in the converged modulus with respect to the variants sample surface.

The magnitude of the size effect, ${l_c}^2$ is a measure of the variation in rigidity with sample size and has been defined as $24{l_b}^2$. It can be observed that it increases with decreasing cell wall thickness (decreasing density) when the samples have continuous surfaces and decreases when the external surfaces are discontinuous (Figure 4.18). The maximum value of ${l_c}^2$ which can be observed is 2 mm^2 and the minimum is -1 mm^2. Interestingly, this is in-line with the results which were observed in the case of the 2-dimensional lattice (Figure 3.8) although the distribution with changing volume fraction may be slightly different. The negative size effect is indicative of how the sample rigidity compares to the homogenised value. The maximum normalised negative size effect can therefore not be any larger than -1 mm^2 for a given material as a larger negative value would suggest that the rigidity ratio can be less than 0 which is of course unphysical.

The characteristic length in bending is observed to increase with decreasing cell volume fraction when the sample surfaces did not intersect the unit cell. In the other configuration, the resulting characteristic length is more problematic to determine as the square of the characteristic length within the equation is a negative value. To resolve the characteristic length, this negative value would need to be ignored in order to quantify a value for the material.

Plotting the square of the characteristic lengths against the sample volume fraction, it can be observed that the magnitude of the size effect is clearly different depending on the prescription of the sample surface. In both cases, the size effect tends to a maximum value with decreasing cell volume fraction. When the volume fraction of the material approaches zero, the magnitude

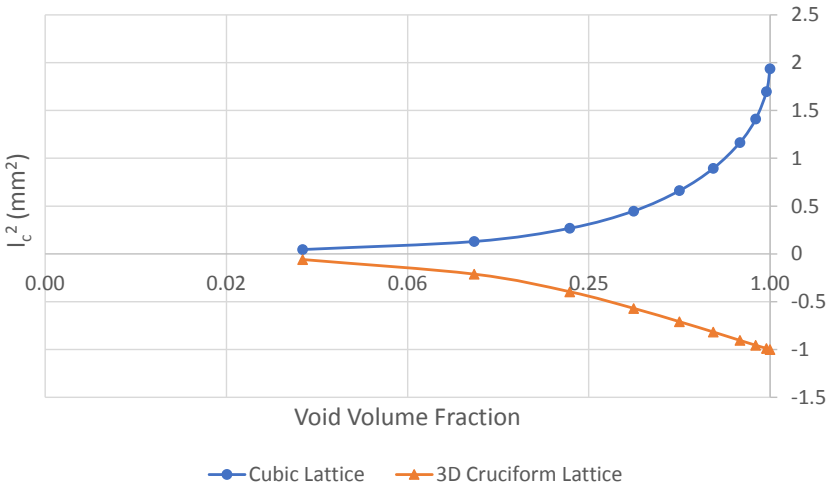

Figure 4.18: Variation in the magnitude of the size effect in bending, $l_c{}^2$ with void volume fraction. Here, the horizontal axis increases with decreasing sample density.

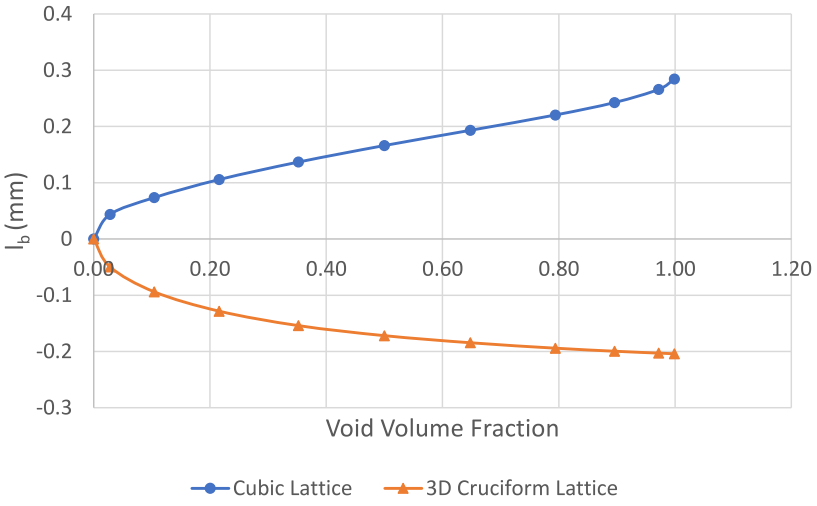

Figure 4.19: Variation in characteristic length in bending with void volume fraction. Here, the horizontal axis increases with decreasing sample density.

of the positive size effect is double that of the negative one.

The actual characteristic length of the material is expressed in mm. When comparing both the open and closed surface samples, the characteristic length of the open cell case matches the theoretical prediction of a 2D planar lattice, albeit with a negative value. The positive characteristic length is $\sqrt{2}$ greater than this value.

The maximum characteristic length in bending is found to be 0.2 mm when the voids intersect the surface and 0.28 mm when the unit cells are complete at the outer surfaces for a cell that is 1 mm square (Figure 4.19). The maximum characteristic length can be better expressed in terms of the unit cell size as $\sqrt{a/24}$ for the 'cubic' cell case and $\sqrt{a/12}$ for the '3D cruciform' cell, where 'a' is the cell spacing.

The variation in rigidity ratio can be seen in figure 4.20 for cubic lattices with various normalised cell wall thicknesses. It can be observed that the positive size effect increases with decreasing cell density when compared to an equivalent solid beam. The magnitude of the size softening effect is generally different to that of the positive effect observed at a given volume fraction. In the case of the 3D cubic lattice it was observed that the positive and negative size effect are equal at approximately 40% void volume fraction. Above this, the magnitude of the positive effect is dominant.

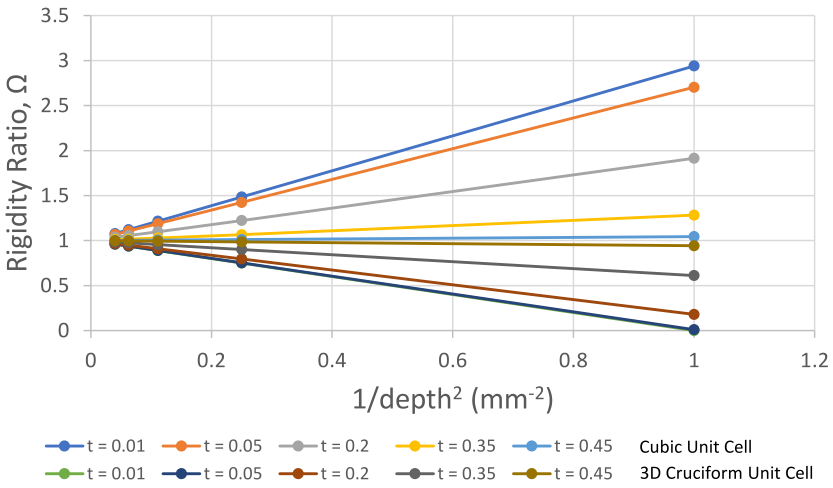

Figure 4.20: Variation in the rigidity ratio with sample size for various cell void volume fractions.

4.5 Twisting of a Bar with Lattice Microstructure

In the previous section, the flexural behaviour of a 3-dimensional lattice structure was investigated to determine the flexural modulus and characteristic length in bending for samples with varying cell density. Size effects are also predicted to be observed in torsion within a micropolar continuum. An investigation similar to the bending analysis was therefore conducted in order to quantify the resistance of the lattice to twisting at various size scales.

The lattice microstructure considered here is cubic in nature. Discrete samples of similar order to the microstructure are therefore required to be cuboidal in nature so as to maintain a consistent material distribution throughout the sample. Bars with a square cross-section were therefore chosen to test the mechanical response of the samples. The downside to using samples with a square cross-section rather than a cylindrical section is that warping will be induced within the sample due to the out of plane effects normal to the cross-section of the bar. While there are closed form solutions which give a good approximation for standard cross-sections, the general micropolar solution for a rectangular cross-section is very complex. As was discussed in chapter 2, Park & Lakes (1987) produced a solution to this problem, but the number of variables involved in the solution does not lend itself well to experimental verification. A simplification to this solution was therefore chosen in order to perform the experimental analysis (See section 2.2.3.). The size effect can be expressed in terms of the torsional rigidity, J' of a beam as

$$J' = G^* \left[I_p + 2{l_t}^2 d^2 \right] \tag{4.34}$$

recalling that G^* is the micropolar shear modulus, I_p is the warping constant of the section, d is the sample depth and l_t is the characteristic length for torsion.

By plotting J'/d^2 against d^2 it is possible to identify the shear modulus from the gradient of the linear portion of the slope which will appear when a large enough set of sample sizes are tested.

Simulations were performed in ANSYS to predict the underlying material parameters. Models were generated with a mapped mesh in the same manner as the flexural tests with SOLID185 continuum elements. To accurately simulate the movement of the beam under torsion, constraint equations were required in order to apply a fixed rotation to the sample. The constraint equations work by taking a rotation or twisting moment and calculating the resulting translational displacements that are required to impose this on the end face of the beam. A pilot node with rotational degrees of freedom is placed at the centre of the cross-section at each end of the beam (Figure 4.21).

The boundary conditions required to impart an axial rotation, θ across a bar with unrestrai-

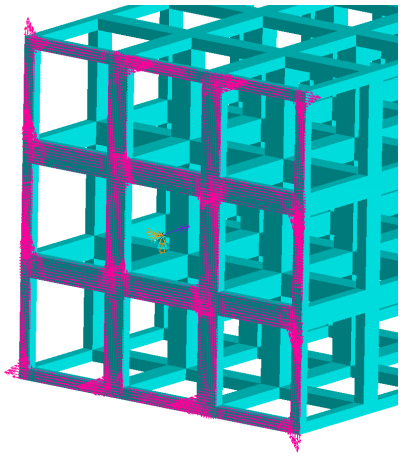

Figure 4.21: Translational forces applied to the end face of the bar by the pilot node.

ned warping conditions are as follows:

$$\begin{aligned}
&\text{Pilot node 1} && u_x = u_y = u_z = 0 && \\
& && \theta_x = \theta_y = 0 && \theta_z = \theta \\
&\text{Pilot node 2} && u_x = u_y = u_z = 0 && \\
& && \theta_x = \theta_y = \theta_z = 0 && \\
&\text{at } (x, y, z) = (L/2, H, B) && u_x = 0 && \qquad (4.35)
\end{aligned}$$

The additional node that is applied on the centre of the beam at the outer edge is required to prevent rigid body motion occurring in the analysis due to an insufficiently constrained model.

A more detailed description of the applied boundary conditions along with a series of benchmark tests on standard solid cross-sections can be seen in appendix A.

Warping within the sample is controlled by denoting which degrees of freedom are coupled from the pilot node to the end face. When the axial displacements are activated in the constraint equations, the end faces will remain plane assuming that the axial displacement on the pilot node is set to zero. Deactivating the coupling of axial displacements has the effect of allowing warping to take place within the sample. The boundary conditions that were employed have been verified by comparing the solution of standard solid sections tested using this method to their theoretical values and can be seen in appendix A.

It was found during initial investigations that the aspect ratio of the beam did not play a significant role in the overall results when unrestrained boundary conditions were applied. To reduce the computational expense required to simulate the material, it was therefore decided

that a fixed length equal to 1 unit cell should be used to model all of the beams of differing sizes. The benefit of doing this was significant as testing samples of fixed aspect ratio requires the number of elements to dramatically increase due to the cubic dependence on the volume.

The models generated in ANSYS consisted of an array of unit cells which were 1x1x1 mm in size. Linear elastic material properties were assigned to the solid component with a Young's modulus of 70000 MPa and a Poisson's ratio of 0.3. As before, the unit cell consisted of 12 orthogonal bars connected at the four outer corners of the unit cell. Each internal member consisted of a square cross-section of thickness 't', which was varied in order to alter the density of the samples. In tandem with this a similar analysis was conducted on beams based on unit cells in which the orthogonal bars intersected at the centre of the unit cell. Here, there are only 6 distinct bars in the unit cell, with a cross-section of '2t'. When assembled in an array, the material is identical to that of the other unit cell, although the topology of the external surfaces on the individual samples will differ (Figure 4.14.).

4.5.1 Results and Discussion

Numerical FE tests subjected the samples to a fixed torque and the angle of rotation was recorded in radians. Each test was conducted under small displacement conditions with ends that were free to warp. It was found as in the case of bending that a positive or negative size effect can be observed depending on how the unit cell is orientated within the sample. When the unit cells do not intersect the surfaces of the samples, a positive trend is observed whereby smaller samples are relatively stiffer than larger samples. If the unit cells intersect the surface, a size softening can be seen with geometrically similar samples becoming stiffer with increasing size.

In total, 10 different cell wall thicknesses were simulated to determine how the mechanical properties varied with cell density. The shear modulus is determined from the slope of the linear portion of the rigidity plot (Figure 4.22 (a)). It is dependent on a large enough set of samples being tested in order to obtain a converged stiffness. A more detailed plot of how the rigidity varies with diminishing sample size can be seen in figure 4.22 (b). The characteristic length, l_t can be interpreted from the intercept of the linear extrapolation with the x-axis. A positive intercept with the y-axis indicates a positive size dependency whereas a negative value indicates that a size softening exists within the material. The magnitude of the intercept indicates the scale of the size effect relative to the size of the microstructural features. A plot of the variation in shear modulus with cell volume fraction is shown in figure 4.23. An approximation for the variation in shear modulus with cell density can be made by fitting a polynomial curve to this figure. It can be approximated to;

$$G^* = \frac{E_s}{2(1+\nu^*)} {V_f}^3 \tag{4.36}$$

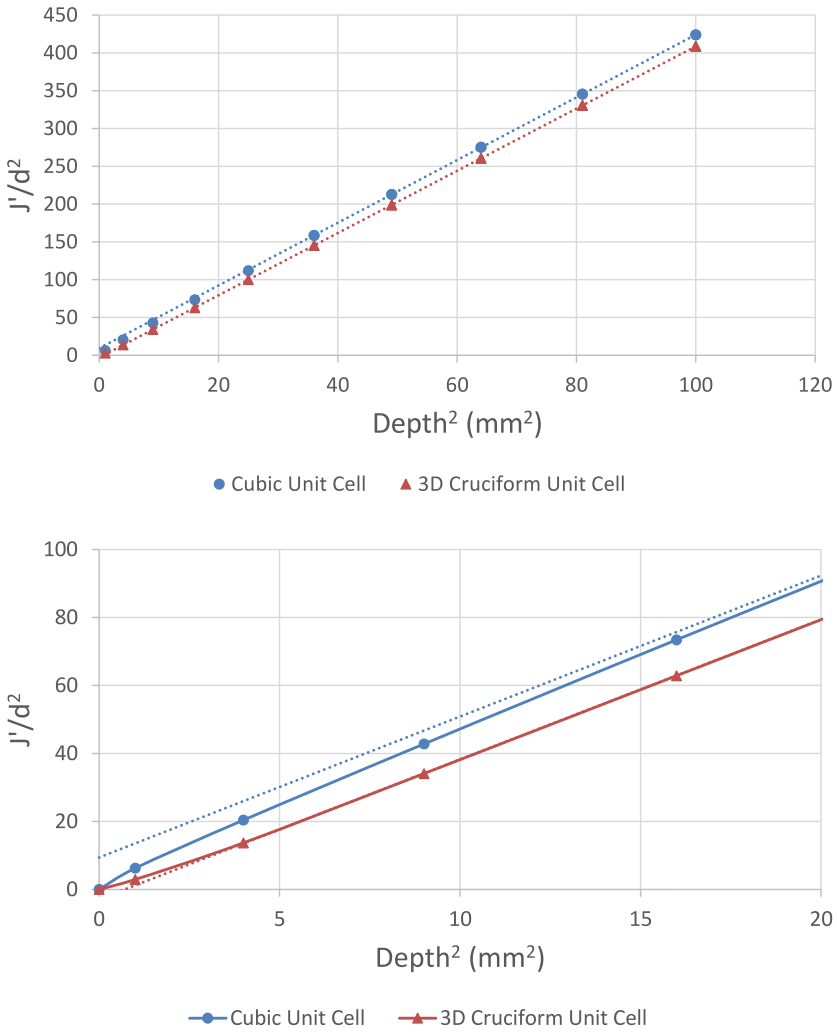

Figure 4.22: Variation torsional rigidity with size for a typical square bar consisting of a lattice microstructure.

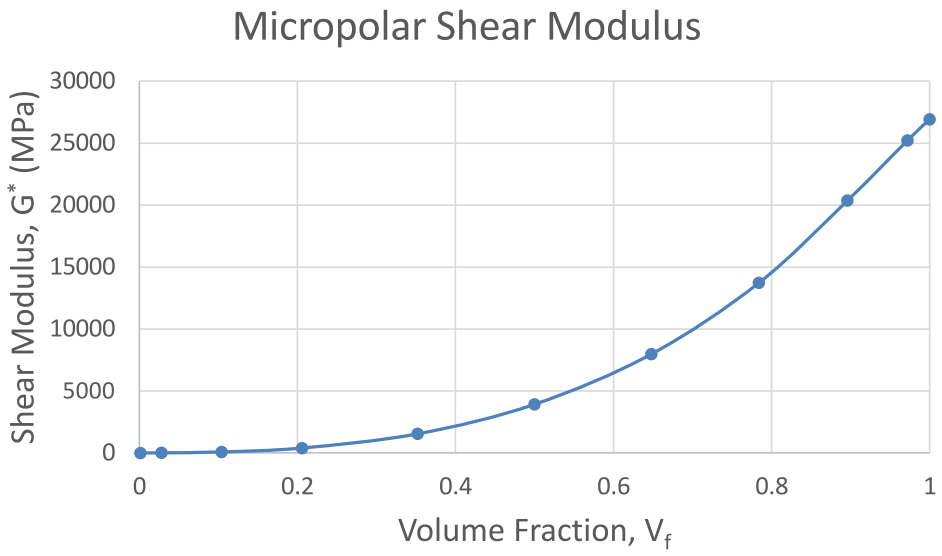

Figure 4.23: Variation in simulated shear modulus with material volume fraction.

where the first term in the equation is equivalent to the shear modulus of the solid material modified to take into account the global Poisson's ratio, ν^* and V_f is the volume fraction of the unit cell. This approximation gives a reasonable value for the micropolar shear modulus when the volume fraction is above 50%. Below this however, the value that is estimated by this equation is much smaller than the actual value. As the cell wall thickness decreases towards a zero value, the shear modulus can be approximated by;

$$G^* = \frac{E_s \eta^4}{2(1+\nu^*)} (2.18\eta + 1) \tag{4.37}$$

The term on the right is an empirical approximation derived from the linear variation in the magnitude of the change in stiffness between the numerical observations and the equation derived in eqn 4.26 which can be seen in figure 4.24.

The magnitude of the variation in shear modulus calculated empirically relative to the FE numerical approximations have been plotted in figure 4.25. At low volume fractions equation 4.37 can be seen to provide a very good fit to the experimental results obtained from the torsion experiments. Above 50% however, the results rapidly diverge. Equation 4.36 converges on the experimental results when the volume fraction is greater than 50%. While the two equations derived here have been shown to give an accurate representation of the variation in the shear modulus with changing cell volume fraction for a 3D lattice, the intermediate region should be treated with caution as the solution will diverge in this zone. It may therefore be more appropriate to simulate materials that approach 50% volume fraction rather than rely on closed

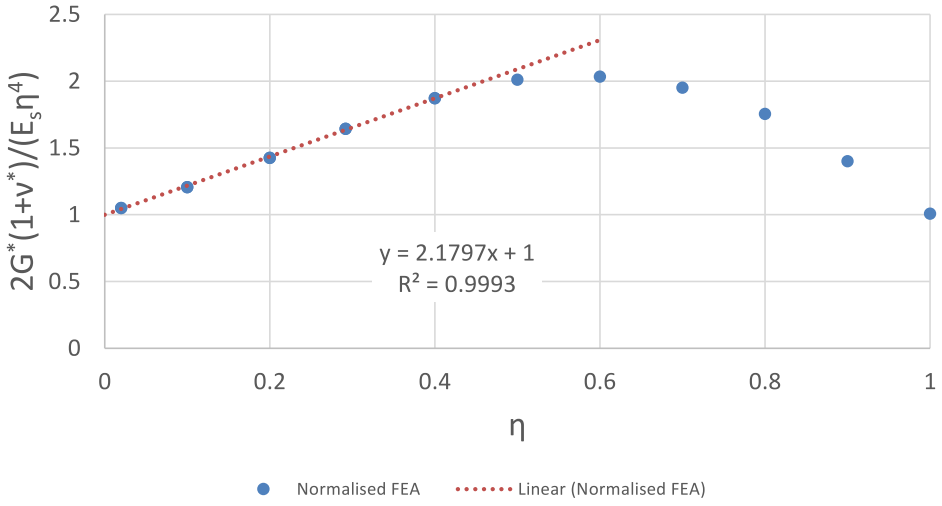

Figure 4.24: Variation in analytical approximation of the shear modulus against simulated values with varying normalised cell wall thickness, η. A linear relationship can be observed when η is less than 40 %.

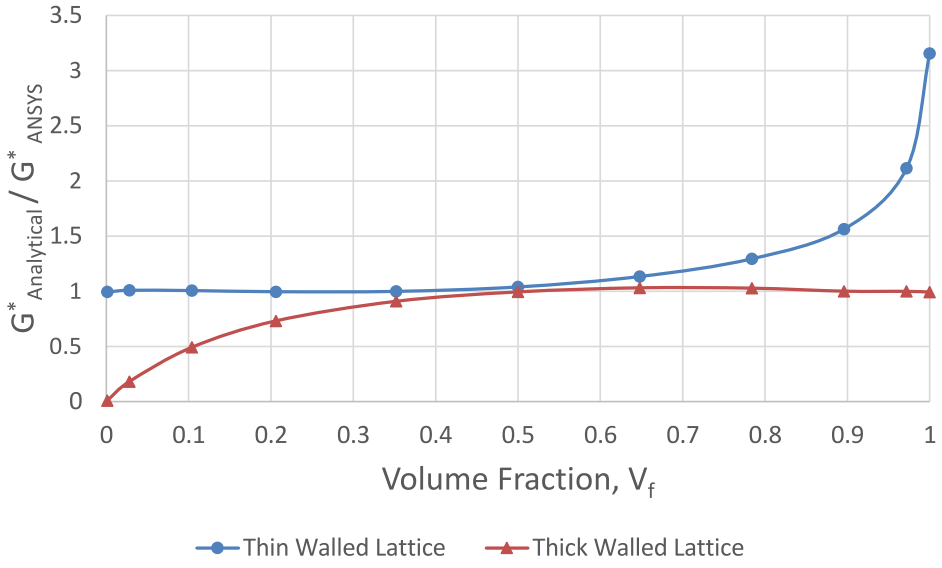

Figure 4.25: Variation in analytical approximation from the simulated values with volume fraction. Equation 4.37 is valid below 50% volume fraction while equation 4.36 is applicable to samples which are greater than 50%. The calculated values are accurate to 5% in this range.

form approximations.

The results obtained here closely match the shear modulus that was found from applying a shear stress to individual unit cells, confirming that the modulus is indeed independent of size scale. While there are computational advantages to simulating a single cell of material compared to a full beam, torsion experiments may be more appropriate for physical tests on real materials.

4.5.2 Characteristic Length

The characteristic length is a measure of how the stiffness of a heterogeneous material varies with size as the sample size tends towards that of the dominant microstructural features. A plot of the variation in normalised torsional rigidity for samples in the 'cubic' unit cell configuration can be seen in figure 4.26. It can be seen that as the thickness of the internal connecting beams is decreased, an increase in relative stiffness is observed as the number of cells through the depth diminishes. In the alternate unit cell configuration when the surface of the sample is corrugated, it is observed that there is a reduction in stiffness in comparison to the converged value which is to be expected (Figure 4.27). There does however appear to be a limit to this loss of relative stiffness for this case. The point of minimum stiffness is seen to shift depending on the number of rows of microstructure that are present within the cross-section of the sample. In dense samples, the relative stiffness is seen to decrease as the number of cells along the edge of the cross-section decreases. When there is only one cell in the cross-section however, it appears that this beam is slightly stiffer than the equivalent 2x2 sample. This is unexpected as the general trend is for an increase in relative rigidity with an increasing number of rows. The most likely cause for this is that the single cell is more resistant to shearing due to the distribution of the solid matter through the cross-section although it cannot be ruled out that there may be some influence due to the boundary conditions in the FE model as the number of contact points increases with sample size. As the material generated from the 'cubic' unit cell case does not exhibit this effect with the same boundary conditions then it is likely that the cell topography is more influential than the applied boundary conditions.

As the cell density decreases, the unit cell beam becomes gradually weaker until it is less stiff than the 2x2 sample. Further reduction in density reveals a slight decrease in relative stiffness in comparison to the denser samples.

The characteristic length in micropolar theory is defined from the relative change in stiffness with varying sample size for a given heterogeneous material. It is dependant however on the experimental size effect being positive in nature. It has been observed that when the unit cells are intersected by the surface of the material sample, that size softening effects can be seen. The magnitude of this softening effect with decreasing sample size does not necessarily correspond to that of the equivalent case when the unit cells are not intersected as has been

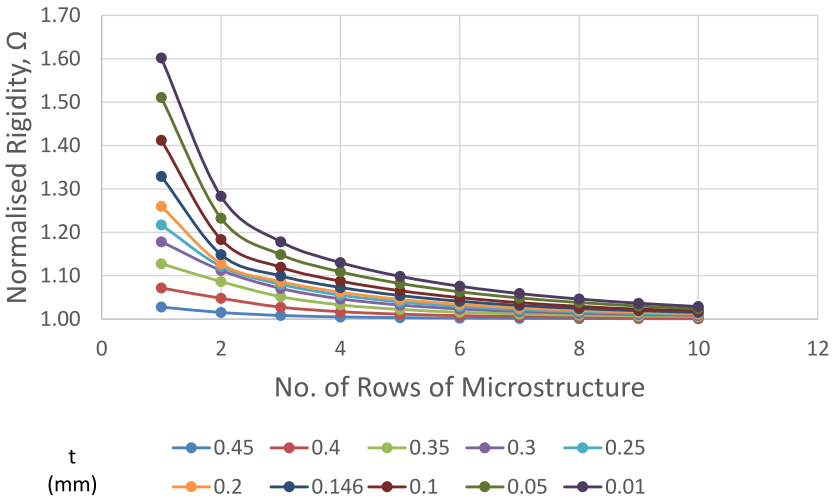

Figure 4.26: Variation in torsional rigidity with varying cell wall thickness with increasing sample depth (Cubic unit cell.).

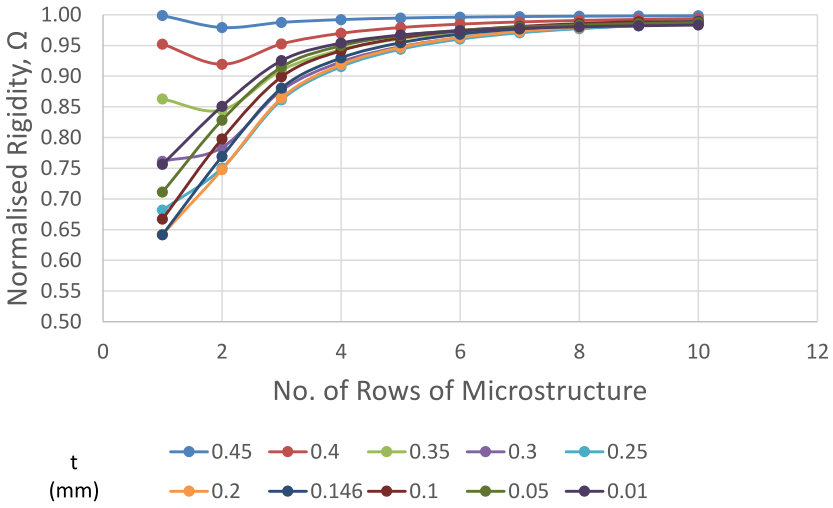

Figure 4.27: Variation in torsional rigidity with varying cell wall thickness with increasing sample depth. (3D Cruciform unit cell.)

shown above.

In lieu of a definitive definition of the characteristic length in torsion for a square bar of constant cross-section, the magnitude of the size effect, ${l_t}^2$ will be used to define the characteristic length. The magnitude of the characteristic length in torsion was defined previously within the rigidity of a rectangular bar as;

$$\frac{TL}{\theta} = G^* \left(I_p + 2{l_t}^2 d^2 \right) \tag{4.38}$$

where $\frac{TL}{\theta}$ is the experimental rigidity, G^* is the torsional modulus of the material, I_p is the torsion constant for a square cross section of depth d and l_t is the characteristic length in torsion.

$$\frac{TL}{\theta d^2} = G^* \left[\frac{2.25 d^2}{16} + 2{l_t}^2 \right] \tag{4.39}$$

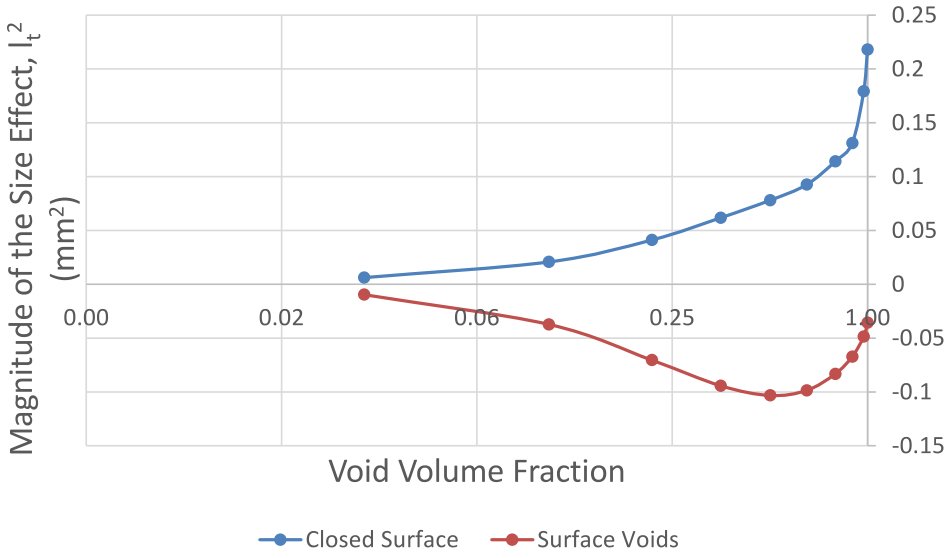

Figure 4.28: Variation in the magnitude of the characteristic length with varying void volume fraction for a lattice beam comprised of orthogonal bars. Negative values indicate that a softening effect is seen with diminishing sample size. The increase in size effect observed with diminishing cell volume fraction is only valid when $t > 0$.

Figure 4.28 shows how the magnitude of the size effect varies with void volume fraction within the material. It can be clearly seen that the magnitude of the size effect is strongly dependent on the void volume fraction and continuously increases with decreasing mass with the cubic unit cell. When the surface of the sample is discontinuous as in the case of samples formed from the cruciform unit cell however, this size effect is distinctly negative. A maximum

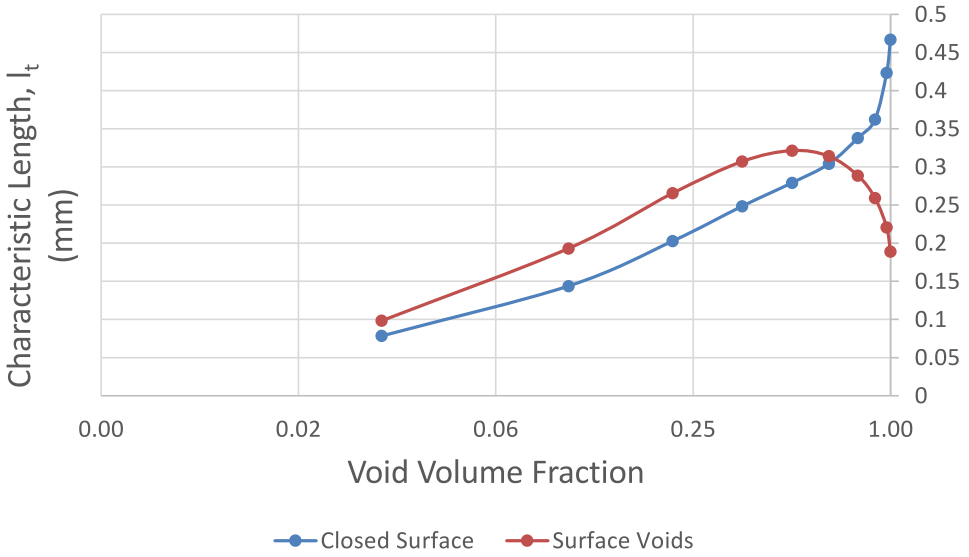

Figure 4.29: Variation in the characteristic length in torsion with varying void volume fraction. The increase in size effect observed with diminishing cell volume fraction is only valid when $t > 0$.

reduction in apparent stiffness can also be observed at approximately 50% volume fraction of solid material.

The characteristic length can be plotted in terms of the volume fraction of the void within the material as seen in figure 4.29. The negative value of ${l_t}^2$ which occurs when a softening effect is observed presents some difficulty in resolving the characteristic length from equation 4.39 due to the fact that the square root of a negative number needs to be determined. The plot in figure 4.29 has assumed an absolute value of ${l_t}^2$ in order to resolve a value for the characteristic length when a discontinuous surface is present. It can be seen that as the cell wall thickness decreases and the void volume fraction increases, that the characteristic length is largely dependent on the prescription of the microstructure within the sample. In the case whereby the material is distributed around the outer edges of the unit cell, it can be seen that the characteristic length increases with decreasing cell wall thickness. As the cell wall thickness tends to zero, it appears that there will be a finite characteristic length in torsion. The case with surface voids initially predicts a larger characteristic length than the equivalent closed cell at low void densities. A maximum characteristic length is observed at approximately 50% void volume fraction. As the void volume fraction is further decreased, the characteristic length decreases to a finite value.

It is clear that the preparation of the surface of a test sample is very important when trying to derive the characteristic length parameters. In many materials, it is not always possible to

prepare a sample that is free from surface defects and will therefore present some scatter under test. As materials with a random microstructure cannot be readily manufactured without some variation in the sample surface due to intersecting of the microstructural voids, it may be more appropriate to characterise them from samples which contain surface defects.

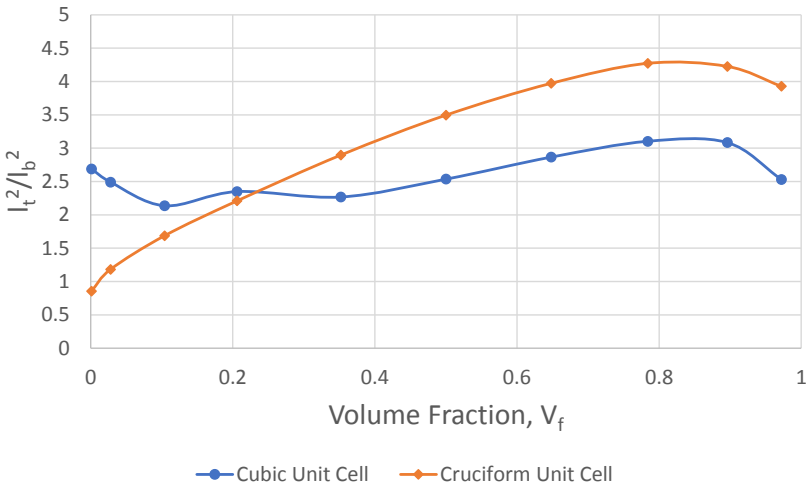

Figure 4.30: Variation in the ratio of characteristic length in torsion to the characteristic length in bending with volume fraction.

In work published by Goda et al. (2014); Goda & Ganghoffer (2015); Rahali et al. (2016), it was reported that the characteristic length in torsion was $\sqrt{2}$ greater than the bending characteristic length within couple stress theory. Here they assumed that the parameter β is negligible in comparison to γ for the materials tested. By recalling the definition for the characteristic length in torsion and bending below, it can be seen that the ratio of ${l_t}^2/{l_b}^2 \approx 2$ when $\beta \to 0$.

$$ {l_b}^2 = \frac{\gamma}{2\left(2\mu+\kappa\right)} \qquad {l_t}^2 = \frac{\beta+\gamma}{2\mu+\kappa} \qquad \rightarrow \qquad \frac{{l_t}^2}{{l_b}^2} = \frac{2\left(\beta+\gamma\right)}{\gamma} \tag{4.40} $$

For the lattice structure, it can be observed that the variation in the ratio of the characteristic length in torsion to bending, l_t/l_b is generally greater than this value which indicates that the contribution of β cannot be ignored (Figure 4.30).

In the material defined by the cubic unit cell, β appears to be always positive and falls within the bounds outlined in equation 2.13 ($-\gamma \leq \beta \leq \gamma, \quad \gamma \geq 0$). β is harder to define with the cruciform unit cell configuration as the value of γ that is found experimentally appears to be negative and falls out with the bounds of equation 2.13 which states that γ should always be positive. However, the resulting values of β seem to be permissible when the material volume fraction is relatively low.

4.6 Anticlastic Effects

When a beam is subjected to a transverse load or bending moment, it can be seen to deflect along the longitudinal axis. However, due to the Poisson's ratio of the material, there will be some lateral expansion or contraction as the beam bends. These lateral effects under bending will cause the beam to deform in the out of plane direction (Figure 4.31.). Work carried out by Frame (2013) determined that the influence of anticlastic effects are minimal below a breadth to depth aspect ratio of 10 and that a plane stress assumption is sufficient to calculate the global stiffness of beams with a constant cross section but varying depth.

While this is a sufficient simplification for a slender homogeneous beam, it is not evidently clear how a heterogeneous material with significant microstructure will behave. Two sets of analyses were performed in ANSYS on beam samples of a heterogeneous lattice subjected to a constant bending moment to quantify the anticlastic effect and what effect suppressing it has on the analysis. In the first set of FE simulations each beam was restrained from deforming in the out of plane direction, perpendicular to the plane of bending as is the case under plain strain conditions. The second set of experiments were identical with the exception that the beams were not constrained through the breadth and were free to distort out of plane. This is much closer representation to how a beam may behave in a physical test.

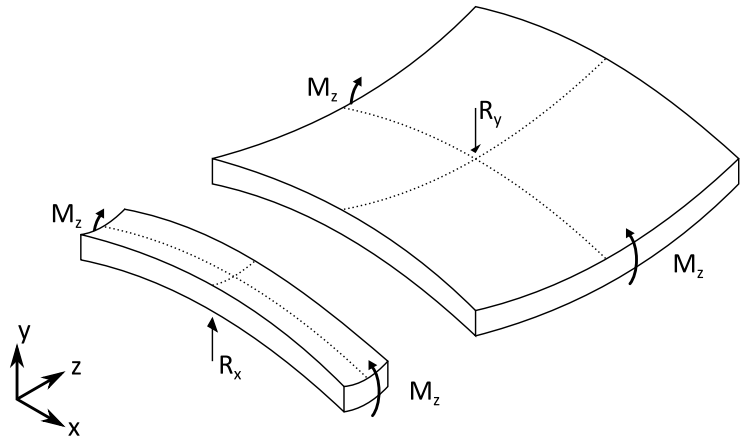

Figure 4.31: Beams subjected to a constant moment load. Wide beams display a distinct out of plane bending effect.

The cubic lattice material that was chosen had a unit cell with outer dimensions of 5 mm and an internal wall thickness of 1 mm which was comparable to the experimental tests to be conducted. Beams were constructed with a length to depth aspect ratio of 5 and the ratio of the breadth to the height was varied from 1 to 6. A length to depth aspect ratio of 5 was chosen in

this analysis as it was observed that this parameter did not adversely affect the relative stiffness of the material when subjected to a constant rotation per unit length. A low aspect ratio is beneficial here in order to minimise the size of the models that were generated. At a breadth to depth aspect ratio of 1, the beams were representative of the samples which were to be tested experimentally. As the width is increased, the beam will tend towards a plate in bending.

4.6.1 Results & Discussion

A constant moment loading was imparted on the end face of each beam and the resulting angle of rotation over the length of the beam recorded. The size effect is observed by plotting the variation in rigidity with respect to sample depth and interpreting the parameters from the linear portion of the graph. The data can be interpreted graphically in two different ways as implied below in equations 4.41 & 4.42.

$$\frac{ML}{\theta}\left(\frac{1}{bd}\right) = \left(\frac{E^*}{12}\right)d^2 + \gamma \tag{4.41}$$

$$\frac{ML}{\theta}\left(\frac{12}{bd^3}\right) = E^* + \frac{12\gamma}{d^2} \tag{4.42}$$

The main difference between the two equations is that in equation 4.41 the modulus can be found from the linear extrapolation that can be observed when a large enough set of samples is analysed. The modulus of micropolar bending, γ is interpreted from the intercept of the line with the vertical axis. In equation 4.42 the modulus can be found from the intercept of the axis and γ from the gradient of the linear trend line. The main difference between the two methods of plotting the data is that small variations in the slope of the linear plot have a greater effect on the intercept with the axis meaning that the calculated data may have some ambiguity. By calculating each parameter from both plots it is possible to obtain a range for each.

The variation in rigidity that was observed with increasing breadth to depth aspect ratio was minimal when the beams were free to distort out of plane and restrained. Suppressing any anticlastic deformation had the effect of slightly increasing the value of E^* and γ. A summary of the converged results can be seen in table 4.1.

It was observed that the rigidity of the beams increased with a decreasing number of cells through the depth of the beam, irrespective of the width of the samples in question which is in line with the general prediction for a micropolar material. The characteristic length, l_b calculated by equation 4.41 or 4.42 in the analysis can also seen to be similar irrespective of the applied boundary conditions.

From the beams that were simulated, the normalised global rigidity was calculated from the resulting angle of rotation, θ when the beams were subjected to a constant bending moment, M.

	Micropolar Flexural Modulus	Micropolar Bending Modulus	Characteristic Length for Bending
	$E^* \, (MPa)$	$\gamma \, (N)$	$l_b \, (mm)$
Anticlastic Effects	363.86	690.75	0.974
Restrained	364.91	679.52	0.965
Anticlastic Effects	360.86	677.25	0.969
Unrestrained	362.03	664.76	0.958

Table 4.1: Variation in the maximum and minimum values of the flexural properties derived from numerical tests.

The largest variation in normalised stiffness between samples of the same depth but differing width occurred when there was only one cell through the depth of the specimen, and decreases with an increasing number of cells through the depth of the samples. However this variation was at most 2% in the plain strain case and 1% when the beam was free to distort out of plane. The micropolar flexural modulus, E^* and modulus of micropolar bending, γ did not display any significant difference with a change in sample breadth to depth aspect ratio.

If the converged flexural modulus of the material is known, then it is possible to calculate the modulus of micropolar bending, γ for a given sample from either equation 4.41 or 4.42. From the analysis performed, it appears that this parameter diverges with increasing sample depth and converges with increasing width for a given length to depth and breadth to depth aspect ratio respectively. Generally it can be seen that as the number of rows of microstructure is increased through the depth then γ tends to initially decrease before gradually increasing again (Figures 4.32 & 4.33.). The values for the micropolar couple modulus, γ, which are found here show some variation with respect to sample depth which varies from the converged values in table 4.1. This variation can be attributed to the experimental numerical procedure as small variations in the calculated rigidity become apparent when an individual sample is analysed due to the cubic dependency of the depth that is introduced by the second moment of area. Samples which are restrained from distorting in the out of plane direction show significant divergence with increasing sample depth (Figure 4.32). Much less variation is observed when the beams are free to distort out of plane although the value of γ does appear to increase with sample depth (Figure 4.33).

The cause of the divergence seen in figures 4.32 & 4.33 is most likely attributed to the cubic dependence on the sample depth that is introduced by the second moment of area. Small variations in the experimental results will appear more significant because of this which highlights the importance of obtaining the correct material modulus. If the correct modulus is not used, then a large variation can be seen as the number of cells through the depth is increased. From experimentation it was found that the value of γ could never be found to converge across

all specimens of varying depth, which suggests that there is another parameter that has a small influence that is not being accounted for. In order to obtain the best approximation of the parameter γ it is necessary minimise the variation over the full range of samples which is only fulfilled when an accurate flexural modulus is found.

This has implications for mechanical testing as it suggests that small variations in the experimental results could negatively influence the overall micropolar properties that are derived. However, one positive point that has come out of this analysis is that the samples with only one cell through the depth of the material closely match the converged γ value if the experiment is carried out accurately.

It is therefore recommended that the beams should not be suppressed during simulations to allow for the beam to deform in the out of plane direction. This should minimise the variation in the higher order parameters that are derived from the computational experiments and is a closer representation of how the material will behave under physical tests. This analysis has also highlighted that γ is dependent on the breadth to depth aspect ratio of the sample to some degree. As the breadth of the beam is increased to the point where it can be considered a plate, the value of γ converges to a maximum value.

As the characteristic length is dependent on both the material modulus and the couple modulus, it can be seen that this parameter behaves similarly. In all cases the value of the characteristic length converges to a finite value as the length to breadth aspect ratio is increased. The recorded value was found to vary between 0.95 and 1 mm when the beam is allowed to freely deform in the out of plane direction.

While there does appear to be some discrepancy with the apparent convergence of the characteristic length with increasing number of cells through the depth, it should be highlighted that this value is an experimental result and is very sensitive to small variations in the calculated parameters. Also when calculating the individual parameters for each sample, the modulus is averaged from all the experimental data. This could possibly be minimised by incorporating the tensile modulus into the calculation of the characteristic length. Nevertheless, the variation in characteristic length is pretty small and is of similar size to the cell wall thickness which is consistent with micropolar theory.

However, if a sufficiently large set of samples is used experimentally to calculate the flexural parameters, it is expected that the influence of the sample breadth to depth aspect ratio will have minimal effect and should fall within the range of other experimental errors.

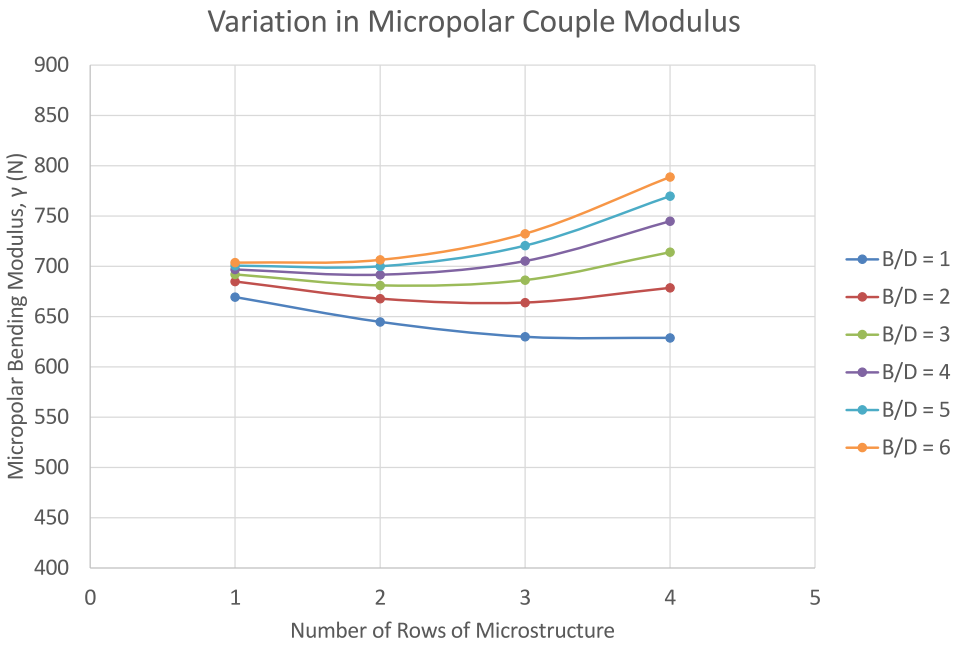

(a) γ from Rigidity vs $1/d^2$

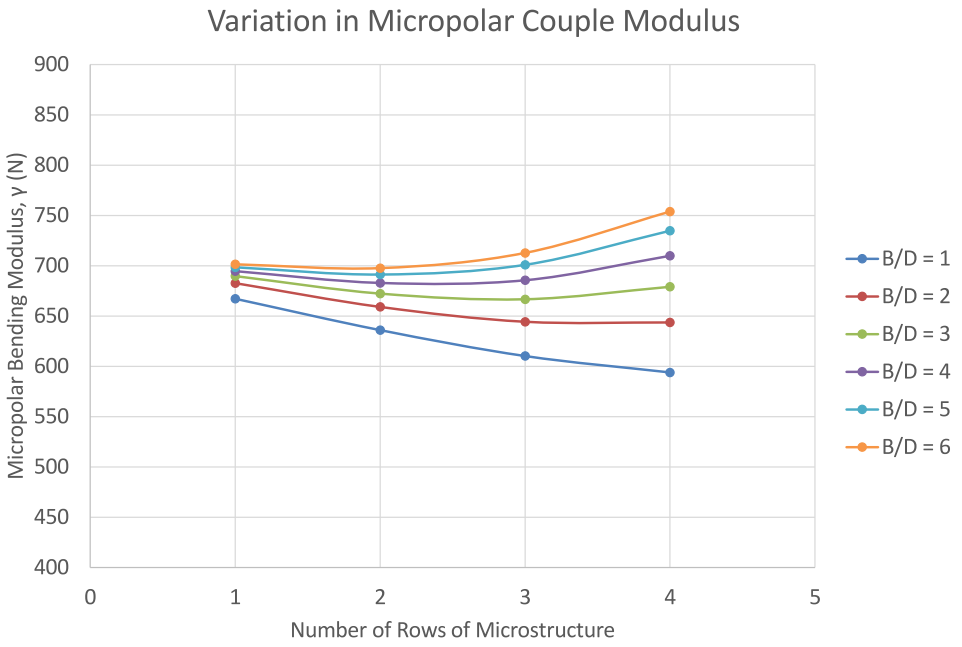

(b) γ from Rigidity vs d^2

Figure 4.32: Variation in micropolar modulus, γ, when out of plane bending effects are suppressed (Plane strain).

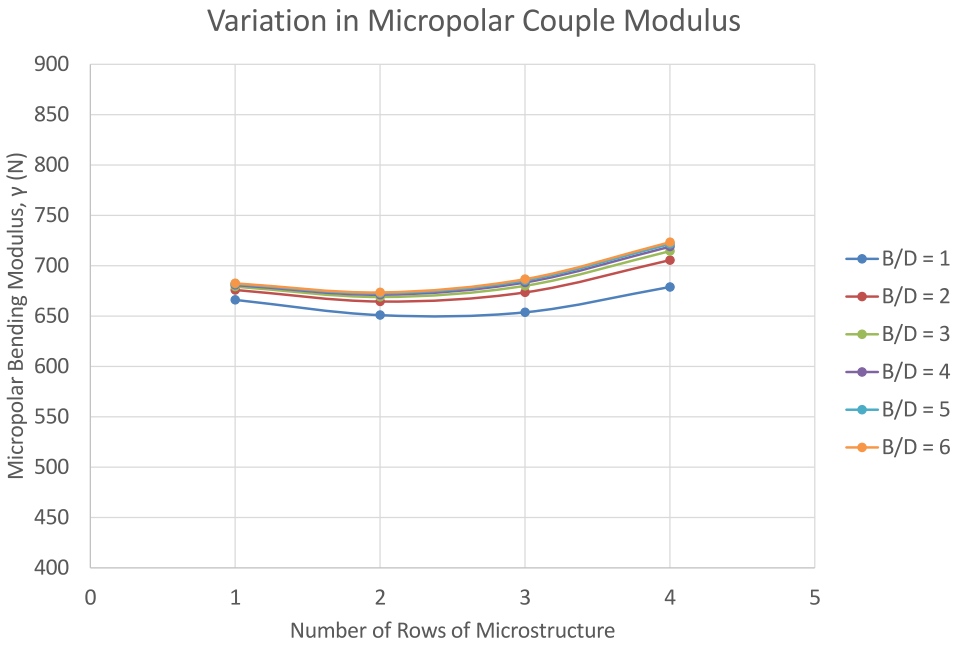

(a) γ from Rigidity vs $1/d^2$

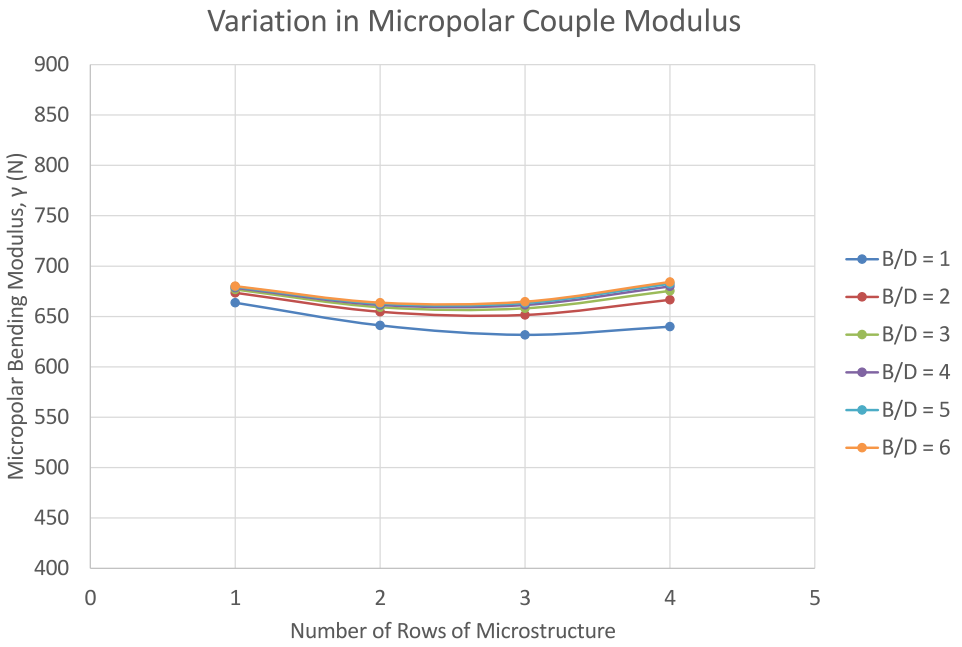

(b) γ from Rigidity vs d^2

Figure 4.33: Variation in micropolar modulus, γ, when beam is free to bend in the out of plane direction.

4.7 Summary & Conclusions

In this chapter, numerical predictions have been developed to characterise the mechanical behaviour of a 3-dimensional cubic lattice structure comprised of an array of orthogonal bars. The Young's modulus, Poisson's ratio and shear modulus were all found to be strongly dependent on the cell size and internal beam thickness particularly at low volume fractions. The parameters were also found to be independent of size and can be resolved from a single unit cell of material. Numerical simulations in flexure and torsion were also conducted to confirm this size independence.

Size effects were found to be strongly dependent on both the prescription of the microstructure within the samples and the material volume fraction of the unit cell. When the surface of the porous material is smooth and relatively continuous as in the case of the cubic unit cell a positive size effect was observed whereby smaller samples were relatively stiffer than larger ones for a given volume fraction in both flexure and torsion. While samples generated from the 3D cruciform cell that have discontinuous surfaces displayed identical Lamé parameters to the closed cell case, a size softening effect was observed that is not readily explained within micropolar elasticity. In torsion, the reduction in stiffness due to the size softening effect appears to be limited by the volume fraction of the material, with a maximum size effect being observed at a volume fraction of 50%.

Numerical predictions were also made to resolve the Young's modulus, Poisson's ratio and shear modulus of the lattice with varying volume fraction, that allow for the general mechanical properties to be predicted for a given cell wall thickness assuming that the underlying solid material which makes up the unit cell is linear-elastic isotropic. In general, it was found that there is not one formulation which can be used to describe these parameters over the full range of available volume fractions. The Young's modulus and shear modulus found in flexure and torsion experiments respectively closely matched those which were obtained from the uniaxial and simple shear experiments.

While the greatest increases in stiffness are observed with diminishing volume fraction, it should be highlighted that the overall stiffness of the samples decreases too, so any potential gains may be limited by other structural considerations.

It was also observed that in flexure, the width of the sample had some minor influence on the characteristic length of the material, but the discrepancy is reasonably small assuming that anticlastic effects are not suppressed in the model.

Chapter 5

Numerical Investigation of an Orthogonal Lattice with Internal Braced Members

In this chapter, size effects within the mechanical behaviour of 3-dimensional orthogonal lattice braced with internal supports is investigated. A combination of uniaxial tension, symmetric shearing, pure bending and torsion are performed on samples of this material of differing sizes with a square cross-section. The diameters of the connecting beams within the lattice are also varied independently to quantify how the magnitude of the mechanical properties and resulting size effect changes with density.

5.1 Introduction

In the previous chapter the mechanical properties of an orthogonal cubic lattice were identified within the context of a micropolar continuum. It was found that in this case the size effect was dominated by the flexural behaviour of the unit cell, with the maximum size effect occurring as the volume fraction tends to zero. In order to explore how the size effect varies in a material which has a more significant resistance to shear, a unit cell with a lattice which was braced by 4 diagonal beams intersecting at the volumetric centre of the cell was investigated (Figure 5.1).

In comparison to the previous analysis, the interior beam members were cylindrical in nature rather that rectangular in order to reduce the complexity in modelling the joint interactions. The analysis was carried out for a fixed unit cell measuring $5 \times 5 \times 5$ mm with the exterior and interior beam diameters being varied to study the influence of material volume fraction. The interior connecting beams were varied separately from the exterior beams around the perimeter to compare the effect of bending and shear dominated heterogeneous materials. The outer cell walls consist of quarter cylinders with radius 'r' that are centred on the outer edge of the cell radiating inwards. This configuration was chosen as it meant that adjoining cells would form cylindrical beams. An example unit cell can be seen in figure 5.1. The parameters SX,

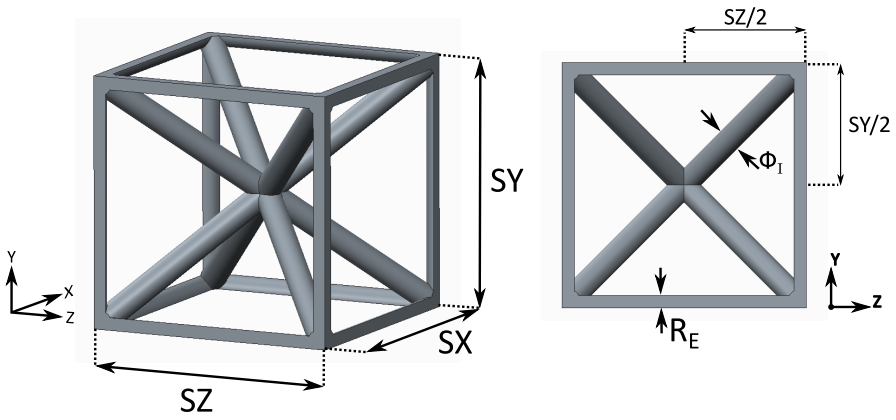

Figure 5.1: Braced cube with diagonal cross members.

SY and SZ represent the cell spacing in each of the 3 major axes; r and ϕ are the radius and diameter of the beams respectively. Subscripts E and I denote the exterior and interior beams respectively.

5.2 Numerical Simulation Boundary Conditions

In order to fully identify the material properties of the lattice structure, a series of numerical simulations were performed. The effective Young's modulus and Poisson's ratio of the structure were obtained by applying a uniaxial displacement to the cell. Only minimum constraints were applied transverse to the loaded surface, allowing the model to freely contract transversely yet prevent rigid body motion.

The boundary conditions were as follows:

$$\begin{array}{lllll} X1 \text{ Face:} & u_x = 0 & u_y = 0 \text{ at Z} = 0 & u_z = 0 \text{ at Y} = 0 & \\ X2 \text{ Face:} & u_x = 0.01 & u_y = 0 \text{ at Z} = 0 & u_z = 0 \text{ at Y} = 0 & (5.1) \end{array}$$

Where the denoted faces represent the exterior surfaces which are perpendicular to the associated axes as in figure 4.9. The resulting properties were obtained from the reaction forces in the direction of loading and the transverse displacements on the end face.

The shear modulus, G^* was obtained by subjecting the unit cell of material to a pure shear load. The boundary conditions for this test were:

$$\begin{array}{lll} X1 \text{ Face:} & u_y = 0 & u_z = 0 \\ X2 \text{ Face:} & u_y = 0.01 & u_z = 0 \\ Y1 \text{ Face:} & u_x = 0 & u_z = 0 \\ Y2 \text{ Face:} & u_x = 0.01 & u_z = 0 \\ Z1 \text{ Face:} & u_z = 0 & \\ Z2 \text{ Face:} & u_z = 0 & (5.2) \end{array}$$

The final test that was carried out on a cubic unit cell sample of the material was used to obtain the bulk modulus. This test involved subjecting every face in the cube to a constant uniaxial deflection to measure the reaction forces during contraction with the following boundary conditions:

$$\begin{array}{ll} X1 \text{ Face:} & u_x = 0.01 \\ X2 \text{ Face:} & u_x = -0.01 \\ Y1 \text{ Face:} & u_y = 0.01 \end{array}$$

$$\begin{aligned} Y2 \text{ Face:} \quad & u_y = -0.01 \\ Z1 \text{ Face:} \quad & u_z = 0.01 \\ Z2 \text{ Face:} \quad & u_z = -0.01 \end{aligned} \tag{5.3}$$

The bulk modulus was obtained from the relative change in volume of the cube and the reaction forces in the system.

The properties of the underlying solid component in the lattice were linear elastic and consisted of a Young's modulus, E_s , of 2000 MPa and a Poisson's ratio, ν, of 0.3. All of the properties that were obtained above are expected to be sample size independent and are not predicted to exhibit any distinguishable size effect in micropolar theory.

In order to fully categorise the material within the micropolar continuum, further tests must be undertaken to obtain the flexural and torsional properties of the material. The method of size effects was utilised in the same manner as the previous chapters in order to obtain the characteristic lengths in bending and torsion for the material. Each sample consisted of a bar with square cross-section and fixed aspect ratio. The number of cells across the depth of the sample was varied in order to find these additional material properties.

5.3 Numerical FE Simulation Setup

The simulations were conducted in ANSYS APDL using the higher order 3D SOLID187 continuum elements. Each element was in the form of a triangular prism with 4 corner nodes and 6 mid-side nodes. Each node had three translational degrees of freedom. Tetrahedral elements were chosen for the analysis rather than brick elements as the added complexity of modelling the joints in the structure was more suited to an unstructured mesh.

In order to simplify the generation of the mesh within the model, an eighth of the unit cell was initially generated and meshed. By generating the complete unit cell through reflection of the initial portion, this ensured that continuity was maintained between the placement of the nodes at the opposite faces of the unit cell. Ensuring that the nodes on each face match up meant that as the material was generated through propagation of the unit cell, then the inter-cell boundaries matched up exactly. For this analysis the initial model was generated in the solid modelling CAD package CREO Parametric due to the added complexity of modelling the intersections at the joints within this material. While this method is not as efficient as direct generation in ANSYS, parametrising the model within CREO allowed for models to be generated consistently and accurately. The unit cell within the model was propagated in the same manner as the other models generated in ANSYS to form a lattice comprised of an assembly of unit cells.

5.4 Results of FE Simulations

5.4.1 Uniaxial and Pure Shear Loading

In total, 15 different configurations of the lattice were tested by varying the respective diameters, ϕ_I & ϕ_E, of the interior and exterior beams independently. The volume fraction of the unit cells being investigated ranged from around 2-40% solid material. By varying the exterior and interior diameters of the beams within the lattice, it was possible to observe the influence that these parameters had on the constitutive properties of the material. In general, the material does not follow the isotropic homogeneous relation $E_s = 2G_s(1 + \nu)$.

From the simulations which were performed, it was observed that the Young's modulus of the material increases with volume fraction. It can be observed from figure 5.2 that when the exterior beam diameters are varied with respect to the internal beams, that the Young's modulus is strongly dependent the density of the unit cell. Conversely, if the diameter of the interior members are varied with respect to the exterior beams then the increase in Young's modulus with volume fraction is weak by comparison (Figure 5.3).

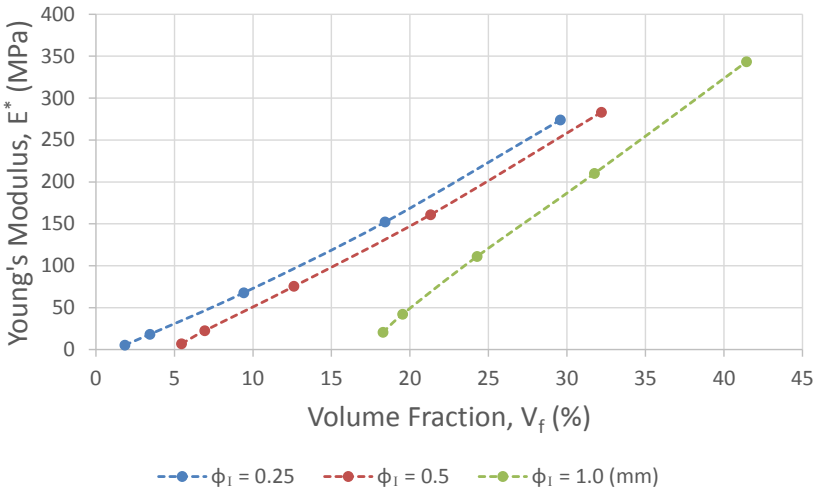

Figure 5.2: Variation in Young's modulus with material volume fraction. Here, the interior beams are of fixed diameter while the exterior beam diameter is varied.

The Shear modulus on the other hand is strongly influenced by the interior connecting beams (Figure 5.4). It appears that the external members only offer a weak resistance to shearing by comparison (Figure 5.5).

The Poisson's ratio of the material is strongly influenced by the diameter of the exterior beams in the unit cell (Figure 5.6.). Interestingly, decreasing the thickness of the exterior beams relative to the interior connectors has the effect of increasing the observed Poisson's ratio of the

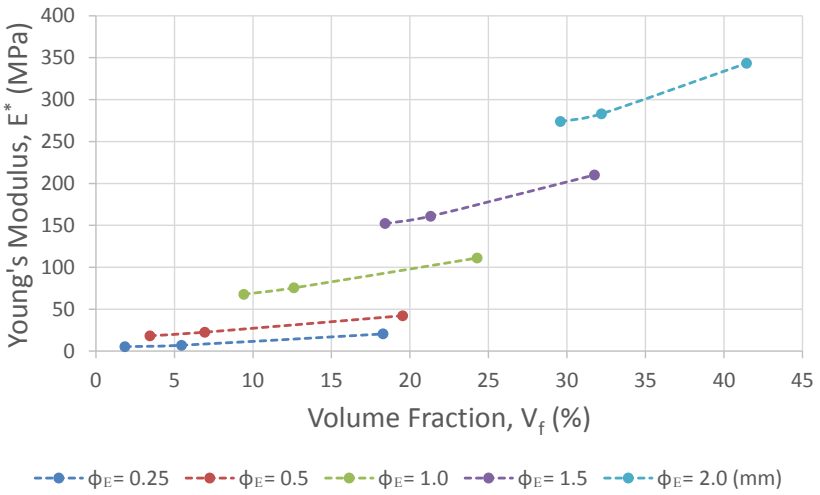

Figure 5.3: Variation in Young's modulus with material volume fraction. Here, the exterior beams are of fixed diameter while the interior beam diameter is varied.

material for low volume fractions. Conversely, by fixing the exterior diameter and decreasing the interior beam diameter, a reduction in Poisson's ratio is observed with decreasing volume fraction. This effect is observed to be strong at low volume fractions, but quickly converges as the volume fraction increases. In general terms, the change in Poisson's ratio can be explained by dividing the unit cell into two separate parts. When the exterior beams are dominant as was the case of the orthogonal lattice in chapter 4 then the Poisson's ratio will tend to zero as the volume fraction decreases due to a lack of contraction within the lattice. The interior beams on the other hand also bend when subjected to a uniaxial load. If bending in the interior beams dominates, then the overall contraction within the cell will tend to increase thus enabling the Poisson's ratio of the unit cell to be greater than that of the solid material component.

The Bulk modulus of the material did not show any obvious dependence on the interior or exterior beam diameters and was largely dependent on the cell volume fraction in the range that was considered. This is apparent in figure 5.7 where it can be observed that samples with differing beam diameters, but similar volume fraction have an identical bulk modulus. The full numerical results obtained for the Young's modulus, Shear modulus, Poisson's ratio and Bulk modulus are summarised in table D.1 within appendix D.

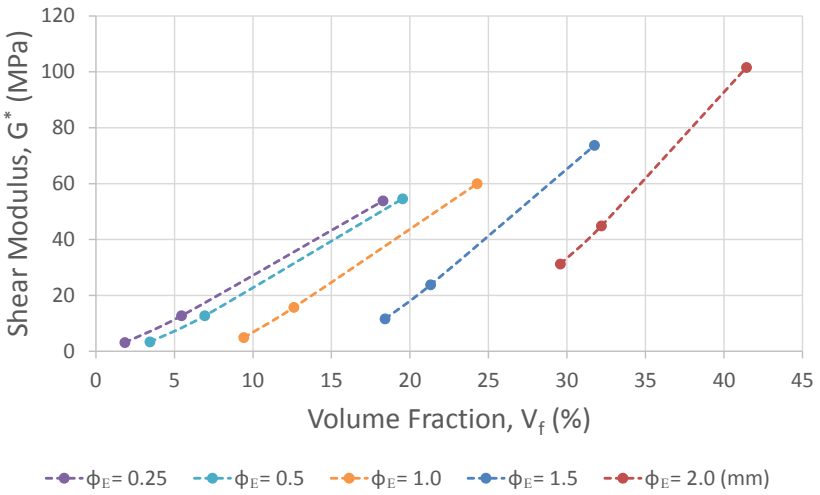

Figure 5.4: Variation in shear modulus with material volume fraction. Here, the exterior beams are of fixed diameter while the interior beam diameter is varied.

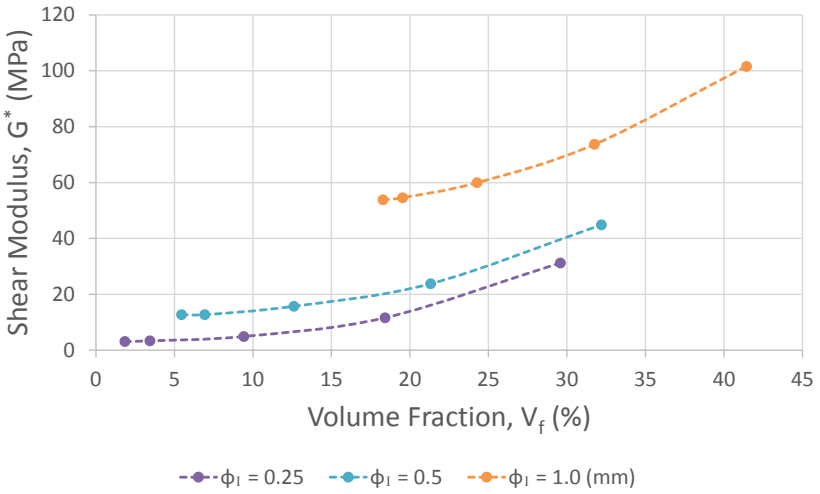

Figure 5.5: Variation in shear modulus with material volume fraction. Here, the interior beams are of fixed diameter while the exterior beam diameter is varied.

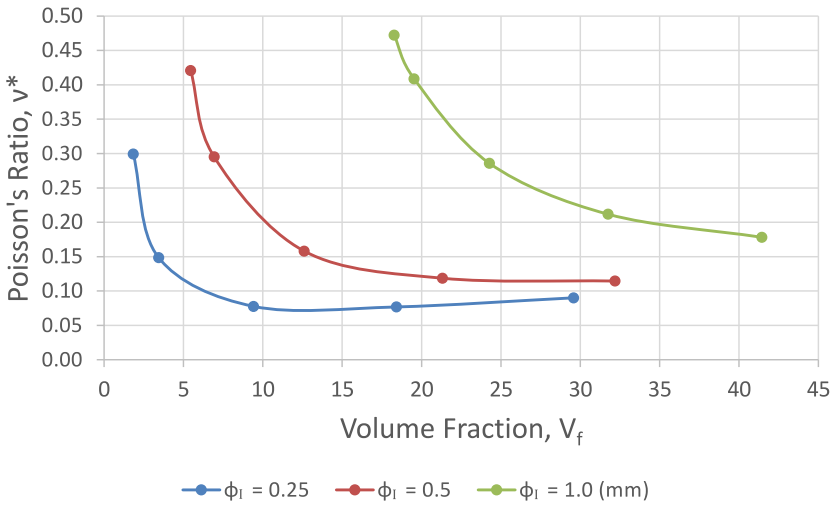

Figure 5.6: Variation in Poisson's ratio with material volume fraction. Here, the interior beams are of fixed diameter while the exterior beam diameter is varied.

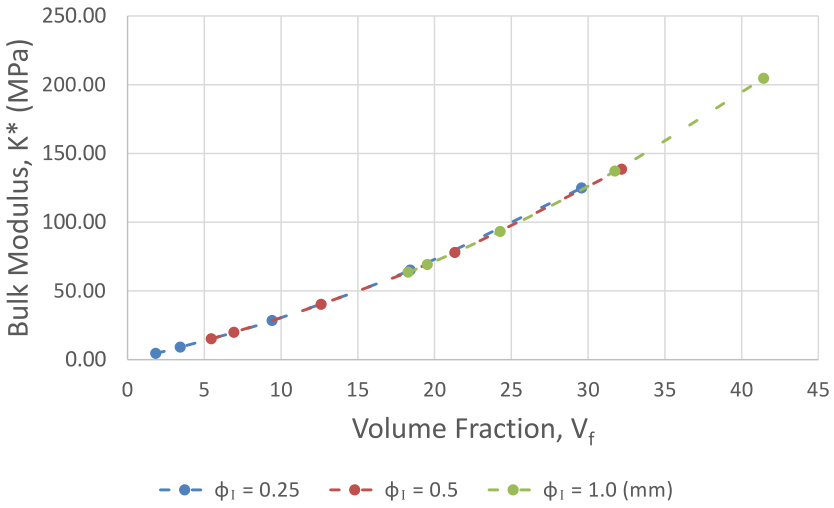

Figure 5.7: Variation in bulk modulus with material volume fraction. Here, the interior beams are of fixed diameter while the exterior beam diameter is varied.

5.4.2 Numerical Simulations in Flexure

Samples of the material were simulated in flexure by applying a constant bending moment to beam samples with a square cross-section and a constant aspect ratio in the same manner as outlined in the previous flexural simulations. Prior to conducting the FE analysis, an initial assessment was undertaken to determine whether the length to depth aspect ratio of the samples influenced the apparent rigidity of a specimen with fixed depth. As the size of the models which could be simulated within the FE software was limited due to the number of elements and nodes that are required to simulate a single unit cell, it was necessary to find the minimum aspect ratio which could accurately resolve the rigidity of a sample at a given depth.

The unit cell which was chosen to perform the convergence test consisted of interior and exterior beams which were 0.5 mm in diameter. This corresponded to a solid volume fraction of 6.9%. Samples were simulated with between 1 and 3 cells across the breadth and depth of the sample over a range of length to depth aspect ratios which varied from between 1 & 10.

The rigidity of each sample was calculated from the angle of rotation through which the beam is deflected and the corresponding reaction moments. Samples were normalised by the rigidity of the corresponding sample with an aspect ratio of 10 to determine how the rigidity converges with increasing sample length.

From figure 5.8 it can be seen that there is a weak correlation between the length to depth aspect ratio and the normalised rigidity of beam samples subjected to a pure bending moment. The rigidity of the sample is observed to converge with increasing length at a given beam depth. As the number of cells through the depth of the sample increases, the normalised rigidity at a given aspect ratio is also seen to increase. At low aspect ratios, the change in rigidity with varying sample depth is noticeable, although the greatest variation in rigidity occurs when the number of cells through the depth is increased from 1 to 2. The normalised rigidity also converges with increasing sample depth.

An aspect ratio of 6 was therefore chosen to conduct the subsequent analysis as the full set of samples were able to be modelled with the available computational resources and the variation in normalised rigidity was within 1% of the converged result which was deemed acceptable for the analysis.

Samples of the material were simulated in flexure by applying a constant bending moment to beam samples with a square cross-section and a length to depth aspect ratio of 6. The number of cells across the breadth and depth of the sample was varied between 1 and 6 cells.

From the rigidity plots generated, a micropolar flexural modulus and characteristic length were obtained in the same manner that was described in chapter 4. The flexural modulus identified for each material was identical to the Young's modulus observed in the uniaxial simulations. In bending, the general trend observed was that the characteristic length increases

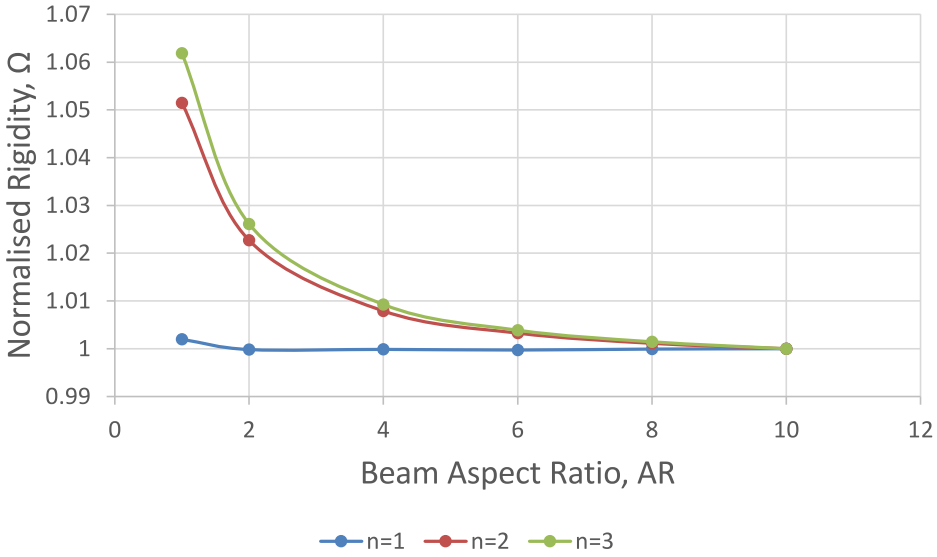

Figure 5.8: Influence of sample aspect ratio on the normalised beam rigidity for a sample where $\phi_E = \phi_I = 0.5$ mm $SX = 5$ mm. Samples converge with increasing aspect ratio and number of cells through the depth. Beams of equivalent depth are normalised against the sample with an aspect ratio of 10.

with void volume fraction which can be clearly seen in figure 5.9 when the diameter of the exterior beams is fixed. The presence of internal diagonal members within the unit cell has the effect of limiting the magnitude of the characteristic length. It can be seen in figure 5.10 that as the void volume fraction is decreased by varying the diameter of the internal beams, ϕ_I, the magnitude of the size effect decreases and the position of the maximum size effect varies. Increasing the void volume fraction above the point of maximum characteristic length results in a diminishing size effect. The magnitude of the characteristic length seen in figure 5.10 is of similar order to that observed in the orthogonal lattice albeit the maximum relative increase in stiffness is limited due to the presence of the internal connecting beams.

5.4.3 Torsional Characteristics

Each sample was subjected to a constant axial rotation over the length and the resulting reaction moment was recorded in the same manner as chapter 4. Unrestrained axial boundary conditions were applied at the end faces in order to allow the beam to warp freely. Further details on the applied boundary conditions can be found in appendix A. Initial torsion simulations carried out showed that there was no significant dependence on the aspect ratio of the samples with a square cross-section subjected to a fixed angle of rotation when the end faces are not constrained axially. It was therefore decided that an aspect ratio of 2 was to be used for all torsion tests to

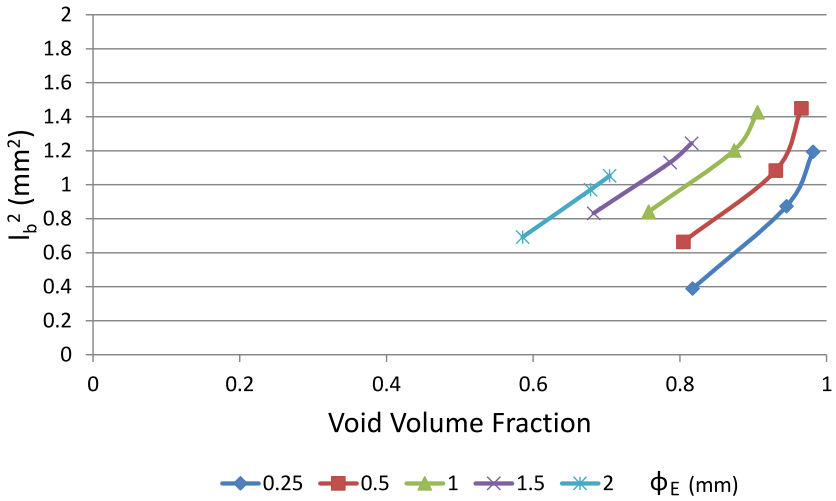

Figure 5.9: Variation in the magnitude of the characteristic length with fixed exterior beam diameter.

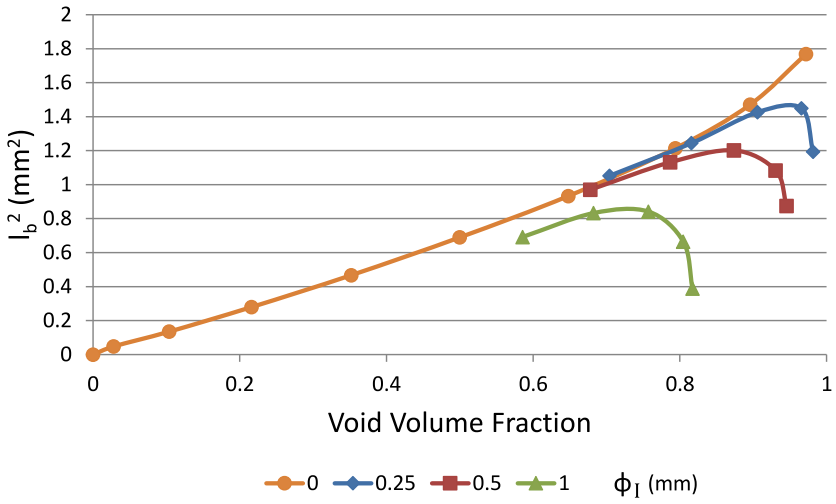

Figure 5.10: Variation in the magnitude of the characteristic length with fixed interior beam diameter.

minimise the size of the computational simulations. In total a set of 6 samples were tested for each material. The specimens were tested at equal length to depth aspect ratios, with varying sample depth to obtain the micropolar shear modulus and characteristic length for torsion using the method of size effects.

From the results of the simulations it was found that the micropolar shear modulus of the cellular structure at a given volume fraction closely matches the values obtained from the pure shear tests on a single unit cell. The magnitude of the characteristic length in torsion, ${l_t}^2$ was also obtained for each sample. It was observed that depending on the diameter of the beams within the lattice that the size effect observed could either be positive or negative in nature (Figure 5.11). This is in contrast to the cubic lattice analysed in the previous chapter which only displayed a positive size effect that increased with diminishing cell volume fraction. By plotting the variation in characteristic length with void volume fraction, it is possible to observe how the diameter of the beams which define the unit cell influence the size effect within the material. In figure 5.11 the diameter of the external beams was fixed and the variation in characteristic length is plotted as the diameter of the interior beams is reduced. It can be observed that when the diameter of the external beams is significantly larger than the interior beam diameter that the observed size effect increases with decreasing volume fraction which is in-line with what was observed in the case of the cubic lattice. The position and magnitude of this maximum size effect appears to be dependent on both the cell density and the ratio of the interior and exterior beams within the cell. It is expected that the maximum possible size effect that can be observed will tend towards that of the cubic lattice when the internal beam diameter approaches zero.

In contrast to the cubic lattice unit cell, the interior beams which are present here have a much greater influence on the size effect as the cell volume fraction decreases. When the internal beams are similar to or greater than the diameter of the beams situated on the exterior of the unit cell, a negative size effect is generally seen. The magnitude of this negative size effect appears to converge towards a maximum value with increasing void volume fraction as the diameter of the exterior beam diminishes (Figure 5.12).

While only a subset of the possible unit cells that can be constructed by varying the interior and exterior beam diameter within the cell have been considered, it is expected that the size effects which are observed here will diminish as the cell volume fraction approaches that of a classical solid.

The parameter β, which is one of the micropolar material moduli, can be derived from the characteristic lengths and the modulus of micropolar bending, γ. Due to energy considerations, the value of Beta is predicted to fall within the bounds $-\gamma \leq \beta \leq \gamma$. It was found that β did not generally fall within the required bounds to satisfy micropolar elasticity. In this configuration, although a positive size effect was obtained in bending, the interior diagonal beams within

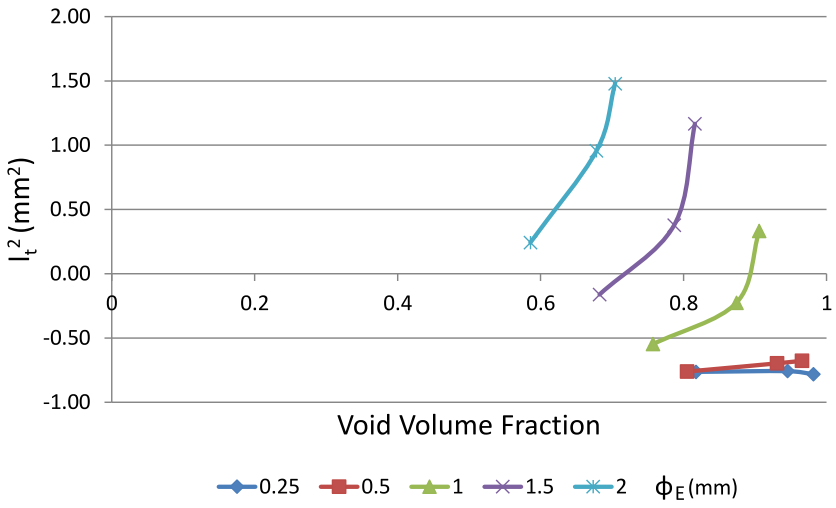

Figure 5.11: Variation in the magnitude of the characteristic length for torsion with void volume fraction when exterior beam diameters are fixed.

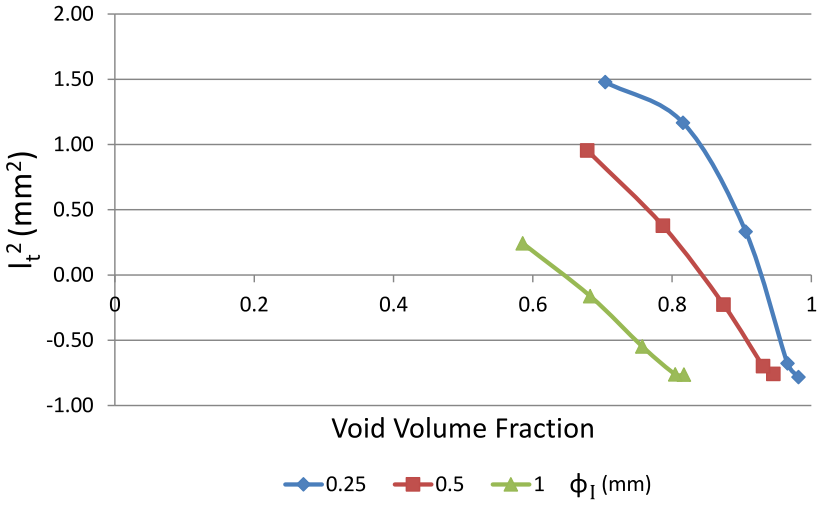

Figure 5.12: Variation in the magnitude of the characteristic length for torsion with void volume fraction when interior beam diameters are fixed.

the unit cell creates a strong size softening effect which dominates unless the exterior beam diameter is large enough to dominate under torsion. For this reason, β tends to fall out-with the lower bounds that are defined for a micropolar continuum.

5.4.4 Mixed Cruciform Unit Cell in Torsion

At the cellular level, the unit cell which is chosen to represent the microstructure of the material has been shown in the previous chapter to have a considerable effect on the mechanical behaviour of discrete samples which are of similar order to the individual cells. Size softening effects are observed when the surfaces of the sample are discontinuous. In the previous section it was observed that in torsion, the interior cell structure can contribute to softening effects with diminishing sample size which are not necessarily observed in bending. This was attributed to the fact that the reduction in stiffness which is brought upon by the interior beam members dominates over any stiffening which may be gained from the beams situated at the exterior of the cell.

In this section, an alternate configuration of the braced cubic lattice is investigated in torsion to ascertain how the observed size effect varies. In this case, the positioning of the unit cell is offset by half of the cell wall spacing within the sample in the same manner of the orthogonal lattice to form a 'mixed cruciform' unit cell (Figure 5.13). The homogenised elastic constants of the unit cell are identical to those considered in the previous section, but the differences in the localised stiffness variation are apparent at sample sizes which approach that of the unit cell.

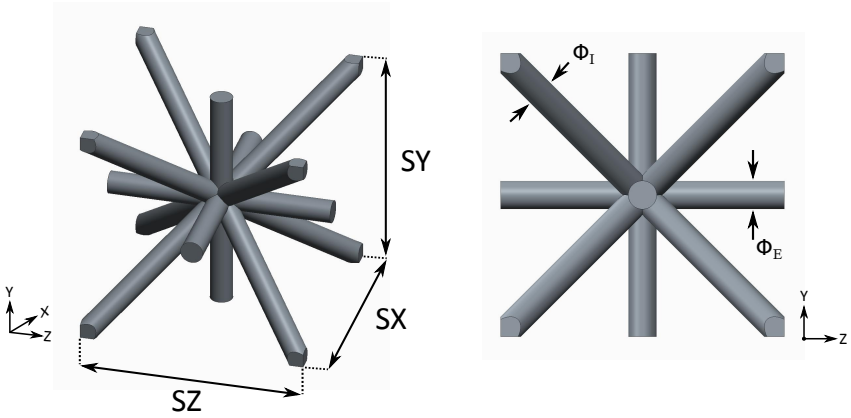

Figure 5.13: Alternate unit cell configuration of the braced cubic lattice.

Rectangular bar samples of square cross-section with differing volume fractions which were controlled by the interior and exterior beam diameters, ϕ_I and ϕ_E were tested at varying samples sizes in the same manner as before under fixed displacement boundary conditions. It

was found in general that this configuration was more compliant than the equivalent braced cubic lattice when samples were tested in torsion. However, the magnitude of the variation in rigidity is largely dependent on the diameter of the beams within the cell. When the exterior beam diameter was significantly larger than the interior beams, then the difference in rigidity was generally much larger in the case of the braced cubic cell. As the interior beam approached the diameter of the exterior beam or was larger, then a reduction in rigidity was apparent at smaller sample sizes. In this case, the unit cell configuration had less influence on the overall rigidity of the sample.

The magnitude of the characteristic length calculated here is found to be negative across all the volume fractions which were tested. In general, it can be seen that decreasing the diameter of the exterior beams within the unit cell has the effect of increasing the magnitude of the size softening effect at a given interior beam diameter. As in the case of the braced cubic unit cell, increasing the diameter of interior beams increases the magnitude of the size effect, although a reduction in stiffness is observed in this case. It also appears that the maximum reduction in relative stiffness occurs at an intermediate volume fraction which is dependent on the interior beam diameter. A summary of the magnitude of the characteristic lengths with respect to interior and exterior beam diameter can be seen in figures 5.14 and 5.15.

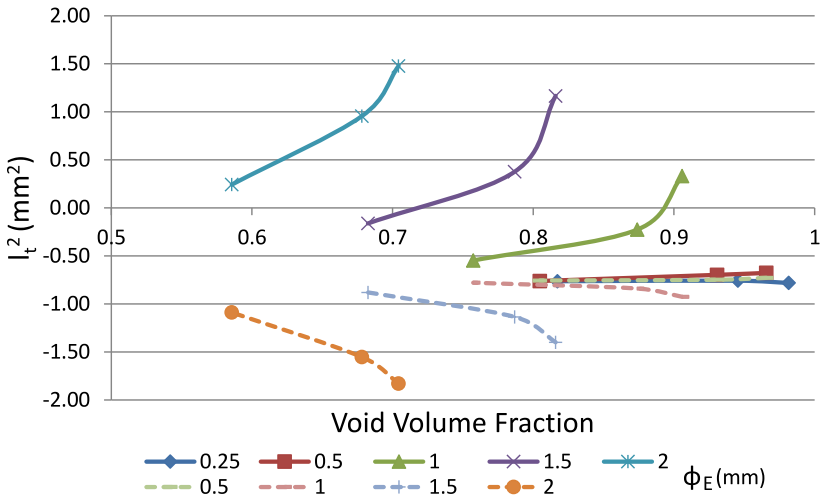

Figure 5.14: Variation in the size effect with volume fraction in torsion observed when the unit cell is intersected by the sample surface. (Denoted by broken lines.) The diameter of the exterior beams are fixed. Solid lines denote 'closed' cell samples.

While it is possible to quantify the magnitude of the size effect, there is a limit to how this can be applied to a micropolar elastic model when a reduction in stiffness with decreasing sample size is observed. It can be seen from figure 5.15 that the magnitude of the size effect for a given material generally varies in size and magnitude depending on the relative position of

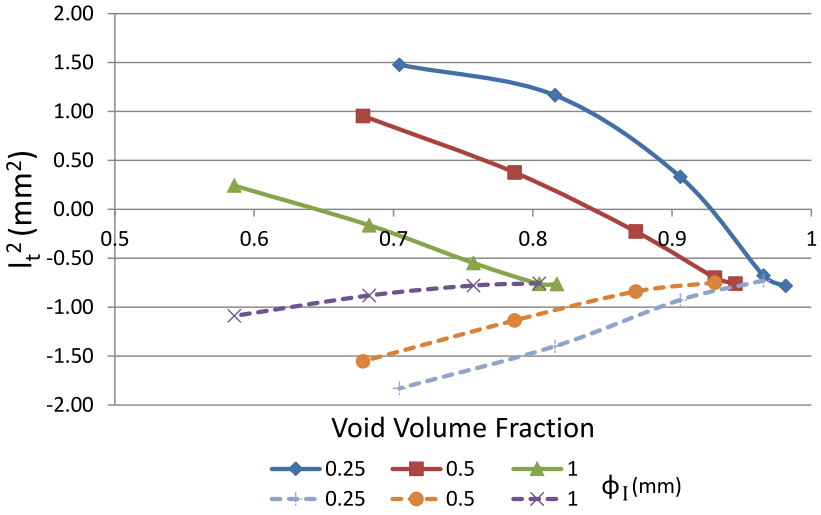

Figure 5.15: Variation in the size effect with volume fraction in torsion observed when the unit cell is intersected by the sample surface. (Denoted by broken lines.) The diameter of the interior beams are fixed. Solid lines denote 'closed' cell samples.

the unit cell within a bar sample. The data produced here can be thought of as upper and lower bounds for the likely size effects which could be obtained experimentally for a given material depending on the positioning of the unit cells within the test specimen. Interestingly however, it can be seen that size effect will converge in both cases when the interior beams are more dominant than the exterior beams in the lattice.

5.5 Beam Element Model

Modelling repetitive lattice structures with continuum elements is both time-consuming and computationally intensive. This method is generally favoured however as the key geometric features that characterise the material can be fully accounted for. However, in the case of a low density lattice with slender ligaments, the number of nodes and elements required to achieve an accurate solution can become prohibitively large. In structural analysis, beam elements are commonly used to model general beam & frame problems. Low density lattice structures can be thought of as similar to a structural frame when the interior members that form the material are slender. It is the aim of this section to investigate the applicability of using beam elements to simulate the likely response of an equivalent structural solid. The resulting size scaling effects that may be observed will be compared to the continuum models developed in the previous section.

A simplified model of the braced lattice considered in the previous section was therefore constructed which takes into account the cross-sectional area of each individual beam. Joints

were modelled as an array of nodes which connect the beams together. Each model was generated in ANSYS APDL from a parametrised script using the higher order BEAM189 elements. BEAM189 is a 3 node quadratic beam element which takes into account shear deformation effects. Each node has 3 translational and 3 rotational degrees of freedom aligned to the x,y and z axis in a standard 3D Cartesian coordinate system. Parametrising the model has the advantage that a wide range of configurations could be tested by running a batch file and incrementing the desired variables.

As was the case in the previous section, the diameters of the exterior and interior beams within the unit cell were varied in order to alter the cell volume fraction. Each bar was constructed with a square cross section to enable each sample to be readily tested in both flexure and torsion. Samples were tested at a constant aspect ratio with between 1 and 10 rows of cellular microstructure through the depth of the sample. A relatively high aspect ratio was chosen to minimise any effect that the boundary conditions may have on the deformation of the end faces under loading.

Models were tested in both flexure and torsion using the method of size effects that has been described in the previous chapters. From the simulations that were carried out, the flexural modulus, E^*, shear modulus, G^*, and characteristic lengths l_b & l_t were calculated under displacement boundary conditions.

5.5.1 Beam Element Results

From the simulations that were performed, it was observed that the flexural modulus of the beam element model closely matched that of the continuum elements when the material volume fraction was relatively low (Figure 5.16). Above a volume fraction of around 20%, the beam element model tended to underestimate the material modulus. Generally, the observed shear modulus followed a similar trend, converging with decreasing volume fraction (Figure 5.17). However, when the diameter of the interior diagonal beams is much greater than the exterior beams within the unit cell, then it can be observed that the beam element model significantly underestimates the resistance to shear in comparison to the continuum element model. This result is to be expected as the beam element models do not fully take the deformation of the material at the joints within the structure into account. At low volume fractions, the influence of this on the overall deformation of the structure is minimal due to the fact that the deformation is primarily a result of bending or twisting within the beam members. At larger volume fractions, such approximations are not appropriate.

The characteristic length in bending followed the same general trend with the beam element models as in the continuum based simulations (Figure 5.18). The magnitude of the characteristic length in this case was observed to be marginally greater in the beam element model compared to the solid model generated from continuum elements. The magnitude of the diffe-

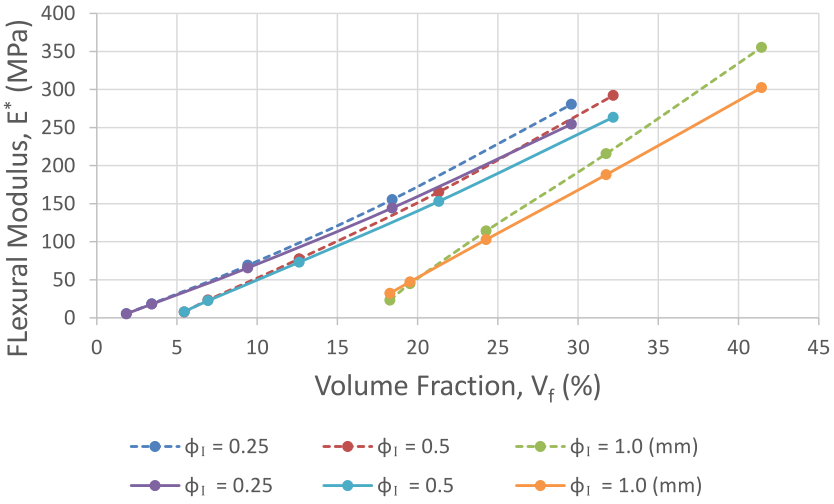

Figure 5.16: Comparison between the flexural modulus derived by beam elements and solid elements at varying volume fraction. The beam element model is represented by solid lines. Solid elements are denoted by broken lines.

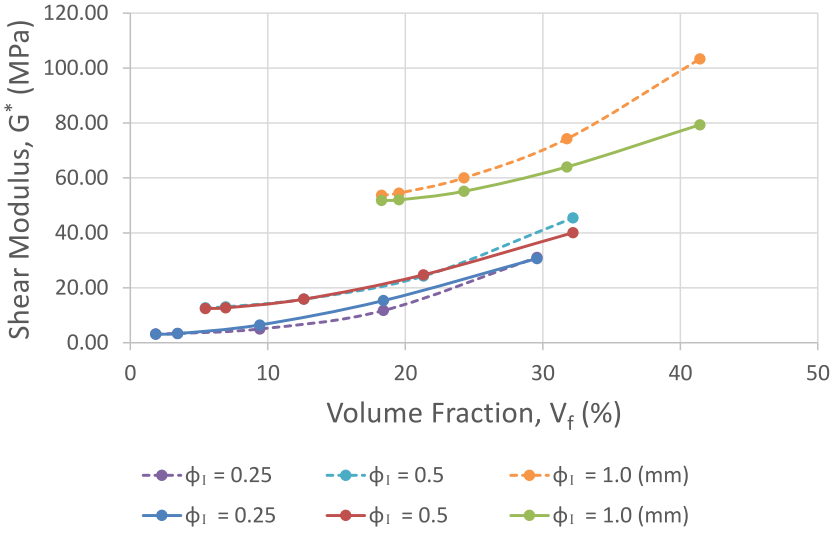

Figure 5.17: Comparison between the shear modulus derived by beam elements and solid elements at varying volume fraction. The beam element model is represented by the solid lines. Solid elements are denoted by broken lines.

rence between the results in the two models generally increases with material volume fraction which is to be expected as the beam element model does not fully account for the true response at the joints within the unit cell. By and large though, the beam element models give a reasonable measure of the size effect which may be seen in flexure.

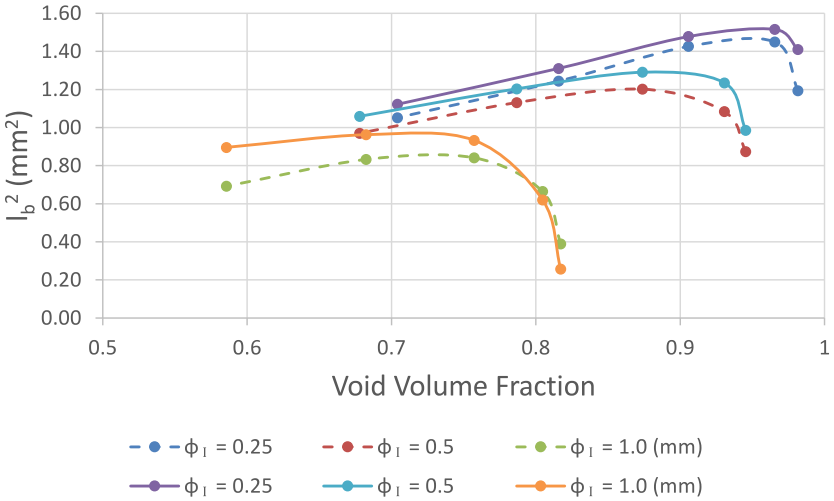

Figure 5.18: Variation in the characteristic length in bending with void volume fraction. Beam elements models are represented by the solid lines while solid elements are denoted by broken line.

In torsion, the magnitude of the size effect observed in the beam element models only matched the solid models when the exterior beams in the unit cell were slender, and the material volume fraction was less than 20 % (Figure 5.19). The variation in characteristic length with void volume fraction follows the general trend that was observed with the continuum elements, but the resulting size effect is largely overestimated. A consequence of this is that in some configurations, a size stiffening effect is predicted where a general softening is observed with decreasing specimen size in the continuum element models. When both the interior and exterior members in the unit cell are slender, the size effect is similar to that seen in the solid models.

It is therefore recommended that while beam element models can be used as an indicative measure of the likely size effects which might be observed in a lattice structure, continuum elements are much better suited to modelling the structural response particularly when the interior beams are not slender.

5.6 Summary & Conclusion

In this chapter it has been shown that lattice structures which have interior connecting beams can display size effects consistent with those predicted in micropolar elasticity. The magnitude

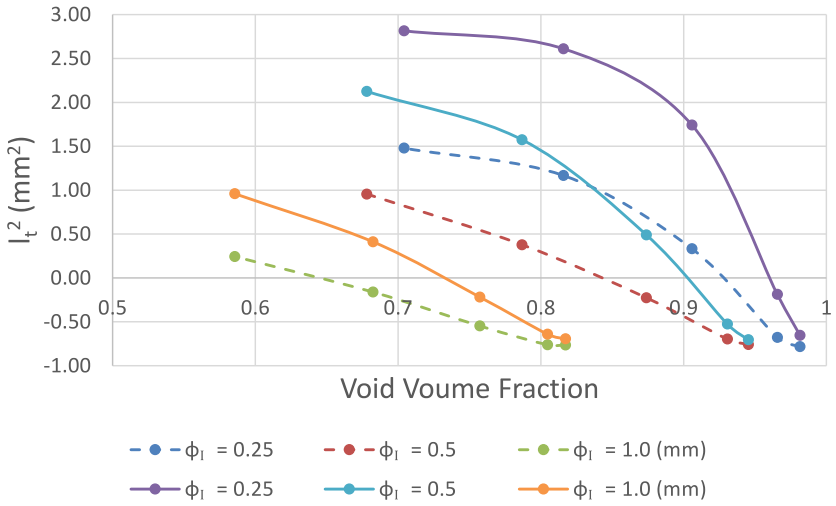

Figure 5.19: Variation in characteristic length for torsion with void volume fraction. Beam element model are represented by solid lines while solid elements are denoted by broken lines.

of the size effect is however limited by the presence of the interior beams. In bending, a size stiffening effect is always observed in the case of the cubic unit cell with internal braced members. In torsion however, the size effect is strongly dependent on the internal structural members which can lead to a size dependent softening effect for many configurations. The optimum size effect for this structure is strongly dependent on both the relative size of the exterior and interior beams and the mode of loading which it is to be optimised for.

The results of the braced cubic lattice are interesting as it indicates that it may be possible for a material to have no voids exposed at the surfaces, but still display sample softening if the internal geometry is such that it is more dominant than the stiffening effects that are related to material forming on the exterior surfaces. The occurrence of negative size scaling effects are not predicted within the micropolar continuum. It is possible that in this scenario, the interior bracing is acting similarly to a rigid inclusion within a compliant matrix.

Beam element representations of the same material have been shown to display similar size effects to those modelled with continuum elements. Care must be taken however as complex joint interactions may not be adequately described unless the cell volume fraction is reasonably low. For slender lattice structures however, beam elements offer the potential to significantly reduce the computational resources required as compared to full model generation with continuum elements.

Chapter 6

Effective Mechanical Properties of a 3D Printed Material

In the previous two chapters, the mechanical properties of three-dimensional cellular lattice structures were investigated from a series of computational FE analyses. In order to verify that the numerical analysis performed are representative of the physical behaviour of real materials, a series of experimental tests are required to be conducted. It has been identified that additive manufacturing processes offer the most likely solution to generating the complex cellular structures within the novel materials, but the suitability of the underlying solid material forming the cellular matrix requires a thorough mechanical investigation.

The contents of this chapter consists of a preliminary investigation into the applicability of using a 3D printed photopolymer as the base material to investigate size effects within lattice structures. Mechanical tests including uniaxial tensile and 3-point flexural loading were conducted to verify that the photopolymer (VeroBlackPlus by Stratasys Ltd.) was reasonably isotropic within acceptable limits. While it was observed that the material only has a weak dependence on the print direction for samples of similar size to the internal features within the proposed lattice, the material does appear to be slightly viscoelastic in nature which may need to be accounted for in the mechanical material model.

6.1 Introduction

With the recent advancements in additive manufacturing technologies it is now possible to print complex 3-dimensional structures with minimal effort. While this has many advantages in rapid prototyping objects for developmental purposes, it also offers the possibility to create specifically designed structural metamaterials with tailored microstructures that are specific to a given application.

A large variety of different additive processes currently exist which offer unique ways to create 3-dimensional objects. The biggest difference that exists between the technologies however, is the way in which the layers are formed during construction and the level of detail or resolution which is obtainable with each process. Some of the additive manufacturing processes that currently exist include extrusion, light polymerised, powder bed and powder fed based technologies.

One of the most popular extrusion based methods is fusion deposition modelling (FDM). In FDM, beads of a thermoplastic polymer material are heated up and extruded onto a build surface using a computer controlled mechanical system. As the polymer is extruded it will harden, allowing layers to be created through a systematic and repetitive process. This manufacturing method is applicable for a wide range of common polymers including acrylonitrile butadiene styrene (ABS), polycarbonate (PC) and high-density polyethylene (HDPE). The main disadvantage however is that the objects generated are limited in structural complexity due to the fact that the process does not readily support overhangs meaning that only simple extruded voids can be created. More complicated shapes are now supported with this method by implementing removable support structures within the build process, but this does not translate well into the design of heterogeneous solids.

Powder-fed deposition is based on passing granular metal particles through a nozzle which are melted with a high-powered laser before being deposited on the print surface. This process works similarly to an ink-jet printer, depositing material axially along the x-axis before being incremented in the y and z plane to construct the desired object. A wide range of different metals can be utilised with this approach including aluminium, titanium and stainless steel. As well as creating new objects, powder-fed deposition also has the advantage of being able to add to existing materials if required. Again this process does not readily support the inclusion of overhangs and internal voids due to the lack of supporting material.

Powder-bed based methods are available for both polymer and metal object creation. In this process, a laser is typically used to selectively sinter or melt granular particles of material that are contained within a working area. Once a cross-section of the object to be formed is created, the supporting print bed is lowered so that another layer of particles can be added to the part. As a constant volume of granular particles are held within the working area, voids and overhangs

can be manufactured by using the unsintered particles to support the newly solidified material. Closed cell structures are not supported with this method however, due to the fact that there is no mechanism to remove the unwanted particles without the inclusion of drainage holes.

Polymerisation involves the use of an ultraviolet light source to transform liquid polymer resin into a solid state material. The two main approaches to deposition modelling using photopolymer materials involve either stereolithography and digital light processing (DLP) or ink-jet based techniques in the construction of solid parts. In the case of stereolithography, the model to be constructed is sliced into a series of very thin horizontal layers using 3D modelling software. Each layer is formed by projecting and simultaneously curing each cross-section onto the surface of a vat of photopolymer resin. By either lowering or raising the print bed from the surface of the resin, additional layers can be added until the model is generated. In printers whereby the base plate is incremented down into the vat of liquid, the user is restricted to constructing open cellular structures as any uncured resin must be free to drain away from the object after completion. The alternative method to the conventional stereolithography technique is to use an inverse setup whereby the created object is lifted from the surface of the resin. In this case, light is projected through the bottom of the liquid resin and focused at the top surface. Layers are formed by dipping the bottom surface into the resin and curing the bottom surface before incrementing the platform upwards. Unlike in the previous set-up, there is the potential to create closed cell structures as the part is being continuously lifted out of the liquid resin. One limitation of this method which would need to be overcome however is that some liquid is drawn into and subsequently trapped in the internal void due to the capillary action of the liquid.

More recently a form of DLP printing has been introduced by Carbon Technologies which claims to be able to produce parts through a continuous process that is not commonly available with other current technologies. The continuous liquid interface production (CLIP) process revolves around a “dead zone” of uncured resin which is created between the light window and the part being constructed. As resin flows beneath the part during printing, a continuous interface of liquid is maintained throughout the build. It is claimed by the manufacturer that this process leads to near isotropic material properties within the cured resin that are not seen in traditional techniques which have more pronounced layers due to the fact that the model is cured in distinct layers. With this process however thermal curing is required after model generation to maximise the overall mechanical properties of the part.

The final method of digital printing that will be discussed is the ink-jet style systems. In this process, uncured resin is sprayed onto the print bed while being simultaneously cured with ultraviolet (UV) light. The part is constructed by translating the jet in the x-axis, then subsequently incrementing in the y and z axis respectively to build up a series of cross-sectional layers. One advantage of this technique is that multiple jets can be used in order to create an

object which has an array of different colours or material properties. A filler material can also be implemented within one of the jets which can be used as a removable support material that allows for the creation of complex shapes. Another benefit of this printing process is that fully closed cell structures can be generated with the use of a support material. The downside however is that the support material cannot be removed, and will therefore have to be incorporated within the design of the metamaterial.

6.2 Additive Manufacturing Printing Process

While all the above technologies offer novel ways of constructing metamaterials with tailored macroscopic mechanical properties, one question that needs to be addressed however is how the manufacturing process influences the overall material properties of the structure. In particular, the influence of the print direction on material stiffness has to be investigated to determine if there is any directional dependence on the mechanical properties of the system.

Tailored heterogeneous materials have the potential to offer improved mechanical properties as compared to their homogeneous counterparts through an increase in stiffness and reduction in relative weight. One key requirement when generating such materials is that they should have consistent and predictable properties which are not influenced by the manufacturing process. It has been shown in the previous sections that tailored heterogeneous materials can be created which display novel material characteristics under simulated numerical test conditions. In order to verify that the simulations are representative of actual conditions, a series of experiments need to be performed on physical samples of the material. To minimise the influence of external factors within the experimentation, the underlying solid material which is used to generate the macroscopic material microstructure must behave in a consistent and reliable fashion. Ideally a linear elastic, isotropic solid would be preferable for this application. The rational behind this section is to determine if there is any significant directional dependence on the tensile and flexural modulus of samples printed in a typical 3D printer.

The 3D printer chosen to manufacture the test samples was an Objet Eden350v rapid prototyping machine from Stratasys Ltd. The Objet Eden350 printer is a high end professional 3D printer which is capable of printing complex geometric shapes. It is an ink-jet style printer that uses liquid photopolymer and UV light to spray and solidify the material in a repetitive layering process. Complex features including voided structures are possible with the use of a soluble support material. The printer has a maximum build size of $342 \times 342 \times 200$ mm and is accurate to between 20-85 microns for features up to 50 mm in size. Larger models are accurate to 200 microns.

The printing process is based on the PolyJet technology that has been developed by Stratasys Ltd. (2017) and works by spraying a heated liquid photo-polymer onto the surface of

the printer bed that is cured with UV light. Photopolymers are classified in the same category as thermosetting plastics in that they generally stay permanently set once cured. The curing process involves exposing the liquid resin to an ultraviolet light source which causes the material to rapidly solidify. The print head consists of an array of 8 nozzles which deposit the photopolymer systematically. It moves parallel to the print bed surface, travelling left to right on the x-axis. The print head then increments itself in the y-axis and repeats this process in order to create one cross-sectional layer of the object. It is then incrementally raised in the out of plane z-axis before repeating the process until the desired object has been fully constructed. A diagram of the general print process can be seen in figure 6.1. Where overhangs exist in the model, a soluble rubber like filler material is injected onto the surface which acts as a support for the subsequent layers. After construction, this material can be readily removed with a water jet or dissolved in a solvent.

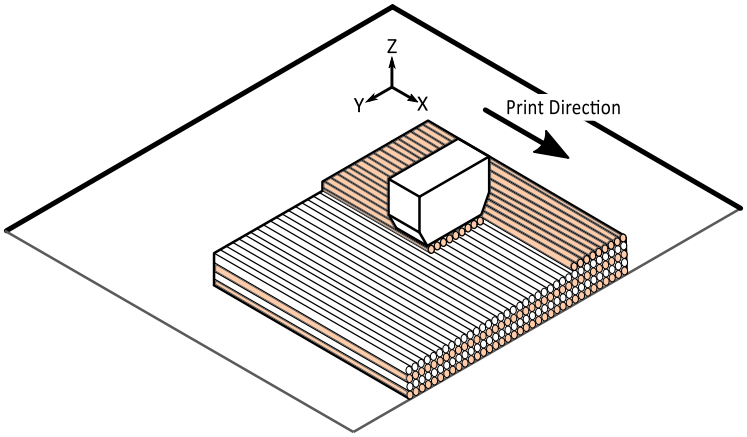

Figure 6.1: Print head injection process. A fine layer of the liquid polymer is sprayed onto the top surface before being cured with UV light.

As the printing process is directional, it is possible that there will be some variation in the material properties of the constructed objects depending on their orientation within the printer during the build phase. It is desirable that the solid material (printed photopolymer) is reasonably isotropic to minimise any additional material parameters which may influence the observed mechanical properties of the heterogeneous metamaterial. The orientation of the samples within the printer may also be a contributing factor to the overall mechanical properties of the generated parts. Figure 6.2 is an example of the different ways in which the parts can be printed. Here, each sample is aligned parallel to either the x, y or z major axis which determines how the layers within the specimen are orientated.

Figure 6.3 demonstrates how the orientation of the sample within the printer affects the direction of the layers that are built up within the part. Samples orientated in the x-axis consist

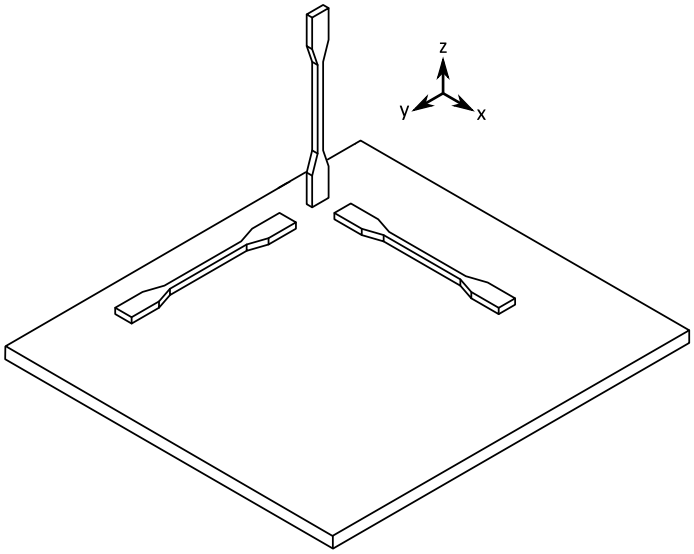

Figure 6.2: Possible orientation of the samples within the printer. Samples have been aligned to either the x, y or z axis.

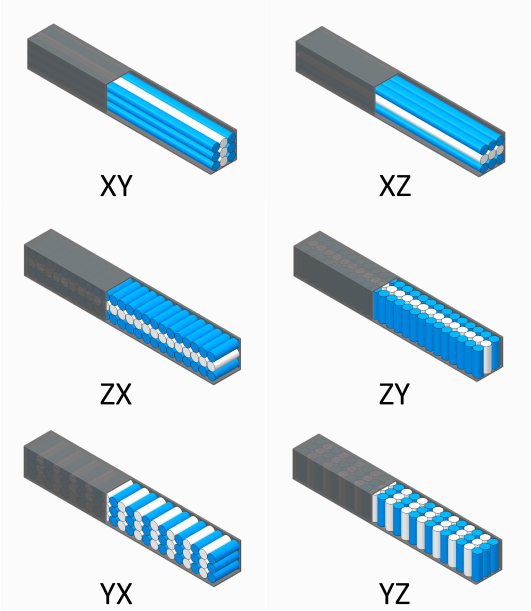

Figure 6.3: Orientation of the layers within a printed sample with respect to the placement within the printer. Alternating blue and white cylinders denote incrementation in the y-axis. Each sample can be orientated in two different ways after production.

of long strands of material extruded axially within the sample. Aligning the samples in the y-axis has the effect of reducing the length of the fibres within the part and increasing the number of rows of material required to generate the sample. In this orientation, the polymer is deposited along the length of the beam before building up the next layer. When the samples are orientated in the z-axis, the beam sample is constructed in this case by building up layers of the cross-section. Again the printed layers of polymer will be short as in the case of the y-orientated samples, but the number of overall layers in the sample will also increase significantly.

6.3 Polymer Material Characteristics

In order to investigate how the print orientation affected the mechanical characteristics of the polymer sample, it was proposed that a series of experiments should be performed in order to determine the tensile and flexural stiffness of the solid material. The photopolymer chosen as the base material was VeroBlack Plus (RGD875). It is a rigid material with a quoted modulus of elasticity and flexural modulus of between 2000-3000 MPa and 2200-3200 MPa respectively.

One of the main considerations which needed to be addressed when testing structures constructed from a systematic layering process is whether there are any anisotropic effects introduced in the material due to the directional nature of the build process. A similar investigation was carried out by Mueller et al. (2015) that focussed on determining the mechanical properties of the photopolymer VeroWhite Plus (RGD835). The mechanical properties listed by the manufacturer are identical for RGD875 and RGD835, with the exception being that RGD835 has a greater ash content. ($\approx 0.26\%$ compared with $\approx 0.02\%$ in VeroBlack Plus.) Here, samples were manufactured in a Stratasys OBJET500 Connex3 3D printer to the ASTM D638-10 standard.

It was reported that samples which were oriented longitudinally in the z-axis (out of plane from printing surface) had measurably lower material properties as compared to those aligned to the X and Y axis, which can be attributed to an increased number of layers within the sample and therefore more intersections will be formed within the sample. It was concluded that the weakening effect of increasing the number of internal layers must be more dominant than any added benefit that might be gained from an increased UV exposure due to the additional build time required in this orientation. It was also suggested that the material may be over cured due to the increased build time, but this was not verified in the experimentation. The mean modulus of elasticity that was recorded for samples oriented in the X and Y axis was 2918 MPa. The modulus of samples aligned in the Z axis was found to be 2686 MPa.

6.4 Tensile Testing of a 3D Printed Photopolymer

6.4.1 Experimental Setup

The proposed lattice structure that was to be ultimately tested consists of an array of orthogonal bars (Figure 4.1) with cell walls between 1 and 2 mm thick. Within the sample, the internal beams are oriented in the 3 major axes that align to the machine print direction. To verify that the mechanical properties of VeroBlack Plus were consistent at this scale, tensile dumbbell samples were manufactured to determine the material properties with respect to print direction. Three different samples were manufactured with the major axis of the samples aligned to the X, Y and Z axis of the printer respectively (In the same manner as figure 6.2). In order to account for any localised variations in the test specimens, 3 copies of each tensile specimen were produced. The final design of the dumbbell shaped test specimen can be seen in figure 6.4. The reduced section is 30 mm in length with a square cross-section measuring 2.5 mm $\times$ 2.5 mm. The thickness of the section was chosen as it was comparable in size to the geometry of the internal members within the proposed metamaterial. The total spacing between the shoulders is 40 mm. The maximum width of the tensile sample at the grip section was 5 mm. For continuity, the spacing of the grips within the machine were also held constant at 45 mm. The full tensile sample specifications and positioning within the machine are summarised in table 6.1.

Total Length	L_0	60	mm
Total Width	W_0	10	mm
Thickness	T_0	2.5	mm
Transition		5	mm
Transition Radius	R	10.6	mm
Length of Reduced Section	L_g	30	mm
Reduced Section Thickness	T_g	2.5	mm
Grip Spacing		45	mm

Table 6.1: Tensile test specimen geometry.

The length to depth aspect ratio of the straight section in the dumbbell sample was 12. The advantage of creating a specimen with a slender centre section is that it meant it could also be used to determine the flexural stiffness of the material in a subsequent test. A square cross section was also chosen for the samples as it meant that only half the number of test specimens were needed to fully evaluate the material.

The specimens were tested in a Bose Electroforce 3200 mechanical testing machine under displacement control. The apparatus consisted of a 450 N load cell with grip attachments connected to a fixed support and a linear actuator motor which was used to impart a displacement

on the test specimen.

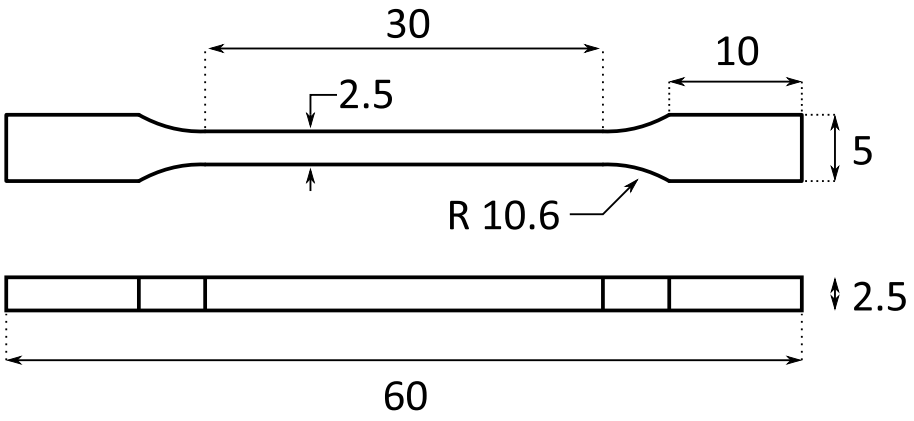

Figure 6.4: Tensile test specimen (All units are in mm.).

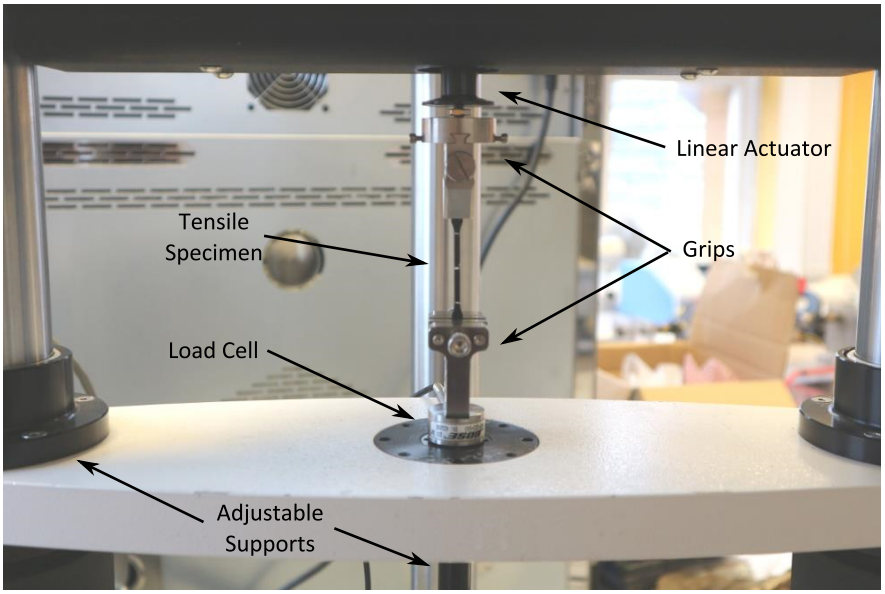

Figure 6.5: Tensile test experimental setup.

The experimental procedure was performed as follows: Each sample was inserted vertically into the machine by first clamping the specimen to the grip attached to the linear actuator. Once it was verified that the actuator was zeroed in position, the lower grip was then adjusted until it was in line with the bottom of the sample before being clamped in place. By following this procedure, it helped to minimise any initial stress being applied to the specimen before the start of the test. The final step before running the test sequence was to turn on the machine and zero the instrumentation. To ensure that the positioning of each sample was secure and consistent, specimens were marked 7.5 mm from the end of the specimen prior to insertion. A diagram of

the test setup can be seen in figure 6.5. In total, a 2.5 mm gap was left between the end of the grips and the transition shoulder to minimise any localised stresses which may influence the test. A typical set of tensile test specimens is show in figure 6.6.

Each test was performed by extending the sample to a fixed displacement at a given rate. In order to quantify the level of viscoelasticity that may be observed within the sample, each sample was then held in place at the maximum displacement for 30 seconds and the stress relaxation rate was measured. The sample was then unloaded at the same rate as it was loaded, returning it to its original state. The test was repeated for each sample and the resulting material modulus was calculated from the linear portion of the stress-strain plot.

Prior to undertaking any tests, the machine was tuned using the in built software in order to calibrate the equipment to the approximate stiffness of the samples. This was an important step as it allowed the machine to calculate the correct voltage to apply in order to displace the linear actuator appropriately. Failure to do this can result in damage to the specimen or system.

Figure 6.6: A selection of the tensile test specimens printed at different orientations within the printer. The outer white markings denote the positioning of the grips on the sample.

Due to a lack of strain gauges or extensometer at the time of testing, measurements were recorded from the absolute displacement of the machine actuator within the testing apparatus. As the quoted modulus of the photopolymer was relatively small in comparison to the components within the tensile testing machine, it was assumed that any external movements would be negligible by comparison to that of the sample. One thing however which cannot be accounted for in this test, is the variation in localised strain that will occur between the gauge section and the clamping location. Finite element analysis of a test specimen consisting of a linear elastic, isotropic material subjected to a constant strain loading indicates that the shoulder transition for this sample has a non-negligible amount of strain across this section and therefore must be included in the calculation. Taking the grip spacing as the gauge length overestimates the

modulus, while using the centre section underestimates it. Closer inspection of the results indicates that the average local strain across the shoulder region is approximately the same as the central section which goes some way to explaining why this section should be included in the overall analysis.

A closer approximation to the true modulus of the material was made by dividing the sample into regions with a common cross-section to model the samples as a set of springs in series. The change in cross-section over the transition shoulder region was estimated by the average cross-section across the length of the transition.

The maximum deflection and resulting Young's Modulus can be estimated as follows:

$$\begin{aligned} w_{mx} = \sum_{1..n} w_n &= \frac{P}{E_s} \sum_{1..n} \left(\frac{L_n}{A_n} \right) \\ &= \left(\frac{P}{E_s} \right) \left(\frac{L_1}{A_1} + \frac{2L_2}{A_2} + \frac{2L_3}{A_3} \right) \end{aligned} \tag{6.1}$$

$$\Rightarrow E_s = \frac{P}{w_{mx}} \left(\frac{L_1}{A_1} + \frac{2L_2}{A_2} + \frac{2L_3}{A_3} \right) \tag{6.2}$$

Where L_1,L_2,L_3 and their corresponding areas, A_n are in this case the length of the reduced section, the shoulder and the grip sections not restrained by the clamp respectively. For the samples that have been manufactured, the material modulus can be expressed as:

$$E_s = 6.40537 \left(\frac{P}{w} \right) \tag{6.3}$$

where P/w is the gradient of the load-displacement curve that is observed experimentally.

A static analysis performed in ANSYS on a geometrically identical tensile specimen correlates well with this estimation and is within 1.2% of the modulus of the sample. It is therefore very likely that the conducted experiment is underestimating the actual modulus of the material and should be corrected using equation 6.3.

That being said as the results cannot be definitively verified, it has therefore been proposed that the quoted modulus will be given within a range that accounts for the variation in gauge length which may be present within this experiment. While this will ultimately not give a definitive answer to the material modulus, it will allow for a comparative analysis to be performed between the samples. Tests will also be undertaken later to determine the flexural modulus which will help to further identify the elastic properties of the samples.

The ASTM standard test method for tensile testing of plastics D638-10 (ASTM International, 2014) states that the speed of testing for a sample of this size should be tested at the

lowest possible speed that will cause rupture between 0.5 - 5 minutes of testing. The tensile strength of VeroBlack Plus is stated as 50-65 MPa by the manufacturer, which suggests that a rate of 1 mm/min would be appropriate for the test. It was desired however that this test should be non-destructive and only induce a small strain on the sample, so several loading rates were tested to determine the minimum speed which produced consistent results. The samples were initially loaded at rates which varied from between 5×10^{-3} mms^{-1} and 4×10^{-2} mms^{-1} to a displacement between 0.1 and 0.2 mm. It was observed that the initial gradient of the load deflection curve was sensitive to the applied displacement rate. From the initial test, it was apparent that in tension, the sample behaves in a viscoelastic fashion, with the observed stiffness of the sample decreasing with time. Further to this, as the rate of loading decreases, it is apparent that the overall response is significantly non-linear which can be seen in figure 6.7. While all cases produced an initial linear response, the gradient was observed to decrease with

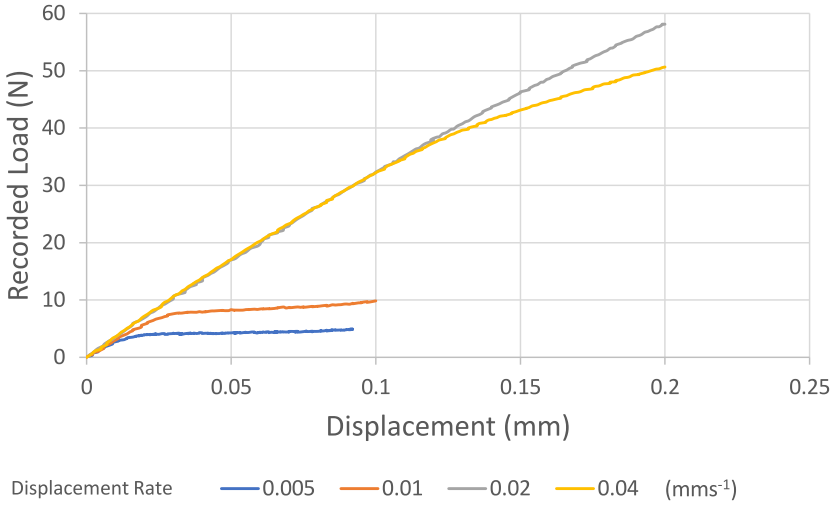

Figure 6.7: Comparison of the typical response of the material subjected to different rates of loading for samples printed in the x orientation.

a reduction in loading rate. It was decided that two different loading rates would be used to determine the response of the samples. The two different test speeds applied were 1.2 mm/min and 2.4 mm/min which corresponded to 0.02 mm/s and 0.04 mm/s respectively. It can be seen in figure 6.7 that both rates have a very similar initial response which suggests that the rate of loading is sufficiently fast to capture the linear elastic response of the polymer.

6.4.2 Tensile Test Results

Once the data for each test was collated, a plot of the applied force against the resulting displacement was generated to obtain the tangent modulus of the material. It was felt that calculating

the tangent modulus of the material with respect to time was more appropriate in this experiment as a noticeable amount of viscoelasticity was measured in the initial tests. The gauge length that was assumed for all samples was 30 mm, which equalled the length of the reduced section within the sample. The calculated area from which the load was acting on was also derived from the cross-section of the reduced section of the test specimen. A typical set of results can be seen in figures 6.8 & 6.9. Here, it can be clearly seen that each sample behaves similarly when it is initially loaded or unloaded during the test. Some variation is observed to occur between the samples as the total applied load increases. The plots shown in figures 6.8 & 6.9 are for the samples which were printed with the sample orientated longitudinally in the Y axis of the printer. A large variation in the total recorded load is seen in these samples which are generally not observed in the other two sets of samples. While this indicates that there might be some variation between sample quality or the accuracy of the experimental set-up, it will be shown below that the initial tangent modulus appears to be very consistent and in-line with that recorded in the samples printed in the other orientations. In all experiments it was observed that significant stress relaxation occurs when the samples are held at a fixed displacement which highlights the need for testing at an appropriate strain rate.

The stress relaxation that was observed in this material when it was held at a constant strain appeared to be pretty consistent between tests. It can be observed in figure 6.9 that after holding the sample at a fixed displacement for 30 seconds that there is very little change in the reaction force acting on the load cell which suggests that the sample has reached a steady state. After the sample was released, it can be seen that the force being applied to the system does not completely disappear. The resulting force applied to the system is observed to be negative which shows that the sample has undergone some permanent or semi-permanent deformation. The hysteresis loop that is seen in figure 6.8 represents the strain energy that is lost in the system.

A summary of all the tensile experiments that have been carried out is shown in figures 6.10 - 6.12. In each graph, a comparison between the calculated tangent modulus at half second intervals is shown. It can be observed that the maximum tangent tensile modulus is around about 1750 MPa. This is fairly consistent irrespective of print direction, but there does appear to be some variation between the samples that have been printed in each set. The samples printed in the X orientation appear to have performed the most consistently throughout the testing process. It should be noted that sample Xs1 is not recorded in the 0.04 mms^{-1} experiment due to being damaged by the testing machine.

From the experiments, one of the Y samples does appear to display a marked decrease in stiffness with respect to time in comparison to the others during the loading phase. This marked response is not observed when the sample is unloaded however which suggests that initial modulus which is derived is representative of the material. Overall however, it can be

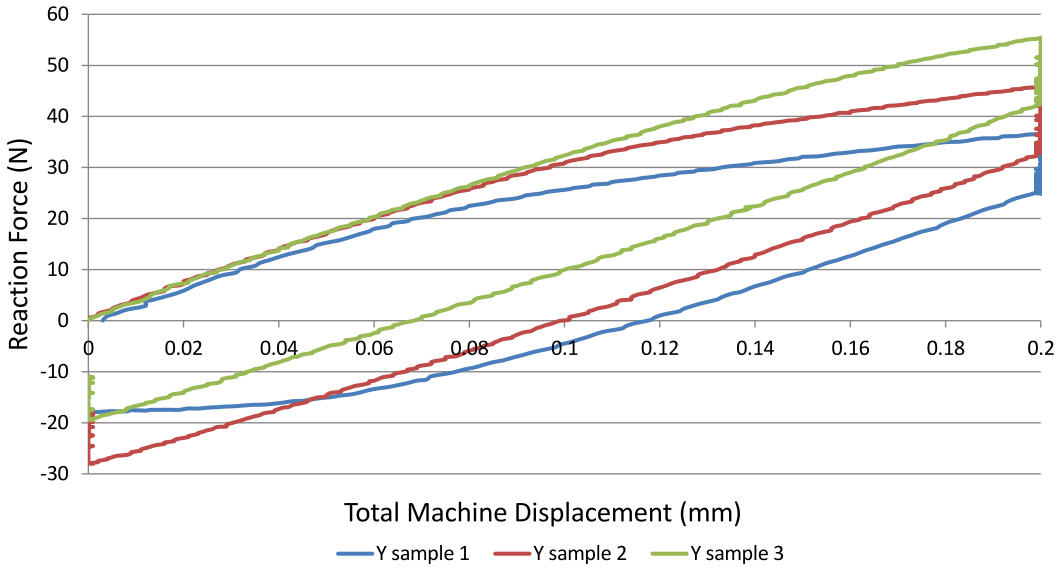

Figure 6.8: Variation in load with displacement for a typical set of tensile test specimens.

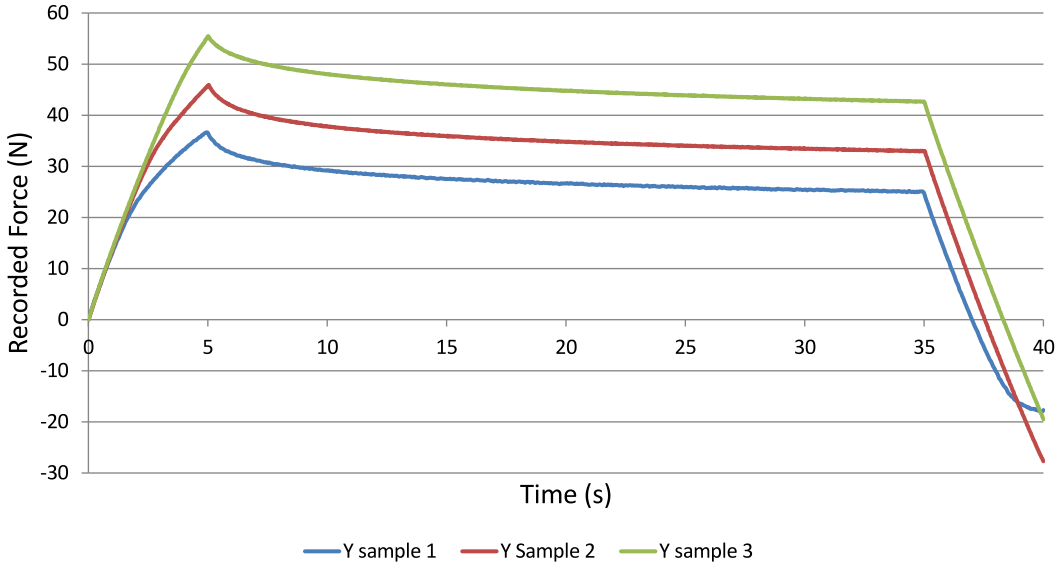

Figure 6.9: Variation in load with time for a typical set of tensile test specimens.

seen that the calculated modulus is reasonably stable when tested at 0.02 mms^{-1} or above.

Generally speaking, it can be seen that the material appears to be reasonably independent of the orientation within the printer. The most influential factor on the observed tensile modulus appears to be the time dependant nature of the polymer which is quite significant in tension. The modulus obtained here is marginally smaller than the tensile modulus which is quoted by the manufacture (2000-3000 MPa). By taking into account the variation in sample cross-section through the specimen in equation 6.2 it can be estimated to be approximately 2335 MPa which falls within the quoted material specification. It has therefore been decided that the flexural properties of the polymer should also be investigated before performing any tests on a printed heterogeneous structure to give a clearer understanding of the polymer properties.

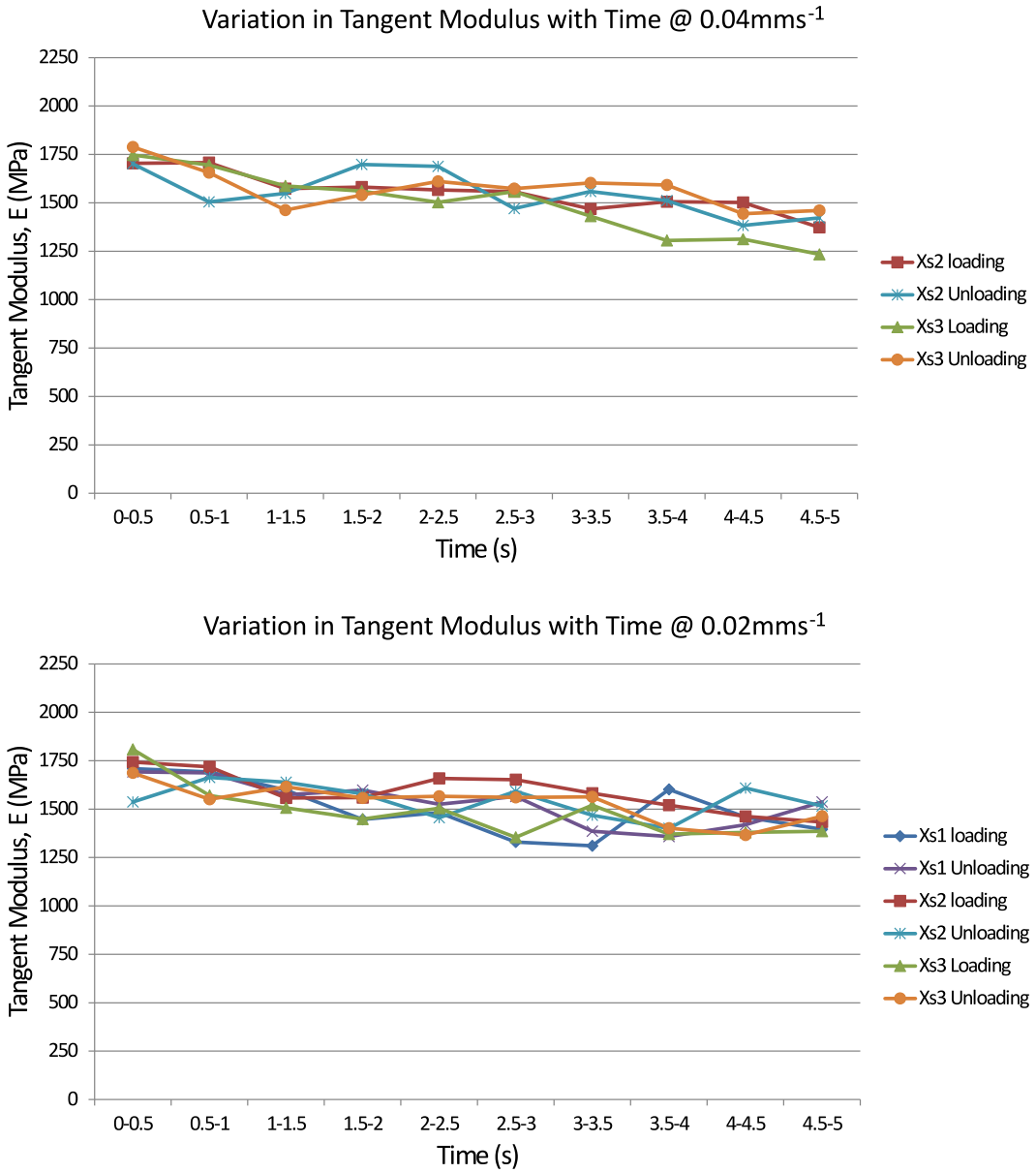

Figure 6.10: Variation in observed tangent modulus with time for samples that are aligned to the x-axis during manufacturing.

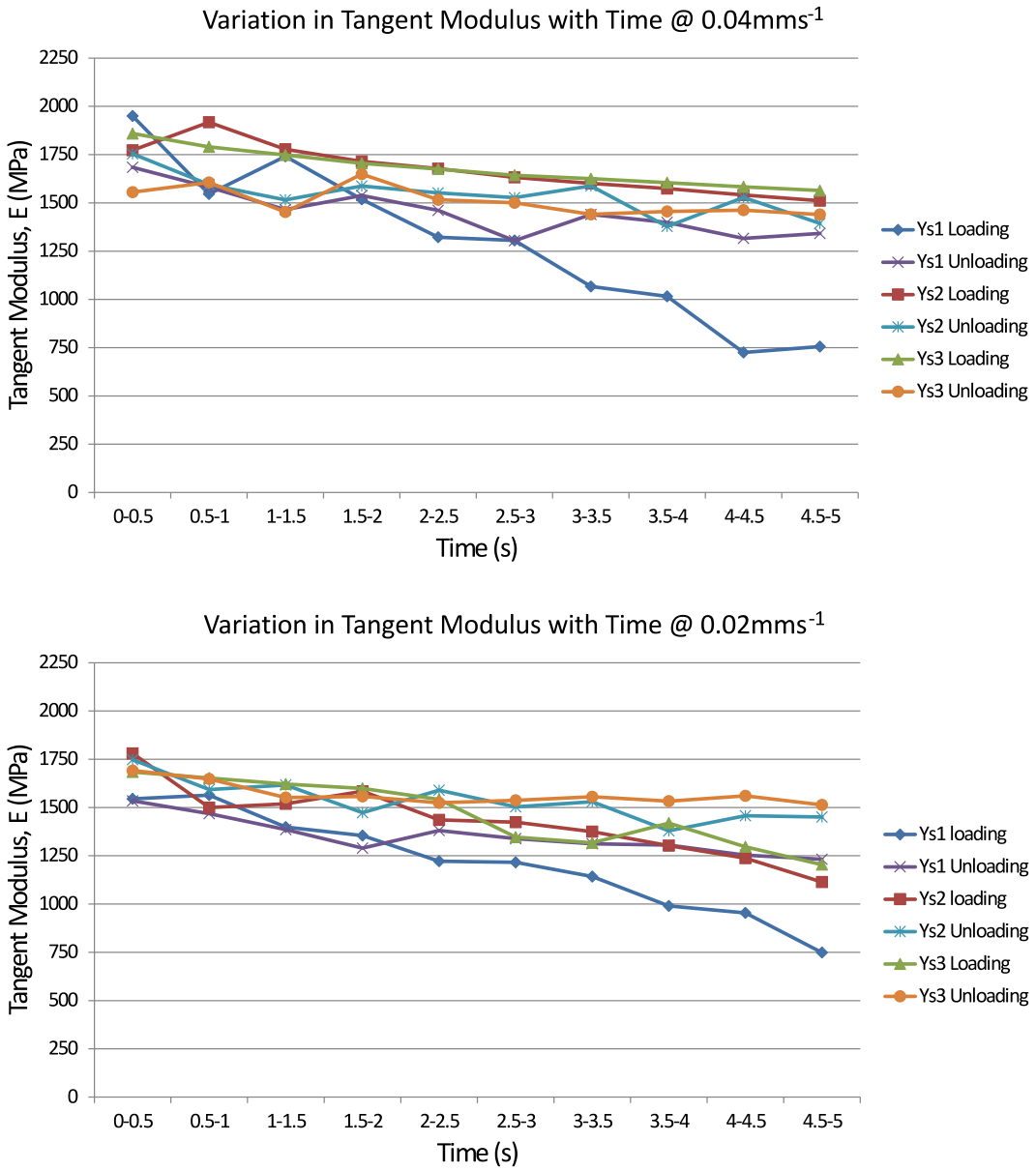

Figure 6.11: Variation in observed tangent modulus with time for samples that are aligned to the y-axis during manufacturing.

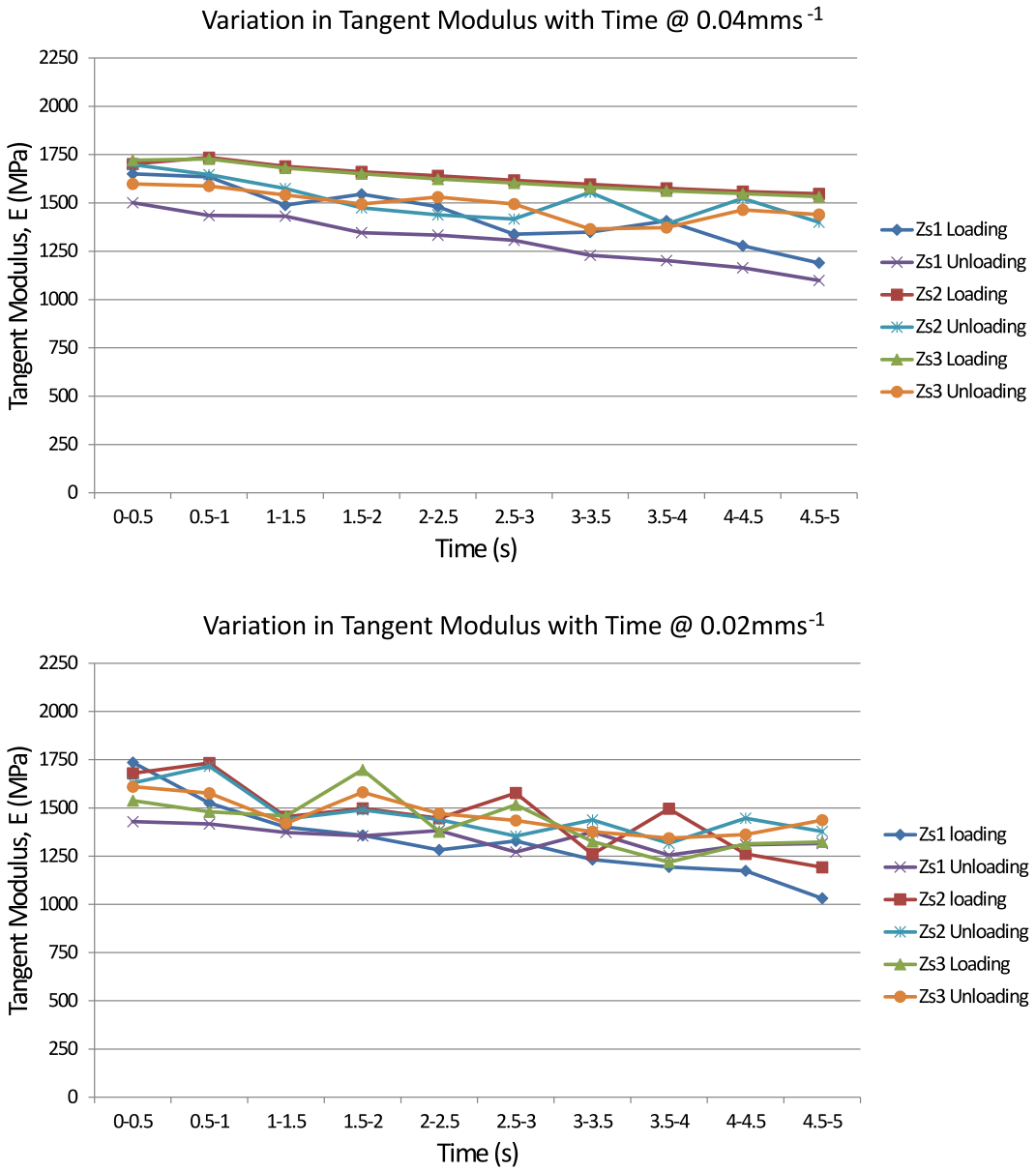

Figure 6.12: Variation in observed tangent modulus with time for samples that are aligned to the z-axis during manufacturing.

6.5 3-Point Bending of Vero Black Samples

It was shown in the previous section that the observed tensile modulus of the samples printed from VeroBlack Plus was relatively independent of the specimen print direction. The results however were at the lower end of the manufacturer's quoted specification. A second set of experiments will therefore be conducted from 3-point flexural tests to determine if the mode of loading has any influence on the stiffness of VeroBlack Plus. Flexural loading of the polymer samples is an important step in characterising its mechanical properties as unlike in the tensile test each sample can be orientated in two separate directions which may be influenced by the manufacturing process.

6.5.1 Experimental Setup

All tests were performed at a room temperature of approximately $20°C$, which was thermostatically controlled by an air conditioning unit within the laboratory. While the tensile modulus of the samples printed with the VeroBlack Plus polymer showed that the samples behaved relatively similarly to each other in the X and Y orientation, some loss in stiffness was observed in the samples printed in the Z axis. To further investigate the material behaviour, flexural tests were undertaken on samples with a cross-section of 2.5×2.5 mm to identify how the experimental flexural stiffness was in comparison. The samples used were identical to those seen in figures 6.4 & 6.6.

The reduced section of the dumbbell samples had a square cross-section of 2.5×2.5 mm and a total length of 30 mm, giving the beam a total length to depth aspect ratio of 12. It was proposed that each sample should be tested in two perpendicular directions as demonstrated in figure 6.13. Position 'A' in this diagram denotes samples which are aligned with the tabs orientated vertically while samples that are given the suffix 'B' are rotated by 90 degrees. The purpose of doing this was to determine whether the orientation of the layers built up within the polymer sample has any significant influence on the observed flexural modulus.

The tests were performed on the Bose Electroforce 3200 linear testing machine with a 450 N load cell. The test set-up consisted of a load cell that was attached to the linear actuator with an extended loading arm. The specimen was centred on an adjustable bar with reaction support pins with a radius of 1.3 mm. The dimensions of the bar were such that it was several orders of magnitude stiffer than the samples to be tested. The loading pin that was attached to the linear actuator also had a radius of 1.3 mm. A diagram of the apparatus is shown in figure 6.14. Data was collected at a rate of 20 Hz, giving a total of 200 data points for both the loading and unloading portion of the experiment.

Each sample was measured and marked at the loading points prior to testing. The test was performed by positioning a sample onto the reaction supports, and adjusting the centre support

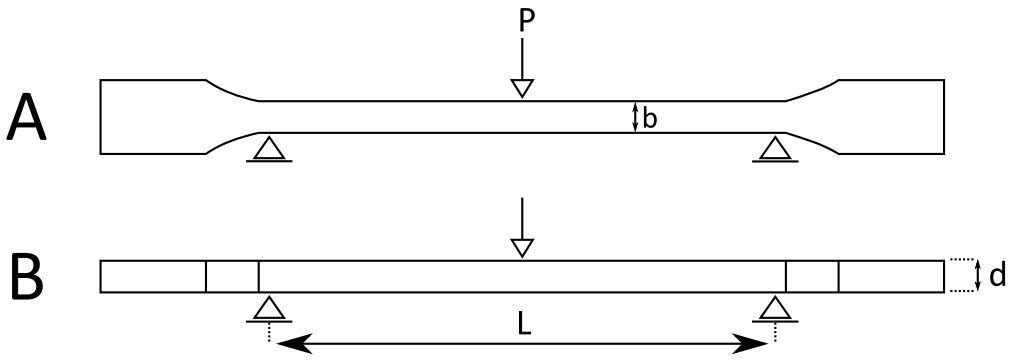

Figure 6.13: Possible dumbbell sample orientations within the testing apparatus.

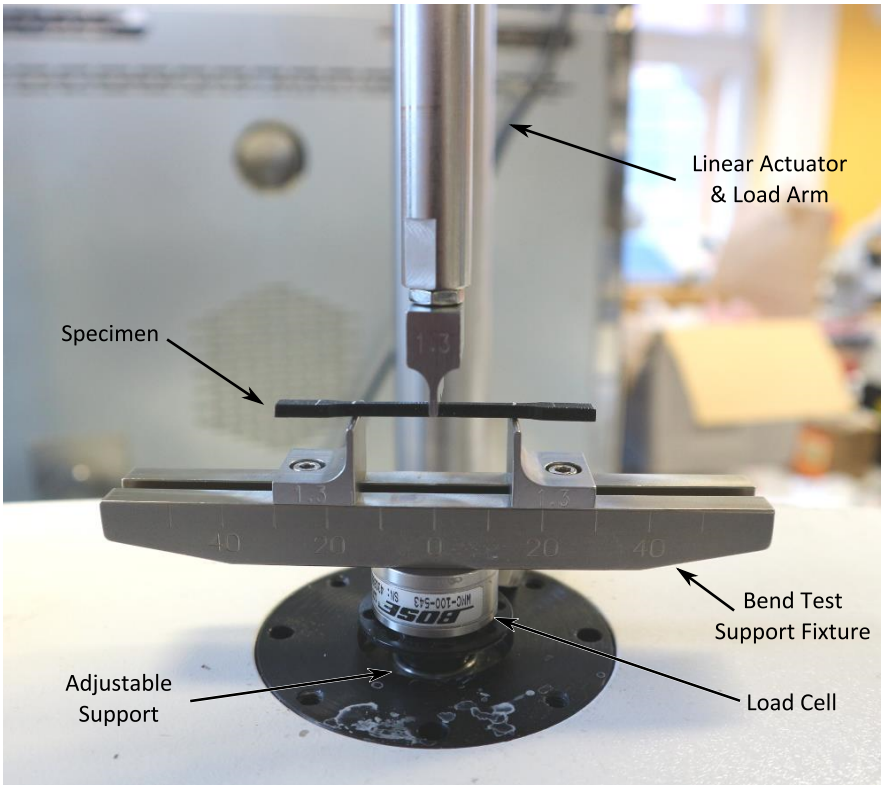

Figure 6.14: 3-point bending setup of small specimen samples.

column until the top surface of the specimen was just touching the loading arm. Once the sample was lined up and the apparatus tightened, the load cell and linear actuator were zeroed prior to running the test.

Samples were deflected to approximately 0.5 mm at a rate of 0.05 mms^{-1} under displacement control conditions. As the material is more compliant when tested in flexure than in tension, a larger deflection was required to be applied to the sample in order to produce a response that could be accurately recorded on the load cell. A deflection of 0.5 mm was therefore chosen as it was substantially smaller than the depth of the beam samples and is predicted to give a response in the region of 5-10 N at maximum displacement.

After the initial loading phase, each sample was held in place for 30 seconds before being released at -0.05 mms^{-1}. While holding the sample at a fixed displacement was not necessary to determine the elastic properties of the material, it is helpful to give a good indication as to the viscoelastic response under flexure.

6.5.2 3-Point Flexural Test Results

Initial tests showed that under flexure, the response of the samples was linear. A typical load deflection curve is shown in figure 6.15. Some viscoelastic response was apparent under load, but overall the influence was minimal in comparison to the tensile tests. Stress relaxation within the sample induces some hysteresis when the specimen is held at a constant deflection, but it does not adversely impact the gradient of the slope when the load is removed. As the tests were performed under displacement control conditions, the non-linearities in the experiment are manifested in the response of the load cell due to the change in displacement. This can be clearly seen in figure 6.16. Some minor fluctuations can be observed in the recorded results due to noise within the system, but as the test was carried out with a fairly high data sample rate and it did not unduly influence the gradient of the response curve then it was deemed sufficient to avoid performing any further filtering during or post experiment.

Overall, the response of the samples was reasonably consistent when loaded in flexure. The flexural modulus was recorded from the linear region of both the loading and unloading portion of the test for each sample in each of the possible orientations. The flexural modulus that was observed was generally in the range of 2000-2500 MPa. The most consistent samples were those orientated along the X-axis of the printer. From figure 6.17, it can be seen that the flexural modulus varies from around 2100-2400 MPa. By comparison, the quoted flexural modulus of VeroBlack Plus is given as between 2200-3300 MPa.

The samples were seen to be slightly stiffer when orientated in position A, but the overall variation is quite small. Again the samples printed in the Y-axis were found to have similar stiffness (Figure 6.17). A greater amount of scatter is observed between the samples in this print direction and no obvious differences are seen in relation to the orientation of the sample

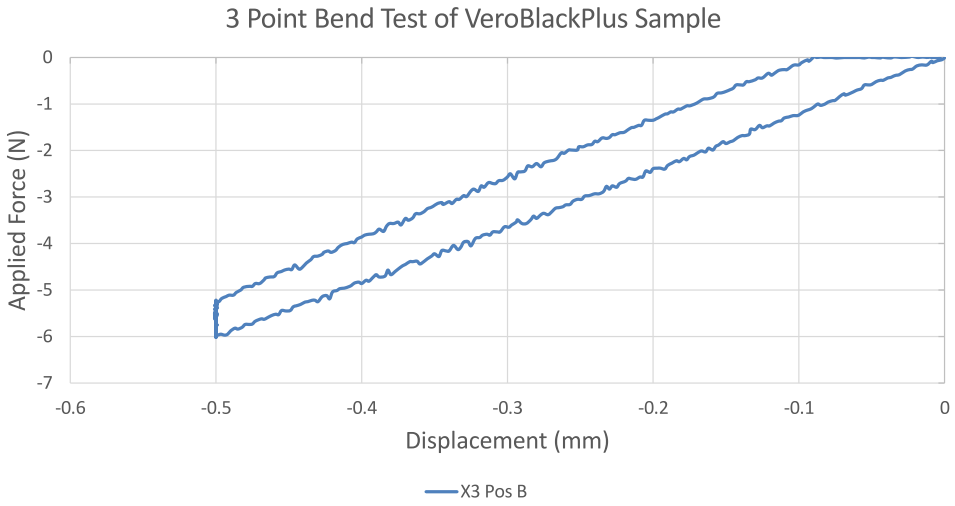

Figure 6.15: Typical load response for a sample of VeroBlackPlus in 3-point bending.

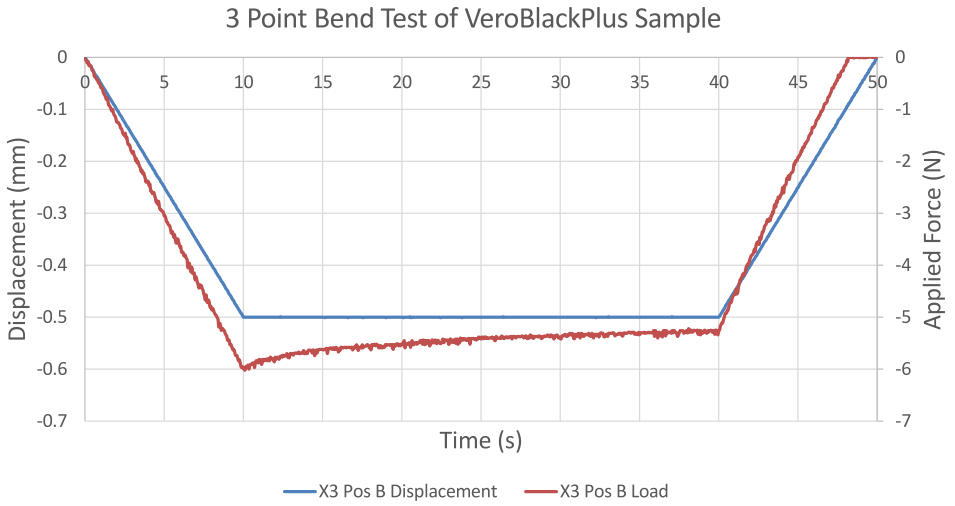

Figure 6.16: Typical variation in displacement with time of a VeroBlackPlus sample in 3-point bending.

within the test apparatus. Some loss in stiffness is observed in the Z samples under flexure (Figure 6.17). Here, the sample moduli were in the range of 1500-2000 MPa. No significant difference was observed with respect to the positioning of the sample in the test apparatus. Specimens that are orientated in the Z-axis of the printer will naturally have a greater number of layers within the sample due to the increased number of passes that the printer head needs to make in order to build the specimen. It can also be visually observed on some samples that the layers do not sit perfectly level, dipping in the centre of the cross-section which may also contribute to the decrease in stiffness (Figure 6.18). One possibility for this is that the movement of the print head is causing some drag on the surface of the sample as it is depositing the polymer. The very small printing surface area is also likely to be a contributing factor to this as well.

Generally speaking, it was observed that a higher modulus was recorded when the sample was unloaded rather than in the initial load section but some scatter does still exist.

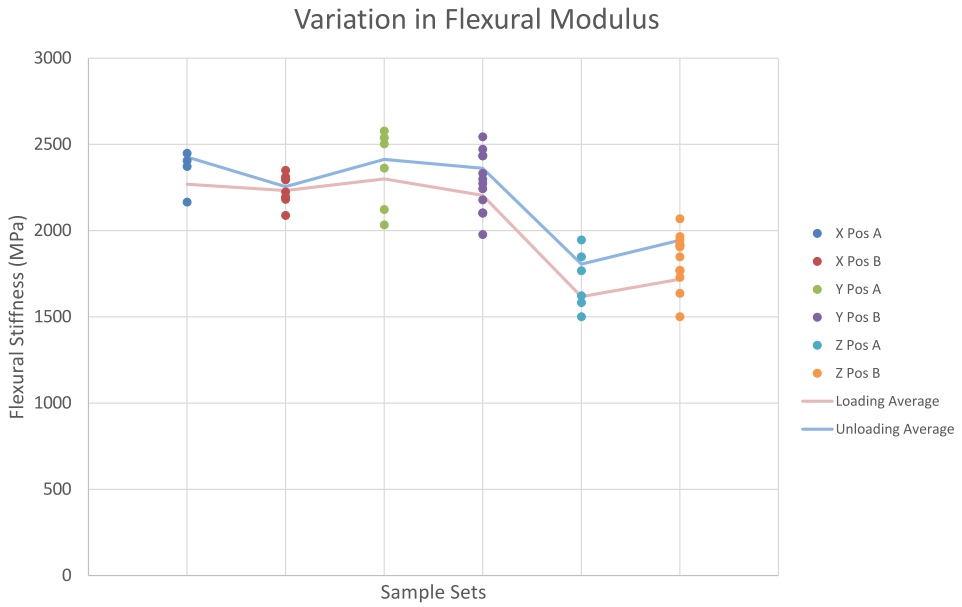

Figure 6.17: Variation in flexural modulus with sample print direction.

6.5.3 Discussion

Overall, it was observed that the samples behaved very similarly in two out of the three print orientations that were tested in flexure. The samples which were printed in the Z-axis were however around 20% less stiff. This suggests that in the case of a 3-dimensional lattice structure, which comprises of an assortment of beams printed in each of the 3 major axis that there

Figure 6.18: Samples aligned to the Z-axis during printing have visible distortion of the layers on the specimen surface.

may be some directional dependence in the overall structure. One significant difference with the full scale material however will be that a much greater surface area will be used to print the polymer, with any voids being filled with a support material. It is hoped that this increase in surface area, along with extra support material will help to improve the properties of the beams oriented in the Z-axis. No significant difference was observed when the samples were rotated by 90 degrees within the testing apparatus. In comparison to the tensile tests, the flexural modulus that was derived experimentally was found to be significantly higher.

It is not expected that the measured tensile modulus will be identical to the flexural modulus of the material due to the distinct differences in the loading conditions. In a uniaxial test, the applied stress is directly related to the resulting strain within the sample. The material modulus is found from the gradient of the stress-strain plot and is constant for a linear elastic material.

In a 3-point bend test however, the response is a combination of both beam bending and shearing at the supports. The stress within the sample will also vary through the depth due to the fact that the top surface will be subjected to compression while the bottom surface is in a state of tension. The calculated flexural modulus can therefore vary depending on the sample size and aspect ratio. From the manufacturer specified material properties, it is expected that the flexural modulus should be around about 10% greater than the tensile modulus.

The experimental tensile results produced a modulus that is in the region of 1750 MPa. By taking into account the likely localised deformation across the full sample, the maximum possible tensile modulus was estimated to be approximately 2335 MPa from equation 6.3 which is much closer to the experimental flexural results.

While the flexural modulus that has been derived by experimentation is at the lower end

of the manufacturer's specification, the results are fairly consistent between samples that were printed in the same orientation. Indeed, there is very little variation in samples that are printed in the X or Y axis of the printer. Some loss in stiffness is observed in the samples that are aligned to the Z axis of the printer. Here, the specimens are found to be approximately 20% less stiff in flexure. This suggests that a material formed from a lattice of orthogonal beams may be slightly anisotropic in one direction. It is hoped however that this will not greatly influence the overall material properties of the samples as the internal beams that will be printed in this direction within the model material will only be subjected to through thickness flexure. This shall be further investigated in the next chapter.

6.6 Conclusion

In this chapter, the tensile and flexural properties of a 3D printed photopolymer (VeroBlack Plus) have been investigated to verify that the mechanical properties were suitable to provide a basis for generating experimental idealised heterogeneous materials that can be subjected to mechanical testing. It has been concluded that while the samples generated do display some viscoelastic properties in tension, consistent results can be achieved by loading the samples at an appropriate rate. Further to this, it was found that consistent results are achievable in flexure with less sensitivity to the rate of loading. It is recommended that samples should not be printed in the Z axis of the printer where possible due to the fact that they appear to be significantly more compliant in flexure.

In the next chapter, a series of mechanical tests will be performed on samples of a cubic lattice structure composed from an array of orthogonal bars manufactured from VeroBlack Plus to determine if the size effects which have been observed in the virtual computational experiments conducted in chapter 4 can be replicated.

Chapter 7

Flexural Properties of a Polymer Heterogeneous Beam Sample

In the previous chapter, the tensile properties of a 3D printed solid photopolymer were investigated. While it was observed that some variation in the stiffness of the material exists depending on the direction that the internal layers are constructed, the overall variation was reasonably small at the scale which was tested.

In this chapter, a thorough experimental analysis into the flexural properties of a material comprised of a cubic lattice microstructure manufactured by additive manufacturing processes has been performed to compliment the computational FE analysis undertaken in chapter 4.

The heterogeneous beam samples consisting of a regular array of orthogonal lattices were subjected to both three-point and four-point flexural loading within a mechanical testing machine to determine the elastic parameters of the material within the context of a micropolar continuum.

The results of the experimentation show that it is possible to capture size dependent effects consistent with those that are predicted in micropolar theory for materials constructed from a photopolymer resin for both modes of loading. However, some variation in the results exist which is likely to be attributed to the manufacturing process of the samples.

7.1 Introduction

It has been shown in a previous chapter that the observed size effect in a heterogeneous sample under flexure can be maximised when a constant moment load is applied to the samples. While this idealised mode of loading produces the most consistent results, it is hard to replicate in physical tests. It is therefore required that best estimations of the mechanical properties are made by conducting tests which minimise the experimental errors. For a linear elastic homogeneous material subjected to 3-point bending, it can be shown that shear deformation effects are minimised when the beam under test is slender. This assumption however is based on the fact that the stress distribution within the material is continuous. In a heterogeneous sample, the local stress field may not directly relate to the global or average stress within the material in the usual manner due to the local variation in stresses that the heterogeneities introduce. In order to determine the general mechanical properties of a given heterogeneous material it is necessary to look at the average or global stresses within the sample due to the discontinuous nature of the distribution that the heterogeneity introduces. For materials with a significant microstructure, the global stress distribution has also been shown to be dependent on sample size when it is of similar order to the predominant microstructural features which make up the material (e.g. Dai & Zhang (2008)). To fully understand the mechanical behaviour of such materials, it is therefore necessary to determine the best mode of loading which will minimise any experimental errors that may be influential to the results.

It has been shown in a previous chapter that heterogeneous materials comprised of a regular periodic unit cell structure may require the identification of additional constants in order to fully describe how the material behaves at differing size scales. In this chapter, beams of similar aspect ratio, but with varying rows of unit cell microstructure through the sample breadth and depth were tested in both 3 and 4-point bending with the aim of determining the flexural constants within the framework of micropolar elasticity. The effect of shear deformation on the observable properties was considered in three-point bending by varying the aspect ratio of the beams. Similarly, in the second part of this chapter a series of four-point flexural tests were conducted to determine if this mode of loading offered any potential benefits. The main aim of the experiments was to establish whether accurate and consistent material properties could be derived experimentally for a novel heterogeneous material manufactured from additive manufacturing processes. Secondary to this, these experiments provide a comparative analysis of how the FE simulations perform compared to physical samples of the material. This is important as conducting FE analysis of more complex heterogeneous materials may be impractical due to the computational resources which are required and performing experiments may be the only practical way to identify their behaviour.

7.1.1 Model Heterogeneous Material

The 3-dimensional orthogonal lattice analysed in chapter 4 was chosen as the test material. In order to be able to characterise the material in flexure, a set of samples were required to be produced with similar aspect ratio but differing depths to determine any dependency on size and scale. As the 3D printer which was available had a fixed capacity, the specimen size was limited by both the build space available and the minimum feature size that could be accurately resolved in the printer.

It was therefore required that the material met the following requirements:

- The largest sample must be no greater than 340 mm in length.
- A minimum of 4 samples of different sizes, but similar aspect ratio, need to be manufactured in order to obtain a clear indication of any size dependency in the material.
- The microstructure within the samples is required to be of a sufficiently low density that a measurable variation in stiffness can be observed.
- The size of the unit cell which defines the microstructure also needs to be large enough that the printer can accurately reproduce the features consistently without being damaged by either handling or from localised stresses produced under test.
- Samples should be sufficiently slender to minimise any transverse shear effects under loading.

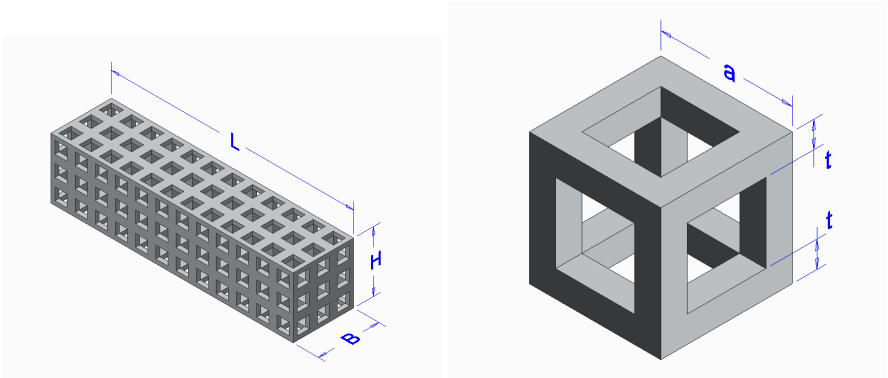

Figure 7.1: Beam with cubic lattice microstructure and example unit cell.

After careful consideration a unit cell of $5 \times 5 \times 5$ mm in size was chosen with an internal cell wall thickness, t of 1 mm. A diagram of the material and the underlying unit cell can be seen in figure 7.1. At this size scale, it was possible to print a set of 4 samples with a square cross-section at an aspect ratio of 16 within the Objet printer (Figure 7.2). The total length of

each sample was thus defined by the beam depth and a fixed length to depth aspect ratio of 16. In addition to this each beam was extended by 4 unit cells in length in order to avoid supporting the samples close to the ends of the beams.

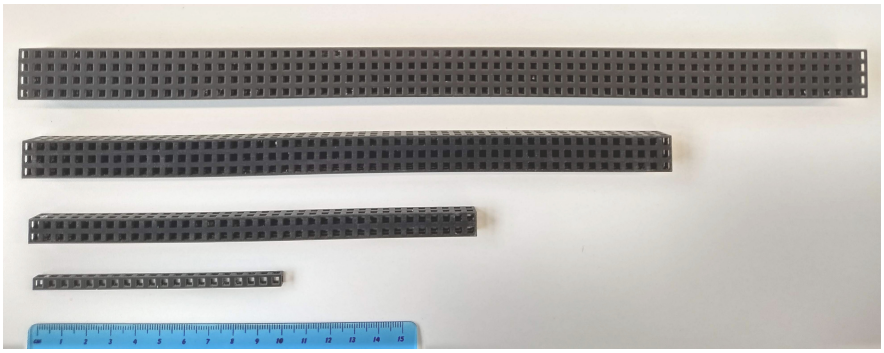

Figure 7.2: A typical set of samples used to perform 3 & 4-point bend tests.

While computational results indicated that the maximum size effect which can be obtained in a cubic lattice is likely to be found at very low material volume fractions, it was observed that localised deformation of the cells around the region where the load is applied may dominate over the predicted bending deformation. The benefit of the unit cell that was chosen is that a significant size effect is likely to be observed that is not unduly influenced by point loading provided that a careful experimental procedure is followed.

In the previous chapter, it was observed that some directional dependence exists in the matrix material in flexure resulting from the sample print orientation. Slender specimens aligned to the Z axis during printing were around 20% more compliant than those printed parallel to the X and Y axes. As the internal beams within the orthogonal lattice will be orientated in each of the three axes, it is possible that some directional dependence may be present within the material.

It was also possible to orientate the lattice specimens within the printer during manufacturing. To determine if this has any effect on the observed mechanical properties, separate sets of samples were produced with the major axis aligned to both the X and Y axes of the printer. No samples were printed in the Z axis as the printer did not have sufficient build space in that direction to accommodate the full range of samples required.

The orientation of the samples within the testing apparatus is another factor which may influence the measured mechanical properties due to the layering process of the 3D printer. Samples with a square cross-section were therefore beneficial as it allowed for each sample to be rotated and tested without altering the test setup. In this way, it can be determined if the printed material exhibits any transverse anisotropy due to the internal layers that result from the manufacturing process.

The results of the experiments will be compared with the numerical solutions which were obtained from a FE analysis of the material under consideration.

7.2 3-Point Flexural Loading of a Cellular Lattice Beam Sample

7.2.1 Experimental Setup

The tests were conducted in a Bose Electroforce 3200 linear testing machine with a 450 N load cell attached to the central indenter in the same manner as was described in the previous chapter (See figure 7.3.). In order to accommodate the full range of samples within the testing apparatus, a custom support fixture was manufactured. A detailed description of this can be found in appendix C.1.

One of the issues which became apparent during the design of the experiment was that in order to test the full set of samples the machine should be able to accept a range of samples at differing sizes and also have a load cell which is capable of being able to accurately measure the applied load. As the aspect ratio in each set of tests was constant, the load required to displace a linear elastic homogeneous equivalent beam is primarily dependent on the change in breadth between samples. However, since the reaction force is also dependent on the aspect ratio cubed, a comparatively small load is required to impart a given deflection onto a slender beam which will rapidly increase with a decreasing length to breadth aspect ratio. This is also compounded by the fact that the stiffness of low density lattice samples is directly related to the ratio of the cell size to wall thickness squared.

It was shown in a previous chapter that the observed experimental material modulus is largely dependent on the length to breadth aspect ratio in three-point bending. The rate at which the samples were loaded was also a contributing factor in the tensile tests. With this in mind, two loading rates of 0.05 mms^{-1} & 0.08 mms^{-1} were chosen. Each sample was also tested at an aspect ratio of 10 and 16. The specimens were also tested in two different positions by rotating each one by ninety degrees about the major axis in the same manner that the dumbbell samples were tested in the previous chapter. The motivation for this was to determine if the layering process during manufacturing had any significant impact on the transverse properties of the discrete samples. In the results, the relative position of the samples has been labelled as either ‘A’ or ‘B’. Position A denotes samples in which the Z-layers are aligned parallel to the horizontal axis and is representative of the orientation during manufacturing. In position B the sample is positioned so that the Z-layers run parallel to the vertical plane. An example of a sample under test can be seen in figure 7.3.

Each test was conducted by applying a fixed rate of displacement to the linear actuator for 10 seconds to deflect the specimen vertically. Samples were then held in place at the maximum

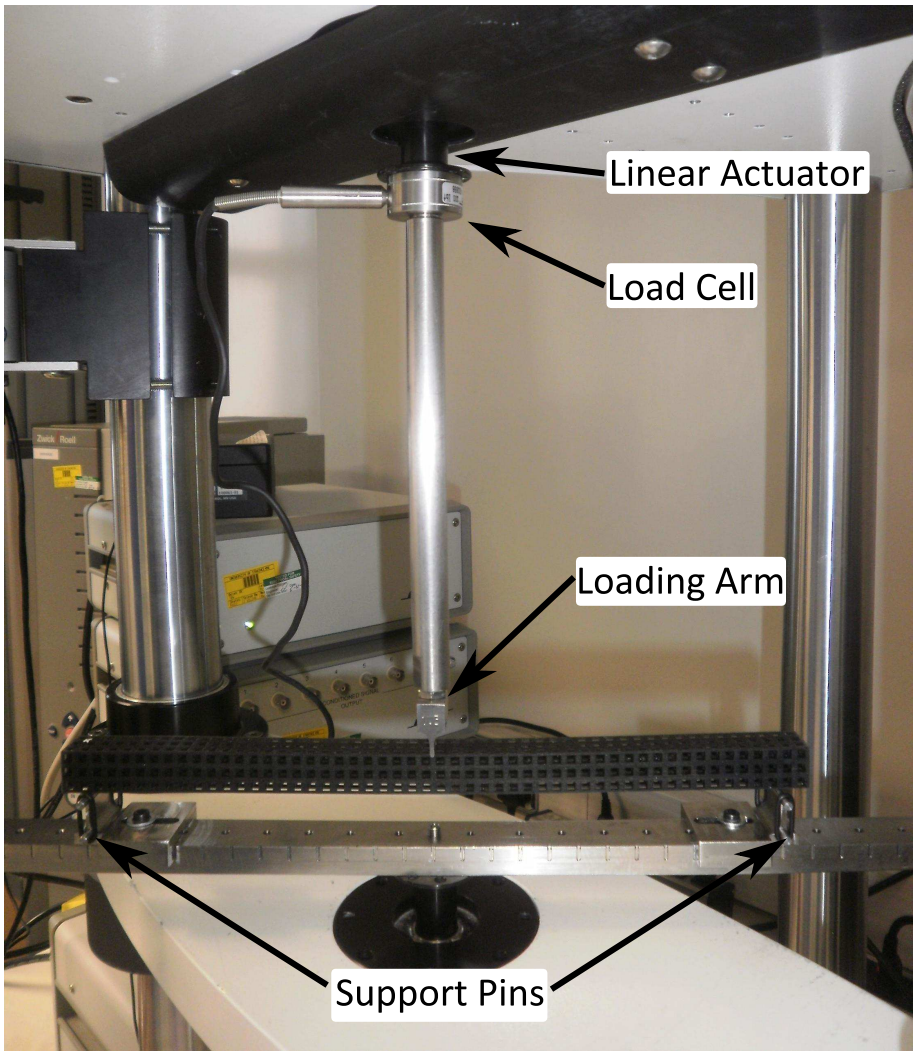

Figure 7.3: Deflection of a typical beam sample in 3-point flexural loading within the experimental apparatus.

displacement for 30 seconds before being unloaded at the same rate over a 10 second period. A sampling rate of 20 Hz was also used to capture the data during the test phase.

In the initial tests conducted, it was observed that an appreciable amount of background noise was recorded in the raw data when the samples were loaded within the lower range of the load cell capacity. It is likely that in this range the machine is very sensitive to small variations in the response which are amplified by the system. For this reason, the machine was calibrated for each specimen prior to testing in order to minimise the likely variation in the response. While the load-deflection slope appeared to be generally linear, the background noise increased the uncertainty within the experiment. To address this, a 1 Hz filter was applied to the machine software prior to conducting each test in order to minimise any background noise which may be induced within the system. A typical plot of the variation in load with deflection of a test sample can be seen in figure 7.4. Some stress relaxation is observed when the samples are held at a fixed deflection, but the general response is linear.

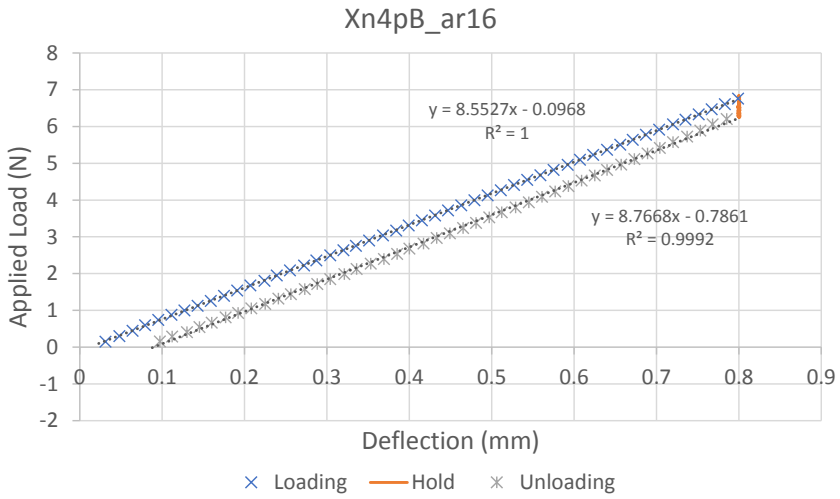

Figure 7.4: Variation in load with deflection for a typical sample tested in 3-point bending.

The resulting sample stiffness was obtained by analysing the captured load deflection data to determine the linear region. As numerous tests were conducted, a MATLAB script was developed to facilitate this process. A detailed description of this can be found in appendix C.3.

In total, sixteen sets of experiments were conducted using the groups of samples which contained between one and four cells through the breadth and depth. The tests carried out were as follows: X samples in position A at an aspect ratio of 10 and 16; X samples in position B at an aspect ratio of 10 and 16; Y samples in position A at an aspect ratio of 10 and 16; Y samples in position B at an aspect ratio of 10 and 16. Each test was conducted at a loading rate

of 0.05mms^{-1} and 0.08mms^{-1}.

The resulting stiffness data was normalised against sample breadth and plotted against the inverse of the sample depth squared to verify that a size dependency does indeed exist in the material. The flexural modulus and characteristic length were then extracted for each set of samples using equation 2.37 when a linear region was observed.

7.2.2 Experimental Results

Once the experimental data was collated, an in-depth analysis of the results was performed. As stated above, the flexural modulus and characteristic length can be derived from the linear region in a plot of stiffness against the inverse of sample size. The resulting experimental data for beams with an aspect ratio of 16 loaded at 0.08mms^{-1} have been included in figures figures 7.5 to 7.8. It can be seen that a generally linear increase in stiffness was observed with decreasing sample size in all cases, with little variation between the stiffness observed when loading or unloading the sample. The variation in stiffness between sets of samples appears to be similar, but further analysis is needed to reveal the physical material constants. Similar plots were also obtained for the beams at the lower aspect ratio and loading rate.

As the unit cell which defined the material was constant in all samples, any variation in mechanical properties is likely to be attributed to the orientation at which it was printed and subsequently tested at. Figures 7.9 and 7.10 display the variation between the flexural modulus which was calculated from each set of samples in 3-point bending at the two length to depth aspect ratios considered. It can be observed in all cases that there is very little variation between the calculated modulus for samples loaded at 0.05mms^{-1} and 0.08mms^{-1} which suggests that the rate of loading is sufficiently fast that any viscoelastic effects may be safely ignored. The orientation of the samples within the 3D printer during manufacturing appears to have a noticeable effect on the resulting properties. In all cases, samples which were orientated in the 'Y' axis of the printer during manufacturing appear to be at least 10% more compliant than the equivalent specimen which was aligned to the 'X' axis of the printer.

The orientation of the samples within the mechanical testing apparatus was also observed to influence the flexural modulus. When loading the beams perpendicular to the way in which they were printed (position 'B'), it was found that the material was slightly more compliant in this orientation as compared to position 'A'. In all cases it was observed that the material appeared to be marginally stiffer when unloaded as compared to being loaded. Comparing figures 7.9 and 7.10 with each other, it is clear to see that the apparent flexural modulus decreases with beam aspect ratio which is in line with the general theoretical predictions for 3-point flexural loading.

The full set of experimental mechanical properties have been summarised in tables 7.1 and 7.2. In general, it can be observed that the couple modulus, γ and characteristic length, l_b,

decrease with sample aspect ratio. This is expected as localised shearing in the beam becomes more significant and the reduction in stiffness that it introduces may dominate over any potential gains in stiffness that can be obtained from the microstructural topology. These parameters show a similar variation in magnitude with respect to sample print direction and test orientation when compared to the trends which were observed for the flexural modulus. However where the flexural modulus was seen to increase in magnitude, γ and l_b decreased. Overall however the variation in characteristic length was quite small ranging from $0.714 - 0.99$ mm for the samples at a length to breadth aspect ratio of 16. Comparing the samples printed in the 'X' direction with those orientated in the 'Y' axis, it can be observed that the calculated characteristic length is slightly greater in the 'Y' specimens for all cases. While the rate of loading does appear to have some slight effect on the results, this cannot be fully verified without testing a greater number of samples.

Sample	Aspect Ratio	E^* (Nmm^{-2})	γ (N)	l_b (mm)
X Pos A	16	430.03	438.25	0.714
	10	397.19	384.39	0.696
X Pos B	16	404.49	531.01	0.810
	10	390.94	448.48	0.757
Y Pos A	16	380.06	592.59	0.883
	10	356.25	524.83	0.858
Y Pos B	16	354.5	688.69	0.986
	10	336.13	601.65	0.946

Table 7.1: Variation in observed micropolar material properties derived from experimental 3-point bend tests of samples loaded at 0.08 mms^{-1}.

Sample	Aspect Ratio	E^* (Nmm^{-2})	γ (N)	l_b (mm)
X Pos A	16	412.52	491.07	0.771
	10	392.70	349.71	0.667
X Pos B	16	393.22	553.92	0.839
	10	379.38	421.74	0.746
Y Pos A	16	360.24	619.14	0.927
	10	341.85	550.76	0.898
Y Pos B	16	356.90	701.21	0.991
	10	329.91	574.87	0.933

Table 7.2: Variation in observed micropolar material properties derived from experimental 3-point bend tests of samples loaded at 0.05 mms^{-1}.

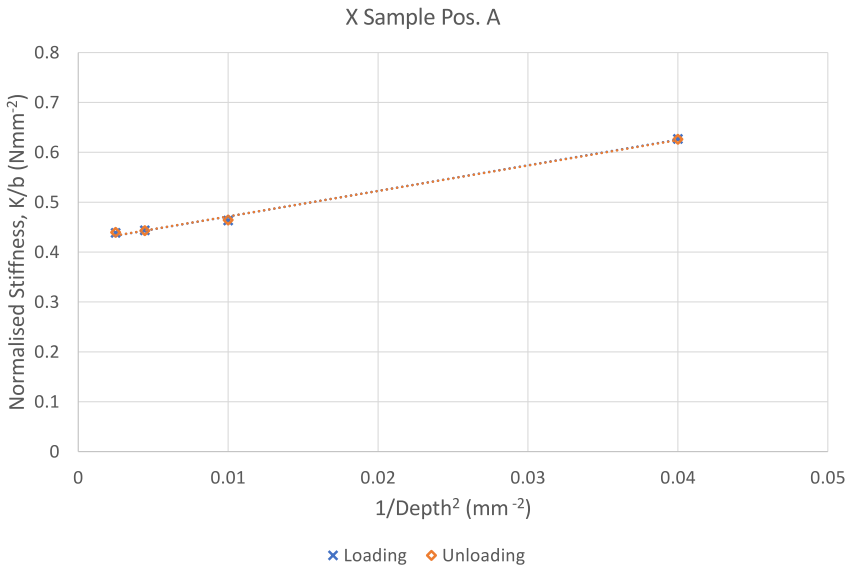

Figure 7.5: Variation in normalised flexural stiffness with sample size at an aspect ratio of 16 when loaded at 0.08 mms^{-1}.

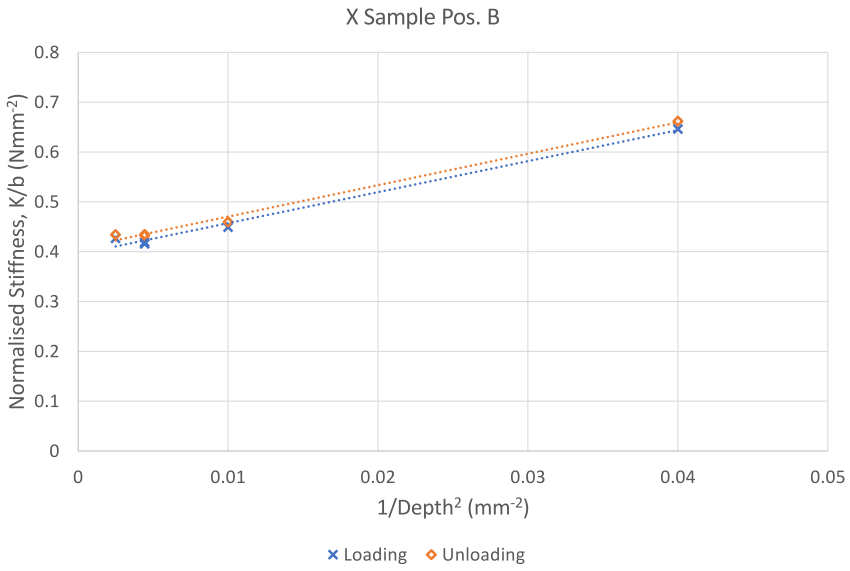

Figure 7.6: Variation in normalised flexural stiffness with sample size at an aspect ratio of 16 when loaded at 0.08 mms^{-1}.

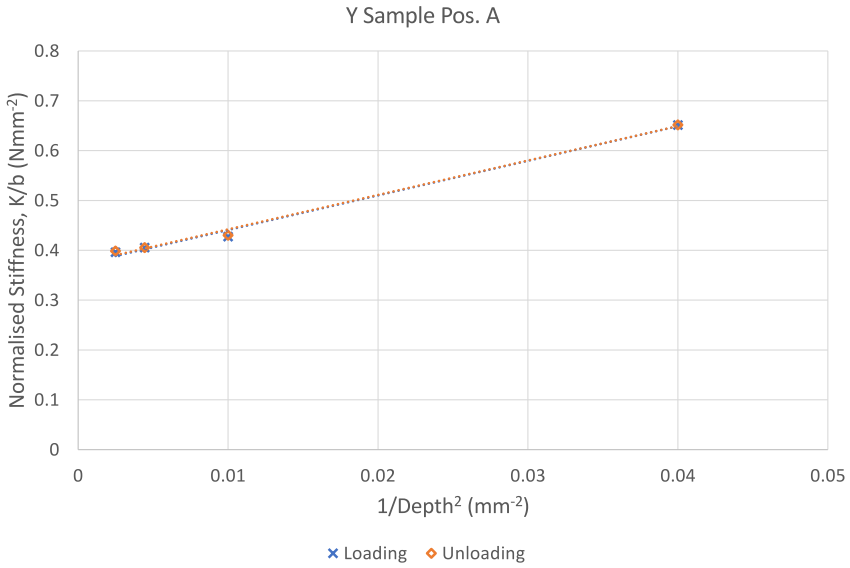

Figure 7.7: Variation in normalised flexural stiffness with sample size at an aspect ratio of 16 when loaded at 0.08 mms^{-1}.

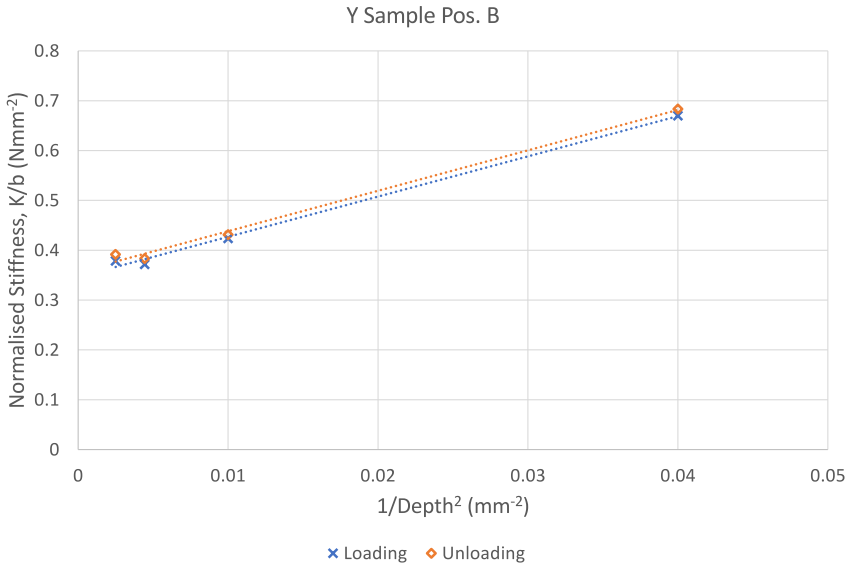

Figure 7.8: Variation in normalised flexural stiffness with sample size at an aspect ratio of 16 when loaded at 0.08 mms^{-1}.

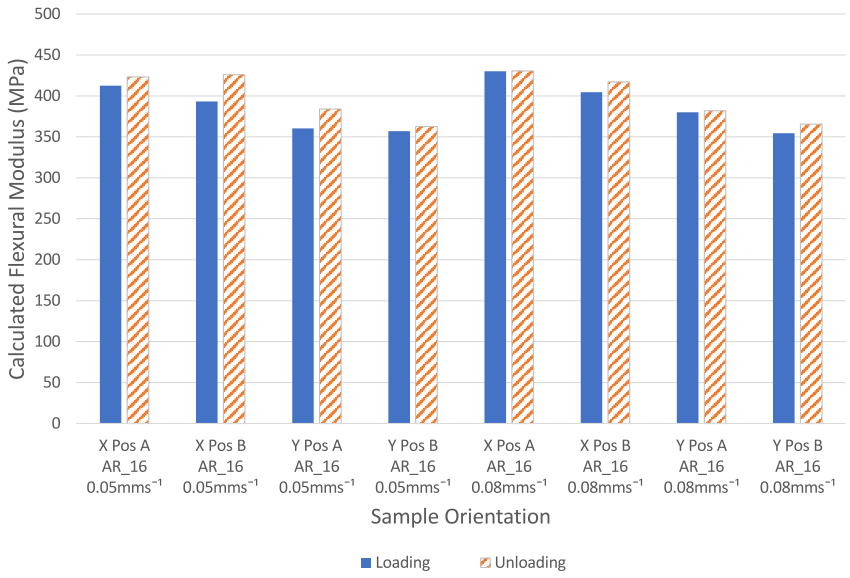

Figure 7.9: Variation in the flexural modulus of the lattice samples with print direction and sample orientation at an aspect ratio of 16.

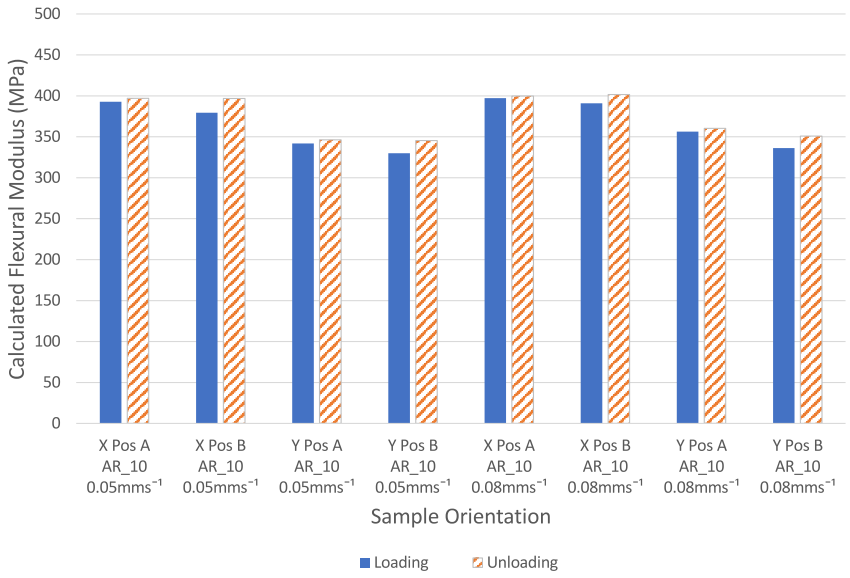

Figure 7.10: Variation in the flexural modulus of the lattice samples with print direction and sample orientation at an aspect ratio of 10.

7.2.3 Computational FE Simulations

A complementary series of FE flexural simulations were carried out to compare the results of the experimental tests to idealised numerical simulations. Half symmetry models of the beams used in the experimental tests were generated in ANSYS by the same method used in Chapter 4. The solid matter within the material was modelled as a linear elastic solid with a Young's modulus of 2 GPa and Poisson's ratio of 0.3. These parameters were chosen as they were similar to that of the experimental tensile modulus of the 3D printed polymer obtained in the previous chapter.

To match the experimental setup as closely as possible, the overall size of the beam was fixed and the aspect ratio was varied by altering the horizontal position of the supports. In total 3 different length to depth aspect ratios were considered to observe how the relative change in stiffness from a short to slender beam affects the properties in flexure. The samples were subjected to fixed displacement boundary conditions under simulation which was in-line with the experimental setup.

The boundary conditions for three-point bending under half symmetry loading were as follows:

Left support	$UY = UZ = 0$	on bottom surface	
Centre of beam	$UY = 0.5$ mm	on top surface	
	$UX = 0$	on end face	(7.1)

where UX, UY and UZ denote displacements in the direction of the sample length, depth and breadth respectively.

7.2.4 Results of Computational FE Analysis

Previous FE simulations predicted that the tensile modulus of this material was in the region of 350 MPa with a Poisson's ratio of 0.092. The flexural modulus obtained by subjecting the beam to a constant moment load was slightly larger at 360 MPa.

The variation in predicted beam stiffness with size can be seen in figure 7.11. Here, the stiffness is normalised to account for the variation in aspect ratio during the tests and is plotted against the inverse of the sample depth squared. The results of the FE analysis are summarised in table 7.3. From figure 7.11, it can be seen that some reduction in stiffness is observed in comparison to the ideal case even when the aspect ratio is set to 16, however the flexural modulus was measured to be 351 MPa which is within 3% of the converged value.

While it has been observed that it is not ideal to test these samples at a length to depth

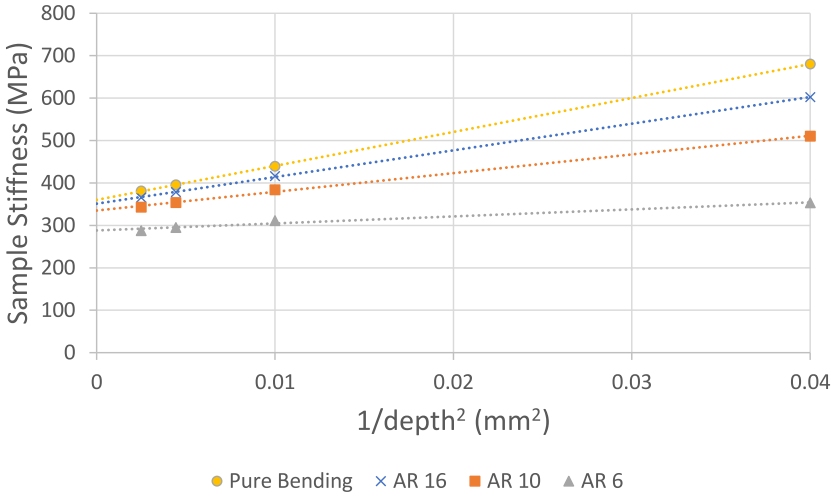

Figure 7.11: Variation in sample stiffness with aspect ratio for beams subjected to 3-point bending as predicted from finite element analysis.

Number of Rows in Set	Aspect Ratio	E^* (Nmm^{-2})	γ (N)	l_b (mm)
3Pt 1..4	Pure	360.2	667	0.96
	16	351.2	523.8	0.86
	10	335	367.2	0.74
	6	288.06	137.9	0.49
3Pt 2..4	Pure	361.7	643.2	0.94
	16	349	557.3	0.89
	10	329.6	451.5	0.83
	6	280	263.4	0.69

Table 7.3: Variation in apparent micropolar material properties derived from 3-point bend test simulations.

aspect ratio of 16, it is the maximum possible size that can be manufactured with the facilities which were available at the time. From the results of the simulations, it can be observed that at this aspect ratio the derived properties are converging on the idealised solution for the material in bending, and the magnitude of the size effect is in line with that of the material. An improvement of the estimation can be made by discounting the smallest sample in the set as this appears to have the greatest reduction in relative stiffness. This has been included in table 7.3. The downside to this however is that the number of data points available to predict the modulus of micropolar bending and the characteristic length is only 3 which relies on accurate test conditions. Ideally, a larger sample set would be used in order to capture the converged material properties.

The characteristic length for the material at a given length to depth aspect ratio was determined by calculating the flexural modulus and couple modulus, γ from the linear portion of the plotted data and equation 2.37. In the idealised case where the beam is subjected to a constant moment load at each end face, the characteristic length of this material was found to be 0.94 mm. At an aspect ratio of 16, the characteristic length determined was 0.86 mm from the FEA simulations. It is clear from table 7.3 that as the aspect ratio of the sample decreases, the apparent characteristic length diminishes significantly, indicating that the analytical solution which is used to derive the properties becomes less valid as the aspect ratio is reduced.

7.2.5 Discussion of 3-Point Bending Experimental Results

A predominantly positive size effect was observed when samples of the material were loaded in 3-point flexural loading. From the experiments which were carried out, it was observed that the magnitude of the size effects obtained were also in agreement with the FE predictions. Subtle differences in the mechanical properties were observed which can be partly attributed to the anisotropic nature of the matrix material, but the overall variations were reasonably small. The aspect ratio of the samples was shown to be a significant factor under 3-point loading, with a decrease in relative stiffness being observed which corresponded to a reduction in aspect ratio. While it was shown in the FE analysis that an aspect ratio of 16 was not optimal for testing the material in 3-point bending, the experimental modulus and characteristic length were within 2.5% and 10% respectively of the predicted converged result.

The manufacturing equipment and test apparatus limited the use of more slender beam samples. While it would have been possible to scale down the unit cell within the printed material to increase the overall sample aspect ratio, it would also have reduced the thickness of the internal beams within the cellular structure. As the smallest feature within the current material had a cell wall thickness of 1 mm it was felt that decreasing the cell size further may compromise the structural integrity of the samples. The flexural modulus observed at an aspect ratio of 16 was 351 MPa in the FE analysis, while the physical tests indicated that it varied between

355-430 MPa. The characteristic length obtained from the FE simulations was between 0.86 and 0.89 mm at an aspect ratio of 16. In comparison, the experimental characteristic length was found to range from 0.71 to 0.99 mm (See table 7.4.). As the experimental procedure has more uncertainty than the numerical simulations it is encouraging that the observed material properties are similar.

	E^* (Nmm^{-2})	l_b (mm)
Numerical	351	$0.86 - 0.89$
Experimental	$355 - 430$	$0.71 - 0.99$

Table 7.4: Comparison of the variation in flexural modulus and characteristic length obtained by experiment and numerical simulation for samples tested in 3-point bending at an aspect ratio of 16.

The variation in experimental modulus of the samples is primarily attributed to the layering process during manufacturing and its orientation with respect to the direction of loading. The FE model is based on a linear elastic isotropic matrix material to describe the solid within the cellular structure. As this is a simplified representation of the polymer in the physical specimens there are bound to be some intrinsic differences in the overall results. It has been shown here however that these differences can be minimised with careful experimental techniques.

Some dependence on the orientation of the samples within the printer has been observed in the flexural modulus and characteristic length of the material which was manufactured and tested. It is therefore very important that manufactured specimens are aligned to the same axis during printing to minimise any variations in stiffness which may not be associated with size-scale effects in the material. The transverse material properties of the samples also appear to have some directional dependence resulting from the layering process which suggests that the material is slightly anisotropic. However, as the variation in stiffness is small, it may be sufficient to classify the lattice structure as orthotropic of cubic class.

The flexural modulus and characteristic length of the material depends on a linear extrapolation being observed when samples of differing size, but similar aspect ratio are tested in flexure. A linear response is predicted for this material at a test aspect ratio of 16 in 3-point bending for the sample depths considered. In general, the experimental results agreed with this prediction when all 4 sizes of samples were analysed with an R-squared value of 0.98 or greater being observed. As the smallest sample in the set is likely to deviate furthest from the predicted trend line, it is logical that this data point can be omitted from the results to improve the prediction of the experimental mechanical properties. However, it was observed that for samples plotted against the inverse of the depth squared that the output data does not produce a very good fit for some of the sample sets, indicating that there may be some experimental

uncertainty. The R-squared value of the plots varied considerably, indicating that the predicted trend line was less certain.

As only a limited number of samples were tested which had similarly orientated internal layers within the solid matrix material, it would be recommended that further tests should be carried out to differentiate between the mechanical properties which are attributed to the manufacturing process and the experimental uncertainty. The experimental procedure was reliant on the absolute displacement of the machine to determine the overall deflection of the specimen under test. An independent measurement of the deflection with respect to time at the centre of the beam may offer a slightly more accurate depiction of the deformation under loading.

While testing a set of 4 samples appears to produce a reasonable correlation between stiffness and sample size, it may be more beneficial to analyse a larger range of specimen sizes to improve the statistical accuracy of the experiment. This may be particularly important in materials which display a non-linear variation in stiffness with sample sizes approaching zero thickness.

One of the inherent difficulties with this method is that small variations in the calculated stiffness of individual samples may have a significant effect on the apparent mechanical properties of the material. Care must therefore be taken to achieve accurate results. While the experimental results correlate well with the numerical predictions, there is a degree of scatter in the individual samples which may be misinterpreted if a sufficiently large sample set is not considered. For this reason, it would be recommended that the minimum number of samples which should be tested is 4 and that a reasonable range of sample sizes is considered to account for variations due to scale. Having said that, the size effects which exist as the sample size diminishes becomes significant in applications where thin layers of the material are used for structural applications so must also be considered.

Overcoming the limitations of testing materials which are dependent on both size and scale at multiple size-scales is inherently difficult. The main problem with this method is that to obtain accurate results, one must distinguish between the size effects which are inherent to the material and any localised effects which are induced by the experimental setup. It is therefore imperative that the stiffness of the material is tested for convergence at each size scale considered by varying the sample aspect ratio. Other considerations which need to be made include the placement of the indenter and supports as localised loading effects may also obscure any observable size effects. For materials which have a very low volume fraction, the ideal test aspect ratio may be too large to conduct experimental tests with the available equipment in 3-point flexural loading. FE simulations of the material or another mode of loading may be more appropriate in this case. In the next section, 4-point flexural loading will be investigated to determine if this mode offers any quality improvements to the experimentally observed parameters.

7.3 4-Point Flexural Loading of a Cellular Lattice Beam Sample

While three-point flexural tests have been shown to give a reasonably accurate representation of the intrinsic size effects that are present in a relatively dense heterogeneous material, it has been observed through computational simulations that this mode of loading may not be adequate for testing very low density cellular structures. Another mode of loading commonly used to evaluate the flexural properties of materials is the 4-point bend test. One possible advantage of using a 4-point flexural test over 3-point bending is that the central section of the beam, between the two points of loading is in theory subject to constant moment loading thereby minimising the influence of any shear component on the response of the beam. However, the added complexity of the experimental setup requires more thought.

It is the aim of this section to investigate the suitability of four-point loading as a means for evaluating the flexural properties of an engineered heterogeneous solid.

7.3.1 Experimental Setup

Samples were subjected to four-point flexural loading in a Bose Electroforce 3200 linear testing machine which had a 450 N load cell attached. A custom indenter was manufactured in order to evenly distribute the load to two points on the top surface of the beam sample. The design of the indenter was similar to the support beam which was manufactured for the three-point tests albeit with a reduced span to minimise the mass of material attached to the linear actuator and load cell. The pins on the indenter had a 3 mm diameter and were designed to be fully adjustable across the length of the span. A more detailed description of the design of the indenter can be found in appendix C.1. The full experimental test setup with a sample in situ can be seen in figure 7.12. Prior to conducting all tests, the mechanical testing machine was calibrated with the supports attached and a specimen in place to capture the correct dynamic response within the machine under displacement control conditions.

As with the three-point flexural tests which were conducted in the previous section, the overall length to depth aspect ratio of the section under flexure was limited by the maximum specimen size which could be manufactured. It was therefore decided that the overall aspect ratio of the samples would remain fixed at 16 as in the case of three-point bending, while the aspect ratio of the beam section positioned between the two indenter's was varied to determine if this had an effect on the overall results of the experiment. In total, two different indenter spacing ratios were investigated which were equivalent to a length to depth aspect ratio of 8 and 12 for the sample under test.

During the test, specimens were deflected at a fixed rate for a total of 10 seconds, before being held in place at the point of maximum deflection for 30 seconds. Samples were then unloaded at the initial rate for 10 seconds to return the specimen to its original position. From

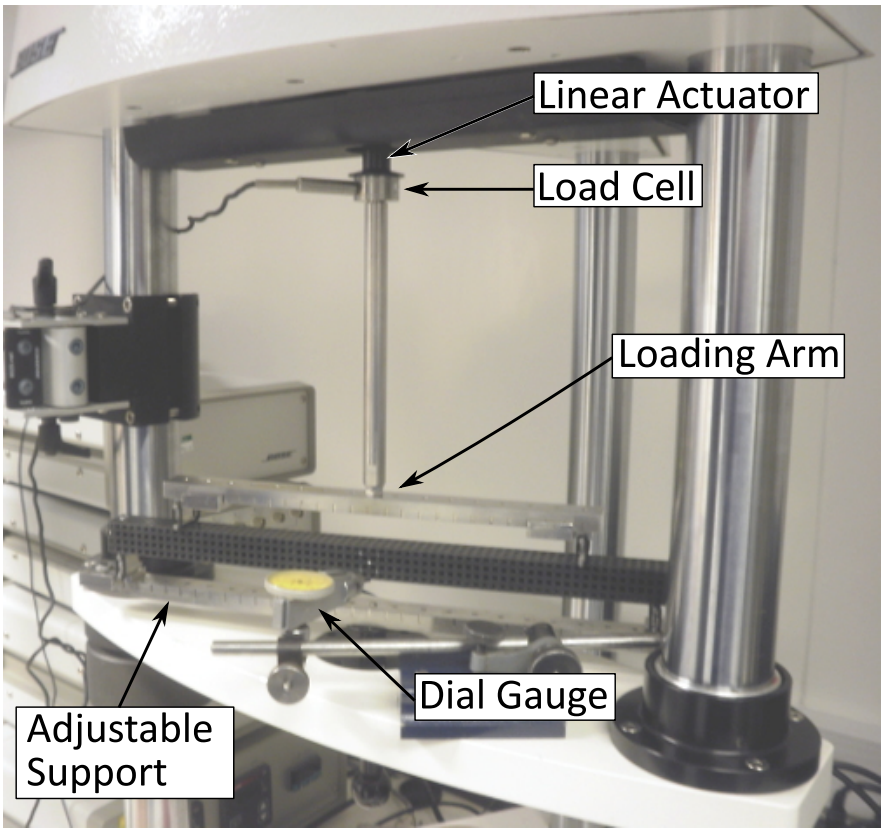

Figure 7.12: Four-point bending experimental test setup.

the resulting data the stiffness of the sample was obtained from the gradient of the linear region in the load-deflection plot. In all tests a sampling rate of 20 Hz was used to capture the response of the specimen. The maximum displacement at the centre of the beam was determined with the aid of an analogue rotary dial gauge which had a precision of ± 0.005 mm. The displacement on the dial gauge was recorded at the end of the initial loading phase. A greater displacement is required to be placed upon the sample with an inner aspect ratio of 8 in comparison to the sample with an aspect ratio of 12 to impart the same force in a solid beam under four-point flexural loading. In order to keep the applied load within the same range for each set of tests, the rate of loading was varied slightly to account for this. The high aspect ratio samples were loaded at 0.03 mms^{-1} and the lower aspect ratio samples at 0.05 mms^{-1}. As only a limited number of samples were available to test, each experiment was repeated 3 times per sample to verify that a consistent response was obtained.

The standard equation for the deflection of a solid beam with continuous cross-section subjected to a four-point flexural load can be derived from Euler-Bernoulli theory. The vertical displacement at the point of loading, w_1, and the maximum deflection, w_2, at the centre of the beam can be expressed as:

$$w_1 = \frac{PL_1^2}{12E_sI_s}\left(2L_1 + 3L_2\right) \tag{7.2}$$

$$w_2 = \frac{PL_1}{48E_sI_s}\left(8L_1^2 + 12L_1L_2 + 3L_2^2\right) \tag{7.3}$$

$$\Delta w = (w_2 - w_1) = \frac{PL_1L_2^2}{16E_sI_s} \tag{7.4}$$

where P is the reaction force at the load cell, E_s is the Young's modulus of the material and I_s, the second moment of area of the section. The parameters L_1 and L_2 denote the distance between the supports and loading arms as shown in figure 7.13.

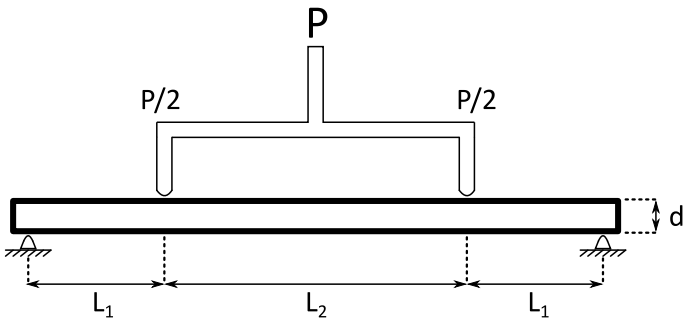

Figure 7.13: A slender beam subjected to four-point flexural loading.

In order to determine the flexural modulus of the material, the relative displacement between the point of loading and the centre of the beam, Δw, is calculated to determine the stiffness of the central section. It can be shown from a static analysis that the central section of the beam does not have any external shear forces acting on it under four-point loading, with a constant bending moment acting in this region. Indeed, equation 7.4 is identical to that of a beam of fixed length, L_2, being subjected to a constant bending moment at each end if the applied moment is equal to $PL_1/2$. The main drawback to 4-point bending however is that the stress field within the sample becomes more complex along the length of the sample due to the multiple points of loading. The additional complexity of the experimental setup and increased number of displacement points is another reason that four-point bending is not utilised more often.

Equation 7.4 can be modified to represent a heterogeneous beam within a micropolar continuum by introducing the higher order terms associated with the flexural rigidity which were previously discussed. The variation in the stiffness of the central section can therefore be ex-

pressed as:

$$K_{(L_2)} = \frac{P}{w_2 - w_1} = \frac{16}{L_1 L_2^2} \left(E^* I_s + \gamma A \right) \tag{7.5}$$

The flexural modulus of the material and associated characteristic length can be interpreted from the method of size effects. By plotting the variation in flexural stiffness with respect to the inverse of sample depth squared, as in equation 7.6, the micropolar couple modulus may be determined from the gradient of the linear portion of the plot while the flexural modulus is measured from the projected intercept with the vertical axis.

$$\frac{K_{(L_2)}}{I_s} = \left(\frac{P}{w_2 - w_1} \right) \left(\frac{3 L_1 L_2^2}{4 b d^3} \right) = \left(E^* + \frac{12\gamma}{d^2} \right) \tag{7.6}$$

7.3.2 Preliminary Experiments

One of the problems encountered when trying to determine the mechanical properties of the material from 4-point flexural tests was that two points of measurement were required to be taken for the vertical displacement of the sample while simultaneously recording the force which was imparted on the beam. Ideally, both the deflection at the point of loading and horizontal centre of the beam should be recorded simultaneously with respect to time.

In the experiment, the crosshead displacement and reaction forces were continuously recorded. The central deflection was determined by placing a dial gauge under the beam at the centre of the span. As the dial gauge was an analogue component independent of the testing machine, only the maximum displacement of the specimen could be obtained with any certainty. The variation in central displacement with the applied load could therefore not be determined. Instead, an estimation of the load which corresponds to this deflection was calculated from the gradient of the load-deflection plot at the point of loading and calculating the corresponding load when the actuator is fully displaced. While this is not ideal, it is the best estimation that could be made with the current setup.

The experiment was conducted under displacement control at a constant rate of loading. Once the support bar and two-point indenter were adjusted to the correct spacing, the beam sample was positioned in place taking care that the points of contact were aligned to the corresponding edge of the unit cell. The indenter was then brought into contact with the specimen until a small load was recorded on the system. The dial gauge was then centred with respect to the midpoint of the sample span and breadth before being adjusted until it was in contact with the bottom surface of the beam. At this point, the scale on the dial gauge was zeroed along with the linear actuator and load cell. By conducting the experiment in this manner, the maximum displacement recorded should be equal to the total deflection at the centre of the beam

relative to its initial position. Imparting a small pre-load to the specimen also has the effect of taking up any initial slack associated with the indenter coming into contact with the specimen, minimising any initial variation in the gradient of load-deflection slope which is not related to the mechanical properties of the material. Once each experiment was conducted, a MATLAB script was used to determine the gradient of the load-deflection response at the point of loading. The resulting data was then used to determine the variation in stiffness of each sample in the dataset.

In the first instance, the variation in stiffness of the samples was determined from the relative change in displacement between the point of loading and the centre of the span using equation 7.6. While this worked well under idealised static load conditions within the context of FE models, the experimental results did not display a variation in stiffness with respect to sample size which was in-line with the numerical predictions. It was observed that equation 7.6 was very sensitive to small variations in the relative displacement of the two points which had a large effect on the calculated beam stiffness. As a result, no clear correlation between sample size and stiffness variation was observed using this formulation. A typical plot of the results for one set of samples as compared with the FE simulations can be seen in figure 7.14. Results were normalised to take into account the variation in flexural modulus between the FE model and the physical material. It can be seen that while a general increase in sample stiffness was observed with decreasing size, the beam with two cells through the depth appears to be significantly stiffer than the other samples.

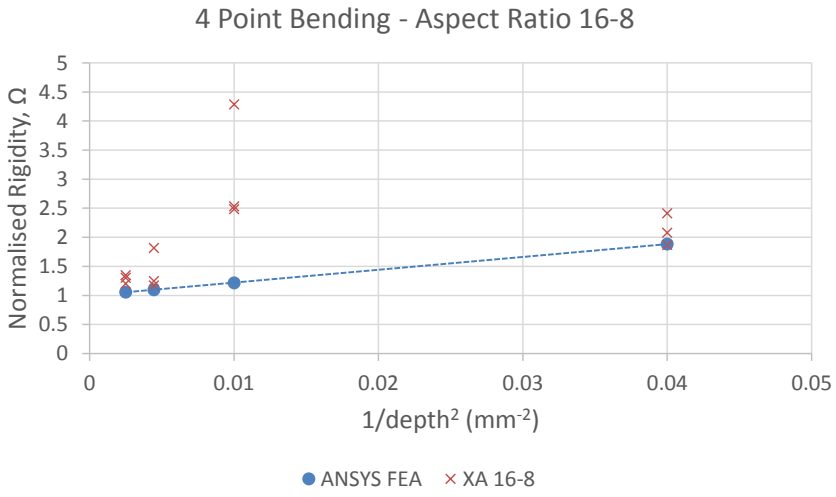

Figure 7.14: Comparison between normalised stiffness of FEA models with experimental samples. A poor correlation between sample size and stiffness is observed when equation 7.5 is used to derive the mechanical properties.

While the results derived from equation 7.4 are generally poor, it can be observed that some

experimental data closely matches the FE predictions. From analysing the results, it appears that the biggest discrepancy between the tests is the variation in deflection at the centre of the span. Under displacement control conditions, the central deflection should in theory be approximately the same for all samples assuming that the displacement at the point of loading is fixed. The variation in stiffness of individual samples is expected to be revealed in the reaction force which is recorded. It is therefore likely that either the displacement of the linear actuator does not fully represent the actual deflection at the point of loading or that the dial gauge measurement is inaccurate. As care was taken to make sure that the specimen was in contact with the indenter before recording the response, it is most likely that central deflection is not as expected. While this could be a result of inaccuracies in the dial gauge, it is unlikely as each experiment was repeated several times with similar deflections being recorded at the centre of the span. It may be that some samples are indeed stiffer, but the increase in stiffness which is predicted from this formulation appears to be unrealistic.

As only one point of reference was taken for the maximum displacement, an accurate representation of the stiffness of the section under load is reliant on a linear response being observed throughout the test. If the response of the material under test is not linear throughout the experiment, then it is possible that the observed stiffness taken from one point of reference may not be an accurate representation of the general response.

As equation 7.4 is very sensitive to small changes in the relative displacement between the point of loading and maximum deflection, the analysis was repeated by calculating the stiffness of the beams from the maximum displacement of the beam as derived from Euler-Bernoulli beam theory which was presented in equation 7.3. It is expected that the total deflection will have some contribution due to shearing at the outer sections of the beam sample in comparison to the central section which is not fully accounted for. However, the contribution due to shearing in the outer section should be minimal in comparison to three-point bending.

Rearranging equation 7.3 in terms of the aspect ratio of the inner and outer section that are under load, the apparent modulus which is dependent on sample size can be given as;

$$\begin{aligned}\left(E^* + \frac{12\gamma}{d^2}\right) &= \frac{P_{max}L_1}{4bd^3w_2}\left(3(2L_1+L_2)^2 - 4L_1^2\right) \\ &= \frac{P_{max}(AR_0 - AR_i)}{8bw_2}\left(3AR_o^2 - (AR_o - AR_i)^2\right) \\ \text{where } P_{max} &= \left(\frac{P}{w_1}\right) w_{1(max)}\ , \\ AR_o &= \frac{(2L_1+L_2)}{d}\ , \quad AR_i = \frac{L_2}{d}\end{aligned} \tag{7.7}$$

7.3.3 Experimental Results

Sets of 4 samples with similar aspect ratio but differing size were tested at two different spacing ratios in the manner described above. In addition to testing each sample at two differing indenter spacing ratios, the orientation of each sample within the testing machine was considered to check the transverse mechanical properties. As before, samples were printed in both the X and Y orientation within the printer to assess the performance of the material when the orientation of the layers is altered. The resulting experimental stiffness plots can be seen in figures 7.15 - 7.18. It was observed that a linear relationship was generally found between the variation in specimen stiffness with respect to the inverse of the depth squared for all sets of samples. Extreme outliers were excluded from the trend data but have been marked in red on the plots. The flexural modulus and characteristic length for each set of samples under test have been summarised in table 7.5.

Sample	Position	Aspect Ratio AR_o/AR_i	E^* (MPa)	γ (N)	l_b (mm)
X	A	16/12	441.4	660.7	0.896
X	B	16/12	443.3	746.6	0.918
Y	A	16/12	415.4	713.05	0.926
Y	B	16/12	374	919.4	1.109
X	A	16/8	423.5	667	0.887
X	B	16/8	452.7	765.1	0.919
Y	A	16/8	381.7	841.2	1.05
Y	B	16/8	385.6	968.3	1.12

Table 7.5: Summary of the results of the 4-point flexural tests.

Overall, the flexural modulus which was obtained from the experiments was reasonably consistent when the inner aspect ratio was reduced from 12 to 8 for samples printed in the same direction. The sample Y-A at an aspect ratio of 16-12 (See figure 7.18.) was the only exception to this observation, but this may be a result of a relatively poor linear extrapolation being observed in the experimental results. Removing the results for the sample with three cells through the depth from the analysis improves the results somewhat. The transverse flexural modulus obtained by rotating the samples by 90 degrees within the testing apparatus does not appear to be significantly different which indicates that the printed material displays cubic orthotropy which is consistent with the geometry of the lattice unit cell. Again, the orientation of the samples within the printer appears to be significant, with a decrease in stiffness being observed in samples aligned to the Y axis when compared to those aligned to the X axis of the printer.

While the flexural modulus appears to be reasonably consistent, the couple modulus, γ, obtained varies quite considerably. The primary reason for this is due to the fact that small

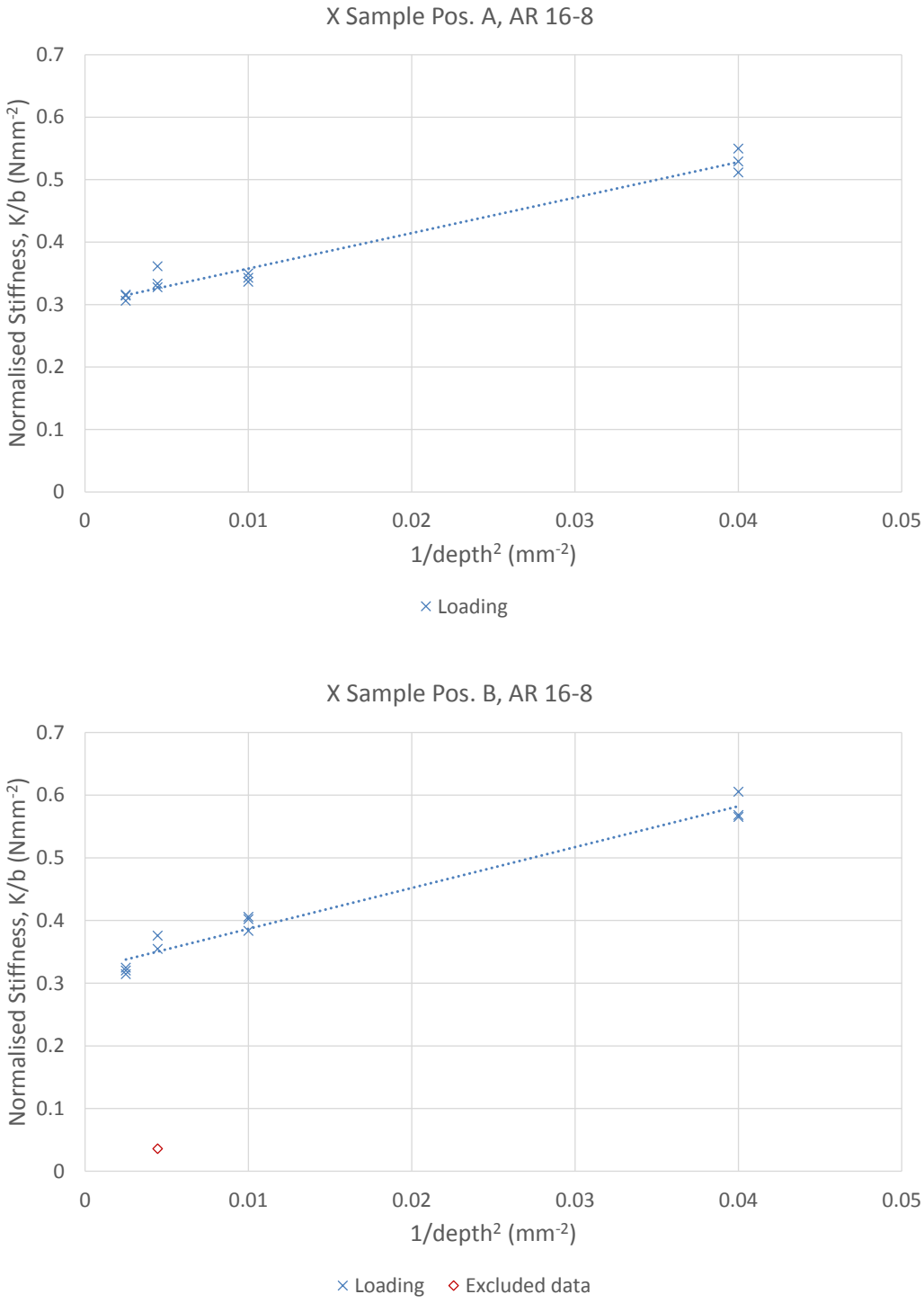

Figure 7.15: Variation in flexural stiffness with sample size at an aspect ratio of 16-8.

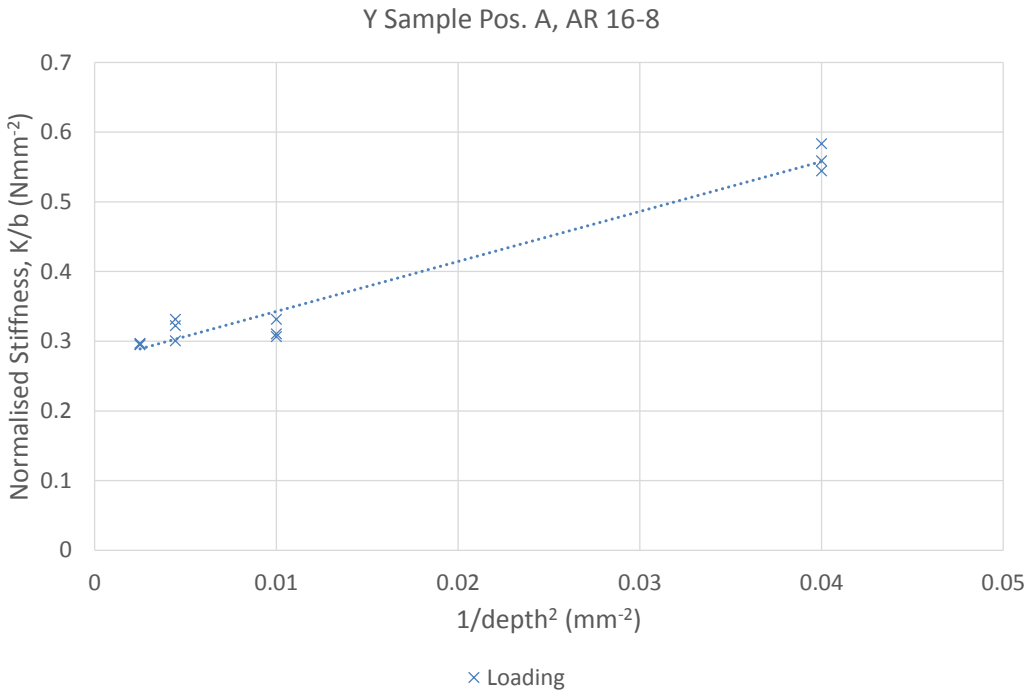

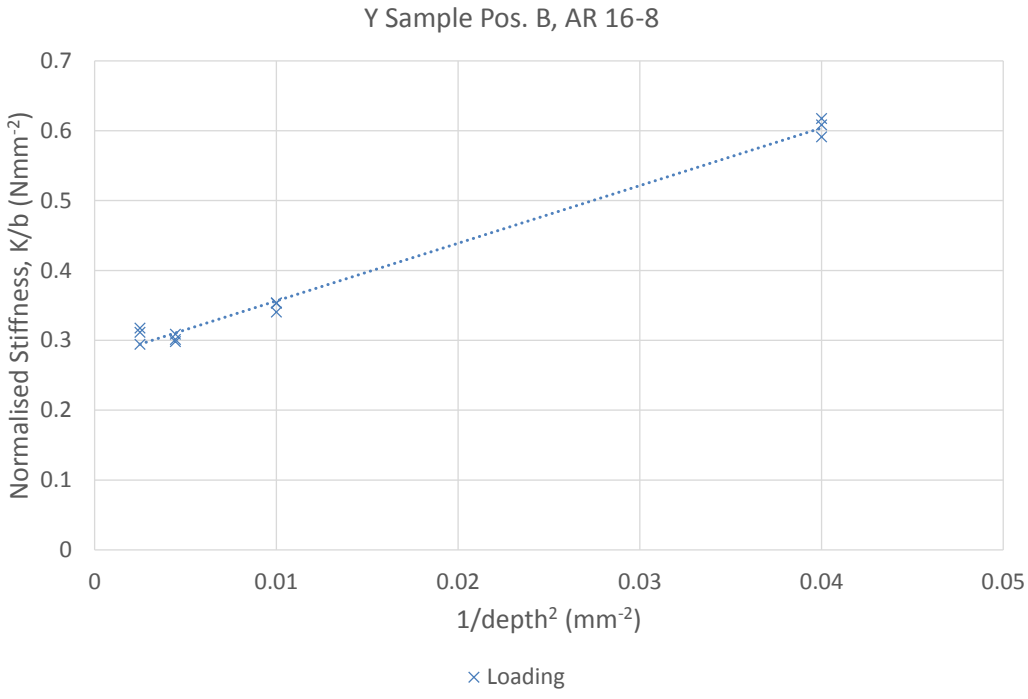

Figure 7.16: Variation in flexural stiffness with sample size at an aspect ratio of 16-8.

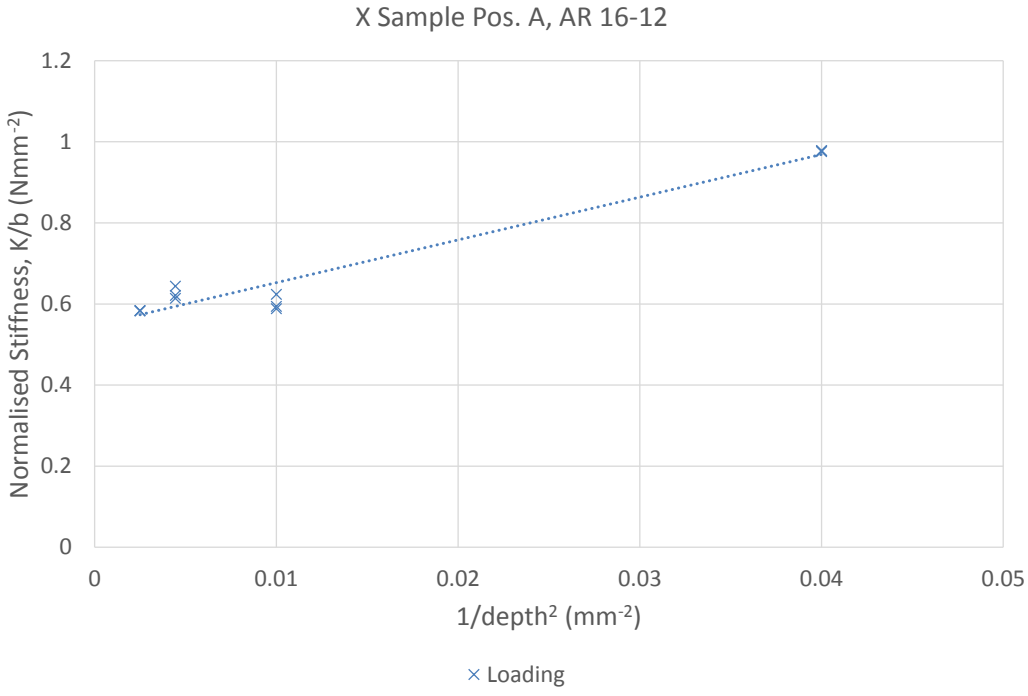

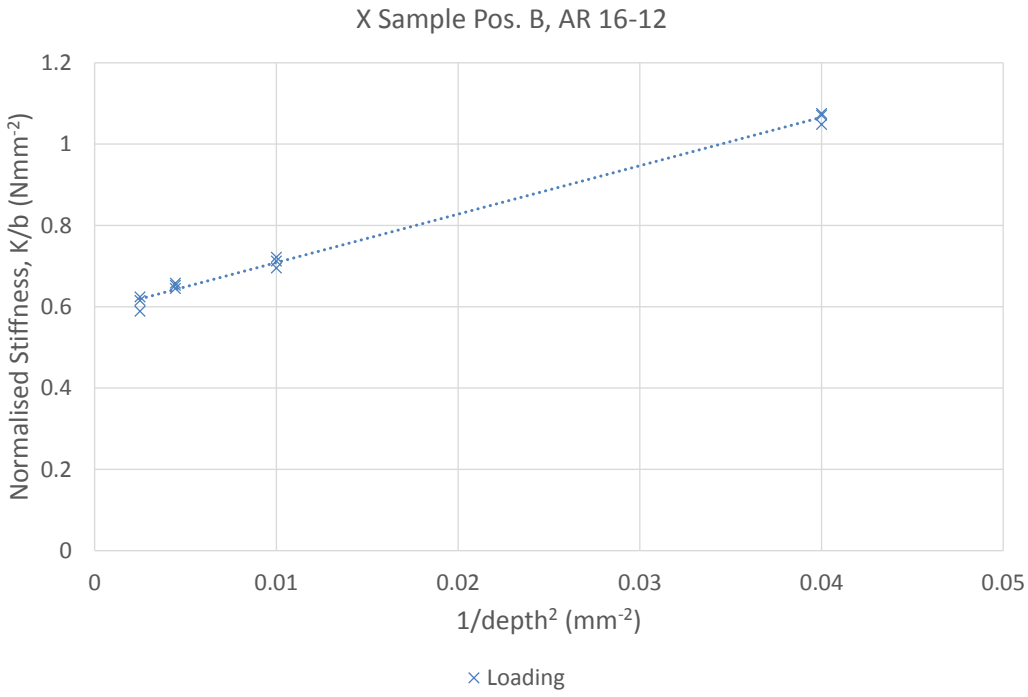

Figure 7.17: Variation in flexural stiffness with sample size at an aspect ratio of 16-12.

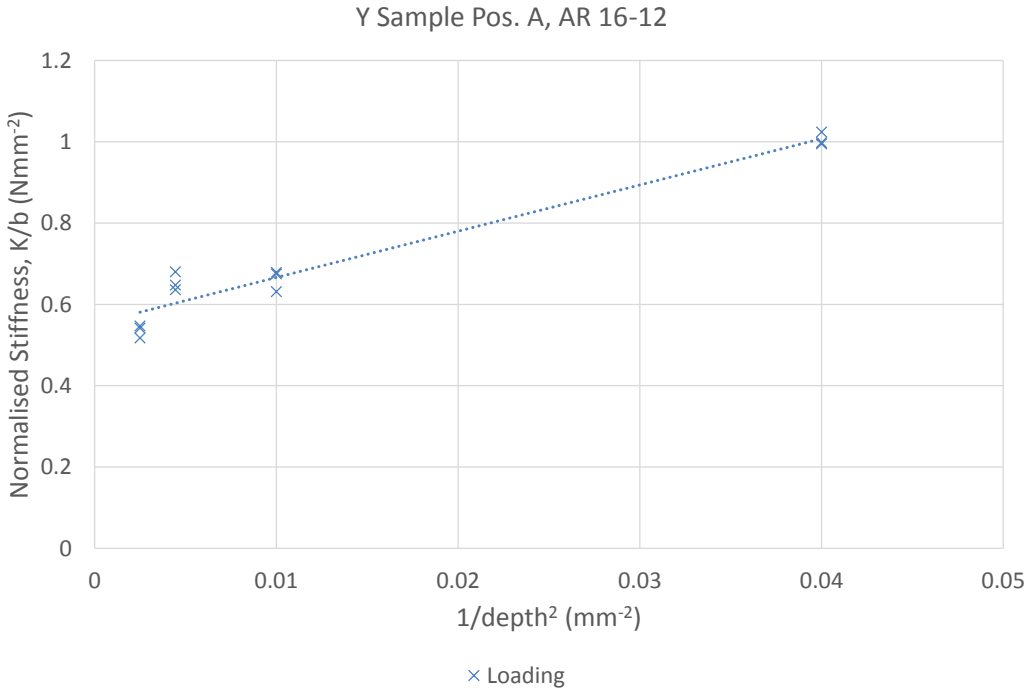

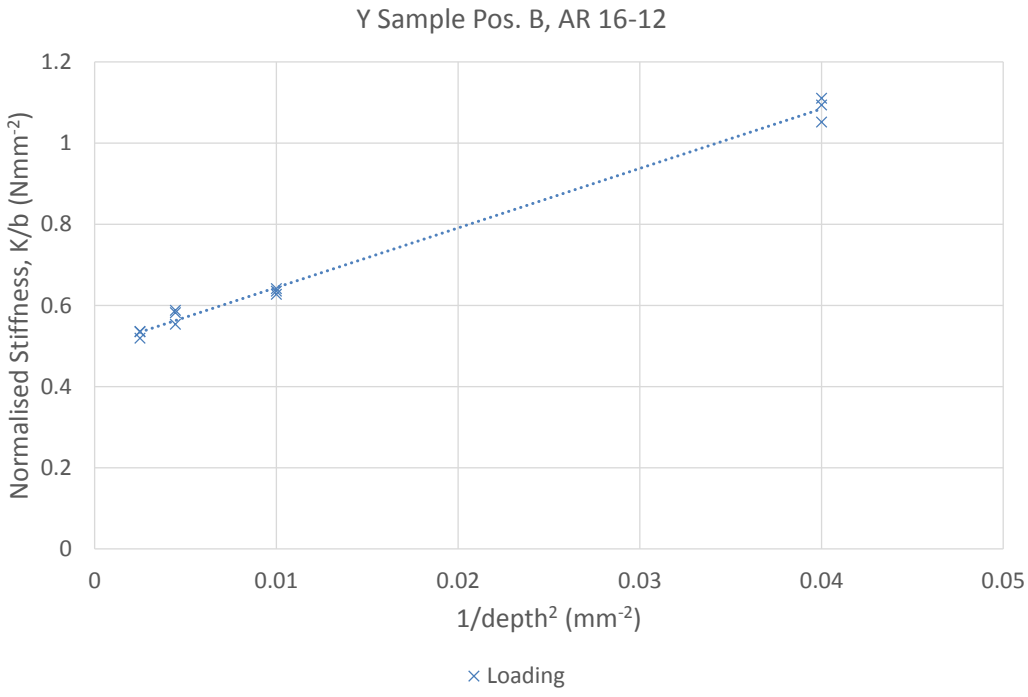

Figure 7.18: Variation in flexural stiffness with sample size at an aspect ratio of 16-12.

variations in the recorded stiffness of individual samples can significantly alter the gradient of the experimental slope which is used to derive this parameter. However, the characteristic length in bending that is obtained for the material is reasonably consistent irrespective of the test conditions.

In comparison to the three-point bend tests, the flexural modulus found from four-point bending appeared to be greater. This is expected as the total deformation is primarily due to bending within the beam with less influence due to localised shearing at a given aspect ratio.

Numerical FE simulations of the samples under four-point loading were also carried out. The results have been summarised in table 7.6 and compared to an equivalent sample of the material subjected to a constant moment load.

	E^* (MPa)	γ (N)	l_b (mm)
Pure Bending	360.2	667	0.962
$AR_o = 16, AR_i = 12$	361	663.8	0.959
$AR_o = 16, AR_i = 8$	360.6	662.3	0.958

Table 7.6: Micropolar properties from 4-point bending simulations in ANSYS.

It can be seen that at an inner aspect ratio of 12 and 8, the experimental micropolar flexural parameters are consistent with the results determined by applying a constant moment load. When the stiffness of each sample is normalised to take into account the variation in aspect ratio, the difference in stiffness of the individual corresponding samples is insignificant. This is an encouraging result as in comparison to the 3-Point bending tests, there appears to be less dependence on the overall aspect ratio of the samples meaning that a more accurate result could potentially be obtained from the limited sample sizes that can be manufactured in the 3D printer.

The flexural modulus which was obtained for the FE models was slightly smaller than the physical test specimens. This is expected however as the simulation was based on the lower estimate of the tensile modulus of the polymer which was determined experimentally. As it is a linear elastic static analysis, the results can be scaled as appropriate to fit the experimental data. No scaling should be required to correct the characteristic length as it is primarily a function of the cellular geometry.

It can be seen that the characteristic length for bending determined by the simulations appears to be very consistent with the experimental results. The characteristic length of the material was found to be in the range of $0.89 - 1.12$ mm, which is close to the value of 0.96 mm predicted in the FE analysis. While the modulus of the simulated material is slightly less stiff than that of the experiments, it is encouraging that the characteristic length is of similar size as this parameter should be modulus independent assuming that the underlying geometry

is the same. Indeed, by plotting the normalised simulated results alongside the experimental values, it can be observed that a good correlation exists (Figure 7.19).

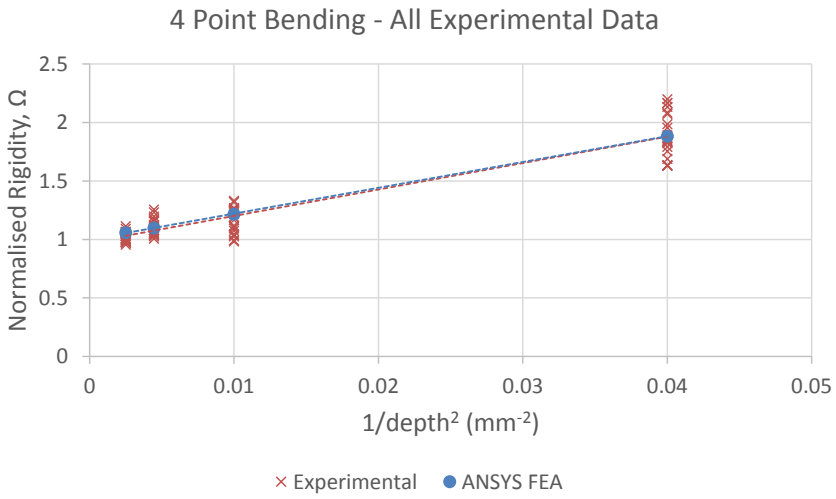

Figure 7.19: Variation in normalised flexural stiffness of all experimental data as compared with FE simulations in ANSYS. Data is normalised to account for the variation in sample breadth and test aspect ratio.

7.3.4 Discussion of 4-Point Experimental Results

The results of the experiment have shown that the lattice structure which was investigated exhibits size dependant variations in the stiffness which are consistent with a micropolar theory. A small degree of anisotropy was recorded when the samples were rotated by 90 degrees within the test apparatus, however the variation in flexural modulus was relatively small considering the inherent experimental uncertainties. By and large, the samples appeared to be slightly stiffer when rotated by 90 degrees from the original print direction. The characteristic length also appears to be marginally greater in this configuration.

The results of the experiment are a good indicator that the FE element simulations sufficiently represent the physical behaviour of the structured lattice material. The simulations do not inherently capture the small variations in the mechanical properties which can be observed due to the polymer matrix material and the sample manufacturing process. While further tests may be required to isolate experimental variations from localised mechanical behaviour, it is expected that the FE models could be improved with a more detailed material model that accounts for any directional variation in the polymer. The general purpose of this experiment however, was to verify that the size dependent nature of the manufactured material was primarily a response of the underlying microstructural distribution. An isotropic matrix material is

favourable in this situation as the number of variables which need to be resolved are minimised. While the polymer matrix material is not completely isotropic, the influence due to any anisotropies appears to be minimal as compared to the size effect which is observed, which suggests that the 3D printing technology used is a suitable tool for manufacturing novel heterogeneous solids.

It is recommended that in order to improve the accuracy of the experimental results obtained by 4-point bending, that continuous displacement measurements should be recorded at both the point of loading and sample centre throughout the experiment to enable a more accurate depiction of how the reaction forces vary with the displacement over time. The ratio of support span to indenter spacing did not appear to have any significant influence on the mechanical properties which were obtained experimentally, although this may be a more important factor in very low density materials where localised shearing may become a significant contributing factor.

7.4 Summary of Flexural Testing Experiments

In this chapter, 3-point and 4-point flexural tests were conducted on samples of a porous heterogeneous solid manufactured in a 3D printer. It was shown by the method of size effects that this material is capable of exhibiting a variation in flexural stiffness corresponding to specimen size that is consistent with a micropolar elastic solid. The magnitude of the size effect and flexural modulus observed was also shown to be comparable to numerical FE simulations of a geometrically similar material constructed from an isotropic linear elastic solid matrix.

The experiments conducted in four-point flexural loading were observed to provide a more accurate estimation of the micropolar properties of this material at a length to depth aspect ratio of 16 when compared to three-point bending experiments. However, the accuracy of the results was largely dependent on careful sample preparation and experimental techniques being adhered to. The procedure for three-point loading is simpler, although the observed properties are largely influenced by the sample aspect ratio. Very slender samples may be required to accurately characterise low density cellular solids which may not always be practical. While it has been demonstrated that this mode of loading is sufficient to characterise denser samples, a convergence study may be required to confirm that any variation in stiffness (or lack thereof) is related to sample size rather than test aspect ratio. The maximum size of the sample which could be tested by the method of size effects was limited by both the build capacity of the 3D printer and the available experimental apparatus. While testing 4 samples was found to be sufficient in this case, a greater number of increasing size may be required for other materials.

It has been shown that the 3D printing process is capable of producing material samples which can be used to adequately characterise the size dependant mechanical properties which

are seen in micropolar materials. A limitation of this technology however, is that the materials generated in this manner are restricted in size by the print area of the machine, limiting potential uses to small scale applications. However, developing a clear understanding of the mechanical properties of such materials may lead to increased utilisation when the technology allows for greater production sizes and volumes.

While the printed material does exhibit some viscoelastic effects in flexure which can be attributed to the printed photopolymer, it was observed that this could be minimised by loading samples at an appropriate rate. The orientation of the samples within the printer during manufacturing also had an effect on the stiffness of the samples, with those aligned to the X axis being noticeably stiffer than samples aligned to the Y axis. This was primarily attributed to the sequential layering process during manufacturing. The calculated characteristic length of the material was also observed to show some variation due to sample print orientation, however the overall variance was small and hard to distinguish from other experimental errors. Sets of samples should therefore always be printed at the same orientation in order to capture the correct response of the material. Individual samples also display some anisotropy in the orthogonal axis, but the variation in stiffness appears to be less significant.

Improvements that could be made to the experimental process include taking displacement measurements that are independent of the mechanical apparatus in both the 3-point and 4-point flexural tests. A continuous measurement of the central deflection in the 4-point tests may also improve the results in that mode of loading. Furthermore, testing multiple samples of similar size that were manufactured to the same specification would also be preferential to differentiate between experimental errors and variations in the samples. Overall though the initial investigations that have been carried out here indicate that the material performs fairly consistently in accordance with the numerical predictions of the FE models.

Chapter 8

Experimental Analysis of a 3D Cellular Lattice in Torsion

In the previous chapter, the flexural properties of a material composed of a cubic lattice cellular microstructure was measured experimentally by the method of size effects to obtain both the flexural modulus and characteristic length in bending. To fully define the material in the context of a micropolar continuum, additional elastic constants are required to be determined.

In this chapter, samples of the material were tested in torsion to determine the experimental shear modulus, G^*, and characteristic length for torsion, l_t. These values were then compared to those which were determined by the FE numerical simulations presented in chapter 4.

The cubic lattice structure investigated was shown to be capable of displaying size effects in line with the numerical FE simulations, however some discrepancies were observed with the magnitude of the characteristic length. Generally the shear modulus was in line with the numerical predictions. It is recommended that further tests should be carried out in order to clearly define if the variations are a direct result of the manufactured material or an improved experimental setup is required.

8.1 Introduction

Numerical simulations performed in chapter 4 indicated that a material which consists of a regular array of 3D cubic lattices may exhibit size effects consistent with a micropolar elastic solid when constrained by boundary conditions which simulate twisting about the longitudinal axis of a slender bar.

While the flexural testing of heterogeneous materials which exhibit size-scale dependant properties can be relatively straightforward and is fairly well-discussed within the literature, few experimental tests have been performed to determine how such materials perform when loaded in torsion. The majority of experimental torsional tests on materials which display micropolar properties have been conducted in collaboration with R. Lakes et al. (e.g. Lakes (1983, 1986); Rueger & Lakes (2016)). Generally speaking the research has focussed on materials with a stochastic microstructure such as bone and open or closed cell polymer foams to identify the additional higher order constants. Here, the shear modulus and characteristic length are typically determined from the method of size effects by testing samples of ever decreasing diameters under torsion. The coupling number, N and polar ratio, ψ are interpreted by matching the experimental data to analytical predictions.

Typically, a broadband viscoelastic spectrometer was utilised in the experiments to generate a torque on cylindrical specimens while minimising any external frictional forces which may affect the results. Due to the stochastic nature of the materials, careful sample preparation is needed to minimise the influence that surface damage may have on the results as partially exposed cells on the exterior surfaces may introduce localised variations in specimen stiffness. This problem is not unique to torsion and is a fundamental consideration in many research papers concerning materials which show some size-scale dependence (Brezny & Green, 1990; Tekoglu & Onck, 2008; Frame, 2013).

The standard method for determining the shear modulus and torsional stiffness of a homogeneous solid usually involves manufacturing solid cylindrical test specimens of uniform cross-section. Cylindrical samples are preferred since sections which are plane before twisting are predicted to remain plane when twisted about the central axis of the shaft, making the experimental analysis relatively straightforward. Testing non-circular uniform bars in torsion is more complex since sections do not necessarily remain plane when twisted and are inclined to warp due to variations in localised shear stresses around the perimeter of the cross-section. In order to account for this, a warping constant is introduced which is unique to the shape of the sample section. The warping constants for standard solid sections made from simple geometric shapes have been well-established in the literature and can be found in any good engineering text book (e.g. Roark et al. (2002)).

In the case of heterogeneous solids, particularly those with a stochastic microstructure and

high levels of porosity, it has been shown that sample preparation is a highly influential factor when attempting to derive the material constants (Brezny & Green, 1990; Tekoglu & Onck, 2008; Frame, 2013). The cubic lattice microstructure previously defined has a regular periodic structure which is more suited to a structured cuboidal specimen rather than circular cylinders. In this configuration, the specimens can be manufactured without compromising the structure of the cells which define the material. Creating a circular sample would involve exposing the cellular structure at the surface by varying degrees introducing large uncertainties in the analysis. It was therefore decided that a set of rectangular bars consisting of a square cross-section would be manufactured in the same manner as the flexural specimens by varying the number of cells through the sample depth and breadth to asses the mechanical properties.

It is the aim of this chapter to determine if the size effects which have been predicted numerically can be observed in physical experiments. As before, the samples were manufactured by additive processes in an Objet Eden 350 printer by Stratasys Ltd. utilising the photopolymer VeroBlack Plus.

8.2 Experimental Procedure

Experiments were conducted on an Instron ElectroPuls E10000 Linear-Torsion test instrument with a load cell which had a 25 Nm torque capacity and a linear limit of 1 KN. In order to transfer the applied rotational displacement from the actuator to the specimen, a set of custom grips were manufactured which were designed to minimise any axial restraint, enabling the samples to warp freely under loading if desired.

Each grip consisted of an aluminium cylinder which had an array of evenly spaced stainless steel pins inserted onto one face to coincide with the voids in the cellular structure of the test specimens. This enabled the pins to insert directly into the samples. The diameter of the pins used in the grips was 2.5 mm , which was similar in size to the 3 mm square voids within the specimens. A top down view of one grip has been included in figure 8.1 with the cross-section of a typical sample superimposed to indicate the placement. All samples were aligned and centred to the vertical axis of the actuator. Two sets of grips were therefore required to be manufactured to take into account the difference in positioning between samples with either an odd or even number of rows of microstructure through the cross-section. The diameter of the grips were made sufficiently large, that any angular rotation through the length would be negligible under test conditions in comparison to the sample being tested. Stainless steel pins were also chosen with this in mind, due to the fact that it is significantly stiffer than the photopolymer used to construct the test specimens. Detailed engineering drawings of the specimen supports are included in appendix C.2.

As the grips used in the experiments are not a standard configuration, a detailed FE analysis

was undertaken to determine how the pins would interact with the specimen. It was found that some differences were apparent between the shear modulus and characteristic length which were obtained from the FE analysis with the grips included rather than ideal pure torsion boundary conditions, but the variations were reasonably small and deemed acceptable in the context of experimental tests. The full results of this analysis can be seen in appendix B.

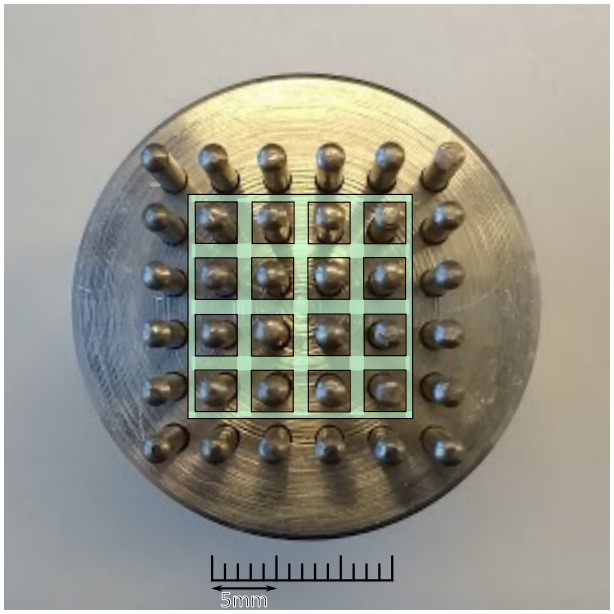

Figure 8.1: Top down view of a grip used to constrain the samples with an even number of rows. The cross-section of a 4×4 specimen has been superimposed to indicate the typical specimen placement.

In order to fully capture the size dependent response of a micropolar material under torsion, a sufficiently large set of samples must be tested at differing sizes to observe any localised variation in stiffness and determine the additional material parameters. Two considerations are required to be made here. The first is that the samples should be small enough to capture the response of the material as it tends towards the size of the dominant microstructural features, which in this case is the unit cell. Larger samples are also required to be tested to determine the converged shear modulus and the magnitude of the size effect.

Ideally samples with a fixed length to depth aspect ratio would be tested to reduce the number of experimental variables. However, as both the equipment which was used to manufacture and also test the samples was constrained by an upper size limit, then a trade off was required to be found between testing slender specimens and having a large enough data set to fully capture the intrinsic behaviour of the material. Initial FE simulations conducted in ANSYS using both restrained and unrestrained boundary conditions suggested that varying the aspect ratio of the bars with a square cross-section had little influence on the calculated material properties.

It was therefore decided that samples of fixed length would be tested instead to maximise the range of samples which could be manufactured.

In total six samples were manufactured with between 1 and 6 cells through the depth of the sample (Figure 8.2). Each sample had a fixed length of 170 mm and a square cross-section. Due to the nature of the grips that were used for the experimental procedure, the smallest sample with only one unit cell in the cross-section was not included in the experiment as this sample did not provide enough points of contact with the grips to be restrained within the apparatus.

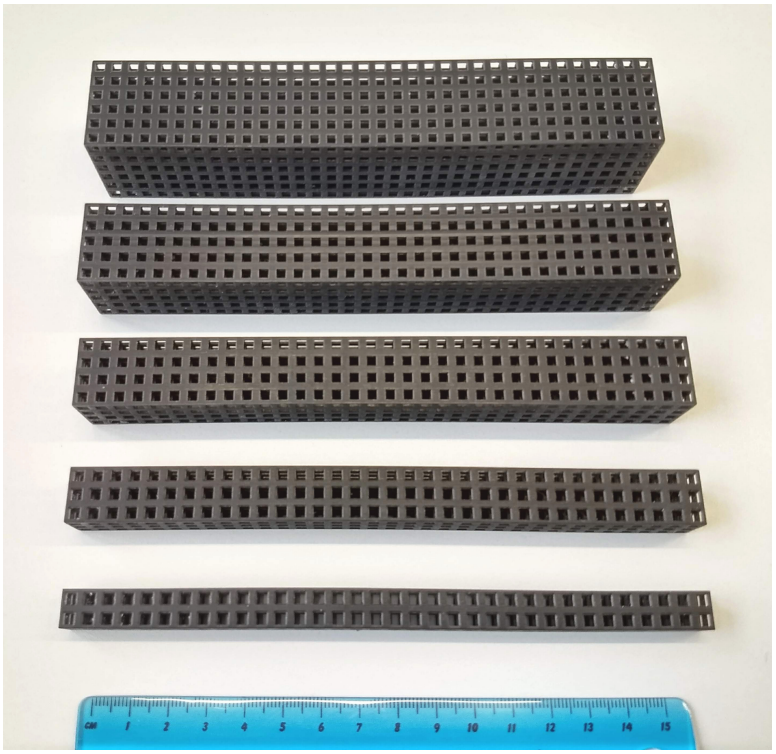

Figure 8.2: A typical set of samples used to investigate the torsional properties of the material.

The FE analysis of the experiment suggested that the depth which the pins were inserted into the samples may influence the observed material properties. With this in mind, insertion depths of 1 and 10 mm were investigated. The rate of loading was also studied to determine if this was an influential parameter. As with the flexural tests, a set of samples have been manufactured which were aligned to both the X and Y orientation in the 3D printer. Unlike in the bending case however, only one set of measurements is required to be taken per sample as the torsional properties are dependent on the combined influence of the layers within the sample.

Before inserting a sample, the top and bottom grips were aligned so that the sample was free to slide vertically. The tests were conducted by first inserting the specimen into the testing

apparatus to the specified depth. A small initial torque was applied to the specimen by rotating the actuator in order to provide enough force to hold the sample in place by friction between the pins and the contact points on the sample. The specimen was then loaded at the specified rate for a 10 second interval. Each sample was held in place for 30 seconds to gauge the viscoelastic response of the material in torsion before being unloaded at the initial rate. A diagram of the experimental setup with a sample in situ can be seen in figure 8.3.

After the experiments were complete, the resulting raw data was processed to extract the linear response between the applied torque and the angle of rotation to determine the torsional rigidity of each specimen.

As was discussed in chapter 4, the exact solution for the torsional rigidity of a micropolar bar of square cross-section was simplified to reduce the number of variables which are required to be obtained in the solution. The characteristic length for torsion, l_t, which defines the magnitude of the size effect can be expressed in terms of the torsional rigidity, J', of a uniform bar as:

$$J' = G^* \left[I_p + 2{l_t}^2 d^2 \right] \tag{8.1}$$

where G^* is the micropolar shear modulus, I_p is the warping constant of the section and d is the sample depth. By plotting J'/d^2 against d^2 it is possible to identify the shear modulus, G^*, from the gradient of the linear portion of the slope which can be observed when a large enough set of sample of increasing size are tested. The characteristic length, l_t, is interpreted from the intercept with the vertical axis from the linear gradient.

8.3 Results of the Torsion Tests

After the data for each test was collated, a plot of the variation in torque with applied angle of rotation was generated to obtain the stiffness of each individual sample. The shear modulus and characteristic length for torsion were then estimated by plotting the torsional rigidity divided by the square of the depth vs. the depth squared for each individual set of samples. A typical set of results can be seen in figures 8.4 and 8.5.

In general a linear variation in torque with applied angle of rotation is observed when the individual samples are tested. The hysteresis loop which can be observed in figure 8.4 indicates that some stress relaxation is taking place in the material when the sample is held in position at the point of maximum loading. As this did not appear to have any significant effect on the gradient of the response recorded, it suggests that the rate of loading is sufficiently fast to ignore this effect.

In total, 5 samples of fixed length were tested with a varying number of cells through

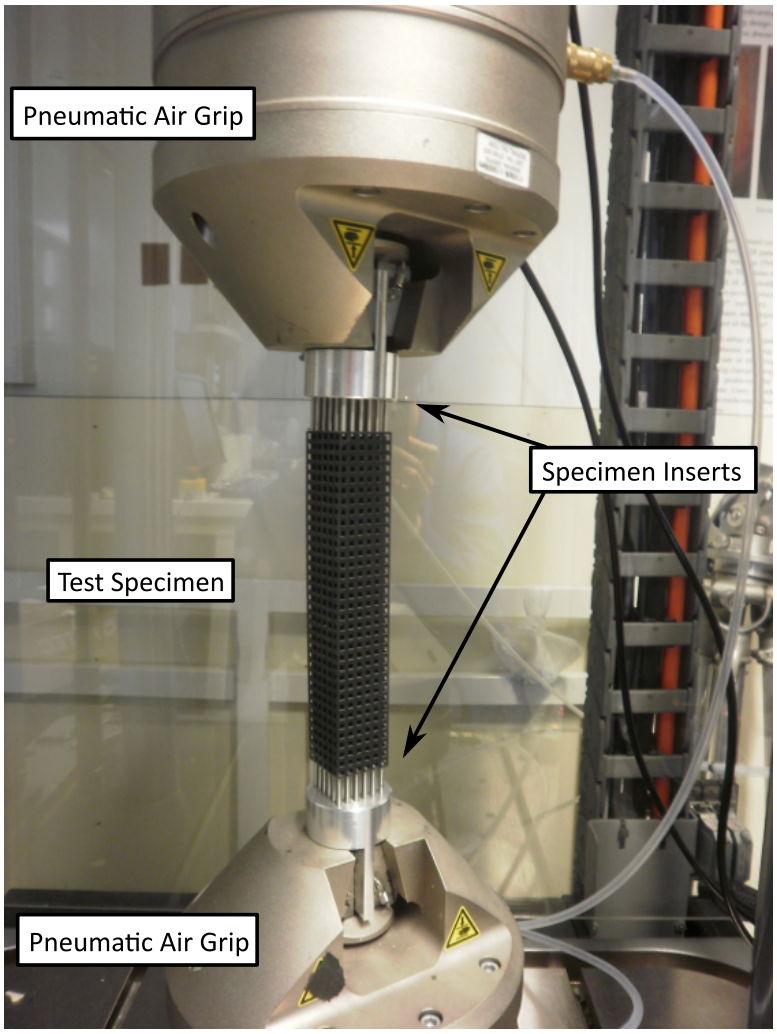

Figure 8.3: A specimen loaded in torsion. The load cell and rotational actuator not shown in this picture are connected to the upper pneumatic air grip.

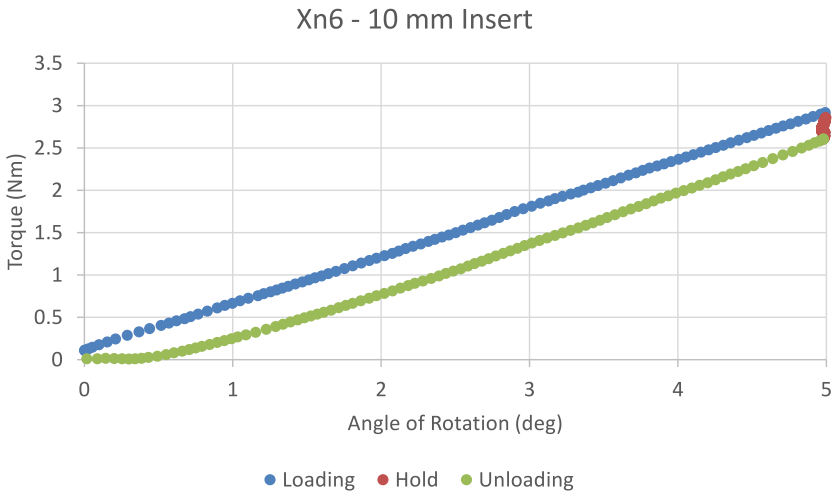

Figure 8.4: Variation in torque with applied angle of rotation for a beam printed in the x orientation with 6 rows of cells through the breadth and depth. The sample stiffness can be interpreted from the linear region in the loading and unloading slope.

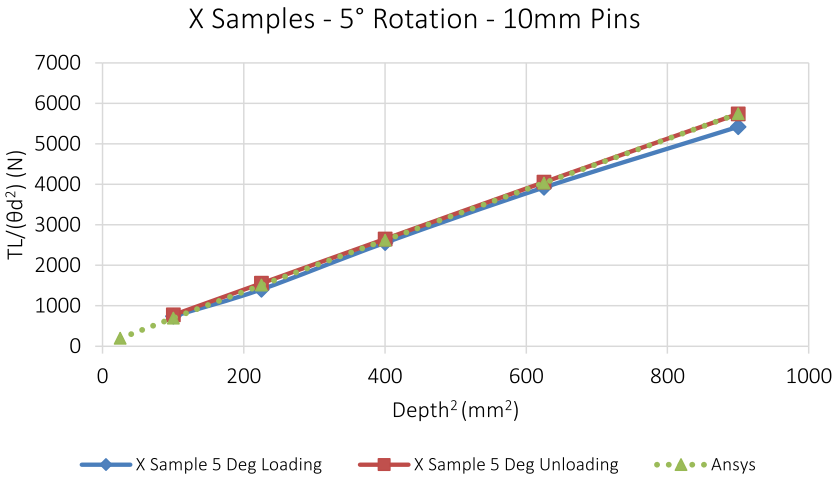

Figure 8.5: Variation in the torsional rigidity of the material at varying size scales when printed in the x orientation. Here, pins are inserted 10 mm into each sample under test.

the depth of the specimen. The experiments which were performed looked at both the insert depth of the pins used to restrain the samples and the rate at which the load was applied to the specimen. The converged shear modulus calculated was reasonably independent of the samples which were used and the designated loading conditions, ranging from between 41 - 44 MPa. This compared comparatively well to FE simulations of the bars subjected to pure torsion boundary conditions with unrestrained warping that predicted a micropolar shear modulus of 44.8 MPa.

While the converged shear modulus obtained was in-line with the simulated predictions, the stiffness of the individual beams displayed some localised variation. This can be clearly seen in figures 8.6 & 8.7 which show how the relative stiffness converges with increasing sample depth for pin insert depths of 1 and 10 mm respectively. The stiffness in this case has been normalised by the homogenised warping constant and tends towards the shear modulus of the material with increasing specimen size. It should also be noted that the scale of the vertical axis in these figures was chosen to clearly identify any differences between the samples.

Generally speaking the discrete sample stiffness converges asymptotically towards a minimum value with increasing sample size which is in-line with the analytical theory and numerical FE predictions. In the case whereby the pins are only inserted 1 mm into the specimen, it can be observed that in general there is very little variation between the stiffness of samples orientated in the X or Y direction during the printing process. The rate at which the load was applied did not appear to have any significant influence in this case. When the experimental data is compared to the FE analysis, it can be seen in figure 8.6 that when there are two rows of voids through the breadth and depth that the sample is significantly stiffer than was predicted by the simulation. As the number of cells through the depth is increased, the observed change in stiffness appears to follow the FEA predictions more closely however it appears slightly more compliant.

When the experiment was repeated with the pins inserted 10 mm into the samples, a similar trend to figure 8.6 was observed, but a larger degree of uncertainty appears to be present within the results. From figure 8.7 it can be seen that stiffness of the samples with two cells through the depth falls within the range of the FE predictions, but a substantial variation in stiffness is recorded for similarly sized samples. As in the previous case the samples appeared to be slightly stiffer when unloaded. It is hard to draw a conclusion into which parameter has the greatest influence as there were only one set of each sample available to test, but it is likely that the angle of rotation may have some influence as the total torque which is imparted is dependent on both the sample length to depth aspect ratio and the angle of rotation which may introduce more uncertainty when low loads are applied. However, as the results were fairly consistent when the pins were only inserted 1 mm, it is likely that the increased pin depth is also a significant factor.

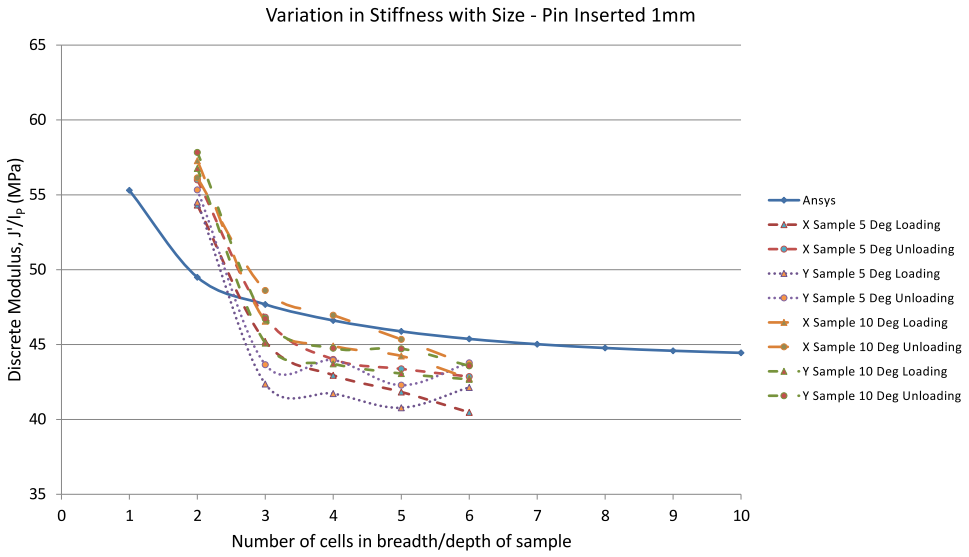

Figure 8.6: Variation in discrete sample stiffness with size. Pins are inserted to a depth of 1 mm.

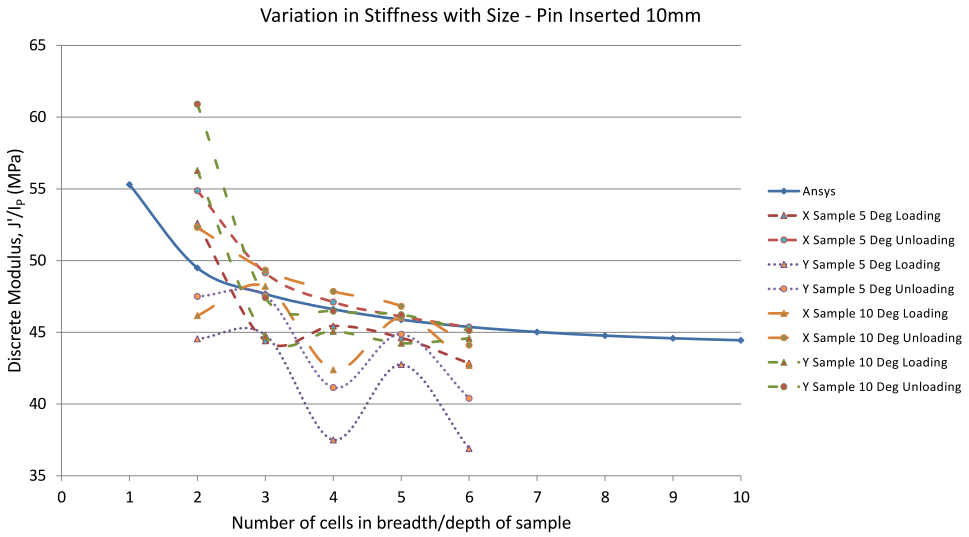

Figure 8.7: Variation in discrete sample stiffness with size. Pins are inserted to a depth of 10 mm.

A value for the characteristic length in torsion, l_t, was determined from each group of samples and compared to the FE predictions. As the smallest specimen was observed to be generally stiffer than the FE predictions, it was discounted from the analysis. The set of data used was deemed suitable if the R-squared value of the linear portion was greater than 0.99 and 3 or more data points were available. The results of each test have been summarised in tables 8.1 & 8.2. In the experiment whereby the pins were inserted 1 mm into the specimen, the characteristic length was observed to vary from between 1.1 - 1.75 mm. By comparison, the FE analysis predicted a characteristic length of approximately 1.09 mm. In the analysis, a characteristic length could not be obtained for the Y specimen rotated to 5 degrees as a negative size effect was observed. As this goes against the general trend of the other tests, it is safe to say that the results in this case are not correct. This highlights the need for implementing rigorous experimental procedures in order to minimise the chance of erroneous results. It also highlights one of the difficulties that exists with characterising materials with significant microstructure.

In the case of the 10 mm tests, the R-squared value of the linear extrapolation was slightly smaller for some sets of data when compared to the previous set of tests. The characteristic length obtained in this case varied from 1.13 - 1.97 mm.

5° rotation.					
Sample	Phase	R^2	G^* (MPa)	${l_t}^2$ (mm^2)	l_t (mm)
X	Loading	1.0	38.93	2.81	1.68
X	Unloading	1.0	41.64	1.82	1.35
Y	Loading	0.999	41.87	-0.17	Invalid
Y	Unloading	0.999	43.46	-0.08	Invalid
10° rotation.					
Sample	Phase	R^2	G^* (MPa)	${l_t}^2$ (mm^2)	l_t (mm)
X	Loading	0.999	41.54	2.22	1.49
X	Unloading	0.999	41.88	3.05	1.75
Y	Loading	1.0	41.87	1.23	1.11
Y	Unloading	1.0	42.70	1.55	1.25

Table 8.1: Observed shear modulus and characteristic length in torsion for experiments conducted with a pin depth of 1 mm.

8.4 Discussion

From the results of the experiments, it can be seen that minimising the contact applied between the pins and the sample appears to give more consistent results compared to when the grips

5° rotation.					
Sample	Phase	R^2	G^* (MPa)	${l_t}^2$ (mm^2)	l_t (mm)
X	Loading	0.998	42.22	1.73	1.316
X	Unloading	1.0	44.10	1.998	1.41
Y	Loading	0.975	35.85	3.897	1.97
Y	Unloading	0.988	39.23	3.24	1.80
10° rotation.					
Sample	Phase	R^2	G^* (MPa)	${l_t}^2$ (mm^2)	l_t (mm)
X	Loading	0.993	41.96	2.00	1.41
X	Unloading	0.998	42.45	3.29	1.81
Y	Loading	1.0	44.36	0.19	0.44
Y	Unloading	1.0	44.43	1.276	1.13

Table 8.2: Observed shear modulus and characteristic length in torsion for experiments conducted with a pin depth of 10 mm.

are inserted further to make contact with multiple cells in the sample. Extending the depth to which the pins are inserted may have the effect of reducing the overall rotation across the length of the sample since the pins will be in contact with multiple cells at one time.

Another possible source of uncertainty is that the gauge length used was based on the portion of the beam not constrained by the pin inserts. As the angle of rotation in the test was based upon the machine displacement rather than the localised measurements on the sample surface, it is possible that there is some uncertainty in this measurement. This would partly explain why the 10 mm tests were less accurate as the variation in displacement angle between the gauge points and the machine may be more significant.

Having said that, there was no significant difference between the shear modulus which was obtained for each test configuration. The largest degree of scatter appeared when the smallest sample was tested, which suggests that at very low loads, the experimental setup is more sensitive to variations when the pins are inserted further into the sample.

Experimentally, it was harder to determine the mechanical properties in torsion when compared to the flexural tests. The results presented here were interpreted by plotting the variation in torsional stiffness against the sample depth squared rather than the inverse of sample size which was used in the bending experiments. This is primarily because it is predicted that materials with a coupling number that is less than 1 will display a non-linear variation in stiffness as the number of cells through the depth approaches zero. When the inverse of sample size is plotted, variations in the stiffness of individual samples are amplified on the small scale, making it hard to extract an accurate linear response. While this had no significant effect on

the plotted data in flexure when the samples investigated were slender, it was observed that in torsion, the variation in stiffness was distinctly non-linear for small samples when the data was plotted in this manner.

The maximum capacity of the load cell in the Instron machine is 25 Nm, which was the smallest unit available at the time of testing. One trade-off that was required to be made with this experiment is that a balance needs to be found for the range of loads applied to the samples. This is due to the fact that the aspect ratio of the samples varies, meaning that the applied torque required to impart a given rotational displacement decreases with increasing aspect ratio. As the internal size dependent length scale parameter is measured by the relative change in stiffness between the samples then small uncertainties in the measurements may be significant. The maximum applied torque to rotate the beam with 2 cells in the depth was approximately 0.1 Nm and for 6 cells it was in the region of 6 Nm. While the rotational load applied to the most slender samples is at the lower end of the load cell capacity, the response of the material was found to be linear under test, with very little noise generated in the output. This is a trade-off which has had to be made however, as the overall size of the sample which can be manufactured and also tested was limited by the available equipment.

The characteristic length, l_t, which was obtained for the material in torsion was found to vary from between 1.11 - 1.97 mm . The results of the idealised FE analysis in ANSYS suggested that l_t was approximately 1.14 mm with unrestrained boundary conditions, while the FE model of the experimental setup (see appendix B) predicted that l_t was in the range of 1.38 - 1.51 mm . While the variation in the experimental value and idealised prediction appears to be quite substantial, it is encouraging that it is in-line with the prediction of the FE model of the assembled apparatus. One notable difference between the idealised simulations and the physical tests was that the sample with a 2×2 cross-section was markedly stiffer than the FE predictions. This was also noted in the FE model of the experimental apparatus, which suggests that this increase in stiffness is a result of the experimental setup rather than a characteristic of the material.

8.5 Conclusion

While the results of the experiments show reasonable agreement with the FE predictions, it can be clearly seen that some variation does exist. One of the inherent problems associated with quantifying localised variations in stiffness of a material across various size scales by the method of size effects is that small variations in the stiffness of individual samples can have a large effect on the stiffness variation which is required to predict the converged parameters. While it can be observed that there is a relative increase in stiffness with decreasing sample size in comparison to the classical case, the rate at which it increases is seen to go up with

diminishing size close to the origin. Therefore, to calculate the converged shear modulus and characteristic length, a suitably large sample set has to be considered. The variation in stiffness close to the origin is useful however in determining the coupling number and polar ratio of the material, although no attempt to do this was made in the above analysis.

The polymer used to construct the samples does show some signs of being viscoelastic when loaded in torsion which is consistent with the flexural tests. Stress relaxation can be observed when the samples are held in position at the point of maximum load, but in general a linear response between torque and angle of rotation is seen when the sample is loaded and unloaded which suggests that the rate of loading used was appropriate for the test. The local variations in stiffness of the samples which were observed are therefore likely to be a result of the experimental apparatus and the depth at which the pins were inserted into the samples. Some variation was also observed due to the direction of the layers within the material and the angle to which the samples were rotated, but as it is relatively small, a larger set of samples would be required to be tested in order to categorically verify this.

As the idealised FE analysis of the beams indicated that there was no significant difference between samples which were free to displace axially and the fixed boundary conditions for slender bars subjected to torsion, then it is likely that constraining the samples may allow for more consistent results to be found as the experimental procedure may be simplified. Another possible way in which the experiments could be improved is to measure the angle of rotation of the bar relative to the loading points in the sample rather than the machine displacement in order to minimise any localised variations in the experimental apparatus which may be affecting the results. While this can be obtained manually with the aid of some markers and video recording equipment, unless there is automated feedback to the load cell within the testing apparatus, it is hard to determine how this varies with respect to time. In general, taking only one measurement point is unreliable since there is no way of determining the variation in slope with time.

While there appears to be less variation in the stiffness of individual samples of similar size when the pins are only inserted 1 mm into the bars under investigation, the sample which has 2×2 cells in the cross-section shows a marked increase in stiffness, the magnitude of which is not predicted by the idealised FE simulations. As it has been indicated by the analysis which was conducted in appendix B that this may be a result of the experimental apparatus, then it may be necessary to revise the experimental procedure in order to adequately characterise the mechanical response as the sample size diminishes. Nevertheless, it appears that a reasonable estimation of both the shear modulus and characteristic length of the material can be made for this material with the resources which were available.

Chapter 9

Summary, Future Work & Conclusions

In this chapter, the results of the numerical simulations and experimental tests are discussed within the context of the aims which were outlined at the beginning of this thesis. The importance of distinguishing between the size effects associated with the mechanical response of the material and localised variations synonymous with testing discrete samples has also been considered within the context of a micropolar elastic continuum model. Finally, the limitations of the current research are considered before some recommendations for further improvements and scope for future work will be put forward.

9.1 Summary Discussion of Present Work

A model material composed of a periodic, cellular lattice was manufactured and shown to display size dependent variations in stiffness when individual samples were tested in both flexure and torsion. Micropolar constitutive properties, namely the flexural modulus, shear modulus and characteristic length for both bending and torsion were identified which closely matched the solution to numerical simulations and analytical predictions.

The motivation for conducting this research was to firstly explore the nature of size effects within structured 3-dimensional cellular materials and identify the relevant mechanical properties associated with quantifying these effects. In addition to this, the use of additive manufacturing processes was investigated as a means to replicate and physically test such materials. This is an important area of research as structured cellular materials are very hard to manufacture from traditional processes. Identifying ways in which this can be achieved will enable a greater number of heterogeneous materials to be manufactured and tested, thereby complementing the wealth of more theoretical work on generalised continua which is available in the literature.

The size effects which may be observed when a heterogeneous material is loaded in either bending or torsion have been shown to be highly dependent on how the sample is prepared, the volume fraction and mass distribution within the unit cells which define the cellular material. It was shown by Frame (2013) that the positive and negative size effects observed in the materials which he studied were of similar magnitude but opposing sense. From this he postulated that positive size effects may be inferred from experiments conducted on materials with surface intersecting voids. It was shown here however, that while the size effects in flexure and torsion were generally opposing when samples with a continuous exterior surface were compared to those whose surface intersected the cellular microstructure, their magnitude varied with cell volume fraction for a given microstructural geometry. Therefore, predicting the correct micropolar properties solely from samples which display negative size effects may not be that straightforward.

The size effects which result from testing samples with a discontinuous surface are not associated with any degrees of freedom in addition to those which have already been introduced. The reduction in stiffness with decreasing sample size is due to the fact that the exterior surface layer cannot transfer the applied load as effectively as the core. These effects are not accounted for in the micropolar continuum model which was considered in this thesis, however, it does appear that the size effects are intrinsically linked.

While negative size effects are primarily associated with micropolar material samples which have a discontinuous exterior surface, it was observed in chapter 5 that this was not always the case. Here, materials composed from cubic cells with internal cross members displayed a nega-

tive size effect in some configurations when the samples were prepared with a smooth exterior surface. It appears that in this case, when the internal connecting beams are much greater in diameter than the exterior beams, the size softening effect associated with the former dominates over any gains in stiffness which are attributed to the exterior beams. This is an important result as it demonstrates that a cellular material with a continuous outer surface is capable of behaving in a manner which is not predicted by micropolar elasticity, suggesting that a more general model may be better suited to defining these materials. No such effect was seen in bending.

Size effects have been shown to be hard to identify and may be obscured if the continuum model does not fully capture the deformation under loading (Dunn & Wheel, 2016). In chapter 3, it was also shown for a low density 2D cellular lattice that Timoshenko theory may provide a better solution to the bending of very low density beams in comparison to a Euler-Bernoulli based micropolar model by accounting for the significant contribution from shearing which contributes to the overall deformation of the beam. However, identification of the correct additional parameters may require first conducting idealised numerical simulations before fitting experimental test data to analytical models.

While size effects in model materials have been studied experimentally for planar solids, this is the first time to the author's knowledge that a truly 3-dimensional structured cellular material has been tested in both flexure and torsion to identify its size dependent mechanical properties. The use of additive manufacturing processes to achieve this has also demonstrated the applicability and versatility of this technology as a platform to design and test structured heterogeneous solids.

The importance of conducting accurate experiments cannot be understated. Determining the correct mechanical properties of the material required much consideration to minimise effects which are not included within the continuum model. In this thesis, a robust analysis of the printed material was undertaken by considering the effect of sample aspect ratio, rate of loading, print direction and loading mode in order to achieve the most accurate assessment with the resources which were available. Complementary FE simulations were conducted to help design and validate all experiments.

The general agreement of the physical tests with numerical simulations conducted in ANSYS indicates that this method may be used in place of physical tests. However, one of the inherent problems with discrete modelling of 3-dimensional cellular solids at multiple size-scales is that the resources required to obtain a solution to the simulation are very computationally intensive, limiting the size of the material sample which may be numerically investigated. This may be particularly evident in very low density materials as the number of elements required to resolve an accurate solution increases dramatically. It has been shown in chapters 2 & 5 that beam element models of the material may be able to capture the size-dependent mechanical

response. However, as the analysis is somewhat simplified in comparison to continuum models, some inherent differences do exist, which limit their use to very low density structures. As a result, the use of mechanical tests may be still required in cases where the simulation size exceeds the computational resources which are available.

9.2 Future Work and Further Recommendations

While it has been shown that the size effects which were predicted by numerical simulations of the model material closely matched the experimental tests of the samples manufactured through additive processes, there does exist some scope to improve the results in both flexure and torsion. Ideally, the introduction of external deflection measurements independent of the mechanical actuators would potentially improve the accuracy of the measurements taken. This is especially important in the 4-point flexural tests as two measurement points are required to be taken simultaneously. Similarly, in torsion, measuring the angle of rotation at fixed points along the length of the bar may result in a more accurate response being recorded.

It was not possible to obtain all the constitutive parameters required to fully define the materials tested within a micropolar continuum from the experiments which were carried out. The additional constants, namely the polar ratio, ψ and coupling number, N, are usually determined by fitting experimental or numerical results to analytical equations (e.g. Rueger & Lakes (2016)). However, the additional parameters which were introduced by analysing cuboidal specimens (See eqn. 2.44 & Park & Lakes (1987)) made this difficult to do. A more detailed study into the sensitivity of these parameters may reveal more practical ways of determining them from experimental data.

In addition to improving the experimental procedure, it would be desirable to test a greater number of samples of similar size in order to better understand any statistical variations in the printed material. The number of samples which were produced for the analysis conducted here was limited by the high cost which was associated with producing each specimen. As a result each sample was tested multiple times to ascertain the individual constants. While the loads applied to the samples were restricted to small elastic deformations, repetitive testing of individual samples may increase the uncertainties within the analysis.

It was observed in the experimental tests which were conducted that the 3D printed photopolymer was viscoelastic in nature. Some anisotropy was also observed due to the layering process during manufacturing. While the mechanical tests were conducted in such a way to minimise these effects, there may be scope to improve the numerical simulations by incorporating them into the material properties of the model. However, this may require the use of a yet more complex higher order model which is out-with the scope of this investigation. Future advances in additive manufacturing, particularly metallic based could potentially offer more

isotropic matrix materials for conducting experimental tests on novel materials.

The use of additive manufacturing technologies to produce model heterogeneous materials which can stand up to the rigours of mechanical testing has been demonstrated within this thesis. Therefore, there now exists an opportunity to further enhance the range of structured materials which have been documented and physically tested. In addition to other cellular structures with both a stochastic or structured composition, integration of these heterogeneous solids within laminated sandwich core panels for instance may also be investigated within the context of lightweight structural design.

The production of fully closed cell structures is currently limited to materials which incorporate an internal support material rather than hollow voids. While this is not ideal, some preliminary investigations (which have not been included here) have indicated that distinguishable size effects can be captured in samples with a compliant filler material, however, the results did not show good agreement with numerical simulations of a similar material. The development of manufacturing techniques which not only have increased build capacity but can fully replicate closed cell heterogeneous solids with internal hollow voids is something which should certainly be pursued.

9.3 Concluding Remarks

While heterogeneous materials have been shown to have beneficial properties which are useful in structural applications, the identification of the individual constitutive parameters is extremely challenging. Careful sample preparation and rigorous experimental techniques are required to distinguish between the effects of localised loading, surface damage and experimental errors which may impede the identification of the correct mechanical properties.

Additive manufacturing processes such as 3D printing can help to reduce the uncertainty that is introduced by sample preparation assuming that such materials do not introduce additional parameters which need to be accounted for. This research has demonstrated the proof of concept for developing model materials from solids constructed in this way which conform well to the predictions of numerical simulations. However, a best judgement is still required to determine if the chosen continuum model and test methods are appropriate for the material under investigation.

Identifying the relevant mechanical properties of 3-dimensional heterogeneous solids has proved to be a challenging task, but one which is not insurmountable. Ultimately the goal should be to determine mechanical models for stochastic materials which can account for the additional degrees of freedom which the heterogeneities introduce, thereby reducing the need to resolve the material at the microstructural level. Until such time, the importance of conducting physical tests cannot be understated. Ultimately, additive processes are an avenue which should

be exploited to bring otherwise theoretical materials into fruition, enhancing the development of materials which are available to engineers.

Appendix A

Verification of Loading Modes in ANSYS

A.1 Torsional Loading

One of the restrictions that arises when working with conventional, displacement based continuum elements is that moments or torques cannot be applied directly to the structure without being resolved into tangential force components at every point across the load surface. For large problems with a vast number of nodes, ANSYS has several methods which can be used to automatically calculate this for the user.

Continuum elements by definition only have three translational degrees of freedom. In order to apply a torque or moment, the user must either manually determine the correct loads to apply to the model or implement constraint equations which will automatically determine how the load should be distributed. The two main methods that exist in ANSYS to create multipoint constraints (MPC) involve using either the CERIG and RBE3 commands or the surface based constraints that are available in the contact manager.

Distinction should be made between the use of CERIG and RBE3. RBE3, which is a form of rigid body element, is a force distributed constraint that can distribute the force or applied moment that is defined at a master node to a set of slave nodes. The motion of the master node is an average of the slave nodes. In this case, the surface that the load is applied to is free to distort in response to the applied boundary conditions. The CERIG command on the other hand is used to create a rigid region whose motion is constrained by that which is defined by the pilot node. In this case, the loading face will not distort when subjected to an external load assuming that the degree of freedom corresponding to the applied load is constrained. The contact manager is also a useful tool to use when defining either type of constraint as it can also handle large displacement problems if required.

In the case of a bar of uniform cross-section loaded in torsion, a fixed torque or rotational displacement is required to be applied to the end face of the structure. The end face of the structure should also be sufficiently unconstrained that it will be free to warp. Continuum elements by their very nature do not possess any rotational degrees of freedom, so it is therefore necessary to include a pilot node which has a rotational degree of freedom.

One of the restrictions with loading the non-circular sections in torsion is that warping will be induced when a rotational load is applied. In order to model this correctly, the sample should be loaded in such a way that the end faces are free to distort axially under load.

The method outlined is based on the work undertaken by Ramsay & Maunder (2014) who carried out some benchmarking of torsional problems with warping constraints using multi point constraint equations to distribute the applied load in the structure. Before applying this method to general heterogeneous samples with complex microstructures, a set of benchmark analyses were undertaken for various different member cross-sections in order to compare the theoretical predictions with the simulated results.

The general boundary conditions that were outlined by Ramsay & Maunder (2014) were as follows:

Common boundary conditions

$$\begin{aligned} u_x = u_y = u_z = 0 \qquad & \text{at pilot node 1.} \\ \theta_x = \theta_y = \theta_z = 0 \qquad & (x = 0, y = 0, z = 0) \\ u_x = u_y = u_z = 0 \qquad & \text{at pilot node 2.} \\ \theta_x = \theta_y = 0 \quad \theta_z = \theta \qquad & (x = 0, y = 0, z = L) \end{aligned} \tag{A.1}$$

An additional node is required for free warping

$$u_z = 0 \qquad \text{at } (b/2, d/2, L/2) \tag{A.2}$$

Required constraint equations at interface

$$\begin{aligned} U_x, U_y, U_z \qquad & \text{for restrained warping.} \\ U_x, U_y \qquad & \text{for unrestrained warping.} \end{aligned} \tag{A.3}$$

Lower case lettering denotes the boundary conditions which are directly applied to the model while capitalised letters have been used to represent coupled degrees of freedom between the pilot nodes and the area over which the load is applied. Figure A.1 has a visual representation of how the boundary conditions are applied for a prismatic bar that is free to warp. The

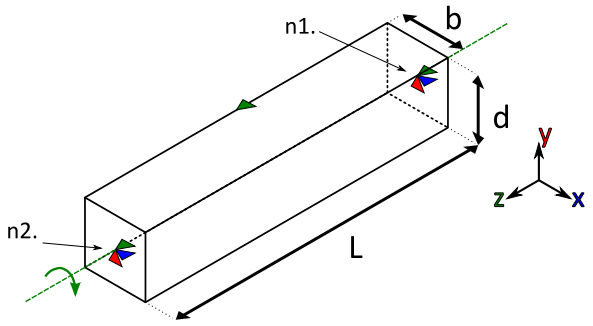

Figure A.1: Boundary conditions for rotational loading with unrestrained warping.

additional axial constraint applied to the middle of the beam is required to prevent rigid body motion occurring in the unrestrained case. In the restrained case this additional node should be removed as it will introduce localised stresses into the model.

In order to translate the loads correctly between the pilot nodes and the end faces of the structure, the constrained degrees of freedom on the target surface need to be specified. For unconstrained warping to occur, the model should be free to move axially at each end. To achieve this, U_z is left unconstrained in the contact equation A.3. Simulating restrained warping requires that the axial constraint is turned back on, to fix the end faces of the beam. As the model is comprised of continuum elements that only have translational degrees of freedom, then the rotational components are not required in the contact equation and can be turned off if desired.

Three test cases (Figure A.2) were created in order to verify that the motion of the beam under examination was consistent with the theoretical predictions that can be readily found in text books (e.g. Roark et al. (2002)). Test case 1 was modelled on a solid circular cylinder. Test case 2 consisted of a bar with a square cross section and the final test case, consisted of an 'I' beam. Each sample consisted of an extruded cross section of 10 mm in length and an aspect ratio of 10. The breadth, B and height, H of the square and 'I' section was 1 mm and the circular rod also had a diameter of 1 mm. The thickness, t of the web and flange in the 'I' beam was fixed at 0.1 mm. Each model was subjected to a fixed rotation and the reaction moment was calculated in order to determine the torsional stiffness of the structure.

In the case of a circular shaft with constant cross section, the shear stress, τ at any point due to a constant toque, T, applied about the rotational centre is perpendicular to the radius and proportional to the distance from the rotational centre and the angle of twist per unit length, θ/L. No warping will be induced in the circular section as the resulting stress in the beam is constant around the circumference of the section at any given radius. This is an exact solution

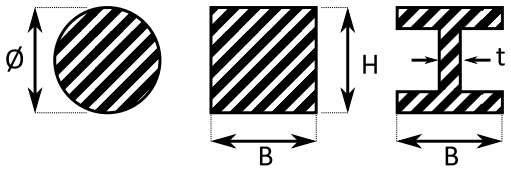

Figure A.2: Circular, Square and I-shaped cross-sectional samples used to validate loading method.

and follows the relation in equation A.4.

$$\frac{T}{I_p} = \frac{\tau}{R} = \frac{G\theta}{L} \tag{A.4}$$

The warping constant, I_p, in this case is equivalent to the polar moment of area and is directly related to the diameter of the bar as follows:

$$\text{Solid Cylinder} \qquad I_p = \frac{\pi\phi^4}{32} \tag{A.5}$$

All other parameters in equation A.4 have their usual meaning.

For a non-circular section the warping constant does not directly relate to the polar moment of inertia. Standard equations for the torsional constant of common cross-sections are frequently listed in text books such as Roark et al. (2002) and have been summarised in table A.1. In the case of the I-section, the subscripts f and w indicate the thickness of the flange and web of the beam respectively.

Each model was loaded and tested independently with both free and restrained axial displacement at each end face. The purpose of this was twofold: firstly to verify that each model is behaving in the manner that is predicted theoretically which is important as the model will be used to predict the properties of materials that do not have closed form analytical solutions. The second motive for testing the models with restrained boundary conditions is that this is a closer representation to what is usually obtainable through physical experiments and can be used as a good indicator as to how much variation in the sample stiffness might be observed under these conditions. Large variations in the torsional stiffness from the free warping case would indicate that some correction would be needed to any experimental tests, so it is therefore better to minimise any likely variations that could arise from the mode of loading.

A.2 Results of Numerical Simulations

The theoretical predictions for each cross-section have been recorded in table A.1. It can be seen that when the models are loaded in such a way that the ends of the structure are free to rotate, then the converged results are approximately the same as the theoretical predictions when the mesh is sufficiently refined.

As expected, the solid cylinder shows no variation in torsional stiffness or shear stress with free and restrained boundary conditions applied. From figure A.4 it can be observed that no axial stress is recorded in either simulation since there is no warping to constrain which conforms well with the theoretical predictions. The small variations in axial stress which can be seen on this plot are a consequence of the applied boundary conditions and can be safely ignored.

	Beam Cross-Section		
	Solid Circle	Square	I Beam
Torsion Constant	$\frac{\pi\phi^4}{32}$	$\frac{2.25D^4}{16}$	$\frac{\left(2Bt_f^3+Dt_w^3\right)^*}{3}$
	Torsional Stiffness ($NmmRad^{-1}$)		
Theoretical	264.32	378.61	2.692
Unrestrained Warping	264.31	378.48	2.597
Restrained Warping	264.31	379.74	6.264
	Max Shear Stress (Nmm^{-2})		
Theoretical	134.62	181.97	53.57
Unrestrained Warping	134.89	181.93	51.30
Restrained Warping	134.89	181.93	66.48

*This simplification assumes that the web and flange are relatively thin in comparison to the beam depth.

Table A.1: Comparison of the beam stiffness for various cross-sections.

Warping will occur in the square section due to an imbalance of shear stresses acting at the perimeter of the cross-section. A slight increase in torsional stiffness is observed in the square section when the ends of the structure are restrained, but it only equates to a 0.3% variation. Visually, this result can be observed in figure A.5. A large increase in axial stress can be observed at the fixed ends due to the extra restraints which have been applied. Crucially however, it can be seen that the influence of this stress is localised and does not extend very far along the beam. It can therefore be inferred that reducing the aspect ratio of the section under testing is likely to increase the relative observed rigidity due to an increased influence in the edge effects. To test this, the analysis of the bar with a square cross-section was repeated with a length to depth aspect ratio of 2. However, it was observed that the increase in relative stiffness was only 1.5% greater than the slender sample.

The I-beam consists of an open section beam rather than a closed one that is seen in the two previous beams that were analysed. Under a rotational load, the flange in the section is much more compliant at the edges than at the centre of the beam. As a result, the torsional stiffness is dramatically reduced in comparison to the solid sections. In the restrained case, twisting of the section is resisted by both shear stresses and axial stresses when the bar is twisted. A significant variation in torsional stiffness is found when the ends of the I-beam are restrained as compared to the other cross-sections (Figure A.6). Here the increase in torsional stiffness is observed to be 140% which would significantly compromise the results.

It can be observed for the case of the I-beam that the warping stresses induced in the beam with both ends constrained are highly dependent on the aspect ratio of the beam. At very low aspect ratios, the built in section is substantially more rigid than when the beam is purely resisted by torsional shear stresses. This can be clearly seen in figure A.3.

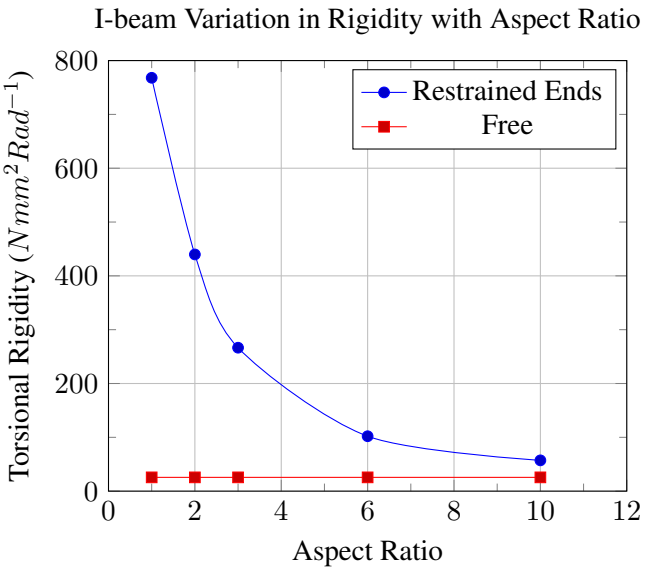

Figure A.3: Comparison of the variation in torsional rigidity with aspect ratio for an I-section beam subjected to free and restrained axial displacement on the end faces.

A.3 Summary

Depending on the sample that is under test, warping has been shown to have a significant influence on the overall stiffness of the sample. In order to minimise the influence of the increase in stiffness due to localised restraining of the sample, it is recommended that as high an aspect ratio is used in torsion testing as possible. Ideally, the samples should be free to warp

in the axial direction throughout to minimise the influence of any boundary condition variations which will ultimately affect the overall results.

It can be seen that when the beam is free to warp at both ends, there is negligible axial stress in any of the beams (Figures A.4 - A.6). This is to be expected as there no reaction forces generated to resist any axial movement of the beams.

While this method has shown to be an accurate way of modelling the torsional properties of a beam, it has been observed that it is sensitive to the mesh density as this directly influences the number of constraint equations which are set up in the analysis. A mesh convergence study should be carried out on any given model in order to verify the accuracy of the results.

This method can also be used to load the structure in other common loading modes. For the case of pure bending of a sample of the material under investigation, the boundary conditions are as follows;

$$\begin{aligned} &u_x = u_y = 0 && \text{at pilot node 1.} \\ &\theta_y = \theta_z = 0 \quad \theta_x = \theta && (x = 0, y = 0, z = 0) \\ &u_x = u_y = 0 && \text{at pilot node 2.} \\ &\theta_y = \theta_z = 0 \quad \theta_x = -\theta && (x = 0, y = 0, z = L) \end{aligned} \tag{A.6}$$

An additional node is required to prevent rigid body motion

$$u_x = u_z = 0 \qquad \text{at } (b/2, d/2, L/2) \tag{A.7}$$

Required coupled degrees of freedom at interfaces

$$U_y, U_z \tag{A.8}$$

Where the applied boundary conditions are consistent with the reference frame in figure A.1. Again rigid constraints have been used here to model the interface between the pilot nodes and the end faces of the beam in order to simulate ideal loading conditions as closely as possible. While simulating uniaxial loading is also possible with this method, it is probably more efficient to use direct displacement boundary conditions without the use of a pilot node.

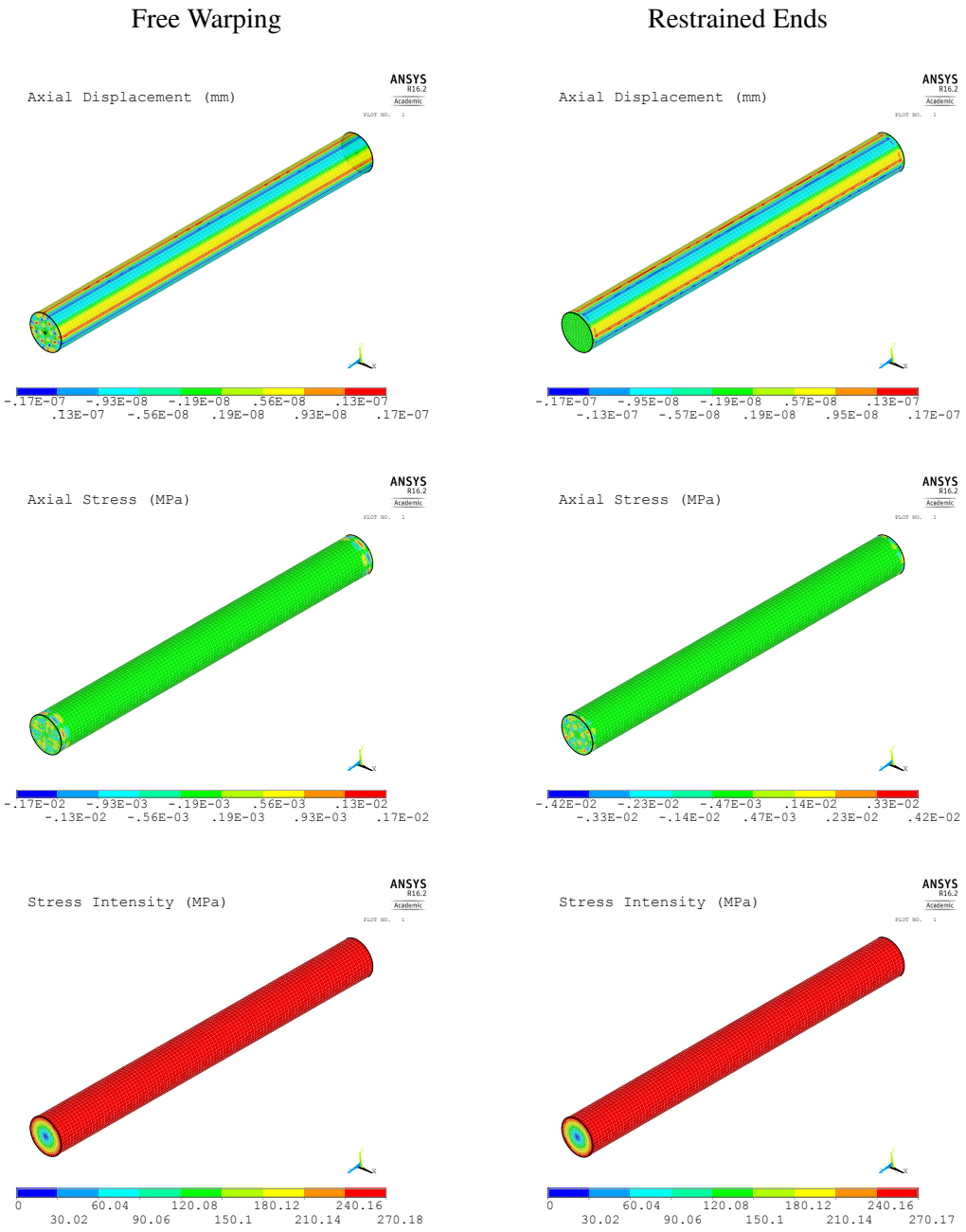

Figure A.4: Cylindrical bar

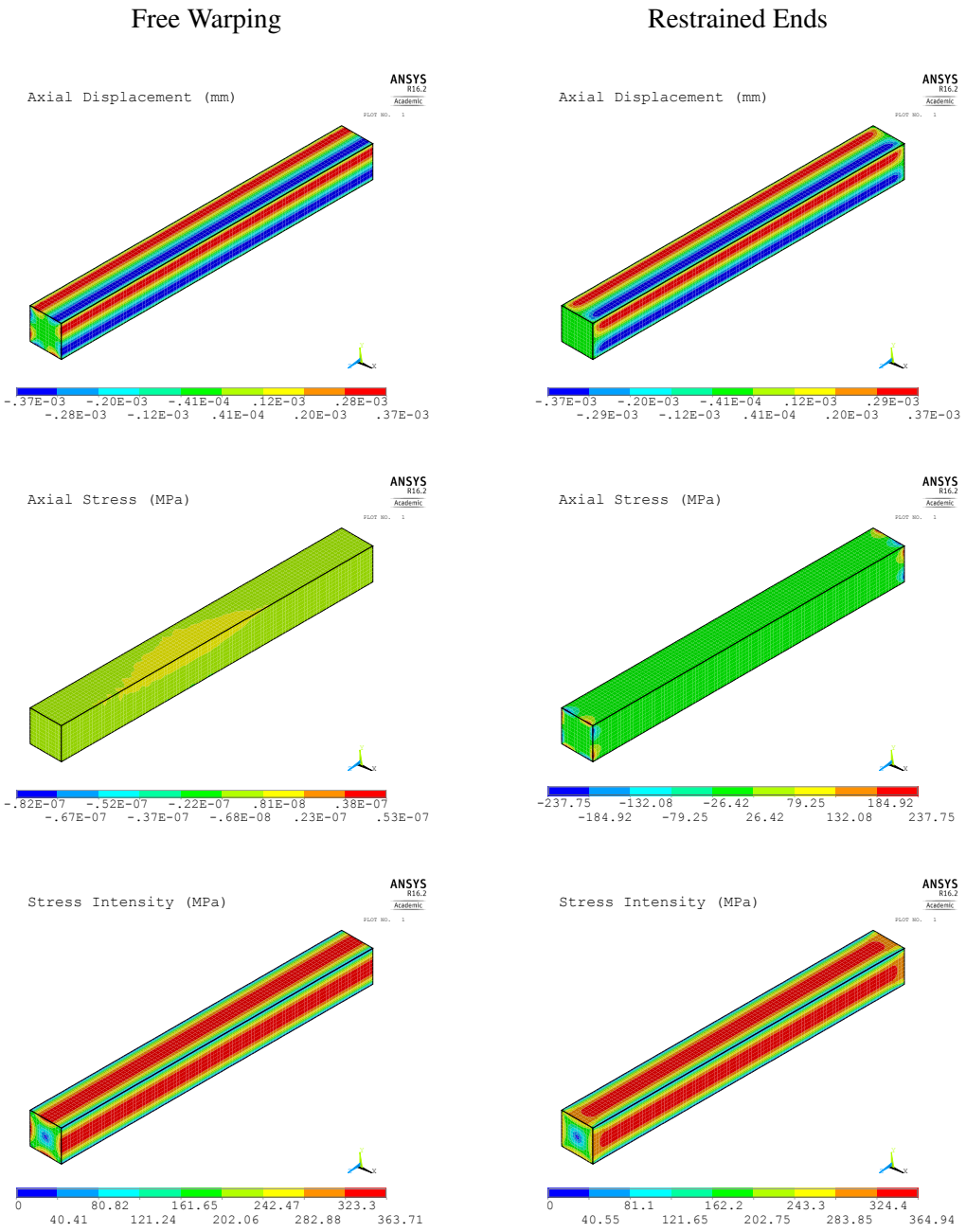

Figure A.5: Bar with square cross-section

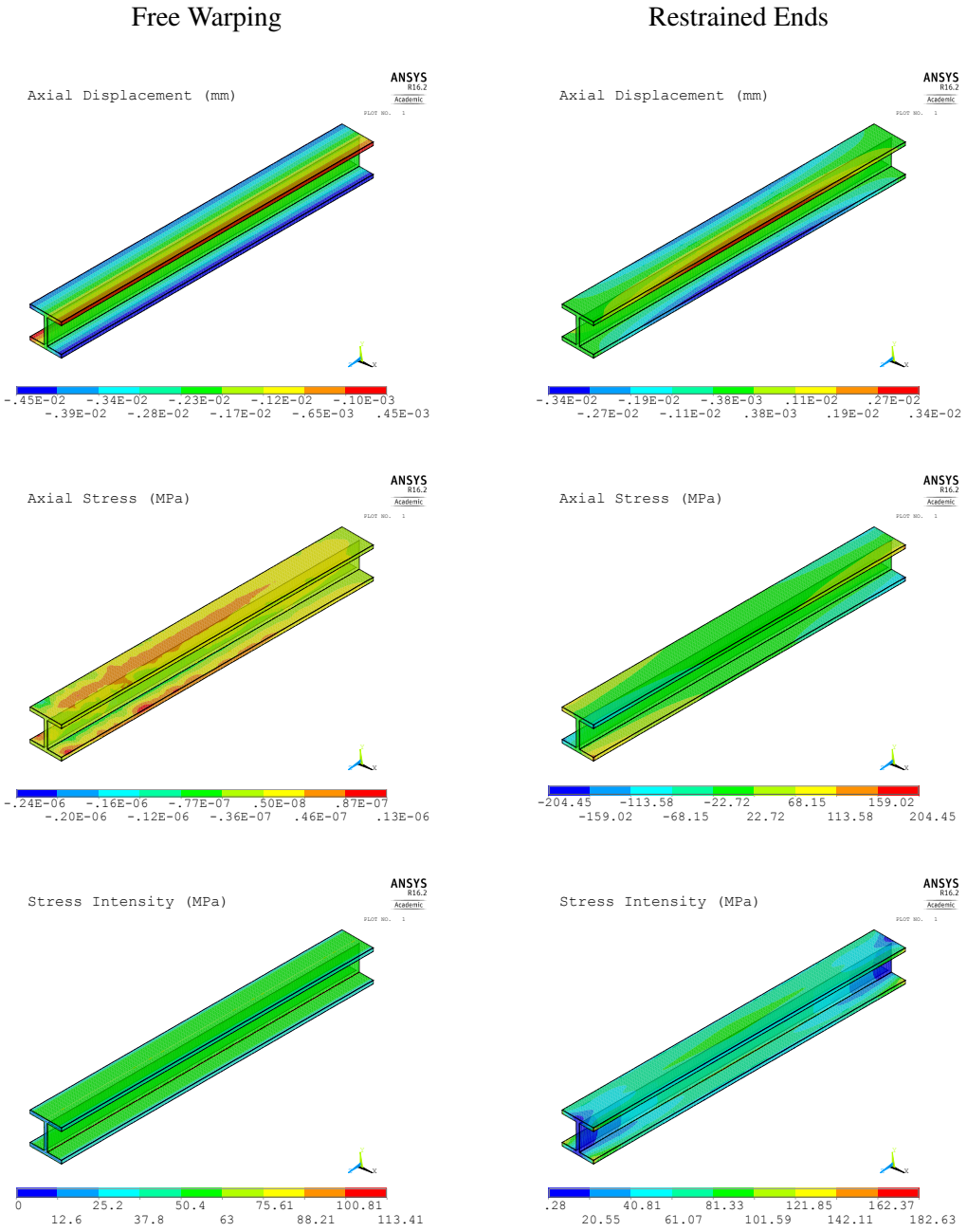

Figure A.6: I-beam

Appendix B

Validation of Experimental Torsional Loading Setup

B.1 Numerical FE Model of Experimental Apparatus

As has been shown in the previous section, the manner in which a bar is loaded in torsion can significantly influence the measured mechanical properties of the material from which it is comprised. The experimental setup for testing the lattice structures therefore required some thought as to what the best configuration was to load each sample while allowing it to warp as freely as possible within the fixings of the test apparatus. One way of achieving this is to take advantage of the sample porosity and insert pins into the array of cells at the end faces of the sample.

The main requirements of the grips were as follows: it should not displace under load relative to the movement of the machine. The sample should be free to displace axially throughout while under load in order to minimise any change in stiffness that might occur due to restrained warping at the ends. The grips should also be capable of supporting a range of different sized samples.

The idea behind having pin inserts in the sample rather than more traditional fixed end plates or clamped conditions is that the pins would allow for the sample to warp freely while minimising any localised effects from holding the sample in place. There is also the advantage that the only axial constraint that the pins will place on the sample are from the friction that is generated between the pins and the test sample. Detailed drawings of the manufactured grips can be seen in appendix C.2.

In order to verify that the chosen method would give an accurate representation of how the samples might distort under load, a parametric computational model was created in ANSYS to verify the motion and resulting forces which were likely to be induced on the bar section.

The experimental setup consisted of an Instron test machine which has the capability of applying linear and rotational displacements to a given specimen. To test the sample of the material in torsion, it was required to create a custom mount that would enable the sample to be held within the machine. A simplified setup was created in order to minimise the computational resources required to run the simulation. The model comprised of two sets of pins which represented the grips and the specimen itself. The base of the grips was not required to be modelled as it is much more rigid than the material under investigation. It was sufficient in this case to model the base as a rigid surface where it connects to the base of the pins. In practice the load is applied to the sample by a rotational actuator under displacement control conditions. To simulate this, the pins were connected to a pilot node using rigid constraint conditions. The pilot node has three translational and three rotational degrees of freedom. By allowing the pilot node to freely rotate around the longitudinal axis and be constrained in all other degrees of freedom, a rotational displacement can be applied that simulates the test conditions.

The first set of pins were fixed in all degrees of freedom at the base in order to secure them in place. The beam under investigation was then inserted into the pins to the required depth. While in the test arrangement the beam may be restrained axially by the friction that is generated by the sample and the grip, the numerical simulation requires some restraints on the component in order to define how it can behave and prevent rigid body motion. To achieve this a pilot node was defined at the centre of each face using rigid constraint equations. By setting the pilot node to only have a rotational degree of freedom in the axial direction, it allows the beam to rotate under an external force. No constraint was coupled between the axial displacement in the beam and the pilot node, allowing the sample to warp if desired. To prevent rigid body motion in the analysis and stop the beam sliding off the grips, one node in the sample was fixed axially. Finally, the second set of pins was inserted into the top of the beam. A pilot node was used to transfer the rotational displacement to the pins in the correct manner and restrain the fixed ends from displacing relative to the rotational motion.

In the experimental set-up, the sample is prevented from displacing axially through the friction generated by the pins from the transverse forces that are applied through the rotational displacement. The constraints were set up in such a way that the pilot node was free to rotate axially and fully constrained in all other degrees of freedom. This approach had the advantage that the relative rotation of the beam could be measured independently at the end of the analysis. An example of a typical simulation model can be seen in figure B.1.

In order to apply the load to the simulated structure correctly, the grips were initially rotated incrementally to allow the components to contact correctly. The initial load step here was influential in whether the analysis solved as too large an increment had the effect of causing excessive penetration, resulting in an unconverged solution. Overcoming this stage in the analysis was mainly a process of trial and error as the number of sub-steps required was seen to

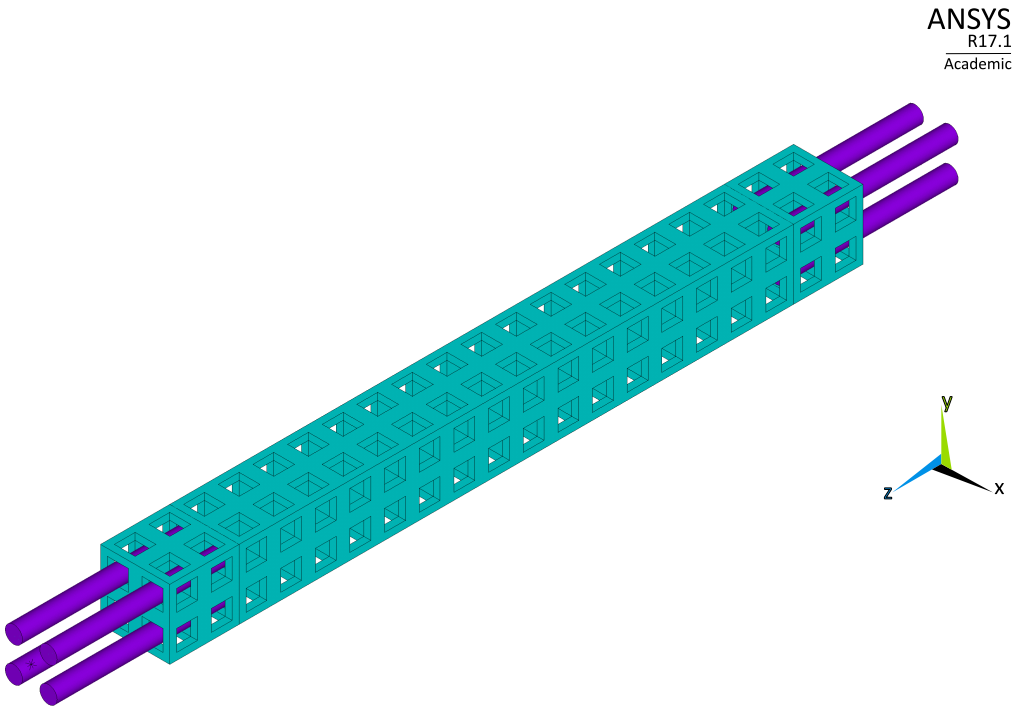

Figure B.1: Simulated setup for experimental torsion tests.

vary with the size of the model and the number of pins used to constrain the sample.

B.2 Results of Numerical Simulations

From the static analysis that was carried out on bars of the cellular lattice material, it was observed that the apparent shear modulus of the material varies when the sample size is of similar order to the unit cells that define the microstructure within the material. Micropolar theory predicts that the shear modulus of the material is in fact constant and the variation in stiffness that is observed is a consequence of the relative sample size with respect to the underlying microstructure of the material. The sample stiffness is therefore expected to converge on a finite value as the sample size increases. While this effect can be distinguished relatively easily through ideal loading conditions, uncertainty still exists with experimental testing. It was therefore felt that it was very important to model the experimental setup in order to minimise any external influence which might mask the true material parameters.

The results of the numerical simulations have been summarised below along with the equivalent results for the same models subjected to fixed and free end boundary conditions (Figures B.2 & B.3.). It can be seen that for this material, the variation in local stiffness under idealised loading is very small when the fixed and free end boundary conditions are compared. The aspect ratio of the largest sample is approximately 5.67 which is relatively low. However, the observed stiffness is less than 2% greater when the end faces are restrained from warping which indicates that the aspect ratio is not an influential parameter.

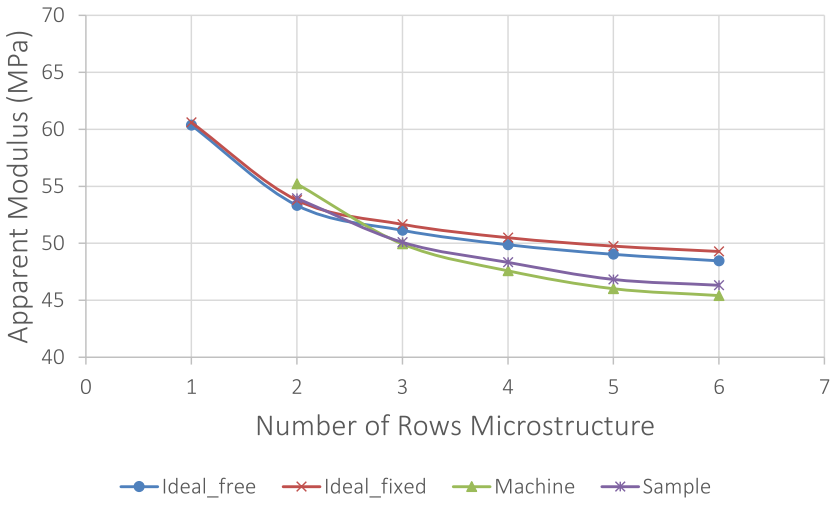

Figure B.2: Variation in apparent shear modulus for individual samples with a pin insert depth of 10 mm. The stiffness is seen to converge with increasing sample size.

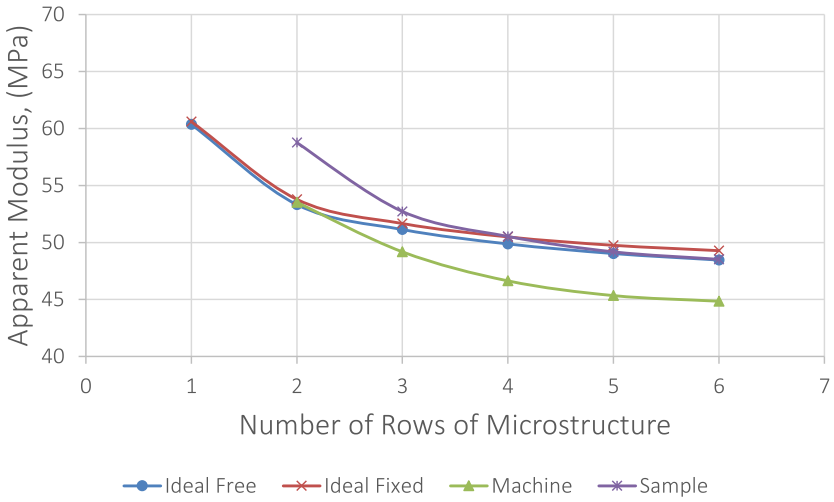

Figure B.3: Variation in apparent shear modulus for individual samples with a pin insert depth of 1 mm. The stiffness is seen to converge with increasing sample size.

Modelling the interaction of the pins with the sample proved to be more troublesome. Several attempts were required to capture the interaction between the pins and the sample of material which was simulated. The main difficulty that arose was determining the number of time steps that were required to enable the contact surfaces to come together at a sensible rate. Incrementing the displacement too quickly had the effect of causing penetration issues between the target and contact elements which in turn may lead to a solution which does not readily converge. Another factor which has been inherent in all problems with large numbers of continuum elements is that the analysis time and required computational resources are very dependent on model size. To minimise this, a coarser mesh was utilised in this investigation. While the coarse mesh does not necessarily yield the converged solution for the material, it was sufficiently close that any changes in stiffness will still be captured and are comparable to the ideal load case simulations at the same element density.

Another consideration which needs to be taken into account in the design of the pin configuration is the distance that they protrude from the support base. This is important as each individual pin will itself be subjected to a bending moment when the rotational load is applied. As the deflection is proportional to the length cubed, then it can be readily seen that long pins will be more susceptible to deflection under load. Lateral deflections in the pins should be minimised as any significant change could alter the effective rotational angle over the length of the pins.

The results for the beam with a 2×2 matrix of cells through the sample cross section showed that inserting the pins into the material had the effect of restraining warping at the ends

of the beam to some degree. After consideration, it was decided that this should be expected as the bar will not rotate relative to the pins in the section which they are inserted into. This can be minimised by only inserting the pins into the first cell of the material, but a trade off would need to be established to account for any localised effects which may occur with such a small contact surface to transfer the load to the sample. As the initial analysis showed that there was a minimal change in stiffness due to restraining the ends of the bar at this sample size, then it was felt that any variations due to gripping the sample would also be minimal.

Reducing the pin insertion depth from 10 mm to 1 mm had only a small effect on the overall stiffness of the specimens. In general, the apparent shear modulus that was observed with the pin at this depth was slightly lower than the previous case when the machine displacement was used to calculate the stiffness of the sample. The actual beam displacement largely overestimated the stiffness for a sample with 2×2 rows of microstructure through the cross section, but matched the idealised case reasonably well in larger samples. One of the main reasons for loading the samples with the pin assembly was to minimise the effects of clamped ends suppressing warping within the sample. Generally speaking, by restricting a sample from warping, the observed stiffness will tend to increase in comparison to an unrestrained specimen. As the samples are generally slightly more compliant than those loaded by unrestrained end conditions, this indicates that there must be some influence from the grips. It is most likely that the grips are displacing slightly under load which will negatively affect the observed sample stiffness. Overall, though as the loads which are being applied to the samples are relatively small, the minimal variation is acceptable.

The length of the pin that is used to grip the material may be influential to the observed sample stiffness. If the spacing between the base of the grip and the bottom of the sample is too large, then the pin may deflect due to the bending moment that forms under loading. In turn, this may alter the overall rotation across the length of the beam, increasing the uncertainty within the recorded results. This effect is exacerbated by reducing the insertion depth for a given pin size as the applied load tends to move towards the tip of the pin. However, reducing the pin insertion depth is preferable as it helps to minimise the portion of the beam which is subjected to localised loads from the grips. It was observed that the beam does not rotate relative to the pins in the section where they overlap. By constraining the lateral movements of the beam in this section it also has the effect of reducing the amount of warping which will occur over this section and will therefore alter the observed results to some degree. Not inserting the pin far enough into the beam on the other hand is seen to be detrimental too as increased localised stresses are observed on the sample due to the small contact area which is distributing the applied load. While it can be seen in figure B.3 that stiffness of the smallest sample is substantially stiffer than the idealised numerical prediction, overall, decreasing the pin insertion depth improves the accuracy of the shear modulus which is observed with this test

configuration.

Pin Insert Depth		G^*	${l_t}^2$	l_t
mm		MPa	mm^2	mm
1	Machine	43.37	2.09	1.45
	Sample	47.07	1.97	1.40
10	Machine	43.83	2.27	1.51
	Sample	44.96	1.91	1.38
Beam Only	Unrestrained	47.54	1.29	1.14
	Restrained	48.47	1.11	1.05

Table B.1: Comparison of the mechanical properties obtained for the sample under ideal conditions and from a simulation of the experimental setup. Separate measurements were recorded using the reaction forces of the machine and also those on the sample itself.

The shear modulus and characteristic length of the material were determined from two points of measurement in the simulation. In the first instance, the torque per radian twist acting on the beam under load was taken from the reaction moments measured in the grips. This is comparable to the measurements taken in the physical experiments and is denoted as 'Machine' in table B.1. The second measurement point used the reaction torques at the end of the bars which is independent of the apparatus and are denoted as 'Sample' in the results. In both cases, the gauge length was taken from the length of the bar which was not constrained by the pins.

The shear modulus which was obtained by taking measurements from the 'Machine' was found to be reasonably independent of the depth that the pin was inserted. However, the modulus was approximately 10% lower than the idealised results. A slight increase in characteristic length was found when the pins were inserted 10 mm into the specimen as compared to only 1 mm, but the variation was relatively small. In both cases the characteristic length for torsion actually measured was greater than the idealised simulations.

The simulated modulus of the material which is found when the pins were inserted to a depth of 1 mm closely matched to the results of 170 mm long samples loaded under idealised conditions when the reaction forces on the sample were considered independent of the pin assembly. The characteristic length was still overestimated however.

The main difference which was observed in the analysis of the experimental setup compared to the idealised simulations was that the axial displacement at the ends of the bars was slightly constrained in the region where the pins were inserted into the sample. Localised stresses were also apparent at the points where the parts met. The axial displacement field was also observed to be offset at an angle in the region of the pins when compared to the inner section of the sample which is a consequence of the localised constraint in displacement which the pins introduce.

In the case of a square beam which is free to warp due to a rotational load applied in the

axial direction, the axial displacement field can be observed to have zero displacement at the outer corners and mid points of the cross-section. In between the points of zero displacement, the beam will warp due to an imbalance in the forces acting on the material. This effect rapidly decreases as you move towards the centre of the beam cross-section as is seen in figure A.5. A similar effect can be observed in the cellular structures, although the displacement field has to morph itself around the voids within the material (Figure B.4.). This result is clearly size-dependent and becomes more significant with decreasing sample size.

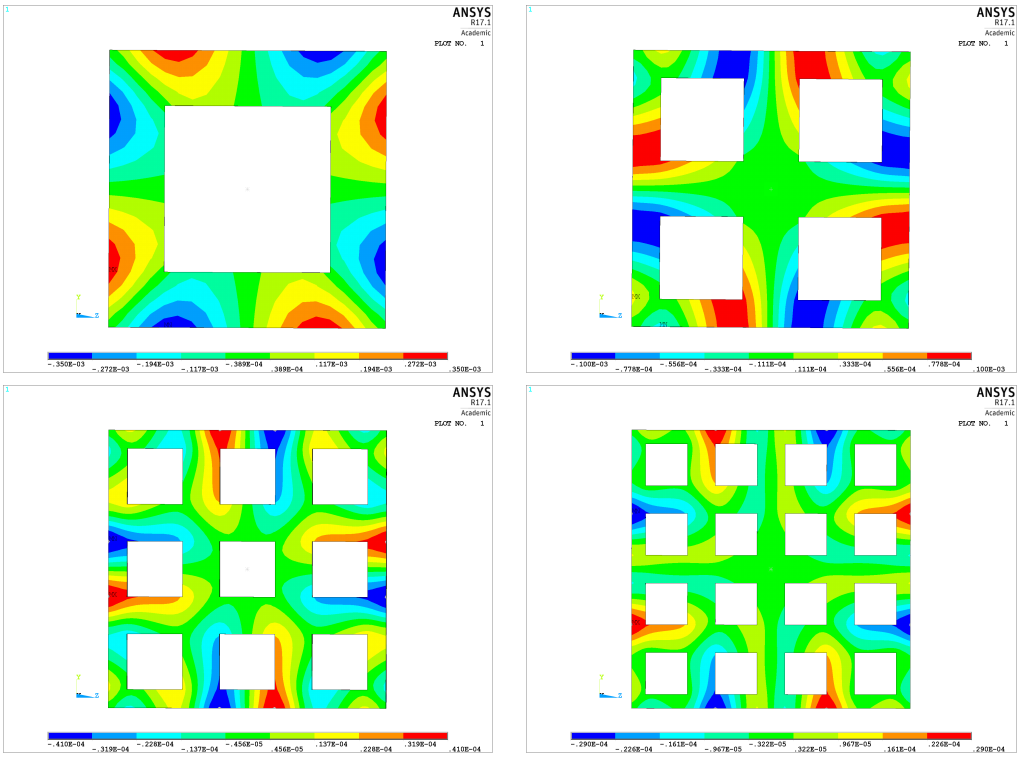

Figure B.4: Typical variation in axial displacement (mm) within the cross-section for a slender bar of various sizes loaded in torsion.

Overall, the simulations have indicated that the mechanical properties which are likely to be found by physical experimentation will have some variation when compared to idealised numerical analysis. It appears that decreasing the depth at which the pins are inserted into the sample is likely to improve the results, but it largely depends on taking localised measurements from the sample rather than those recorded by the machine displacement and load cell. It was observed that the characteristic length in torsion determined from the simulations of the experimental apparatus was slightly larger than the idealised simulations of the material. While this indicates that the experimental apparatus may not be ideal, the overall variation is fairly

small and is likely to be within the expected experimental uncertainty of a physical experiment.

Appendix C

Experimental Tests

C.1 Development of a 3 and 4-Point Bending Support

A custom bending support was required to be designed in order to accommodate the full range of specimen sizes within the test apparatus that were to be tested in both 3-point and 4-point flexural loading. The main requirements of the bar were that the spacing between the supports could be adjusted quickly and accurately while being sufficiently stiff so as not to deform under experimental test conditions.

The bar was designed to accept samples up to a maximum length of 320 mm and 20 mm breadth which coincided with the limits imposed by the 3D printing equipment. It was constructed from a solid steel bar which had an array of equally spaced threaded holes along the length which were used to restrain the adjustable reaction supports. The centre hole was threaded to accept a UNF 10-32 screw, which allowed it to be easily mounted to the existing machine fittings. A set of reaction supports were also manufactured to provide a platform for the test specimen to rest upon. The indenter and reaction supports consisted of 3 mm diameter pins which were held in place by rubber washers. The advantage of this was that it meant the pins were reasonably free to rotate under loading and could also be interchanged with one of a different diameter if so desired. In order to be able to accurately position the supports at the desired location on the bar, a slot was manufactured on the bottom of the reaction support, enabling small adjustments to be made. Each support was held in place by a washer and threaded bolt. A diagram of the support fixture can be seen in figure C.1.

In the case of 4-point bending an additional support was required to be manufactured which would evenly distribute the applied load at two points across the specimen. As the overall span required for the indenter was smaller than the support beam, a bar with reduced span was manufactured to minimise the mass which was attached to the linear actuator and load cell. The slider support and indenter were otherwise identical in design. Detailed drawings of the

manufactured bars and adjustable supports are included below.

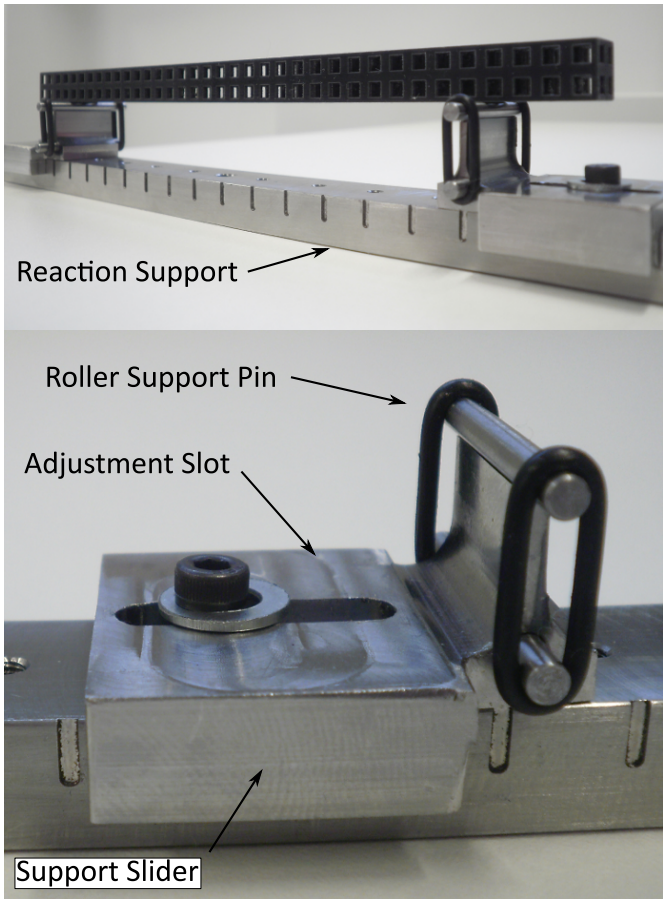

Figure C.1: Support beam manufactured for use in the 3-point and 4-point flexural experiments.

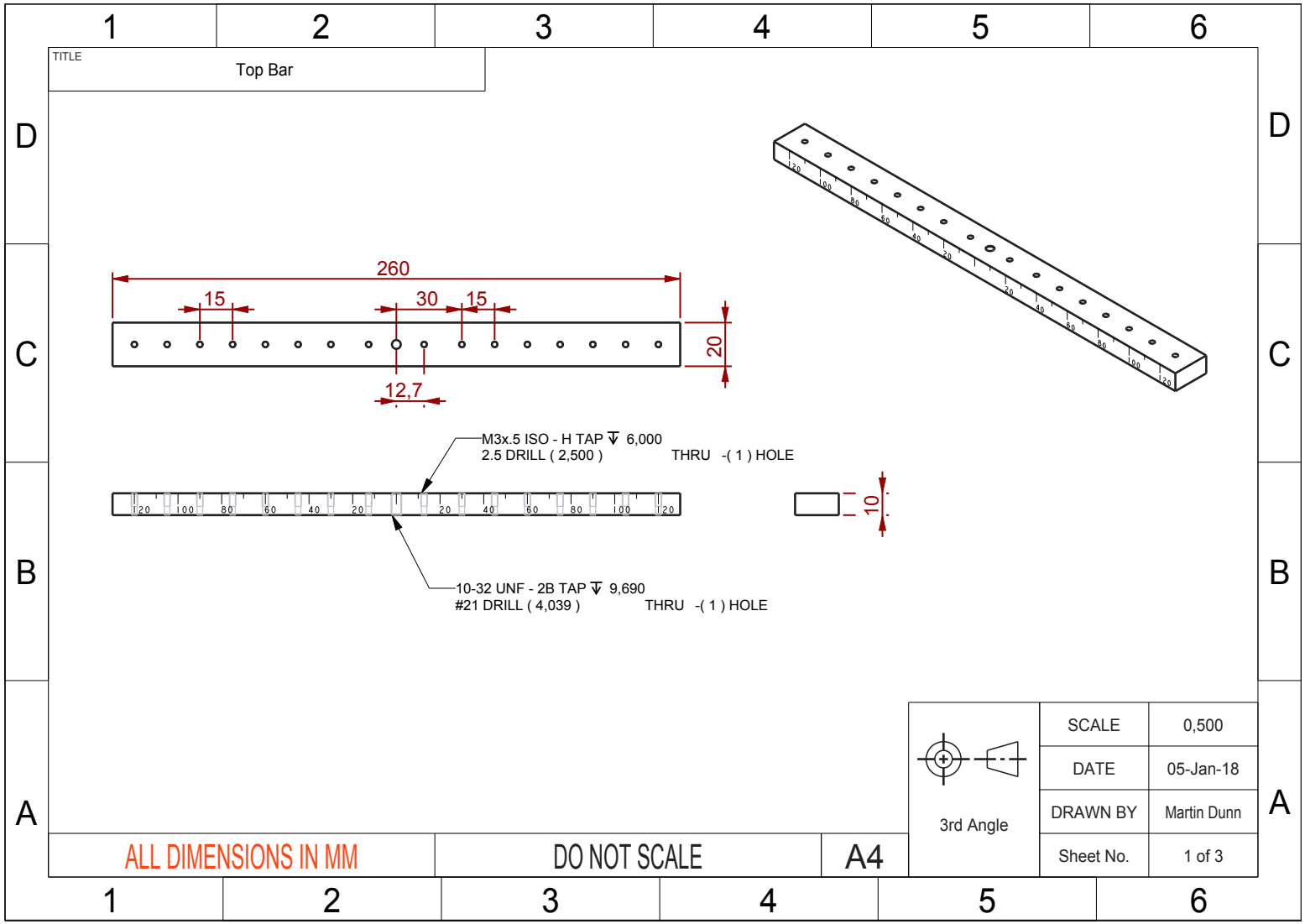
TITLE
Top Bar
260
15
30
15
20
12,7
M3x.5 ISO - H TAP ↧ 6,000
2.5 DRILL (2,500) THRU -(1) HOLE
10
10-32 UNF - 2B TAP ↧ 9,690
#21 DRILL (4,039) THRU -(1) HOLE
3rd Angle
SCALE 0,500
DATE 05-Jan-18
DRAWN BY Martin Dunn
Sheet No. 1 of 3
ALL DIMENSIONS IN MM
DO NOT SCALE
A4

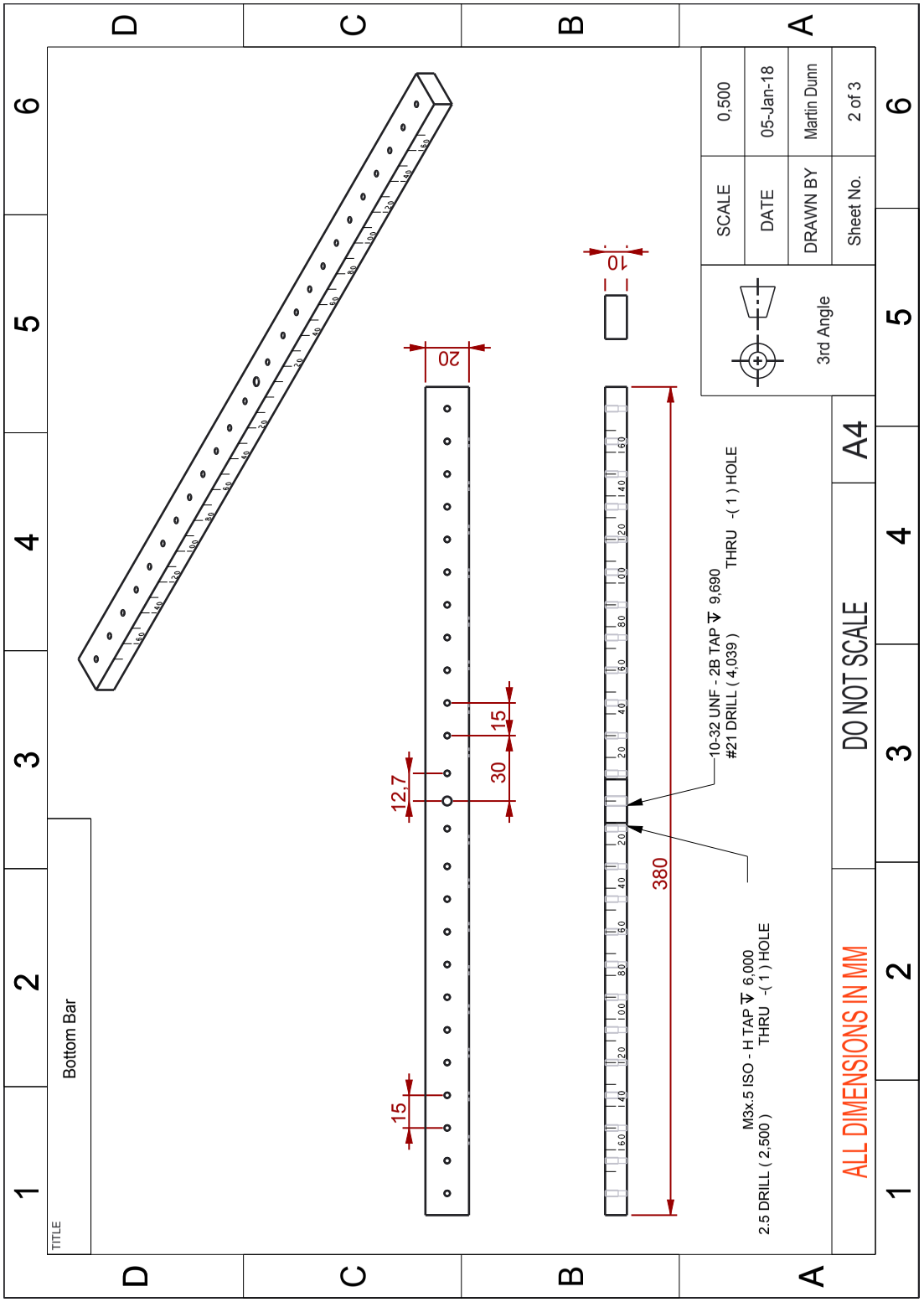
Bottom Bar
TITLE
ALL DIMENSIONS IN MM
DO NOT SCALE
A4
SCALE 0,500
DATE 05-Jan-18
DRAWN BY Martin Dunn
Sheet No. 2 of 3
3rd Angle
20
15
12,7
30
15
10
380
10-32 UNF - 2B TAP ↧ 9,690
#21 DRILL (4,039) THRU -(1) HOLE
M3x.5 ISO - H TAP ↧ 6,000
2.5 DRILL (2,500) THRU -(1) HOLE

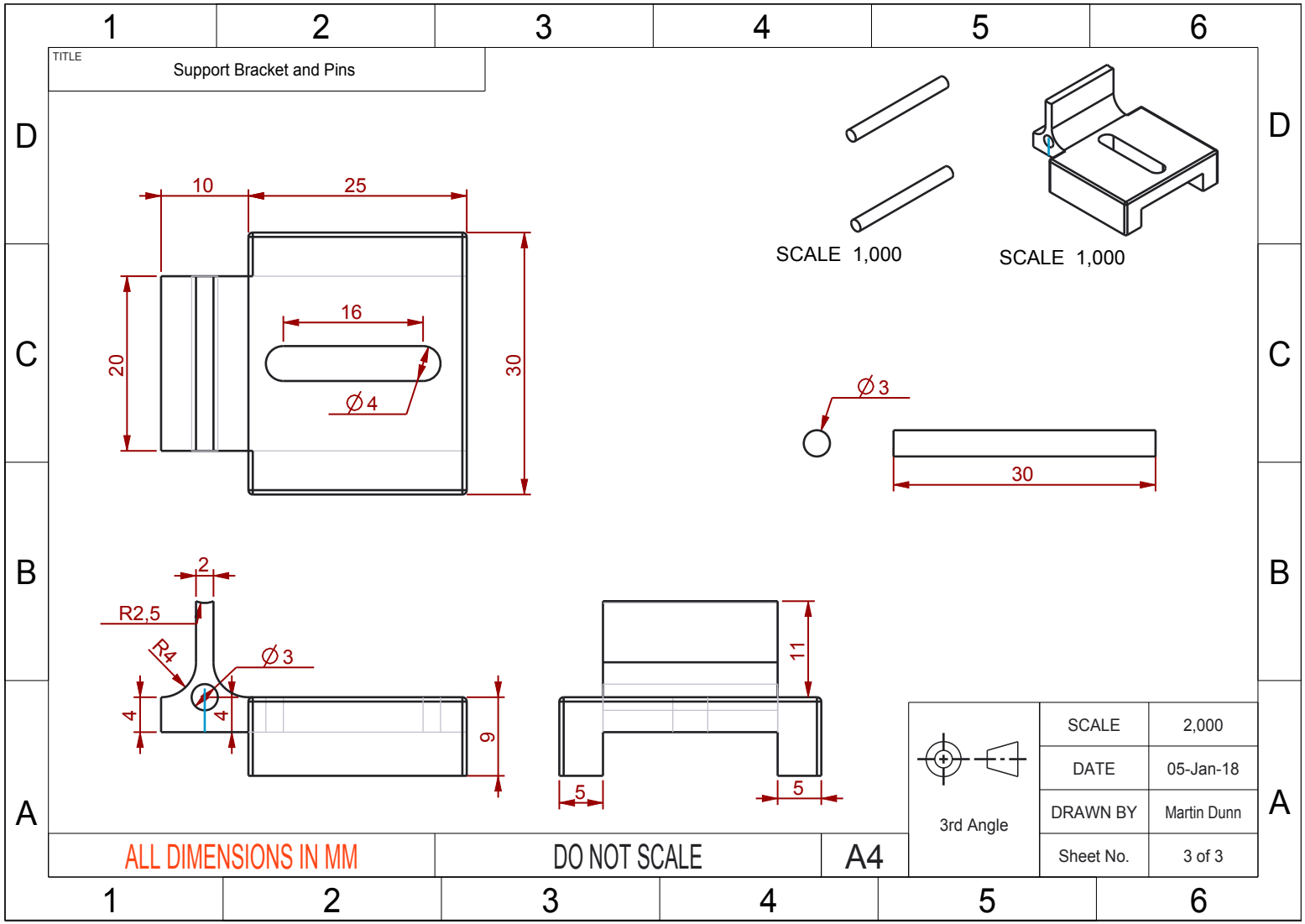
TITLE
Support Bracket and Pins
SCALE 1,000
SCALE 1,000
10
25
20
16
30
Ø4
Ø3
30
2
R2,5
R4
Ø3
4
4
9
11
5
5
ALL DIMENSIONS IN MM
DO NOT SCALE
A4
3rd Angle
SCALE 2,000
DATE 05-Jan-18
DRAWN BY Martin Dunn
Sheet No. 3 of 3

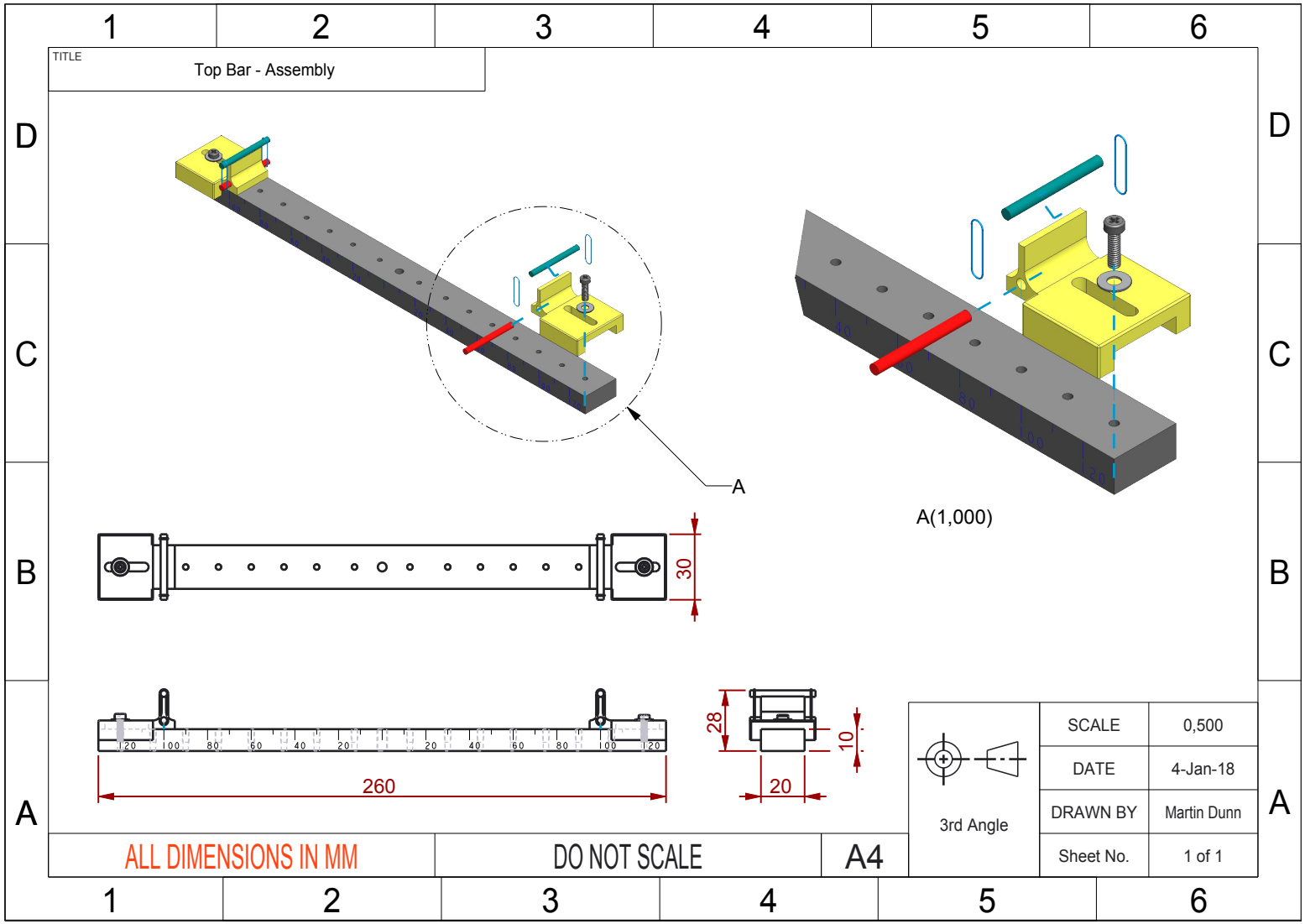
TITLE
Top Bar - Assembly
A
A(1,000)
30
260
28
10
20
3rd Angle
SCALE
0,500
DATE
4-Jan-18
DRAWN BY
Martin Dunn
Sheet No.
1 of 1
ALL DIMENSIONS IN MM
DO NOT SCALE
A4

C.2 Specimen Grips for Torsion Tests

Detailed drawings of the mounts which were manufactured to restrain the material specimens in torsional loading have been included below. Two sets of grips were manufactured with a 5×5 and 6×6 array of pins to accommodate samples with both an odd and even number of rows of microstructure through the sample cross-section. The main body of the sample holders was manufactured from aluminium, while the individual pins were composed of stainless steel. Each pin was held in place by an interference fit.

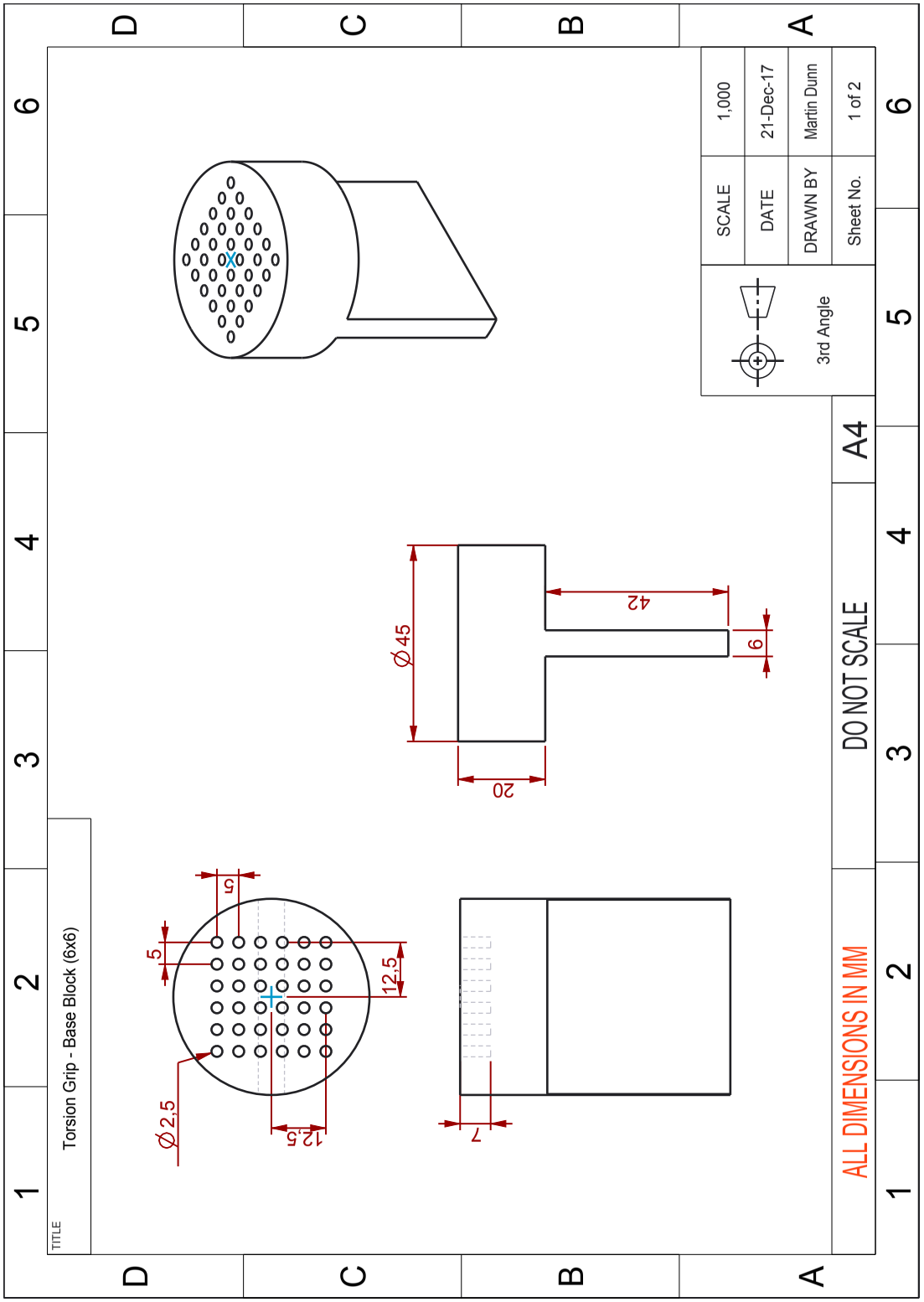
Torsion Grip - Base Block (6x6)
TITLE
ALL DIMENSIONS IN MM
DO NOT SCALE
A4
SCALE 1,000
DATE 21-Dec-17
DRAWN BY Martin Dunn
Sheet No. 1 of 2
3rd Angle
Ø45
42
6
20
7
5
5
12,5
12,5
Ø2,5

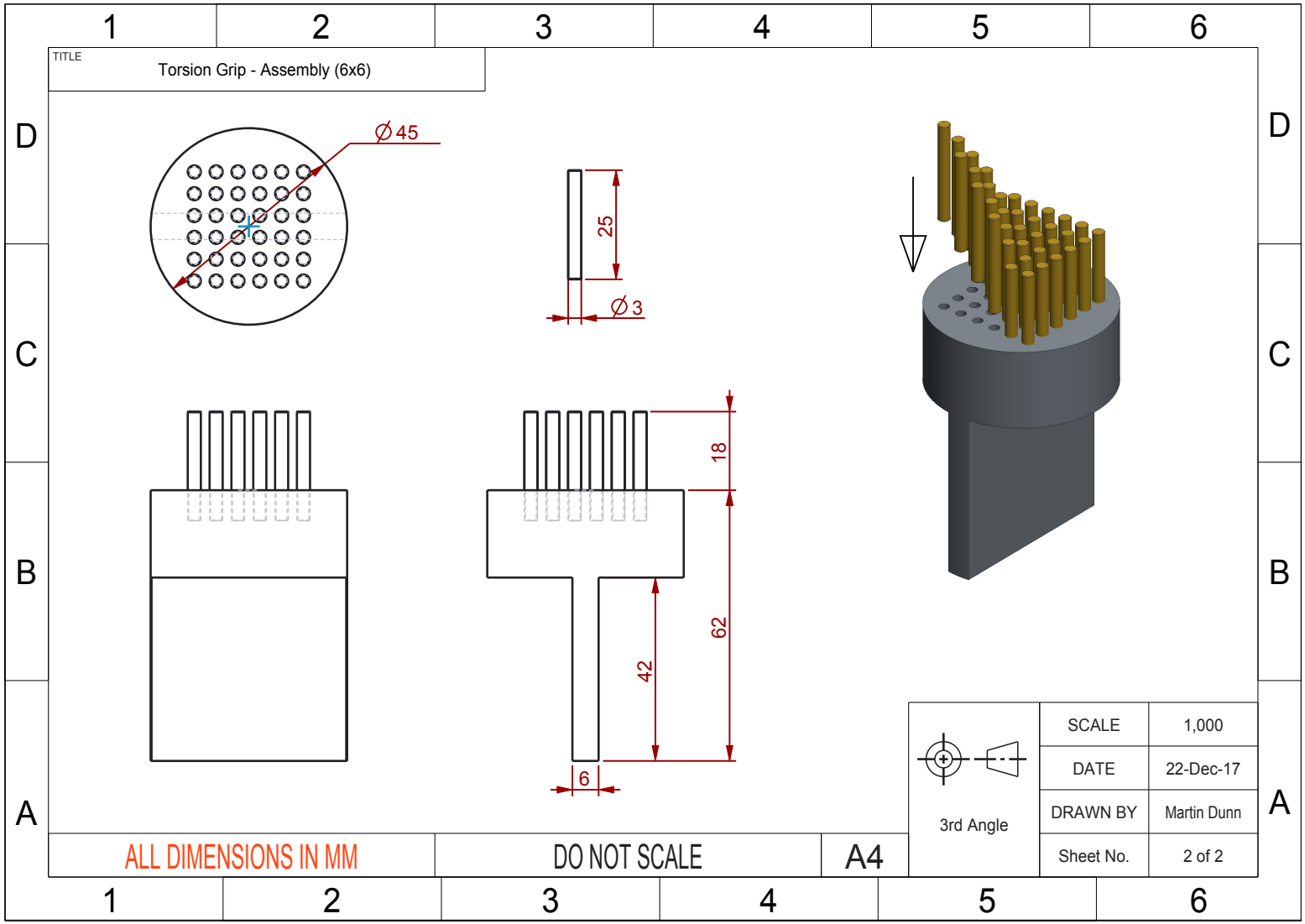
1
2
3
4
5
6
D
C
B
A
TITLE
Torsion Grip - Assembly (6x6)
Ø45
25
Ø3
18
62
42
6
3rd Angle
SCALE
1,000
DATE
22-Dec-17
DRAWN BY
Martin Dunn
Sheet No.
2 of 2
ALL DIMENSIONS IN MM
DO NOT SCALE
A4

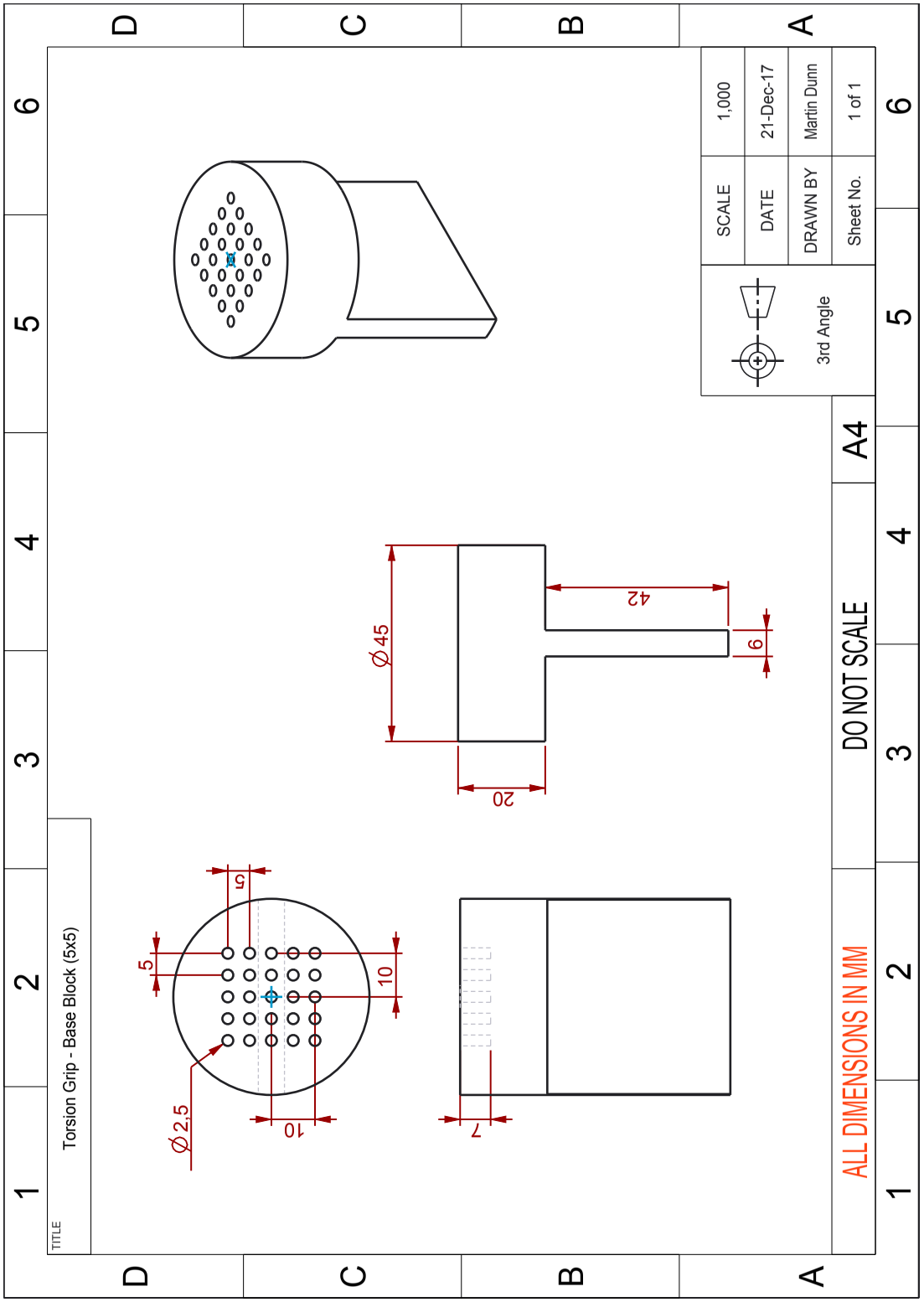
Torsion Grip - Base Block (5x5)
TITLE
ALL DIMENSIONS IN MM
DO NOT SCALE
A4
SCALE 1,000
DATE 21-Dec-17
DRAWN BY Martin Dunn
Sheet No. 1 of 1
3rd Angle
Ø45
42
6
20
5
5
10
10
Ø2,5
7

C.3 MATLAB Data Analysis

One of the problems which was encountered when conducting the three-point flexural tests was that processing the raw data was a relatively slow process which involved manually cropping both the loading and unloading portion of the load-deflection curve to determine the stiffness of individual samples. Another problem which existed initially was that some test data also demonstrated a visible level of background noise in the system due to the small applied loads which required further processing.

A MATLAB script was therefore developed to initially filter any background noise from the raw data before calculating the stiffness of the sample from the linear region of the load-deflection plot. The first stage of the script was to read in the raw data sequentially through a series of loops. This was achieved by developing a naming convention for the test files which contained the variables under investigation. Once the raw time, displacement and load data was read in for a given sample, the initial step was to remove a small portion of data from the beginning and end of the loading stage to minimise the influence of any initial settlement due to the actuator coming into contact with the specimen. As all tests were conducted over a fixed period with a constant sample rate of 20 Hz, then it was possible to identify and isolate the required portion of the conducted test for each sample from the number of data points captured.

To eliminate any unwanted noise in the data, a Butterworth filter was then applied to smooth the output data. The gradient of the smoothed data was then calculated along with the R-squared value which denotes how well the data fits the calculated correlation. If the R-squared value was found to be less than 0.999, then the data was cropped further and the process repeated until a suitable linear region was found. Generally speaking, a linear region was obtained quickly as the data was visually inspected during the test process, but as a safeguard, a limit was applied to the script in order to prevent small data sets being used to represent the sample stiffness.

The resulting stiffness of the samples were collectively recorded in tabular form to facilitate the post-processing of the data. As well as this, a series of plots were generated for each data set to visually verify that a suitable region was selected from the raw data. Tests which displayed a large degree of noise similar to figure C.2 were repeated with a 1 Hz filter applied to the test apparatus, but it is encouraging that the MATLAB script can identify a similar gradient from initially very noisy data. Figures C.2 and C.3 are two examples of unfiltered and filtered tests respectively. The differences in quality of the data are clear to see, however the stiffness which is obtained in figure C.2 closely matched figure C.3 once the data was processed in MATLAB.

A complementary script was also created to determine the stiffness of each sample from the unloading region of the tests.

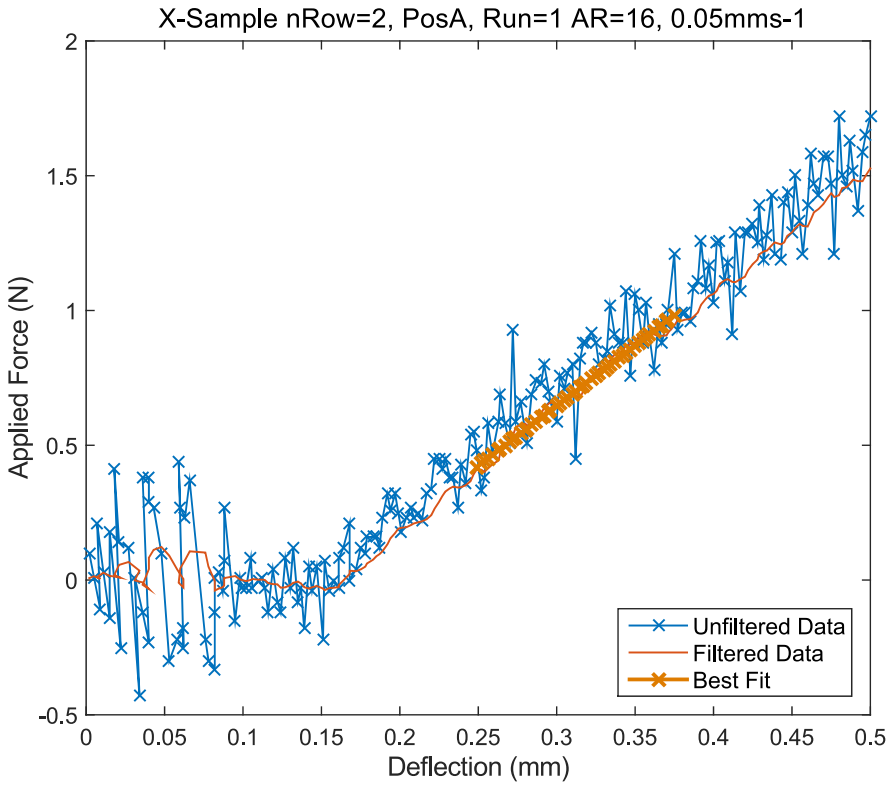

Figure C.2: Variation in load with applied deflection for a slender beam sample. The normalised stiffness, K/b, was calculated to be $0.4458 Nmm^{-2}$. Noisy data is filtered in MATLAB during processing.

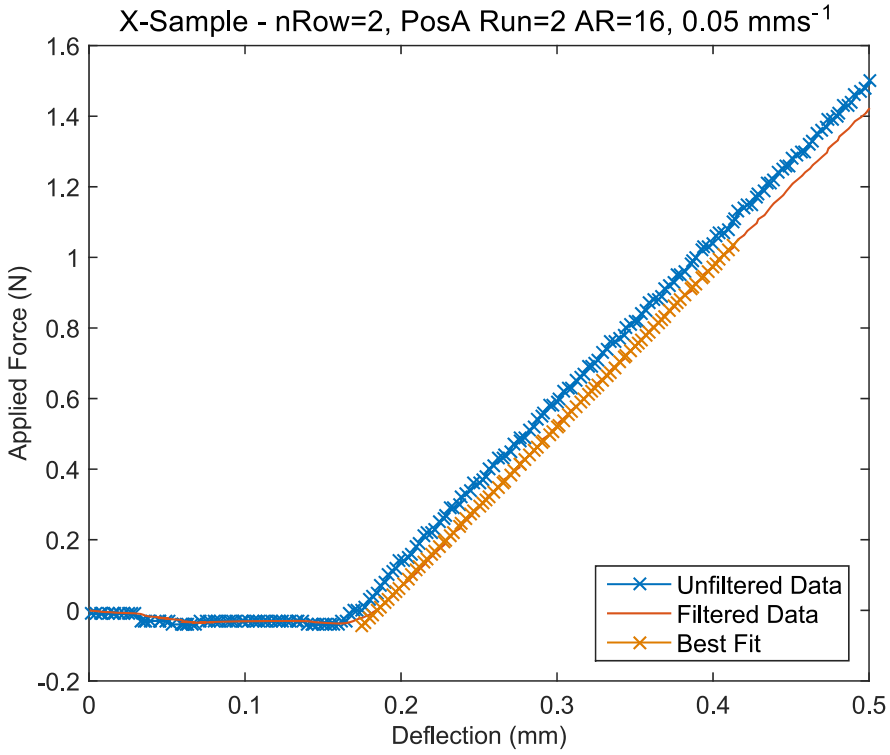

Figure C.3: Variation in load with applied deflection for a slender beam sample. The normalised stiffness, K/b, was calculated to be $0.4534 N mm^{-2}$.

Appendix D

Results of Numerical Simulations

D.1 Braced Cubic Lattice - Mechanical Properties

Braced Cubic Lattice						
ϕ_1 (mm)	ϕ_2 (mm)	V_f (%)	E^* (MPa)	G^* (MPa)	ν^*	K^* (MPa)
0.25	0.25	1.84	5.27	3.13	0.30	4.65
0.50	0.25	3.43	18.22	3.33	0.15	9.10
1.00	0.25	9.42	67.77	4.91	0.08	28.41
1.50	0.25	18.41	152.09	11.61	0.08	65.11
2.00	0.25	29.58	273.88	31.25	0.09	124.89
0.25	0.50	5.46	6.92	12.72	0.42	15.16
0.50	0.50	6.93	22.47	12.70	0.30	19.97
1.00	0.50	12.61	75.40	15.72	0.16	40.34
1.50	0.50	21.32	160.97	23.79	0.12	77.96
2.00	0.50	32.19	283.10	44.84	0.11	138.48
0.25	1.00	18.28	20.43	53.81	0.47	63.67
0.50	1.00	19.53	42.14	54.59	0.41	69.22
1.00	1.00	24.27	111.03	59.95	0.29	93.35
1.50	1.00	31.75	210.12	73.66	0.21	137.17
2.00	1.00	41.43	343.34	101.58	0.18	204.71

Table D.1: Calculated mechanical properties at varying interior beam diameters.

Bibliography

Abueidda, D. W., Bakir, M., Abu Al-Rub, R. K., Bergström, J. S., Sobh, N. A. & Jasiuk, I. 'Mechanical properties of 3D printed polymeric cellular materials with triply periodic minimal surface architectures.' *Materials & Design*, **122**, pp. 255–267 (2017).

Afshar, M., Anaraki, A. P., Montazerian, H. & Kadkhodapour, J. 'Additive manufacturing and mechanical characterization of graded porosity scaffolds designed based on triply periodic minimal surface architectures.' *Journal of the Mechanical Behavior of Biomedical Materials*, **62**, pp. 481–494 (2016).

Anderson, W. B. & Lakes, R. S. 'Size effects due to Cosserat elasticity and surface damage in closed-cell polymethacrylimide foam.' *Journal of Materials Science*, **29(24)**, pp. 6413–6419 (1994).

ASTM International. 'Standard test method for tensile properties of plastics.' (2014). URL `http://scholar.google.com/scholar?hl=en{&}btnG=Search{&}q=intitle:Standard+Test+Method+for+Tensile+Properties+of+Plastics{#}0`.

Beveridge, A. *Novel computational methods to predict the deformation of macroscopic heterogeneous materials*. Ph.D. thesis, Univerity of Strathclyde (2010).

Beveridge, A. J., Wheel, M. A. & Nash, D. H. 'The micropolar elastic behaviour of model macroscopically heterogeneous materials.' *International Journal of Solids and Structures*, **50(1)**, pp. 246–255 (2013).

Bigoni, D. & Drugan, W. J. 'Analytical Derivation of Cosserat Moduli via Homogenization of Heterogeneous Elastic Materials.' *Journal of Applied Mechanics*, **74(4)**, p. 741 (2007).

Blanco, D., Fernandez, P. & Noriega, A. 'Nonisotropic experimental characterization of the relaxation modulus for PolyJet manufactured parts.' *Journal of Materials Research*, **29(17)**, pp. 1876–1882 (2014).

Brezny, R. & Green, D. J. 'Characterization of edge effects in cellular materials.' *Journal of Materials Science*, **25(11)**, pp. 4571–4578 (1990).

Cosserat, E. & Cosserat, F. 'Theory of Deformable Bodies.' *A. Herman and Sons, Paris* (1909).

Cowin, S. C. 'An incorrect inequality in micropolar elasticity theory.' *Zeitschrift für angewandte Mathematik und Physik ZAMP*, **21(3)**, pp. 494–497 (1970).

Dai, G. & Zhang, W. 'Size effects of basic cell in static analysis of sandwich beams.' *International Journal of Solids and Structures*, **45(9)**, pp. 2512–2533 (2008).

Deshpande, V. S., Fleck, N. A. & Ashby, M. F. 'Effective properties of the octet-truss lattice material.' *Journal of the Mechanics and Physics of Solids*, **49(8)**, pp. 1747–1769 (2001).

Dos Reis, F. & Ganghoffer, J.-F. 'Construction of Micropolar Continua from the Homogenization of Repetitive Planar Lattices.' In H. Altenbach, G. A. Maugin & V. Erofeev, editors, 'Mechanics of Generalized Continua,' volume 7 of *Advanced Structured Materials*, pp. 193–217. Berlin, Heidelberg: Springer Berlin Heidelberg (2011).

Dos Reis, F. & Ganghoffer, J.-F. 'Construction of micropolar continua from the asymptotic homogenization of beam lattices.' *Computers & Structures*, **112-113**, pp. 354–363 (2012).

Drugan, W. J. & Willis, J. R. 'A micromechanics-based nonlocal constitutive equation and estimates of representative volume element size for elastic composites.' *Journal of the Mechanics and Physics of Solids*, **44(4)**, pp. 497–524 (1996).

Dunn, M. A. & Wheel, M. A. 'Computational Analysis of the Size Effects Displayed in Beams with Lattice Microstructures.' In H. Altenbach & S. Forest, editors, 'Generalized Continua as Models for Classical and Advanced Materials,' chapter 6, pp. 129–143. Springer International (2016).

Ellis, R. W. & Smith, C. W. 'A thin-plate analysis and experimental evaluation of couple-stress effects.' *Experimental Mechanics*, **7(9)**, pp. 372–380 (1967).

Eringen, A. C. 'Linear Theory of Micropolar Elasticity.' *Journal of Mathematics and Mechanics*, **15(6)**, pp. 909–923 (1966).

Eringen, A. C. 'Linear theory of micropolar viscoelasticity.' *International Journal of Engineering Science*, **5**, pp. 191–204 (1967).

Eringen, A. C. *Microcontinuum Field Theories I. Foundations and Solids*. New York, NY: Springer New York (1999).

Eringen, A. C. & Suhubi, E. 'Nonlinear theory of simple micro-elastic solids—I.' *International Journal of Engineering Science*, **2(2)**, pp. 189–203 (1964).

Frame, J. C. *A computational and experimental investigation into the micropolar elastic behaviour of cortical bone*. Ph.D. thesis, University of Strathclyde (2013).

Gauthier, R. D. & Jahsman, W. E. 'A Quest for Micropolar Elastic Constants.' *Journal of Applied Mechanics*, **42(2)**, pp. 369–374 (1975).

Gauthier, R. D. & Jahsman, W. E. 'Bending of a curved bar of micropolar elastic material.' *Journal of applied Mechanics*, **43(3)**, pp. 502–3 (1976).

Gibson, I., Rosen, D. & Stucker, B. *Additive Manufacturing Technologies*. New York, NY: Springer New York, 2nd edition (2015).

Gibson, L. J. & Ashby, M. F. 'The Mechanics of Three-Dimensional Cellular Materials.' *Proceedings of the Royal Society A: Mathematical, Physical and Engineering Sciences*, **382(1782)**, pp. 43–59 (1982).

Gibson, L. J. & Ashby, M. F. *Cellular Solids Structures and Properties*. Cambridge University Press, 2nd edition (1999).

Gibson, L. J., Ashby, M. F., Schajer, G. S. & Robertson, C. I. 'The Mechanics of Two-Dimensional Cellular Materials.' *Proceedings of the Royal Society A: Mathematical, Physical and Engineering Sciences*, **382(1782)**, pp. 25–42 (1982).

Goda, I., Assidi, M. & Ganghoffer, J.-F. 'A 3D elastic micropolar model of vertebral trabecular bone from lattice homogenization of the bone microstructure.' *Biomechanics and Modeling in Mechanobiology*, **13(1)**, pp. 53–83 (2014).

Goda, I. & Ganghoffer, J.-F. 'Identification of couple-stress moduli of vertebral trabecular bone based on the 3D internal architectures.' *Journal of the Mechanical Behavior of Biomedical Materials*, **51**, pp. 99–118 (2015).

Goda, I. & Ganghoffer, J. F. 'Construction of first and second order grade anisotropic continuum media for 3D porous and textile composite structures.' *Composite Structures*, **141**, pp. 292–327 (2016).

Gu, S., Lu, T. J. & Evans, A. G. 'On the design of two-dimensional cellular metals for combined heat dissipation and structural load capacity.' *International Journal of Heat and Mass Transfer*, **44(11)**, pp. 2163–2175 (2001).

Ha, C. S., Plesha, M. E. & Lakes, R. S. 'Chiral three-dimensional isotropic lattices with negative Poisson's ratio.' *Physica Status Solidi (B) Basic Research*, **1251(7)**, pp. 1243–1251 (2016).

Hassanpour, S. & Heppler, G. R. 'Step-by-Step Simplification of the Micropolar Elasticity Theory to the Couple-Stress and Classical Elasticity Theories.' In 'International Mechanical Engineering Congress and Exposition IMECE2014,' pp. 1–9 (2014).

Huang, F.-Y., Yan, B.-H., Yan, J.-L. & Yang, D.-U. 'Bending analysis of micropolar elastic beam using a 3-D finite element method.' *International Journal of Engineering Science*, **38(3)**, pp. 275–286 (2000).

Javanbakht, Z. & Öchsner, A. *Computational Statics Revision Course*. Springer International Publishing (2018).

Kumar, R. S. & McDowell, D. L. 'Generalized continuum modeling of 2-D periodic cellular solids.' *International Journal of Solids and Structures*, **41(26)**, pp. 7399–7422 (2004).

Kumar, R. S. & McDowell, D. L. 'Multifunctional design of two-dimensional cellular materials with tailored mesostructure.' *International Journal of Solids and Structures*, **46(14-15)**, pp. 2871–2885 (2009).

Lakes, R. 'Experimental microelasticity of two porous solids.' *International Journal of Solids and Structures*, **22(1)**, pp. 55–63 (1986).

Lakes, R. S. 'Size effects and micromechanics of a porous solid.' *Journal of Materials Science*, **18(9)**, pp. 2572–2580 (1983).

Lakes, R. S. & Drugan, W. 'Bending of a Cosserat Elastic Bar of Square Cross Section - Theory and Experiment.' *Journal of Applied Mechanics*, **82(September)**, pp. 1–8 (2015).

Li, T. & Wang, L. 'Bending Behavior of Sandwich Composite Structures with Tunable 3D-Printed Core Materials.' *Composite Structures*, **175**, pp. 46–57 (2017).

Luxner, M. H., Stampfl, J. & Pettermann, H. E. 'Finite element modeling concepts and linear analyses of 3D regular open cell structures.' *Journal of Materials Science*, **40(22)**, pp. 5859–5866 (2005).

Masters, I. G. & Evans, K. E. 'Models for the elastic deformation of honeycombs.' *Composite Structures*, **35(1996)**, pp. 403–422 (1997).

Mindlin, R. 'Micro-structure in linear elasticity.' *Archive for Rational Mechanics and Analysis*, **16(1)**, pp. 51–78 (1964).

Mindlin, R. 'Stress functions for a Cosserat continuum.' *International Journal of Solids and Structures*, **I**, pp. 265–271 (1965).

Mindlin, R. D. & Tiersten, H. F. 'Effects of couple-stresses in linear elasticity.' *Archive for Rational Mechanics and Analysis*, **11(1)**, pp. 415–448 (1962).

Mueller, J., Shea, K. & Daraio, C. 'Mechanical properties of parts fabricated with inkjet 3D printing through efficient experimental design.' *Materials & Design*, **86**, pp. 902–912 (2015).

Nowacki, W. 'The Linear Theory of Micropolar Elasticity.' In 'Micropolar Elasticity,' volume 1, pp. 1–43. Springer (1974).

Nowacki, W. *Theory of Asymmetric Elasticity*. Elsevier, 2nd edition (1986).

Park, H. & Lakes, R. 'Torsion of a micropolar elastic prism of square cross-section.' *International journal of solids and structures*, **23(4)**, pp. 485–503 (1987).

Pradel, F. & Sab, K. 'Cosserat modelling of elastic periodic lattice structures.' *Comptes Rendus de l'Academie de Sciences - Serie IIb: Mecanique, Physique, Chimie, Astronomie*, **326**, pp. 699–704 (1998).

Rahali, Y., Goda, I. & Ganghoffer, J.-F. 'Numerical identification of classical and nonclassical moduli of 3D woven textiles and analysis of scale effects.' *Composite Structures*, **135**, pp. 122–139 (2016).

Ramsay, A. & Maunder, E. 'The Influence and Modelling of Warping Restraint on Beams.' *www.ramsay-maunder.co.uk* (2014).

Reddy, G. & Venkatasubramanian, N. 'On the flexural rigidity of a micropolar elastic circular cylindrical tube.' *International Journal of Engineering Science*, **17(9)**, pp. 1015–1021 (1979).

Roark, R. J., Young, W. C. & Plunkett, R. *Formulas for Stress and Strain*. McGraw-Hill, 7th edition (2002).

Rueger, Z. & Lakes, R. S. 'Experimental Cosserat elasticity in open-cell polymer foam.' *Philosophical Magazine*, **96(2)**, pp. 93–111 (2016).

Schijve, J. 'Note on couple stresses.' *Journal of the Mechanics and Physics of Solids*, **14(2)**, pp. 113–120 (1966).

Stratasys Ltd. 'PolyJet Technology | Stratasys.' (2017). URL `http://www.stratasys.com/3d-printers/technologies/polyjet-technology`.

Tekoglu, C. & Onck, P. 'Size effects in two-dimensional Voronoi foams: A comparison between generalized continua and discrete models.' *Journal of the Mechanics and Physics of Solids*, **56(12)**, pp. 3541–3564 (2008).

Tekoğlu, C. *Size effects in cellular solids*. Ph.D. thesis, University of Groningen (2007). URL `http://www.narcis.nl/publication/RecordID/oai:ub.rug.nl:dbi/45a62baa835ee`.

Underdahl, B. *Digital manufacturing for Dummies*. John Wiley & Sons, Inc. (2015).

Voigt, W. 'Theoretical studies in the elastic behavior of crystals.' In 'Presented at the session of the Royal Society of Science on 2 July 1887,' pp. 1–43 (1887).

Wang, A.-J. & McDowell, D. L. 'In-Plane Stiffness and Yield Strength of Periodic Metal Honeycombs.' *Journal of Engineering Materials and Technology*, **126(2)**, p. 137 (2004).

Waseem, A., Beveridge, A. J., Wheel, M. A. & Nash, D. H. 'The influence of void size on the micropolar constitutive properties of model heterogeneous materials.' *European Journal of Mechanics, A/Solids*, **40**, pp. 148–157 (2013).

Wheel, M. A., Frame, J. C. & Riches, P. E. 'Is smaller always stiffer? On size effects in supposedly generalised continua.' *International Journal of Solids and Structures*, **67-68**, pp. 84–92 (2014).

Yang, J. & Lakes, R. 'Transient Study of Couple Stress Effects in Compact Bone: Torsion.' *Journal of Biomechanical Engineering*, **103**, pp. 275–279 (1981).

Yang, J. & Lakes, R. 'Experimental study of micropolar and couple stress elasticity in compact bone in bending.' *Journal of biomechanics*, **15**, pp. 91–98 (1982).

Yoo, A. & Jasiuk, I. 'Couple-stress moduli of a trabecular bone idealized as a 3D periodic cellular network.' *Journal of Biomechanics*, **39**, pp. 2241–2252 (2006).

Image Bibliography

Figure 1.1 (a) "Reprinted from Chemical Engineering Journal, **174(1)**, Montserrat López-Mesas,Enrique Ruperto Navarrete,Fernando Carrillo,Cristina Palet, Bioseparation of Pb(II) and Cd(II) from aqueous solution using cork waste biomass. Modeling and optimization of the parameters of the biosorption step, pp.9-17, Copyright (2011), with permission from Elsevier."

Figure 1.1 (b) This photo of beehive honeycomb was adapted from an image by an anonymous author taken on March 18 2017 under the Creative Commons 1.0 licence. It was last accessed on November 8 2018 from `https://pxhere.com/en/photo/1183648`.

Figure 1.1 (c) This photo of natural sponge was adapted from the image taken by Johan was uploaded on August 11 2006 and reproduced under the Creative Commons 3.0 licence. It was last accessed on November 8 2018 from `https://commons.wikimedia.org/wiki/File:Sponge-viscose.jpg`.

Figure 1.2 (a) This image of a closed cell metallic foam by Curran2 was uploaded on August 11 2005 and reproduced under the Creative Commons 3.0 licence. It was last accessed on November 8 2018 from `https://commons.wikimedia.org/wiki/File:Closed_cell_metal_foam_with_large_cell_size.JPG`.

Figure 1.2 (b) This image of an open cell polyurethane foam was reproduced with the permission of Gibson LJ and Ashby MF (1997) *Cellular Solids Structures and Properties*. Second Edition (1999), Cambridge University Press.

Figure 1.2 (c) This photo of an aluminium 3D printed lattice structure was reproduced with the permission of Dahlon P Lyles and 3rd Dimension Industrial 3D Printing (3rd Dimension LLC). It was last accessed on November 8 2018 from `https://3dprint.com/29958/3d-printed-aluminum-lattice/`.